

# UC San Diego

## UC San Diego Electronic Theses and Dissertations

**Title**

Tailored net-shape powder composites by spark plasma sintering

**Permalink**

<https://escholarship.org/uc/item/94f0h6bj>

**Author**

Khaleghi, Evan Aryan

**Publication Date**

2012

Peer reviewed|Thesis/dissertation

UNIVERSITY OF CALIFORNIA, SAN DIEGO  
SAN DIEGO STATE UNIVERSITY

Tailored Net-Shape Powder Composites by Spark Plasma Sintering

A dissertation submitted in partial satisfaction of the  
requirements for the degree Doctor of Philosophy

in

Engineering Science (Mechanical and Aerospace Engineering)

by

Evan Aryan Khaleghi

Committee in Charge:

University of California, San Diego

Professor Marc Meyers, Co-chair  
Professor David Benson  
Professor Frank Talke

San Diego State University

Professor Eugene Olevsky, Chair  
Professor Randall German

2012



The Dissertation of Evan Aryan Khaleghi is approved, and it is acceptable in quality and form for publication on microfilm and electronically:

---

---

---

---

Co-Chair

---

Chair

University of California, San Diego  
San Diego State University

2012

## **Dedication**

This dissertation is dedicated to Erin, and my father, without whom I could never have finished this ordeal. Their support kept me going through the darkest times, and I will be eternally grateful.

## Epigraph

Lord Sanenori once said, “As for the things that we don’t understand, there *are* ways of understanding them. Furthermore, there are some things we understand just naturally, and again some that we can’t understand no matter how hard we try. This is interesting.”

...It is natural that one cannot understand deep and hidden things. Those things that are easily understood are rather shallow.



If a retainer will just think about what he is to do for the day at hand, he will be able to do anything. If it is a single day’s work, one should be able to put up with it. Tomorrow, too, is but a single day.



There is surely nothing other than the single purpose of the present moment. A man’s whole life is a succession of moment after moment. If one fully understands the present moment, there will be nothing else to do, and nothing else to pursue. Live being true to the single purpose of the moment.

Everyone lets the present moment slip by, then looks for it as though he thought it was somewhere else... But grasping this firmly, one must pile experience upon experience. And once one has come to this understanding he will be a different person from that point on, though he may not always bear it in mind.



In the Kamigata area, they have a sort of tiered lunch box they use for a single day when flower viewing. Upon returning, they throw them away, trampling them underfoot... The end is important in all things.

**Yamamoto Tsunetomo, *Hagakure***

## Table of Contents

Signature Page.....	iii
Dedication.....	iv
Epigraph.....	v
Table of Contents.....	vi
List of Figures.....	viii
List of Equations.....	xiii
List of Tables.....	xvi
Acknowledgements.....	xvii
Vita.....	xviii
Abstract of the Dissertation .....	xx
Chapter 1. Introduction: Literature Survey.....	1
1.1 Fundamental analysis of spark plasma sintering .....	1
1.2. General overview of densification and structure evolution during SPS .....	15
1.2.1. Densification and structure evolution during SPS of Alumina.....	23
1.2.2. Densification and structure evolution of iron and vanadium carbide .....	25
1.2.3. Densification and structure evolution of tantalum carbide .....	29
1.3. SPS of complex shape components .....	32
1.4. Conclusions of conducted literature survey .....	39
Chapter 2. Research Objectives .....	42
Chapter 3. Shape factor in SPS processing.....	43
3.1. Introduction to spark plasma sintering of alumina .....	43
3.2. Fundamental experiments on the specimen's shape impact on the SPS densification and grain growth kinetics .....	46
3.2.1. Experimental work on the shape impact in spark plasma sintering of alumina using two die designs.....	46
3.2.2. Initial experimental design with two die designs.....	48
3.2.3. Experimental Results on shape impact on SPS of alumina with two die designs.....	50
3.2.4. Discussion of shape impact on SPS of alumina with two die designs.....	60
3.2.5. Introduction to shape impact on spark plasma sintering of alumina with four die designs.....	60
3.2.6. Experimental work conducted on shape impact on SPS of alumina using four die designs.....	62
3.2.7. Results and discussion of shape impact on SPS of alumina using four die designs.....	66
3.3. Modeling of the influence of the specimen's shape in SPS.....	72
3.4. Discussion.....	76
Chapter 4. SPS combined with extrusion .....	78
4.1. Spark plasma extrusion setup and experimental results .....	80
4.1.1. Experimental description for Spark Plasma Extrusion .....	81
4.1.2. Results for densification and grain growth in spark plasma extrusion .....	90
4.2. Results and discussion .....	92

Chapter 5. Processing by SPS of tailored powder composites .....	109
5.1. SPS of tantalum carbide and tantalum carbide-carbon nanotube composites .....	109
5.1.1. Experimental Procedure for SPS of TaC .....	110
5.1.2. Results on the spark sintering of TaC .....	114
5.1.3. Conclusions on the densification and grain growth in spark sintering of TaC .....	124
5.2. SPS of Fe-VC high strength steel .....	125
5.2.1. Preliminary experimental work on Fe-V-C from Fe-0.5V powder .....	127
5.2.2. Preliminary results on Fe-V-C from Fe-0.5V powder .....	129
5.2.3. Experimental work on Fe-15V and Fe-0.5V/Fe-15V mixed powders.....	150
5.2.4. Preliminary results on the Fe-0.5V/Fe-15V mixed steel .....	155
5.2.5. Results of densification and grain growth of Fe-0.5V/Fe-15V mixed steels	161
Chapter 6. Densification and grain growth kinetics in SPS.....	165
Chapter 7. Conclusions .....	185
Chapter 8. Scientific and engineering novelty of research results.....	188
Chapter 9. Appendix .....	189
9.1. Equipment Overview .....	189
9.2. Statistical Analysis of Data for Curve-fitting .....	193
9.3. Taguchi DOE data for Alumina .....	195
Chapter 10. References .....	198



## List of Figures

Figure 1. A temperature and pressure profile for current-assisted multi-step pressure dilatometry that was used to find the creep exponent m.....	5
Figure 2. A diagram of the densification rate vs. relative density at the instantaneous pressure change regions, used to calculate the creep exponent m. ....	5
Figure 3. The measured creep exponent, m, values compared to the sintering temperature of the experiments.....	6
Figure 4. A set of research shows a $\epsilon^{-1/2}$ relationship between grain size and porosity in sintering of alumina, taken directly from Suzuki et al.....	17
Figure 5. Conventional sintering of alumina and yttria (in air) shows a $\epsilon^{-1/2}$ relationship between grain size and relative density, taken from Bernard-Granger et al.....	18
Figure 6. Slip-casting of alumina (in air) confirms a $\epsilon^{-1/2}$ relationship between grain size and relative density, taken from Bernard-Granger et al.....	19
Figure 7. A diagram of the uniform properties in various parts of a square WC-Co-Ni specimen, from Tokita. ....	33
Figure 8. A diagram showing a special SPS die for creating nozzles, where area 54 is the empty space for powder, 38 is the cylindrical center piece, and 87 is the tapered, removable insert. From Kaneuchi and Morita .....	34
Figure 9. A diagram of an spark plasma extrusion setup, from Morsi, et al.....	39
Figure 10. Density evolution curves for -325 mesh alumina powder, sintered for 8 minutes at pressure 37 MPa in a cylindrical (A) and prismatic (B) die, at 1200, 1300 and 1400 C. ....	52
Figure 11. Comparison of density vs. time of alumina powder sintered in two shaped dies, with holding temperature 1300 C and an applied pressure of 50 MPa. (A) 8 minutes at the holding temperature, (B) 15 minutes at the holding temperature , and (C) 40 minutes at the holding temperature.....	53
Figure 12. Density evolution for alumina powder in circular, square a (with sharp outside corners), and square b (with rounded outer corners) dies, sintered at 1300 C for 15 minutes, with an applied pressure of 50 MPa.....	55
Figure 13. A diagram showing a sintered cylindrical specimen (left) and a prismatic specimen (right), with images (at 5,000x magnification) of the center and edge of a cross-section of the specimen. ....	58
Figure 14. The image on the left is the initial SEM image, and the right is the manipulated image with only the pores showing.....	59
Figure 15. Prismatic die design, with aspect ratio of 2.25.....	64
Figure 16. Prismatic die design with an aspect ratio of 4.59. ....	65
Figure 17. A description of where the two SEM images were taken for each specimen, to examine grain structure.....	66
Figure 18. A chart showing the grain size difference in each area, by specimen.....	68
Figure 19. A plot of grain size versus specimen shape shows that average grain size decreases as the aspect ratio of the specimen increases.....	69

Figure 20. The grain structure in the center and corner of the four specimens can be seen. There is little difference between the areas in each specimen. ....	71
Figure 21. (A) The configuration used for square die modeling in COMSOL, with the die being transparent and the punches highlighted. (B) The die model with arrows indicating current density during sintering. The temperature distribution during sintering in a (C) longitudinal cross-section, and (D) a transverse cross-section. ....	74
Figure 22. (A) The configuration used for cylindrical die modeling in COMSOL, with the die being transparent and the punches highlighted. (B) A die model with arrows indicating current density during sintering. The temperature distribution during sintering in a (C) longitudinal cross-section, and (D) a transverse cross-section. ....	74
Figure 23. A picture of the extrusion die, with the parabolic curve for extrusion. ....	79
Figure 24. The design of the curved punch, used for creating specimens with the opposite shape of the die. ....	79
Figure 25. A diagram of the steel ring that will hold the graphite SPS extrusion fixture during the sintering process. ....	83
Figure 26. A diagram showing the designed extrusion die, to be made from graphite or steel. ....	84
Figure 27. The initial aluminum powder used in all of the SPS and extrusion experiments is non-uniform in size and irregularly shaped. ....	85
Figure 28. Grains of varying sizes and shapes are present in the pre-sintered specimen. ....	87
Figure 29. A cross-sectional view of the specimen 1, with SEM images of the approximate regions superimposed. Average grain size is 12.1 $\mu\text{m}$ , and average porosity is 3.1%. ....	94
Figure 30. A cross-sectional view of the specimen 2, with SEM images of the approximate regions superimposed. Average grain size is 14.7 $\mu\text{m}$ , and average porosity is 3.1%. ....	96
Figure 31. A cross-sectional view of the specimen 3, with SEM images of the approximate regions superimposed. Average grain size is 16.0 $\mu\text{m}$ , and average porosity is 3.0%. ....	98
Figure 32. A cross-sectional view of the specimen 4, with SEM images of the approximate regions superimposed. Average grain size is 13.9 $\mu\text{m}$ , and average porosity is 1.8%. ....	100
Figure 33. A cross-sectional view of the specimen 5, with SEM images of the approximate regions superimposed. Average grain size is 15.9 $\mu\text{m}$ , and average porosity is 3.4%. ....	102
Figure 34. A cross-sectional view of the specimen 6, with SEM images of the approximate regions superimposed. Average grain size is 15.9 mm, and average porosity is 4.0%. ....	104
Figure 35. Average grain size gradients versus temperature, showing an increasing grain size difference between the center and side of the specimens as temperature is increased. ....	107

Figure 36. Average grain size gradients versus temperature, showing a slight increase in grain size difference between the center and side of the specimens as temperature increased.....	108
Figure 37. A picture and schematic drawing of our Tensile Rupture Strength setup. ....	112
Figure 38. Temperature and density evolution during sintering of TaC powder heated to 1900 C, with 30 MPA pressure and 5 minutes holding time. ....	116
Figure 39. Temperature and density evolution during sintering of TaC powder heated to 2300 C, with 30 MPA pressure and 5 minutes holding time. ....	116
Figure 40. Temperature and density evolution during sintering of TaC powder heated to 2300 C, with 30 MPA pressure and 20 minutes holding time. ....	117
Figure 41. Temperature and density evolution during sintering of TaC powder heated to 2400 C, with 75 MPA pressure and 10 minutes holding time. ....	117
Figure 42. Temperature and density evolution during sintering of TaC-CNT composite powder heated to 2300 C with 30 MPa pressure and 20 minutes holding time. ....	118
Figure 43. TaC specimen heated to 1900 C, with 30 MPa pressure, 5 minutes holding time, and 68% relative density. ....	120
Figure 44. TaC specimen heated to 2300 C, with 30 MPa pressure, 5 minutes holding time, and 83% relative density. ....	120
Figure 45. TaC specimen heated to 2300 C, with 30 MPa pressure, 20 minutes holding time, and 92% relative density. Significant grain growth is present compared to Figure 20. ....	121
Figure 46. TaC specimen heated to 2400 C, with 75 MPa pressure, 10 minutes holding time, and 97% relative density. The significant grain growth and grain boundary porosity are evident. ....	121
Figure 47. TaC-CNT composite specimen, heated to 2300 C, with 30 MPa pressure, 20 minutes holding time, and 96% relative density. ....	122
Figure 48. . Fe-0.5 V RS powders: a) SEM micrograph and b) EDS microanalysis from metallic powders. ....	128
Figure 49. Sample N. 4 – D< 22 mm, SPS at 700 °C, 15min, 75MPa: (left) center and (right) edge regions. ....	131
Figure 50. Sample N. 2, D< 10 mm, 700 °C, 75MPa: a) external and b) central regions. ....	132
Figure 51. SPS specimens prepared using a die lined with: a) carbon paper, b) BN. ....	133
Figure 52. Sample N.4: 22µm (not etched). A particle that did not incorporate during sintering is evident in the lower center of the image. ....	134
Figure 53. EDX-microanalysis from SPS sintered samples. ....	134
Figure 54. Sample N.4: 22µm (etched). ....	135
Figure 55. EDX-microanalysis from SPS sintered samples. ....	136
Figure 56. EDX-microanalysis from SPS sintered samples. Stainless steel inclusion indicated. ....	137
Figure 57. EDX-microanalysis from SPS sintered samples. Stainless steel inclusion characterized. ....	138
Figure 58. Hardness test points (quarter of cross sectional area) ....	139

Figure 59. . Hardness distribution along different radial locations - (a) Surface layer, (b) Intermediate layer.....	140
Figure 60. Hardness distribution along different axial layers - (a) Edge, (b) Middle, (c) Center. ....	141
Figure 61. Particle size and heat treatment effects on hardness. ....	142
Figure 62. Specimen from 22 $\mu$ m powder. Carbon paper coated die. Effect of carbon diffusion is evident in the increase in hardness value from edge to center.....	142
Figure 63. Specimen from 10 $\mu$ m powder. Carbon paper coated die. Effect of carbon diffusion is again evident from the increase in hardness from edge to center. ....	143
Figure 64. TEM micrograph showing microstructural features of as-sintered SPS Fe- 0.5V RS powders. ....	144
Figure 65. TEM micrograph showing microstructural features of as-sintered SPS Fe- 0.5V RS powders. ....	145
Figure 66. TEM micrograph showing microstructural features of as-sintered SPS Fe- 0.5V RS powders. ....	146
Figure 67. TEM micrograph showing microstructural features of as-sintered SPS Fe- 0.5V RS powders. ....	147
Figure 68. TEM micrograph showing microstructural features of sintered Fe-0.5V powders, after heat treatment at 600 °C for 1 hour. ....	148
Figure 69. TEM micrograph showing precipitation of nanosized (< 5 nm), coherent VC particles in the ferritic matrix, after SPS and heat treatment at 600 °C for 1 hour. ....	149
Figure 70. Selected Area Diffraction Pattern (SADP) with B close to [110] $\alpha$ -Fe with evidence of extra-spots from $V_4C_3$ and surface $Fe_3O_4$ .....	150
Figure 71. Fe-15V RS powders: left) SEM micrograph and right) EDS microanalysis from metallic powders .....	152
Figure 72. XRD spectrum from Fe-0.5V powders. ....	153
Figure 73. XRD spectrum from Fe-15V powders. ....	153
Figure 74. XRD spectrum from as-consolidated (SPS) specimen X. ....	156
Figure 75. . Different etching response from Fe.0.5V and Fe-15V SPS consolidated powders (in the same specimen). ....	157
Figure 76. Different density between left) external and right) central regions of mixed Fe-0.5V/Fe-15V SPS sample V. ....	157
Figure 77. XRD spectrum from SPS consolidated Sample V + heat treating 1 hour at 600 °C. ....	158
Figure 78. TEM image of specimen X, as-consolidated.....	159
Figure 79. Another TEM image of specimen X, as-consolidated.....	160
Figure 80. XRD analysis of specimen X, as-consolidated.....	161
Figure 81. Densification and grain growth behavior for spark sintering of alumina, with a focus on the high density area. We can see that the data clearly fits an $\epsilon^{-1/2}$ relationship, with $k = 0.56$ , a perfect fit for the model (correlation 0.987).....	179
Figure 82. Similar to Figure 81, but without the focus on high density. ....	180
Figure 83. Spark sintering of one grade of titanium, focused on the high density area, shows a $\epsilon^{-1/2}$ relationship between grain size and porosity, with $n = 0.5$ and $k =$ .59, like the ideal model (correlation 0.96). ....	181

Figure 84. Similar to Figure 83, but without the focus on high density. ....	182
Figure 85. Spark sintering of another grade of titanium, focused on the high density area, shows a $\varepsilon^{-1/2}$ relationship between grain size and porosity, with $n = 0.5$ and $k = .5$ , exactly like the ideal model (correlation 0.99). ....	183
Figure 86. Similar to Figure 85, but without the focus on high density. ....	184
Figure 87. Z-axis displacement versus temperature curve used to find the CTE equation for the graphite tooling. ....	190

## List of Equations

Equation 1.	$\sigma_{ij} = \frac{\sigma(W)}{W} \left[ \phi \dot{\epsilon}_{ij} + \left( \psi - \frac{1}{3} \phi \right) \dot{\epsilon} \delta_{ij} \right] + P_L \delta_{ij}$	3
Equation 2.	$\sigma_{ij} = \frac{\sigma(W)}{W} \left[ \phi \dot{\epsilon}_z + \left( \psi - \frac{1}{3} \phi \right) \dot{\epsilon} \right]$	3
Equation 3.	$\sigma_z = A \sqrt{\frac{2}{3} \frac{(1-\theta)}{\theta}} (1-\theta) \left[ \sqrt{\frac{2}{3} \frac{(1-\theta)}{\theta}}  \dot{\epsilon}_z  \right]^m$	4
Equation 4:	$\nabla \cdot \vec{J} = \nabla \cdot (\sigma \vec{E}) = \nabla \cdot [\sigma(-\nabla V)] = -\nabla \cdot (\sigma \nabla V) = 0$	8
Equation 5:	$\rho C \frac{\partial T}{\partial t} + \nabla \cdot \vec{q} = h$	9
Equation 6:	$\rho C \frac{\partial T}{\partial t} + \nabla \cdot \vec{q} = \rho C \frac{\partial T}{\partial t} + \nabla \cdot (-k \nabla T) = \rho C \frac{\partial T}{\partial t} - \nabla \cdot (k \nabla T) =  J  E $	9
Equation 7:	$-\nabla \cdot (\sigma \nabla V) = 0$	9
Equation 8:	$\rho C \frac{\partial T}{\partial t} - \nabla \cdot (k \nabla T) = \sigma  \nabla V ^2$	9
Equation 9.	$G = k G_0 \epsilon^{-n}$	16
Equation 10.	$P = K \ln R$	89
Equation 11.	$\sigma_{\max} = \frac{P}{h^2} \left[ (1+\nu)(0.485 \log \frac{a}{h} + 0.52) + 0.48 \right]$	112
Equation 12.	$\sigma_{\max} = \frac{3F}{2\pi h^2} \left[ (1+\nu) \ln \frac{D_s}{D_L} + (1-\nu) \frac{D_s^2 - D_L^2}{2D^2} \right]$	113
Equation 13.	$\frac{dG}{dt} = f(\rho, T) \frac{1}{G^{n_1}}$ for grain growth	165
Equation 14.	$\frac{d\rho}{dt} = g(\rho, T) \frac{1}{G^{n_2}}$ for densification	165
Equation 15.	$\frac{f(\rho, T)}{g(\rho, T)} G^{n_2 - n_1} = \frac{n G_0 k}{(1-\rho)^{n+1}}$	166
Equation 16.	$\frac{dG}{dt} = \frac{2\Omega\gamma_b D_b^\perp}{RT\delta_b G}$	167
Equation 17.	$\frac{d\rho}{dt} \approx 400 \frac{\Omega\gamma_{sv}\delta_b D_b}{RTG^4}$	167

Equation 18.	$\frac{dG}{d\rho} = \frac{\gamma_b D_b^\perp}{200 \delta_b^2 \gamma_{sv} D_b} G^3 = k_0 G^3$	.....168
Equation 19.	$\frac{1}{G^2} = -k_1 \rho + k_2$	.....169
Equation 20.	$G = \frac{1}{(k_2 - k_1 \rho)^{1/2}}$	.....169
Equation 21.	$G = \frac{k_3 G_0}{\left(\frac{k_2}{k_1} - \rho\right)^{1/2}}$	.....169
Equation 22.	$\dot{G}_{static} = \dot{G}_0 \left(\frac{G_0}{G}\right)^3 (1 - \rho)^{-3/2}$	.....172
Equation 23.	$\dot{G}_{dynamic} = k_1 \frac{G}{\phi} \left[ (\dot{\gamma}_{ij} \dot{\gamma}_{ij}) + \frac{1}{3} (\dot{\epsilon}_{kk}^*)^2 \right]^{1/2}$	.....173
Equation 24.	$\sigma_{ij} = \frac{BW^m}{W} \left[ \phi \dot{\epsilon}_z + \left( \psi - \frac{1}{3} \phi \right) \dot{\epsilon} \right]$	.....174
Equation 25.	$\sigma_z = BW^{m-1} \left[ \left( \psi + \frac{2}{3} \phi \right) \dot{\epsilon}_z \right]$	.....174
Equation 26.	$\sigma_z = B \left[ \frac{1}{\sqrt{1-\theta}} \sqrt{\frac{2}{3} \phi + \psi}  \dot{\epsilon}_z  \right]^{m-1} \left[ \left( \psi + \frac{2}{3} \phi \right) \dot{\epsilon}_z \right]$	.....174
Equation 27.	$\sigma_z = B [1 - \theta]^{\frac{m-1}{2}} \left( \psi + \frac{2}{3} \phi \right)^{\frac{1+m}{2}}  \dot{\epsilon}_z ^m$	.....175
Equation 28.	$ \dot{\epsilon}_z  = - \left( \frac{\sigma_z}{B} \right)^{\frac{1}{m}} [1 - \theta]^{\frac{m-1}{2m}} \left( \psi + \frac{2}{3} \phi \right)^{\frac{1+m}{2m}}$	.....175
Equation 29.	$\frac{\dot{\rho}}{\rho} = \left( \frac{\sigma_z}{B} \right)^{\frac{1}{m}} \rho^{\frac{m-1}{2m}} \left( \frac{2}{3} \frac{\rho^2}{1-\rho} \right)^{\frac{1+m}{2m}}$	.....176

Equation 30.  $\dot{\rho} = \left( \frac{\sigma_z}{G^p B_0 \exp\left(\frac{-Q_{cr}}{RT}\right)} \right)^{\frac{1}{m}} \rho^{\frac{3m-1}{2m}} \left( \frac{2}{3} \frac{\rho^2}{1-\rho} \right)^{\frac{1+m}{2m}} \dots 176$



## List of Tables

Table 1. A comparison between grain size and porosity between the corner and center for a cylindrical and prismatic specimen. ....	59
Table 2. Comparison of grain size and porosity in the center and corner of each of the four specimens, sintered at 1300 °C for 15 minutes. ....	67
Table 3. Average values for all 6 experiments, and the pre-sintered specimen.....	91
Table 4. Values for different regions in Specimen 1, processed @ 330 °C and 69.5 MPa. ....	93
Table 5. Values for different regions in Specimen 2, processed @ 330 °C and 104.2 MPa. ....	95
Table 6. Values for different regions in Specimen 3, processed @ 230 °C and 104.2 MPa. ....	97
Table 7. Values for different regions in Specimen 4, processed @ 230 °C and 69.5 MPa. ....	99
Table 8. Values for different regions in Specimen 5, processed @ 130 °C and 104.2 MPa. ....	101
Table 9. Values for different regions in Specimen 6, processed @ 130 °C and 69.5 MPa.....	103
Table 10. Average grain size development in the side area of 6 specimens.....	106
Table 11. Average grain size development in the center area of 6 specimens. ....	106
Table 12. Density, hardness, grain size, and rupture strength data for five TaC specimens. ....	123
Table 13. Experimental Parameters for Individual Fe-VC Samples.....	130
Table 14. Hardness test spot ID and position description for Fe-VC specimens .....	139
Table 15. Hardness value for five Fe-VC specimens .....	140
Table 16. Data from Fe-0.5V, with carbon additives, specimens.....	162
Table 17. Data from mixed Fe-0.5V with Fe-15V, with carbon additives, specimens ...	162
Table 18. Hardness data comparison between pre-heat treatment and post-heat treatment Fe-0.5V, with carbon additives. ....	163
Table 19. Hardness data comparison between pre-heat treatment and post-heat treatment mixed Fe-0.5V with Fe-15V, with carbon additives.....	163

## Acknowledgements

I would like to thank my advisor, Dr. Eugene Olevsky, for working with me for all these years and helping me produce the best dissertation possible, even when we did not see eye-to-eye.

I would like to thank Dr. Randall German for supporting me and giving me the confidence to take ownership of, and finish, my dissertation.

I could not have done this without my brother, my father, and Erin, and I owe them everything, especially for supporting me when things were difficult. I couldn't have done it without them.

I would like to thank Dr. Scott Hansen for counseling me through my writer's block, helping build my confidence about my work, and encouraging me to finish.

I am extremely grateful for all of the PTL lab members, who I loved working with, and consider my friends (and listed in no particular order): Wei Li, Yen-Shan Lin, Xialu Wei, Diletta Giuntini, Timothy Young, William Bradbury, Cristina Garcia Cardona, Brian Schmaltz, Gordon Brown, Eric Bruce, Rahul Joshi, Rahul Tyagi, Maohung Tien, and Boris Kushnarev

I am also incredibly lucky to have worked with Ridvan Yamanoglu, Ignacio Fernandez Ruano, and all of the French students: Thomas, Vincent, Arnaud, Augustin, Guillaume, Marin, and P.A.

I would like to thank Dr. Steve Barlow for refining my SEM skills and helping me produce wonderful images of my work.

Donovan Geiger is the glue that holds the JDP program together at SDSU, and I have greatly appreciated his help and support over the years.

Chapter 5, in part, is a reprint of the material as it appears in *Scripta Materialia*:

E Khaleghi, YS Lin, MA Meyers, EA Olevsky, "Spark Plasma Sintering of Tantalum Carbide," *Scripta Materialia* 63, 577-80 (2010).

The dissertation author was the primary investigator and author of this paper.

## **Vita**

2004	Bachelor of Science, University of California, San Diego
2006-2011	Teaching Assistant, Department of Engineering, San Diego State University
2012	Doctor of Philosophy, University of California, San Diego and San Diego State University

## **Publications**

### **Refereed Journal Publications:**

1. Evan Khaleghi, Milton Torikachvili, Marc A. Meyers, and Eugene A. Olevsky, "Magnetic Enhancement of Thermal Conductivity in Copper-Carbon Nanotube Composites Produced by Electroless Plating, Freeze Drying, and Spark-Plasma Sintering," *Materials Letters* 79, 256–8 (2012).
2. Eugene Olevsky, Evan Khaleghi, Cristina Garcia, and William Bradbury, "Fundamentals of Spark-Plasma Sintering: Applications to Net-Shaping of High Strength Temperature Resistant Components," *Materials Science Forum* 654-656, 412-415 (2010).
3. E Khaleghi, YS Lin, MA Meyers, EA Olevsky, "Spark Plasma Sintering of Tantalum Carbide," *Scripta Materialia* 63, 577-80 (2010).
4. E Khaleghi, MA Meyers, EA Olevsky, "Uniaxial Freezing, Freeze-drying, and Anodization for Aligned Pore Structure in Dye Sensitized Solar Cells," *Jour. Am. Cer. Soc.* 92, 1487-91 (2009).

### **Contributions to conference presentations:**

1. E Khaleghi, MA Meyers, EA Olevsky, Uniaxial Freezing, Freeze-drying, and Anodization for Aligned Pore Structure in Dye Sensitized Solar Cells, *International Conference on Sintering 2008, San Diego* (2008).
2. Eugene A. Olevsky, Evan Khaleghi, Cristina Garcia, William Bradbury, Randall M. German, Chris Haines, Darold Martin, Deepak Kapoor, Fundamentals of Spark-Plasma Sintering: Net-Shaping and Size Effects, *TMS Annual Meeting, San Diego* (2011) - *planned*
3. Eugene Olevsky, Cristina Garcia, Evan Khaleghi, William Bradbury, Wei Li, Randall German, Impact of specimen shape on temperature and density gradients in spark-plasma sintering, *The 34th International Conference and Exposition on Advanced Ceramics and Composites, January 27-29, 2010 in Daytona Beach, Florida* (2010)

4. Eugene A. Olevsky, Evan Khaleghi, Cristina Garcia, William L. Bradbury, Fundamentals of spark-plasma sintering: Applications to net-shaping of high strength temperature resistant components, *The 7th Pacific Rim International Conference on Advanced Materials and Processing, Cairns, Australia* (2010)
5. Eugene Olevsky, Cristina Garcia, Evan Khaleghi, William Bradbury, Wei Li, Randall German, Shape and size factors in conventional (SPS) and free pressureless (FPSPS) Spark-plasma sintering, *The Materials Science and Engineering 2010 Congress in Darmstadt/Frankfurt, Germany, August 22-28* (2010)
6. Eugene Olevsky, Cristina Garcia, Evan Khaleghi, William Bradbury, Net shaping by spark-plasma sintering, *The World Congress on Powder Metallurgy, Florence, Italy, October* (2010)
7. Eugene Olevsky, Cristina Garcia, Evan Khaleghi, William Bradbury, Randall German Coupled electro-thermo-mechanical analysis of conventional (SPS) and free pressureless (FPSPS) Spark-plasma sintering, *The Materials Science and Technology 2010 (MS&T 2010) Conference in Houston, TX, October* (2010)
8. Eugene Olevsky, Cristina Garcia, Evan Khaleghi, William Bradbury, Wei Li, Randall German, Coupled electro-thermo-mechanical analysis of spark-plasma sintering, *The Materials Science and Technology 2010 (MS&T 2010) Conference in Pittsburgh, PA, October* (2009)

## **Abstract of the Dissertation**

Tailored Net-Shape Powder Composites by Spark Plasma Sintering

by

Evan Aryan Khaleghi

Doctor of Philosophy in Engineering Science (Mechanical and Aerospace Engineering)

University of California, San Diego, 2012  
San Diego State University, 2012

Professor Eugene Olevsky, Chair  
Professor Marc Meyers, Co-chair

This dissertation investigates the ability to produce net-shape and tailored composites in spark plasma sintering (SPS), with an analysis of how grain growth, densification, and mechanical properties are affected.

Using alumina and four progressively anisotropic dies, we studied the impact of specimen shape on densification. We found specimen shape had an impact on overall densification, but no impact on localized properties. We expected areas of the specimen to densify differently, or have higher grain growth, based on current anisotropy in the specimen during sintering, and preliminary results indicated this, but further investigation showed this did not occur. Overall average grain size and porosity decreased as shape complexity increased.

In Fe-V-C steel, we mechanically alloyed two rapidly solidified powders, and used spark sintering to retain the properties imparted during the rapid solidification. We

noticed VC grains being produced during densification, which improved the final properties.

We conducted spark plasma extrusion (SPE) of aluminum to understand the effect on microstructure. We found, through an analysis of the grain structure, that SPE did have a grain deformation potential, and grain size was severely decreased compared to conventional sintering. Dynamic recrystallization did not occur, due to the reduced temperatures we were able to extrude with SPS.

Finally, we examined whether there were particular sintering conditions for SPS that reduced the complexity of the grain growth and porosity relationship to one similar to conventional sintering, of the form  $G = k G_0 \epsilon^{-1/2}$ . We found that although a reasonable case could be made for free sintering, as found in the literature, for hot-pressing and SPS the conditions required go against the common knowledge in grain growth and densification kinetics. We were able to fit our data very well to the model, but the correlated results do not make physical sense.

## Chapter 1. Introduction: Literature Survey

### *1.1 Fundamental analysis of spark plasma sintering*

Spark plasma sintering (SPS), also known as field assisted sintering technique (FAST), electric current assisted sintering (ECAS), current-activated, pressure-assisted densification (CAPAD), pulsed electric current sintering (PECS), plasma activated sintering (PAS), pulsed current hot pressing (PCHP), and several other names, is a densification technique, similar to hot pressing, that utilizes electric current to heat and densify a powder through application of pressure and joule heating of either the powder, or a die holding the powder (or both). SPS consists essentially of conjoint application of high temperature, high axial pressure, and field (plasma) assisted sintering<sup>10</sup>. The field component is associated with electric current passed through a powder specimen. The application of pressure in SPS creates electrical contact between the electrodes, specimen, and the die and also compacts the specimen, making the process similar to conventional hot pressing, but with much higher heating rates. The SPS method has proposed advantages over conventional which have been researched vigorously in the past few years.<sup>1,2</sup>

The advantages of the spark sintering method, which have been widely publicized in research, are faster heating rates, shorter holding times, smaller grain sizes, and denser final materials.<sup>3,4,5,6,7</sup> The main parameters investigated in SPS experiments are sintering temperature, holding time, heating rate, applied pressure, and occasionally a few electrical parameters (current, voltage, pulse frequency). Studies of spark sintering have

shown that it may be possible to sinter materials at lower temperatures compared to conventional sintering, due to many possible factors including exceptionally high heating rates.<sup>8,9</sup>

The name used by the majority of the literature<sup>10</sup> is a bit of a misnomer (used by 66.2% of publications as of 2009), as Hubert, et al.<sup>11</sup> conducted a thorough investigation, and presented serious evidence, for the lack of a plasma in the SPS process. They consolidated many different powders (Al, Al<sub>2</sub>O<sub>3</sub>, NaCl, Mg, and Zn), and searched for plasma formation using *in situ* atomic spectroscopy (AES), direct visual observation, and ultrafast *in situ* voltage measurements. There was no evidence for plasma or sparking using any observation technique, in any powder system.

Specimens produced by SPS have shown improvements in microstructure (including decreased grain growth),<sup>12,13,14</sup> corrosion resistance<sup>15</sup>, and mechanical properties<sup>16,17</sup>, compared to conventional methods.

There are two types of modeling that are applicable to SPS, constitutive and finite element. Constitutive modeling provides a mathematical basis for the physical phenomena occurring during sintering, including densification, grain growth, etc. Finite element modeling provides a method for using computational methods to analyze the physical behavior during sintering. They are not exclusive to each other, but have different foci. Constitutive modeling examines the pore shrinkage, mass transport, and diffusion of the material using established equations. The finite element modeling is concerned with a more overall analysis to the system, such as heat generation, current density, etc., and may include the constitutive modeling as a way of modeling one of the parameters.



We can use the continuum theory of sintering to describe the constitutive behavior of spark plasma sintering. From Olevsky<sup>18</sup>, we can find a general constitutive equation “which describes the macroscopic behavior of a porous body during sintering by relating an external load (corresponding to the stress tensor’s components  $\sigma_{ij}$ ) to the strain rate tensor’s components  $\dot{\epsilon}_{ij}$  by the nonlinear-viscous constitutive relationship”:

$$\text{Equation 1. } \sigma_{ij} = \frac{\sigma(W)}{W} \left[ \varphi \dot{\epsilon}_{ij} + \left( \psi - \frac{1}{3} \varphi \right) \dot{\epsilon} \delta_{ij} \right] + P_L \delta_{ij}$$

Where  $W$  is the equivalent strain rate and  $\sigma(W)$  is the equivalent stress,  $\varphi$  and  $\psi$  are the normalized shear and bulk viscosities (dependent on porosity),  $\delta_{ij}$  is the Kronecker delta, and  $\dot{\epsilon}$  is the first invariant of the strain rate tensor (the volumetric shrinkage rate).

For uniaxial compaction, as in SPS,  $P_L = 0$ , and Equation 1 can be simplified to<sup>19</sup>:

$$\text{Equation 2. } \sigma_{ij} = \frac{\sigma(W)}{W} \left[ \varphi \dot{\epsilon}_z + \left( \psi - \frac{1}{3} \varphi \right) \dot{\epsilon} \right]$$

where  $\dot{\epsilon}_z$  is the z-axis stress component.

The effective stress  $\sigma(W)$  is described by the following equations:

$$\begin{aligned} \sigma(W) &= BW^m \\ W &= \frac{1}{\sqrt{1-\theta}} \sqrt{\varphi \dot{\gamma}^2 + \psi \dot{\epsilon}^2} \\ \dot{\epsilon} &= \dot{\epsilon}_z + 2\dot{\epsilon}_r \\ \dot{\gamma} &= \sqrt{\frac{2}{3}} |\dot{\epsilon}_z - \dot{\epsilon}_r| \\ \varphi &= (1-\theta)^2 \\ \psi &= \frac{2}{3} \frac{(1-\theta)^3}{\theta} \end{aligned}$$

$$\dot{\epsilon} = \frac{\dot{\theta}}{1-\theta}$$

$$B = B_0 \exp\left(\frac{Q_{cr}}{RT}\right)$$

Where  $m$  is the strain rate sensitivity exponent (from power-law creep equations),  $\dot{\epsilon}_r$  is the radial strain rate component (equal to zero for uniaxial compaction),  $\dot{\gamma}$  is the second invariant of the strain rate tensor deviator (shape change rate), and  $\theta$  is the porosity. By using the above list of equations, and substituting them into Equation 2, we can obtain a relationship between applied stress, porosity, and shrinkage rate:

$$\text{Equation 3. } \sigma_z = A \sqrt{\frac{2}{3} \frac{(1-\theta)}{\theta}} (1-\theta) \left[ \sqrt{\frac{2}{3} \frac{(1-\theta)}{\theta}} |\dot{\epsilon}_z| \right]^m$$

Where  $\sigma_z$  is the uniaxial stress, and  $A$  is a microstructure related term.

To utilize this set of equations fully, we need to determine  $m$ .  $m$  is dependent on the type of creep mechanism that is present during sintering, with  $m = 1$  being diffusional creep,  $m = 0.5$  being grain-boundary sliding,  $m = 0.2$  being glide-controlled creep (a type of dislocation creep), and  $m$  between 0.2 and 0.5 being climb-controlled creep (another type of dislocation creep). Under high temperature consolidation, such as sintering, grain-boundary sliding is believed to be the primary mechanism.

Li, et al.<sup>19</sup> devised a series of fundamental experiments in SPS to derive the value of  $m$ , called multi-step pressure dilatometry. By utilizing current-assisted and current-free experiments with a multi-stepping of pressure and holding of temperature, as shown in Figure 1, and carefully measuring the shrinkage, they were able to find  $m$ .

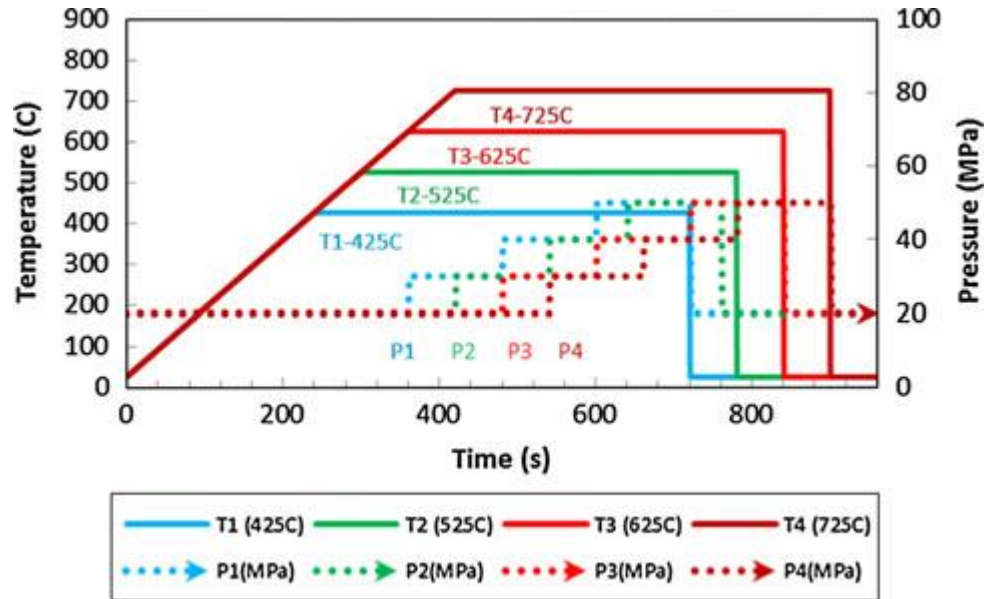


Figure 1. A temperature and pressure profile for current-assisted multi-step pressure dilatometry that was used to find the creep exponent  $m$ .<sup>19</sup>

The pressure was held for 2 minutes and then rapidly changed, creating a nearly instantaneous pressure change (which actually took about 10 s). Figure 2 shows the densification rates at these rapid pressure changes (where it is assumed that over the 10s grain size did not change). By using the stress, strain, and strain rate values at the pressure changes,  $m$  can be calculated by a relatively simple equation.

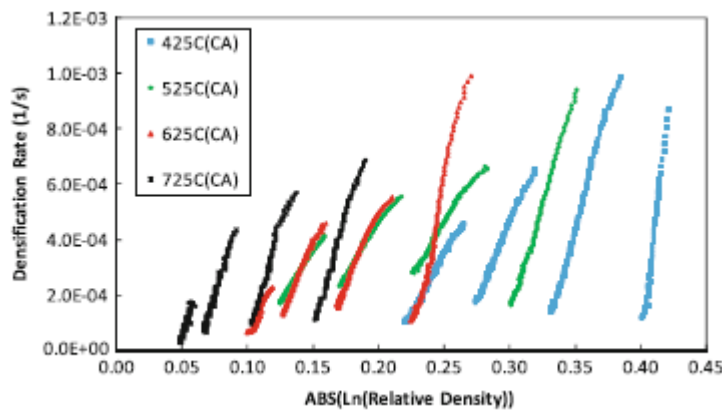


Figure 2. A diagram of the densification rate vs. relative density at the instantaneous pressure change regions, used to calculate the creep exponent  $m$ .<sup>19</sup>

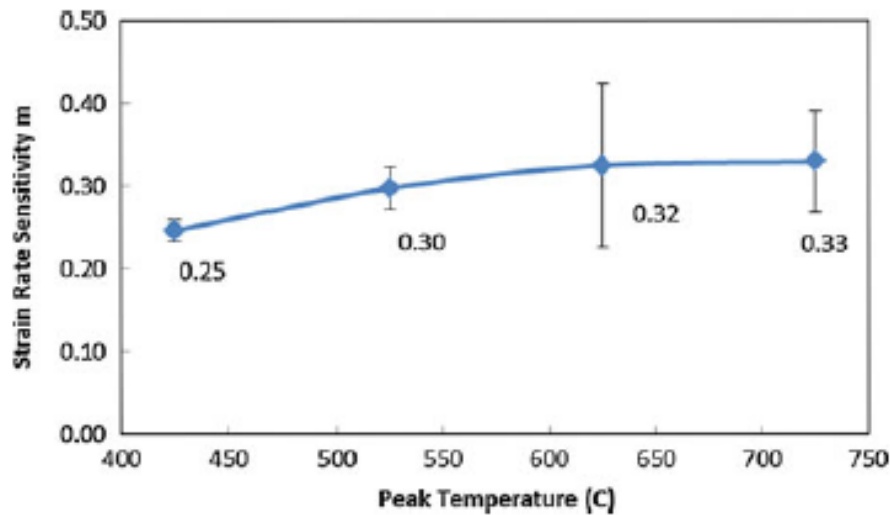


Figure 3. The measured creep exponent,  $m$ , values compared to the sintering temperature of the experiments.

They found that  $m$  varied between 0.2 and 0.4, with the value at 625 °C being 0.26, as shown in Figure 3. This value corresponds to a dislocation-climb controlled creep mechanism.

Olevsky and Froyen investigated the mechanisms of mass transport in SPS, and showed that electromigration may significantly contribute to the acceleration of mass transport.<sup>20</sup> The two major mechanisms of mass transport that contribute to mass transfer for densification are power-law creep, surface diffusion, and grain boundary diffusion.<sup>21,22,23</sup> The driving forces for these mechanisms are applied load, sintering stress (from surface tension on grains/particles in the powder), and electromigration (electric-field motivated diffusion. The main driving forces for electromigration may be high levels of grain-pore and grain-grain interface areas, where the “electron wind” in SPS causes a momentum transfer to the grain atoms encouraging their diffusion. Other

possible mechanisms are an increase in point defect concentration<sup>24</sup>, or a reduction in the mobility activation energy for defects<sup>25</sup>. Work by Raj, et al<sup>26</sup>., showed that the application of an electric field in SPS enhanced dislocation climb in the consolidation of NaCl, either by enhancing dislocation mobility or enhancing self-diffusion by increasing defect density.

If we take the general constitutive sintering Equation 1<sup>9</sup>:

$$\sigma_{ij} = \frac{\sigma(W)}{W} \left[ \varphi \dot{\epsilon}_{ij} + \left( \psi - \frac{1}{3} \varphi \right) \dot{\epsilon} \delta_{ij} \right] + P_L \delta_{ij}$$

$\sigma(W)$  can be given by a linear relationship:

$$\sigma(W) = 2\eta_0 W$$

where  $\eta_0$  is the shear viscosity of the fully dense material.

For diffusional sintering of crystalline materials,  $\eta_0$  is related to the effective diffusion coefficient, as:

$$\eta_0 = \frac{kTG^2}{\Omega} \frac{1}{D_{eff}}$$

where  $k$  is Boltzmann's constant,  $T$  is the temperature,  $G$  is the grain size,  $\Omega$  is the atomic volume, and  $D_{eff}$ , the effective diffusion, is dependent on grain boundary, volume, and surface coefficients,  $D_{gb}$ ,  $D_v$ , and  $D_s$ , respectively, as:

$$D_{eff} = D_{eff}(D_{gb}, D_v, D_s)$$

With these equations, the creep exponent, an understanding of the main transport mechanisms, and measured experimental data, it is possible to understand spark plasma sintering in a fundamental way.

Most of the modeling work in SPS has been dedicated to the numerical analysis of temperature and electric current distributions during SPS<sup>27,28,29,30,31</sup>. It is also necessary to couple the electrical and thermal equations with mechanical equations, to form a complete model capable of handling densification and grain growth. However, most modeling software is not capable of coupling three equations, with COMSOL Multiphysics being the only available. Some authors have included mechanical elements in their modeling, but usually in the form of shrinkage (through z-axis changes), which although applicable to SPS experiments, provides no fundamental understanding of the density variation, densification, and grain changes during processing.<sup>32,33,34</sup>

To model SPS in software (such as for Finite Element Method modeling), we must investigate the current flow, heat flow, and heat generation equations<sup>35</sup>. The equation of conservation of currents solved is expressed as:  $\nabla \cdot \vec{J} = 0$  where  $\vec{J}$  denotes the current density and is equal to:  $\vec{J} = \sigma \vec{E}$ , with  $\vec{E}$  corresponding to the electric field and  $\sigma$  to the electrical conductivity.

Furthermore, for a static problem:  $\nabla \times \vec{E} = 0$ , and which is equivalent to say that the electric field can be expressed in terms of an electrostatic potential denoted by  $V$  with the relationship:  $\vec{E} = -\nabla V$ , resulting in the following second order partial differential equation:

$$\text{Equation 4: } \nabla \cdot \vec{J} = \nabla \cdot (\sigma \vec{E}) = \nabla \cdot [\sigma (-\nabla V)] = -\nabla \cdot (\sigma \nabla V) = 0$$

For heat transfer by conduction, which is the main source of heat transfer in SPS, the equation of conservation of energy in time and space are:

$$\text{Equation 5: } \rho C \frac{\partial T}{\partial t} + \nabla \cdot \vec{q} = h$$

expresses the change of temperature  $T$  with respect to time  $t$ , the heat flux vector  $\vec{q}$  and the heat  $h$  generated by the flowing current per unit volume. The parameters of the equation are the density  $\rho$  and the heat capacity  $C$ . The material law for the heat flux vector is:  $\vec{q} = -k \nabla T$ , where  $k$  represents the thermal conductivity of the material and the heat generated by conduction can be written as:  $h = \vec{J} \cdot \vec{E}$ . The result is a second order partial differential equation:

$$\text{Equation 6: } \rho C \frac{\partial T}{\partial t} + \nabla \cdot \vec{q} = \rho C \frac{\partial T}{\partial t} + \nabla \cdot (-k \nabla T) = \rho C \frac{\partial T}{\partial t} - \nabla \cdot (k \nabla T) = |J||E|$$

The results shown correspond to the solution of a weak coupled version of the equations describing the phenomena:

$$\text{Equation 7: } -\nabla \cdot (\sigma \nabla V) = 0$$

$$\text{Equation 8: } \rho C \frac{\partial T}{\partial t} - \nabla \cdot (k \nabla T) = \sigma |\nabla V|^2$$

The coupling is weak, as the second equation depends on the solution of the first, while the first is independent. An electrical conductivity dependant on the temperature can be used in order to model the more realistic strongly coupled system.

With these coupled electrical and thermodynamic equations, we can model the current and heat flow in SPS. Using the continuum theory of sintering, and coupling a mechanical model to the previous two equations, it may be possible to create a full model for SPS that can predict densification and grain growth.

Several studies by Groza, et al.<sup>36,37,38,39</sup> highlight the capabilities of SPS to produce highly dense products at lower temperatures, and in less time, than conventional sintering. Their studies on  $\text{Al}_2\text{O}_3\text{-TiO}_2$ ,  $\text{Sn}_{0.82}\text{Sb}_{0.18}\text{O}_2$ , Fe with 2% Al, and WC with 10% Co, all show dramatic improvement over conventional sintering (and other techniques). For sintering of  $\text{Al}_2\text{O}_3\text{-TiO}_2$ , using SPS, they achieved 99.5% density ( $3.8 \text{ g/cm}^3$ ) in only 10 minutes at  $1000^\circ\text{C}$ , while conventional sintering for 2 hours at  $1300^\circ\text{C}$  only achieved 75% density ( $2.8 \text{ g/cm}^3$ ). With  $\text{Sn}_{0.82}\text{Sb}_{0.18}\text{O}_2$ , they achieved 92.4% density in 10 minutes at 1163 K, while conventional sintering for 3 hours at 1273 K only produced a final density of 61.3%. When attempting to densify Fe with 2% Al additives, SPS was compared to hot pressing, and SPS was able to produce a density 50% greater than hot pressing ( $7.5 \text{ g/cm}^3$  versus  $5.0 \text{ g/cm}^3$ , respectively), at a lower temperature ( $700^\circ\text{C}$ ). As the temperature was increased to  $1050^\circ\text{C}$ , the final result for hot pressing was still 6.5% less dense than the SPS sample at the same temperature ( $7.5 \text{ g/cm}^3$  versus  $7.0 \text{ g/cm}^3$ , respectively). In WC with 10% Co, the results were even more impressive when SPS was compared to Liquid Phase Sintering. At  $1100^\circ\text{C}$ , SPS achieved 76% density, where LPS only reached 58%.

El-Atwani, et al.<sup>40</sup> conducted a series of experiments densifying tungsten through SPS. They were able to achieve almost no grain growth with 94% density in many specimens, sintered at below the recrystallization temperature of tungsten. However, they also showed in their experiments that varying temperature by up to  $200^\circ\text{C}$  ( $1300 - 1500$ ), or pressure by 66 MPa ( $200 - 266$ ) had little impact on final density, as all specimens within this parameter range were 94% density ( $\pm 0.8\%$ ). Also, several of their experiments experienced severe grain growth as they crossed the recrystallization



temperature. The authors also noted a contamination of tungsten oxide in all of the specimens, which may hinder densification.

Aman, et al.<sup>41</sup> conducted a series of experiments to screen for which of three SPS parameters (heating rate, sintering temperature, holding time, and green processing) was the most influential on final relative density and final grain size (and two other transparency-based parameters). They provide a sound basis in the literature as to why they selected the three parameters they screened for, but it is interesting that they did not select initial grain size as a parameter. They found that 90% of the parameters' effect on final density is dependent on the heating rate and sintering temperature, with the other 10% being due to the other two parameters. They also found that 90% of the parameters' effects on final grain size were solely due to sintering temperature. They have shown that the fewer parameters are relevant to the final results in SPS than previous literature has suggested.

It is also interesting to note that heating rate and sintering time were shown here to have little effect on grain growth, as one of the main claimed advantages of SPS is that short sintering times (a combination of these two parameters) do not give sufficient time for grain growth processes to occur.

In conventional (pressureless) sintering, it has been shown that higher heating rates improve densification by creating a driving force for densification that avoids the non-densifying mechanisms (such as surface diffusion).<sup>42</sup> The high heating rates in SPS should provide the same benefit, as evidenced by similar a benefit noted in microwave sintering.<sup>43</sup> However, in the sintering of  $\text{Al}_2\text{O}_3$  and  $\text{MoSi}_2$ , varying the heating rate

(between 50 and 700°C/min) had no effect on the final density, when specimens were sintered at the same temperature and with the same holding time.<sup>44</sup>

Gua, et al.<sup>45</sup> conducted an investigation into the densification of hydroxyapatite in SPS. They sintered specimens at different temperatures and calculated density and grain size. They found that increasing temperature (from 800 to 1100 °C) had a significant impact on grain growth, but not on densification. This may be due to the majority of their specimens reaching full density and experiencing significant grain growth after this point. They have shown a temperature-grain growth relationship, and confirmed again the existence of grain growth after full densification.

In contrast to the previous studies, Zhou et al., showed that a heating rate in the range of 5-300 °C/min had no influence on the final density of alumina, but did have an effect on the grain size, with a decreasing final grain size with increasing heating rate.<sup>46</sup> Anselmi-Tamburini, et al. observed a similar dependence on grain size on heating rate in the same range as Zhou et al, and no dependence of heating rate on final density, in a study of densification of fully-stabilized cubic zirconia.<sup>14</sup>

Overall, we gather that SPS can be used to sinter specimens at lower temperatures than conventional sintering, while showing very limited grain growth and nearly-full densification. However, material properties like oxidation and recrystallization temperature can still have a severe impact on grain growth and densification, even in SPS.

Several studies in the past few decades have shown an influence of electric field on material processes.<sup>47,48</sup> Chaim<sup>49</sup> conducted a review on the densification mechanisms of nanocrystalline ceramics in SPS, while also providing an analysis with a theoretical

basis. He found that the low voltages used in SPS (6-20 V) were high enough to reach the breakdown voltage for most submicron and nanosized ceramic powders, which would aid in densification.

Tiwari, et al.<sup>50</sup> attempted to simulate the electric field evolution in SPS using ABAQUS and MATLAB. They wanted to calculate the temperature distribution (axial and radial), and the heat and electric flux-fields in the powder/die/spacer assembly. They used a coupled thermal-electrical model using the relevant properties of all of the materials, but they did not also couple a mechanical model (for pressure application). They found that the power requirements to change the surface temperature of the die changed significantly above 1000 °C, from an exponential to a parabolic curve. This means that heating a die in SPS to high temperature requires significantly more power than lower temperature. They also found that the major heat generation in the die is at the die/punch interface, where there is the lowest contact area, and therefore highest current density. Finally, they also found that heat flux in the die is relatively uniform, despite the differences in electrical current in the die.

Xie, et al.<sup>51</sup> investigated the effects of pulsing, and the frequency of pulsing, on aluminum sintering. They densified specimens at various frequencies (0, 10, 40 and 300 kHz), and found no effect of the pulse frequency on any of the final material properties (including density, tensile strength, and electrical resistivity).

Besides electrical-based factors, we must also consider the impact of pressure, and comparisons with hot pressing yield important information. Chaim<sup>49</sup> explained that densification of ceramics with low yield stress, plastic deformation dominates, while in ceramics with high yield stress, grain rotation and sliding are the dominant mechanisms

for densification. He also found that densification in the final stages of sintering of all ceramics is almost entirely governed by diffusion processes. They also found for a cubic zirconia powder, while pressure has no effect on grain size, it has a significant influence on densification. For a MgO powder that was hot pressed, they found that the maximum shrinkage rate was strongly affected by temperature of the material when pressure was applied. They believe this was due to plastic deformation during heating, due a lower yield stress in the material (at higher temperature) when the pressure was applied.<sup>52</sup>

In an investigation of anatase  $\text{TiO}_2$  by hot-pressing, Weibel, et al.<sup>53</sup> found that for small particle size (12 nm) powders, the activation energy for densification was constant with a high range of applied pressure (125 to 600 MPa), and the main mechanism was plastic deformation. However, when the powder particle size was increased to 70 nm, there were significant changes in the activation energy at different temperature ranges, fluctuating of the main densification mechanism between plastic deformation and diffusion related processes (with the aid of surface diffusion).<sup>54</sup>

Skandan, et al.<sup>55</sup> found there was a pressure threshold in sinter-forging (a process involving conventional heating, however, important for understanding SPS mechanisms), below which the pressure has little or no effect on densification, but above which there is an effect on densification. The applied pressure was much less than the yield stress of their nanosized zirconia powder, and they found that as the particle size increased, the applied pressure threshold decreased (from 35 MPa for 6 nm powder down to 10 MPa for 12 nm powder).

Xu, et al.<sup>56</sup> showed that the rate of pressure application (a feature on many SPS machines) significantly affects the densification, with the densification rate increasing with the pressure rate for zirconia.

Based on the literature, there appears to be two states in relation to the applied pressure. If the pressure exceeds the yield strength of the powder particles, plastic deformation occurs and is the dominant mechanism for densification. In this case, the densification rate is much higher than the grain growth rate, so fine grain size is retained while density is increased. In the other state, where applied pressure does not exceed the yield strength, the main mechanisms for densification are diffusion-based.<sup>57</sup>

## ***1.2. General overview of densification and structure evolution during SPS***

Several authors<sup>58,59,60</sup>, among many others, have made claims that spark sintering enhances densification or material properties of finished specimens, however few offer a quantitative basis for the origination of this enhancement or benefit. It has become *de rigueur* when writing a paper about spark sintering to mention these facts, without providing any basis, as they are already established. In order to identify, and clarify, a basis with which to quantitatively establish the benefits of spark sintering over conventional sintering, we conducted a thorough review of the literature related to the most frequent claim made of spark sintering – enhanced densification and minimized grain growth compared to conventional sintering.

In 1962, Bruch<sup>61</sup> first published a paper detailing an inverse square root relationship between grain growth and porosity in sintering, derived experimentally using

alumina with a small amount of magnesia additives. He noted a difference in sintering between sets of specimens, which he termed ‘normal’ and ‘subnormal’, that varied based on higher activation energy for the sintering process and an exponential relationship derived from the experimental data. His determination of the cause of subnormal sintering was due to extreme pore growth and stability that inhibited grain growth and densification, based on sintering specimens to the same density and observing the pores of specimens that were sintered normally and subnormally. The initial basis for this pore growth was unclear, but may have been due to the method of pre-pressing.

German<sup>62</sup> conducted a serious review of grain growth kinetics during sintering, that included Bruch’s work, and rewrote the grain size and porosity relationship to be of the form:

$$\text{Equation 9. } G = k G_0 \varepsilon^{-n}$$

where  $G$  is the grain size,  $\varepsilon$  is porosity,  $G_0$  is the initial particle size,  $k$  is a constant around 0.6, and  $n$  is  $\frac{1}{2}$  (or 0.5).

German also provided several examples from literature illustrating this dependence. Suzuki<sup>63</sup> et al. also experimentally calculated a  $\varepsilon^{-1/2}$  relationship between grain size and porosity in the sintering of alumina, as shown in Figure 4. The main focus of their research was on the high-speed compaction process they developed, however it is merely a method of pre-processing of powders to prepare them for sintering, and has no impact on sintering behavior. As they studied the material properties of their specimens, they deduced that the high strength of their specimens may be related to the centrifugation process which removes residual bubbles and inclusions. This may

encourage the nominal sintering, as defined by Bruch, by closely packing the powders and minimizing pore size.

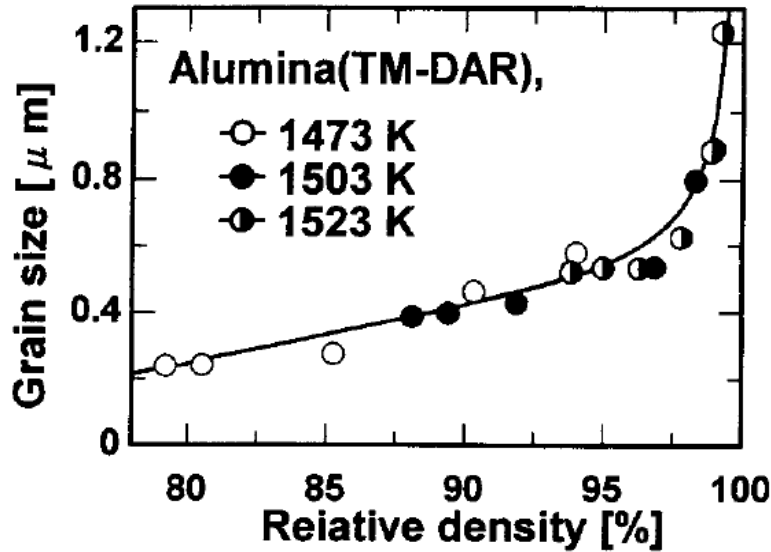


Figure 4. A set of research shows a  $\epsilon^{-1/2}$  relationship between grain size and porosity in sintering of alumina, taken directly from Suzuki et al.<sup>63</sup>

German calculated from the data in Zhao and Harmer<sup>64</sup> a  $\epsilon^{-1/2}$  relationship between grain size and porosity/density for sintering of alumina, including the addition of MgO and FeO as dopants which shifted the grain growth curve. They showed that doping with FeO accelerated grain coarsening and shifting of the curve upwards, while doping with MgO retarded grain coarsening and shifted the curve downwards. The authors (Zhao and Harmer) speculated on the relationship between grain size and porosity, and calculated the relationship as  $dG/dt \sim G^{-3}\epsilon^{-4/3}$ . However, there were some problems with their experimental analysis, and we can speculate since their pre-processing involved adding the dopants through a slurry method, and then pre-compacting the powder into low density pellets (~47% relative density) before calcining the pellets (rather than the powder). This process may leave residual large pores or liquid

between particles if drying was not thorough, and may have fit the subnominal conditions of accelerated pore growth.

Bernard-Granger<sup>65</sup> et al. determined experimentally a  $G \sim \varepsilon^{-1/2}$  relationship between grain growth and relative density (not porosity) for both alumina and yttria in conventional sintering, as shown in Figure 5. Different temperatures and times only affected the final porosity of the specimens, and not their relationship to the model curve.

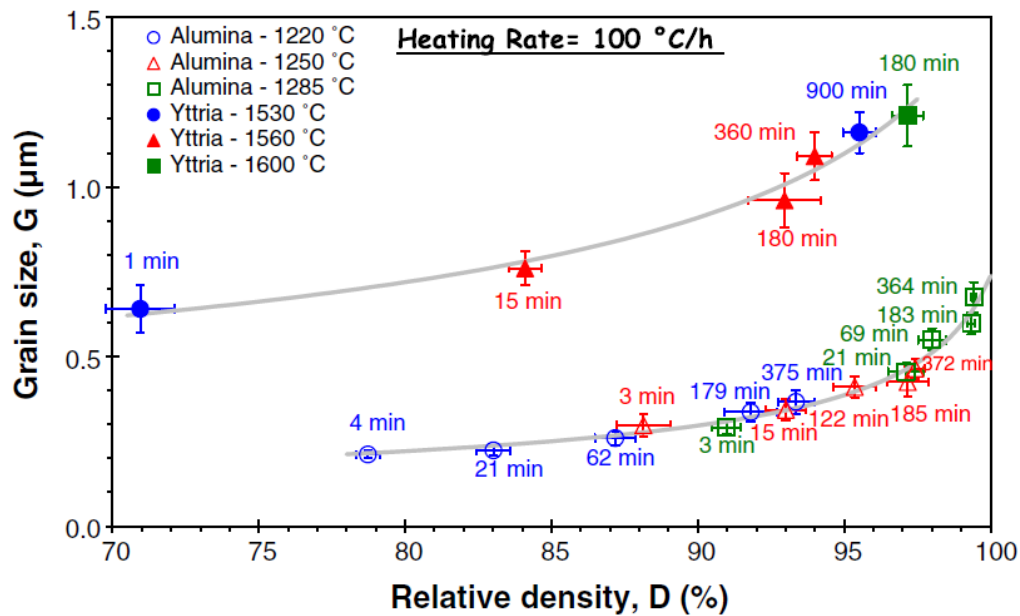


Figure 5. Conventional sintering of alumina and yttria (in air) shows a  $\varepsilon^{-1/2}$  relationship between grain size and relative density, taken from Bernard-Granger et al.<sup>65</sup>

Bernard-Granger<sup>66</sup> et al. also theoretically determined a  $G \sim \varepsilon^{-1/2}$  relationship between grain growth and relative density (not porosity) in slip-casting of  $\alpha$ -alumina, by examining grain growth caused by the grain boundaries and pores and diffusion, and experimentally confirmed the relationship for relative density. In their analysis, the constant  $k$  is a parameter consisting of the diffusion coefficients both through and along the grain boundary, the surface tension between the solid/solid (grain boundary) and



solid/vapor interfaces, the grain boundary thickness, and a numerical constant. All of these parameters are material (or system) dependent, and all of them are constants for their systems. Therefore, it is possible to use a single constant,  $k$ , to represent these terms, however due to the dependence of the above-mentioned diffusion coefficients on temperature, it is likely that  $k$  also depends on temperature. A plot of the slip-casted  $\alpha$ -alumina data is shown in Figure 6. Although the material was the same as the previous paper, the preparation method was different, and significantly more data was collected. This experimental confirmation of a mathematically derived equation of the form  $G \sim \varepsilon^{-1/2}$  is the first to do so.

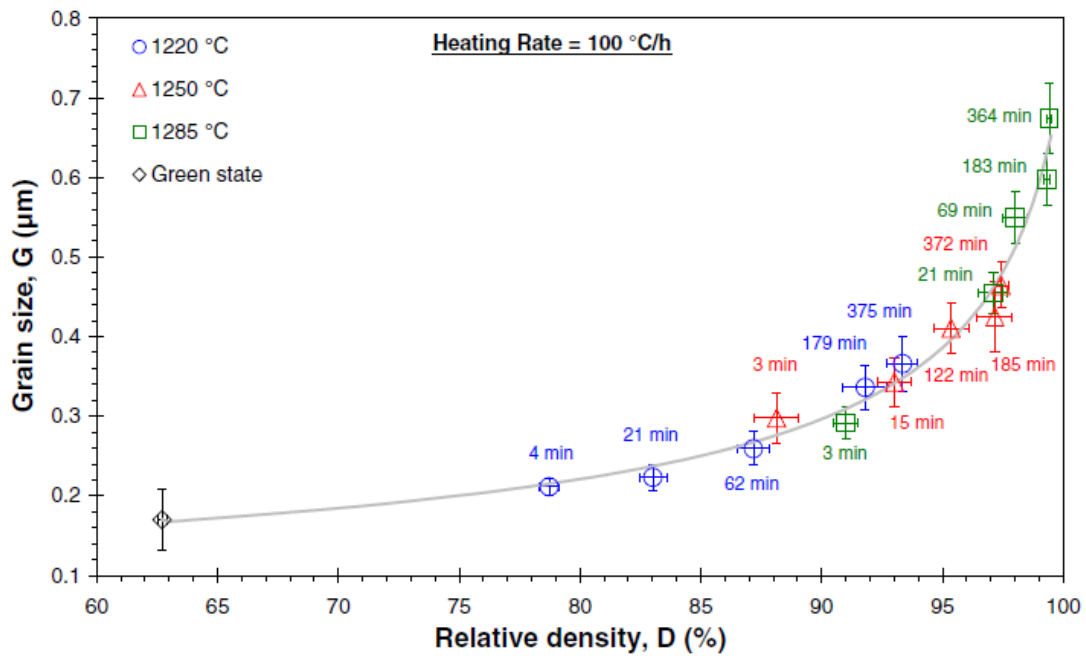


Figure 6. Slip-casting of alumina (in air) confirms a  $\varepsilon^{-1/2}$  relationship between grain size and relative density, taken from Bernard-Granger et al.<sup>66</sup>

He, et al.<sup>67</sup> conducted several experiments on hot-pressing of alumina at different applied pressures. They found that increasing the pressure from 1 to 5 MPa had a significant, positive impact on the final density and overall densification. However, they

also found no difference in densification between applying 5 and 10 MPa. It is not clear what role pressure has on improving densification from these experiments, as they indicate both that higher pressure improves densification and there may be some threshold pressure that much be reached to improve densification, but once it is reached no further improvement is gained by further increasing pressure.

To investigate further the impact of spark sintering on densification rates, we looked at more papers that dealt with spark sintering. Guillard et al.<sup>68</sup> examined the densification of SiC using spark sintering. They showed significant grain growth, but also the ability to achieve nearly full density using SPS, even for this hard-to-densify material.

Olevsky<sup>69</sup> et al. derived the equation  $dG/dt \sim G^3 \varepsilon^{-4/3}$ , confirming the experimental conclusion of Zhao and Harmer twenty years prior, by studying the effects of high heating rates on the spark sintering of aluminum.

Another spark sintering paper, by Cabibbo<sup>70</sup> et al., investigates the densification of Fe-1.5 wt% Mo (FeMo) with 1.5 wt% TiO<sub>2</sub> additives in spark sintering. TiO<sub>2</sub> is used to aid in the thermal stability of the alloy due to the additive's strong pinning force against grain boundary sliding. Despite their efforts, they showed significant grain growth (50 micron to 150 micron) with only a slight increase in density (95-98%). If the main mechanism of grain growth in SPS is grain boundary sliding, as is the case of hot-pressing.

Bernard-Granger, et al.<sup>71</sup> compared the densification of zirconia in SPS and hot-pressing. Although the SPS experiments were conducted in significantly shorter time, both showed similar densification and small grain size results. Both processes exhibited

no grain growth before approximately 97% relative, at which point the SPS specimens doubled in grain size (grains went from 80 to 170 nm) while the hot-pressing specimens only increased 50% in size (grains went from 70 to 110 nm). However, since both processes were able to preserve nanostructured grains, and the expected grain growth for this material in conventional sintering is much larger, the results are similar enough to be equal. These experiments show SPS offers no grain growth advantages over hot-pressing for some material systems, however both offer benefits over conventional sintering.

Langer, et al.<sup>72</sup> conducted a direct comparison between SPS and hot-pressing of alumina. Using the same powders, with the same sintering conditions (heating rate, sintering temperature, initial particle size, applied pressure) except holding time, they achieved the same density, densification, and grain growth in SPS and hot-pressing. Both showed the same improvement over conventional sintering, with higher final density and lower grain growth. They also found that heating rate had no impact on either densification or grain growth, and that the hot-pressing specimens merely needed more time to achieve the same properties as SPS. They also noticed no location variation in grain size in either specimen. They also determined that the primary densification mechanism in both processes is grain boundary diffusion, with similar parameters for both processes. Finally, their plotted relationship between density and grain size is very similar to Equation 9, proposed by Dr. German, with the same  $\epsilon^{-1/2}$  relationship.

Langer, et al.<sup>73</sup> also conducted a comparison between SPS and hot-pressing and zinc oxide. Besides merely comparing the two processes, the authors also sought to examine the presence of electrical current-based enhancements to densification in the SPS process. Unlike their alumina experiments, zinc oxide is semi-conductor and

therefore current effects in SPS should have an impact as current flows through the powder. To test this hypothesis, they conducted SPS using both no electrical insulation of the zinc oxide powder, and alumina felt insulation of the zinc oxide powder. They conducted the SPS and hot-pressing experiments using the same time, temperature, pressure, and heating rate parameters. Due to the limitations of heating rate in hot-pressing, the heating rate of 10 °C/min used was significantly lower than traditionally used in SPS. Their results showed no benefit from using SPS, with both processes having the same densification and grain growth behavior. They also saw no difference in grain size or density between electrically isolated and non-isolated specimens, indicating the current didn't enhance the densification in SPS. Finally, their grain growth versus densification curves show a similarity to Dr. German's Equation 9, as their previous work also did.

Langer, et al.<sup>74</sup> also conducted their hot-pressing and SPS comparison experiments on yttria-stabilized zirconia, similar to Bernard-Granger, et al.<sup>71</sup> They used the same sintering parameters for both processes, except they also conducted several experiments with SPS with higher heating rates. Similar to their two previous studies<sup>72,73</sup>, they found no difference in densification or grain growth between SPS and hot-pressing. When they increased the heating rate, they saw no difference in the densification curves in the range of 30 to 150 °C/min. However, there was a substantial improvement in the densification curve between 10 and 30 °C/min. Since 10 °C/min is a standard heating rate for hot-pressing, and was the heating rate they used in the this and the two previous publications, it is unclear how they claim there is no improvement using SPS over hot-pressing, since heating rates of 30 °C/min and higher are only possible in

SPS and not hot-pressing. Again, they also claim the dominant mechanism for densification is grain boundary diffusion, and again their densification versus grain size curves mirror those of Dr. German's Equation 9 and their previous two publications.

Perera, et al.<sup>75</sup> investigated the densification of  $\text{Si}_3\text{N}_4/\text{SiC}$  composites in HIP and SPS. They found comparable grain growth and densification in both processes, although SPS was able to achieve full density with no holding time. HIP required more than 100 minutes holding time to achieve the same result.

Monteverde<sup>76</sup> compared the densification of  $\text{HfB}_2\text{--SiC}$  ceramics in SPS and hot-pressing. They found that SPS densified the powder more uniformly, with an even final grain size distribution, compared to slight non-uniformity in hot-pressing. The SPS specimens showed improved fracture toughness, but also significant cracking during machining before testing and reduced strength. This indicates a significant residual thermal stress buildup in the specimen due to the rapid cooling from 2100 °C down to 1000 °C in less than 2 minutes. Although rapid cooling in SPS is usually an advantageous feature, due to the preservation of features and properties imparted during sintering, with some hard-to-densify ceramics these residual stresses can significantly reduce some of the mechanical properties of the material.

### **1.2.1. Densification and structure evolution during SPS of Alumina**

Alumina ( $\text{Al}_2\text{O}_3$ ) has been widely studied, both in conventional sintering and spark sintering (and in virtually every other field).<sup>77,78</sup> Because of this extensive background, and a thorough understanding of the material properties, alumina is a good

candidate for further research in spark sintering. One of the important material properties of alumina for our research is the high electrical resistivity (making alumina an electrical insulator), with values ranging from  $10 \times 10^{14} \Omega\text{-m}$  at 25 °C to  $2 \times 10^6 \Omega\text{-m}$  at 1000 °C<sup>79</sup>. This high resistivity emphasizes the heating effects of the die from Joule heating (the main heating mechanism in SPS) during SPS, which is dependent on electric current, since little or no electric current flows through the specimen powder itself due to the extremely low resistivity of graphite ( $1.4 \times 10^{-5} \Omega\text{-m}$ ) compared to that of alumina, making alumina a good representative material for other non-conductive ceramics.<sup>80,81,82</sup>

The preservation of the grain size during densification is closely related to the net-shaping capabilities of SPS. Indeed, a particular macroscopic shape of a processed specimen implies certain thermal and electrical field boundary conditions, which may have a significant impact on the evolution of the material structure during SPS.

Work by Gao, et al.<sup>83</sup>, showed an improvement in densification of alumina through SPS over conventional sintering, at lower temperatures (100 °C lower), but also a more homogeneous microstructure with superior microstructure. However, work by Wang, et al.<sup>84</sup> shows a microstructure inhomogeneity development during SPS of alumina, with the edges of the circular specimens being denser than the center. This contradiction of results demands further investigation.

Most of the current research in spark sintering uses a cylindrical die, composed of graphite, with the specimen powder placed in the hollow center of the die, surrounded by punches on the top and bottom, with graphite foil used both to lubricate the specimen for removal, and also to increase material (and therefore electrical) contact between the die and the two punches. Few papers use prismatic or rectangular dies, and none have the die

shape as a focus of the research.<sup>85</sup> There has been no investigation into the effects of die shape anisotropy on SPS, particularly in regard to grain growth or localized densification. Most of the industrial applications of sintering, require dies with complex shapes to produce parts, and rarely is a final product in the shape of a perfect cylinder. Alumina is a perfect material for this net-shaping application, due to its non-conductive nature, and well understood and established properties.

### **1.2.2. Densification and structure evolution of iron and vanadium carbide**

The potential ability to densify materials at lower temperatures and pressures using spark sintering is of great interest for compacting rapidly solidified (RS) metallic powders. It is well known that using RS techniques (solidification rates  $>10^4$  K/s) it is possible to achieve undercooling as high as 100 °C or more prior to the initiation of solidification. By using this method, large deviations from equilibrium can be obtained which provide the following advantages<sup>86</sup>:

- 1 – large extension of solid solubility, often by an order of magnitude;
- 2 – formation of non-equilibrium or metastable phases and incorporation of desirable second phases like fine dispersoids;
- 3 – reduction of solute segregation;
- 4 – retention of disordered crystalline structure in normally ordered materials and intermetallic compounds;
- 5 – grain refinement, formation of novel microstructures, production of metallic glasses, etc.

Rapidly solidified particulates must normally be consolidated into fully dense bodies before they can be studied or used. The consolidation sequence for these powders traditionally consists of the following: a) cold pressing, b) degassing, c) hot consolidation (sintering), and d) hot working. In order to obtain full consolidation of RS powders/particulates it is necessary to impose relatively high temperatures and pressures. For instance, hot compaction of carbon steels requires temperatures around 900 °C for relatively long holding times.

Most microstructural features obtained by RS processing, and due to non-equilibrium conditions, can be lost due to extended thermal exposure. The utilization of SPS could be extremely helpful to obtain full consolidation of RS materials without losing their original characteristics. It is advantageous to use SPS to consolidate metallic glasses without strong re-crystallization effects, or to consolidate RS-powders of high alloyed hypereutectic Cr-W-V- rich alloys (tool steels).

Previous research on aluminum alloys by Matsugi, et al.<sup>87</sup>, showed that the supersaturated state of aluminum 7075 alloy rapidly-solidified powders was preserved through consolidation in SPS, if the proper rapid-cooling regime was used after sintering. Of the sintering parameters they studied (holding time, cooling rate, maximum temperature, and pulse frequency), only cooling rate and maximum temperature had an effect on the ability to preserve the super-saturated state. SPS was also found to preserve the nanostructure of ball-milled Fe-Co-Cr-V powder for producing bulk magnets.<sup>88</sup> SPS' ability to sinter at lower temperatures than conventional sintering was vital to the success of these experiments, along with the rapid cooling when electrical current is removed after sintering.



SPS may also be used to enhance the properties, improving them in ways not achievable using other techniques. High strength steels suffer from severe corrosion due to their high carbon content and lack of protective additives that reduce strength (as Nickel and Chromium in stainless steels). Hydrogen embrittlement is a destructive corrosive process where hydrogen diffuses into a steel (particularly at high temperature), causing pitting and cracking during the diffusion process<sup>89</sup>. Vanadium carbide has been shown to reduce hydrogen embrittlement when used as an additive in high strength steels, as well as improve the strength of the steel due to its high strength and hardness (being a ceramic carbide)<sup>90</sup>. However, vanadium carbide is difficult to incorporate into steel, and it often breaks down during the long holding time of conventional sintering, with the carbon diffusing into the steel to form Fe-C compounds.<sup>91</sup>

Chicco, et al.<sup>92</sup> studied the use of thermal diffusion processes on tool steels (containing high levels of vanadium) and combining this process with a pre-nitriding process. The most common process of carburizing followed by nitriding creates a soft layer of vanadium nitride on the surface and a thicker layer of vanadium carbide underneath. Since vanadium nitride is softer than vanadium carbide, this is not optimal for the creation of tool steel parts. The authors compared single pre-treatments of gas nitriding, liquid nitrocarburising, and liquid carburizing, and also combinations of these treatments.

Each of the individual processes creates a different surface layer in the material, with different structure but similar properties of increased hardness and brittleness. Application of thermal diffusion vanadization only creates a sharp boundary between the surface vanadium carbide layer and the material beneath.

Combining the two processes creates a functionally graded material where the surface layer is primarily vanadium carbide and the carbon content diminishes steadily away from the surface. The surface layer is similar using only vanadization and not nitriding, however the nitriding process significantly increases the thickness of this functionally graded layer. This functionally graded structure is advantageous for tool steels and other specific applications.

Tanaka et al.<sup>93</sup> investigated the metallographic structure changes in high carbon Fe-C systems after ball milling. They measured the effects of mechanical alloying on FeC systems with carbon content ranging from .17 to .9, starting with pure graphite and pure iron powders. They observed the creation of a lamellar phase after 20 hours of milling, where the graphite formed layers that were sandwiched by iron layers, and an equiaxed structure after 100 hours, where the iron particles all had a similar size.

Feng et al.<sup>94</sup> used combustion synthesis to create VC/Fe in an electric field from graphite, iron, and ferrovanadium precursors. The electric field was used to propagate the combustion wave in the material, after it has been generated. Using this method, they were able to densify the composite using significantly lower temperature (as low as 691 C), and creating more of the vanadium carbide particles in the matrix.

He et al.<sup>95</sup> used SPS to create VC/Fe composites starting from amorphous carbon and ferrovanadium precursors. They ball-milled iron and vanadium to create a mixture that was 51.25% vanadium, and then mixed that with 100 nm particle size amorphous carbon in a 1:1 ratio. The specimens were sintered between 650-1150 °C, at 30 MPa pressure, with the best results happening at higher temperature (up to 1050 °C, where iron

is melted). They successfully produced specimens of 96% relative density with hardness 84.2 HRA, with evenly distributed vanadium carbide particles in an iron matrix.

Many papers examine the relationship between grain coarsening and vanadium carbide additives in steels, with particular interest in the grain growth reduction.<sup>96,97,98,99,100,101</sup> Although an exact calculation of the grain size reduction from vanadium carbide additives is not possible, it is clear from the literature that vanadium carbide (and other carbides, also) plays a significant role in the minimization of austenite grain growth during densification of steel. Frasier et al. showed that a steel with a vanadium concentration in the 10-15% range, and a carbon concentration in the 1-2% range, created the hardest and strongest vanadium carbide steels. Li et al. found that forging below a critical temperature had a significant impact on grain growth in vanadium rich steels.

The conducted literature survey shows that SPS has the potential to create Fe-V-C steels and enhance their properties through the unique combination of decreased sintering temperature and rapid sintering. Enhancing the properties of this material is key to improving its strength and corrosion resistance properties.

### **1.2.3. Densification and structure evolution of tantalum carbide**

Properties of tantalum carbide (TaC) include high strength, high hardness, wear resistance, chemical resistance, as well as the superconductivity at low temperatures.<sup>102</sup> Tantalum carbides are suitable for many applications, including as an abrasive and for machining tools. Besides cutting tools, one of the main uses for TaC is as a reinforcing phase in composites, particularly in composites with tool steel matrices, to increase strength and wear resistance.<sup>103</sup> Recent research suggests TaC may be used as a gate

material for MOSFETs (particularly for high temperature integrated circuits), as an additive in tungsten cathodes in cold-cathode thyratrons (also known as a pseudospark switch), and in many new high temperature, energy applications, such as nuclear or solar propulsion engines for spacecraft.

Production of TaC through sintering is difficult, due to its high melting point of 3880 °C, which is the highest for any stoichiometric compound. Since sintering typically occurs above 50% of the melting point, it is difficult to sinter TaC in conventional furnaces or through hot pressing. The cost of furnaces with adequate insulation and composed of materials that can withstand the required level of temperatures are often prohibitively expensive. Even furnaces for hot isostatic pressing that can reach the needed temperatures, operate with low heating rates, often as low as 5 °C per minute up to temperatures above 2000 °C, thereby rendering unacceptable productivity rates.<sup>104</sup>

Additives can be used to decrease the sintering temperature of TaC, such as boron carbide, hafnium carbide, niobium carbide, nickel, molybdenum, iron, and others, in concentration as low as 50 ppm.<sup>105,106,107,108</sup> These can lead to a reduction in the sintering temperature to as low as 1400 °C in hot isostatic pressing, however, the drawback is extreme grain growth and inability to attain full density, along with decreased mechanical properties. Another method of achieving higher density, and higher strength, is through the use of substoichiometric Tantalum carbide compounds, in the form of  $Ta_{1-x}C_{1+x}$ , where x is between 0.01 and 0.5; however, the sintering temperature is still above 2700 °C.<sup>109</sup> Extreme pressure has also been shown to aid in the densification of TaC and reduce the required sintering temperature, with TaC having been densified to 93% at 1200 °C with a pressure of 4.5 GPa.<sup>110</sup>

Another method for increasing the final density of sintered specimens is a reduction in the particle size of the powders. Research has shown that smaller powders produce a higher final density than coarser powders, particularly when decreasing from the micrometer to the nanometer scale.<sup>111</sup> This indicates that starting with nanoscale powders would be beneficial in sintering a material like TaC, which is normally difficult to densify. However, research by Sommer et al.<sup>112</sup> shows that rapid grain growth can occur (from 100 nm starting particle size to 500 nm grain size) during conventional sintering, particularly in carbide ceramics. This grain growth produces different material properties in the final specimen, although the grain size is still smaller than when sintering from a larger starting particle size. Kim et al.<sup>113</sup> have shown that initial particle size is essential to the final density of sintered TaC, with larger initial particle size indicating a lower final density, using a high heating rate that uses induction of electrical current to heat the die, rather than direct current flow through the die as in Spark sintering. Initial particle size and controlling final grain size while maintaining high density is key to successful applications of materials such as tantalum carbide.

Zhang et al.<sup>114</sup> have shown the capability of hot pressing of TaC to produce high density specimens (94-96%) at a relatively low pressure (30 MPa) and decreased temperature (2300-2400 °C), using a powder that ranges in particle size from .5-2.6  $\mu\text{m}$  (average 1.6  $\mu\text{m}$ ). Their heating rate was 5 C/minute up to the holding temperature, and holding for 45 minutes. At 2400 °C holding temperature, although 96% final density was achieved, the average grain size increased from 1.6  $\mu\text{m}$  to 2.8  $\mu\text{m}$ . However no significant grain growth occurred when hot pressing at 2300 °C, although the final density was only slightly lower (94%). Zhang et al. showed many variations in density

and grain size when different sintering temperatures were used, from 1900 °C to 2500 °C. These dramatic differences indicate the strong influence of small changes of sintering temperature on final density and grain size.

The conducted literature survey on alumina, tantalum carbide, and iron and vanadium carbide, show that SPS is a valid technique for use in the sintering of hard-to-densify materials like tantalum carbide. Because SPS has been widely conducted on alumina, it is a perfect candidate for research into new areas like complex or net-shape applications. Tantalum carbide has not been sintered using SPS previously, so it is a novel material system whose results can be compared to densification by other methods. And Fe-VC is a good candidate for understanding SPS' capability to preserve properties imparted during processing before sintering, while also observing chemical reactions that can occur during SPS.

### ***1.3. SPS of complex shape components***

In this literature survey, we examine the current research on complex shape components produced through SPS, with a focus on extrusion combined with spark sintering.

Tokita examined the capability of SPS to produce square-shaped specimens of various WC-Co-Ni powders.<sup>115</sup> He found that there was no variation in hardness, grain size, or grain distribution, between various points (including the center and corner) of large (70 by 100 by 8-60 mm) square-shaped specimens produced in SPS (as seen in Figure 7). He also found that the mechanical properties of the specimens were superior

to those produced using conventional methods. Finally, he was able to successfully process functionally graded specimens (both horizontally and vertically graded) using these powders in SPS.

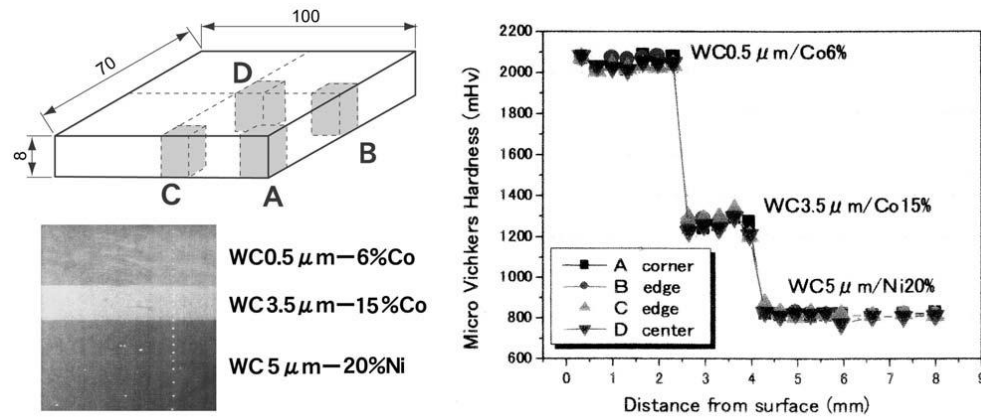


Figure 7. A diagram of the uniform properties in various parts of a square WC-Co-Ni specimen, from Tokita.<sup>115</sup>

A survey of the patents involving SPS provides interesting results.<sup>116</sup> Kaneuchi and Morita<sup>117</sup> developed a special die for creating nozzle-shaped parts in SPS. Using a standard cylindrical die, with insert parts that taper the edges closest to the punch, and a solid cylinder in the center of the powder area, they created a system for making nozzle parts where the finished product can be easily removed from the die (due to the inserts). A diagram from the patent is shown in Figure 8.

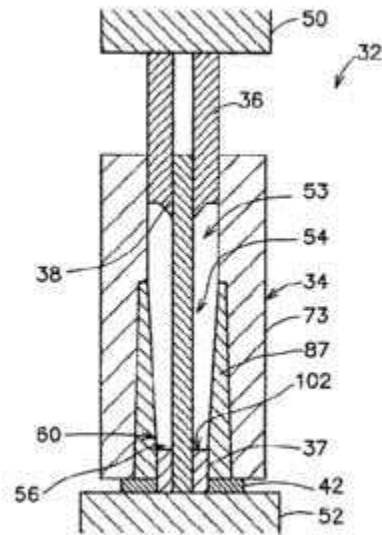


Figure 8. A diagram showing a special SPS die for creating nozzles, where area 54 is the empty space for powder, 38 is the cylindrical center piece, and 87 is the tapered, removable insert. From Kaneuchi and Morita<sup>117</sup>

Yamashita and Wada<sup>118</sup> developed a sintering die for creating an annular magnet in SPS. The die is just a hollow ring, with the special modification that two different current sources are used – one preliminary, low power source to align the domains of the magnet before sintering, and a second, high power source to provide Joule heating.

Okano and Izui<sup>119</sup> developed a method for creating functionally graded rings in SPS, by adding and pressing different powders (of titanium and hydroxyapatite, for biocompatible implants) in subsequently larger diameter dies, and then sintering the final multi-layered cylindrical compacts in a standard, large diameter SPS die.

Ikeda<sup>120</sup> developed a specially designed convex punch for use in SPS, and utilized the lower temperature sintering capabilities of SPS (compared to other sintering



methods), to sinter a concave glass lens at a temperature above the glass transition temperature and below the crystallization temperature.

Nakano, Ide, and Nakamura<sup>121</sup> created a special SPS die that produces another SPS die as the final product. Using a special conical extension on the lower punch face, see Figure, the final specimen is a hollow cylinder or torus that can then be used as an SPS die. The goal of this process is to remove the expensive machining when making dies of hard materials, like carbides, as the net-shape part from this process needs little or no machining. Also, it allows anyone with an SPS machine and inexpensive graphite tooling to produce their own higher quality dies made of better materials than graphite.

Ward<sup>122</sup> developed a die for creating disc brakes, where a backing plate was inserted into the bottom part of the die or punch, and the powder material was densified and bonded to the backing plate during sintering. The top punch had a small recess for the application of graphite powder, for the reduction of contact resistance between the electrode and the to-be-sintered powder.

We can see from the above patents, and the one source in literature, that the idea of producing complex shapes in SPS has been around for a long time, however there has not been significant research in this area.

Extrusion is the process of applying force to push (using a ram) a material of a certain area through a die and out a hole of a smaller area. There are different types of extrusion, determined by whether the billet, container, or die are stationary and where force is applied. It is a well understood material processing technique, with the science behind the process relegated to textbooks, rather than scholarly articles<sup>123,124</sup>. In recent

years, extrusion of new materials systems and extrusion combined with other processing techniques have been of interest.

Mabuchi et al.<sup>125</sup> studied the effects of hot extrusion on the mechanical properties of an Mg-Si-Al alloy. The alloy was initially cast in a green sand mold, followed by extrusion with an extrusion ratio of 100. They achieved grain refinement from 69  $\mu\text{m}$  for the as-cast material, down to 27  $\mu\text{m}$  for the as-extruded material, while retaining the uniform, equiaxed grain shape. They also noted an increase of tensile strength from approximately 125 MPa in the as-cast specimen to 200 MPa in the extruded specimen. Extrusion also helped to disperse, and reduce the size of, the  $\text{Mg}_2\text{Si}$  particles that were present in the as-cast specimen.

Shahzad et al.<sup>126</sup> investigated the grain development after extrusion in Mg-Zn-Zr alloys with two extrusion ratios. They found that the equiaxed grains of the as-received alloys (average grain size 100  $\mu\text{m}$ ) experienced extreme elongation (into thin, string-like grains) during extrusion, combined with some recrystallization. The recrystallization converts the elongated grains into groups of large grains (10-20  $\mu\text{m}$ ) and small, fine grains (2-5  $\mu\text{m}$ ), and does not occur in regions that are Zr-rich and Zn-lean. Their extrusion ratios of 44 and 12 (in two different dies) showed a severe reduction in grain size in the recrystallized areas, but grain volume was essentially retained in areas where no recrystallization occurred. This was mostly due to the material system, where precipitation of Zn and Zr during recrystallization severely impacts the size and phase of individual grains. The elongation effect of grains during extrusion is a well documented phenomenon.

Chandrasekaran et al.<sup>127</sup> explored the effects of materials and temperatures on the extrusion of magnesium alloys. Using an extrusion die with only a 41% reduction in area (corresponding to an extrusion ratio of 1.69), they achieved grain refinement in all of their specimens.

Morsi et al.<sup>128</sup> showed that extrusion can be conducted on a miniature scale, and that the same properties apply as on the macroscale. They preheated aluminum billets (200-300 °C) and extruded them through a square die, using an extrusion ratio of 10 to 32, however the macro-sized billet weighed 458 grams, and the micro-sized billet weighed only 1.2 grams. The extrusion pressures, microhardness measurements, and displacement curves were comparable for both scales. These experiments show that extrusion of small specimens can be directly compared to industrially sized materials production.

Kwon et al.<sup>129</sup> used spark sintering combined with hot extrusion (in a two-step approach) to create an aluminum and carbon nanotube composite. They initially performed SPS on the powder in a standard graphite die, then put the densified specimen into a separate steel extrusion die (with an extrusion ratio of 20), where hot extrusion was performed. The temperature of sintering was 600 °C, while the hot extrusion temperature was a lower 400 °C. Although they used a sophisticated nanoscale dispersion technique to distribute the CNTs uniformly onto the aluminum particles before sintering, some agglomeration occurred where the CNTs amassed in particular areas on the spherical particle surfaces. The starting particle size of 14.82  $\mu\text{m}$  decreased slightly to 13.90  $\mu\text{m}$  grain size after sintering and extrusion processing, and the grains remained mostly equiaxed with little or no elongation deformation caused by the extrusion process. The

presences of aluminum carbide at the grain boundary, significant increase in Vicker's hardness, and some evidence of nanotube bridging at crack locations show that they were able to successfully create this composite using the combination of these techniques using a two-step approach.

Morsi et al.<sup>130</sup> conducted an initial investigation into the combination of spark sintering and extrusion, coining the term "spark plasma extrusion" (SPE). The original patent for the technique originates from 1983<sup>131</sup>, long before the current thrust in SPS research. The technique involves the heating and densification of a powder specimen using electric current, and then subsequent extrusion through an extrusion die, all in the same apparatus and experimental setup. It is not clear if this process involves application of any pressure during heating (and densification), or only during extrusion after densification is already (partially) completed. Using a steel die with an extrusion ratio of 16, Morsi et al. sintered and extruded aluminum specimens at 250, 350, and 450 °C. Their setup was unique in that the SPS machine was produced in their lab, rather than being purchased commercially. They showed that hardness increased in the specimens that were extruded, compared to non-extruded specimens, but they did not characterize grain size, grain growth, or porosity, as is common in papers of this type, or even grain elongation to show the effects of SPE.

Morsi et al.<sup>132</sup> published a second paper using SPE to create aluminum and carbon nanotube composites. They used extremely high pressures (up to 900 MPa), and normal temperatures of 300 to 600 °C. They were able to create single and dual matrix composites using this technique, with single matrix composites having the highest Vicker's hardness and material properties. All of their specimens reached 96-98% final

relative density, however, grain size, grain growth, and grain shape were not considered. Regardless, the technique has been validated by their experiments. A diagram of their die is shown in Figure 9.

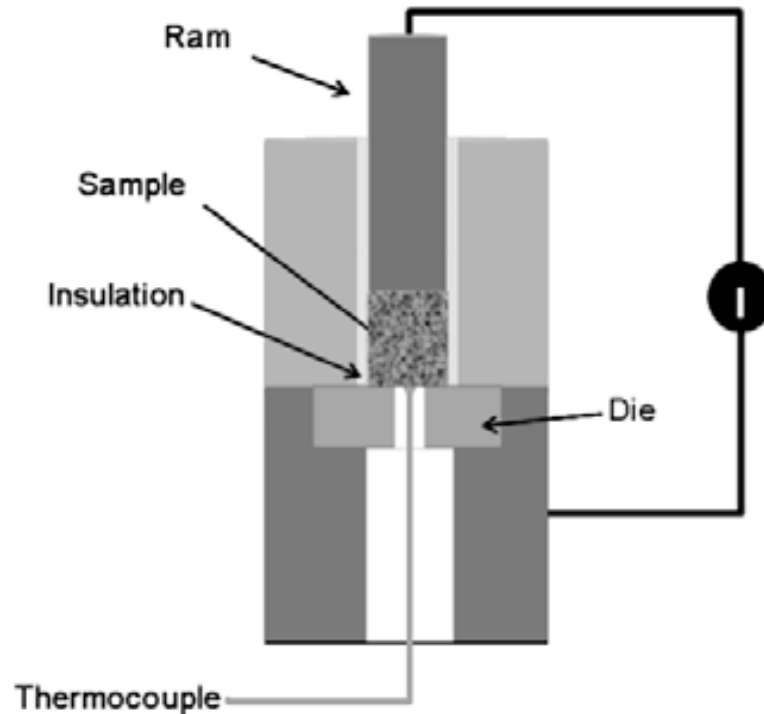


Figure 9. A diagram of a spark plasma extrusion setup, from Morsi, et al.<sup>130</sup>

We can see that extrusion combined with SPS is in its infancy. Some previous work has been conducted in this area, but only a handful of paper have been published, and all within the last three years. The potential to combine these two techniques is great, with proven results of extrusion in refining and decreasing grain size combined with potential decreased grain growth and densification in spark sintering.

#### ***1.4. Conclusions of conducted literature survey***

Spark plasma sintering is a useful tool for sintering materials that are hard to densify, while still providing an opportunity to investigate the fundamental mechanisms of the technique and their relation to material properties, densification and grain growth, particularly when dealing with net-shaping and creating tailored properties during, and after, sintering. Spark plasma extrusion offers the ability to improve and further refine the properties of a material after sintering, without extended processing.

Overall, spark plasma sintering is a hot area of research, and many publications have been produced in the past 10 years, but they have only recently evolved from various simplistic trial-and-error approaches. Despite this abundance of trying the new technique on known materials, there are several material systems of research importance (like carbides, especially tantalum) that have had little or no research conducted at all. No research has definitely identified, or quantified, the improvement or enhancement of material properties that is hotly publicized about spark plasma sintering, and there are several contradictory articles about the roles of particular parameters (heating rate, sintering time, etc.) on the enhancement of those properties.

Another major area of research that has been ignored is a possibility of SPS-based net-shaping, which depends on the ability to use various die shapes in SPS, including extrusion dies. Extrusion is well studied, especially in relation to the development of nanosized grains in processed materials. SPS, which potentially offers a significant grain size reduction for most material systems, and retention of nanosized grains when starting from nanosized powder, has not been combined with extrusion to see the effects on grain refinement. This is likely a technical issue, as designing an extrusion system that carefully utilizes the extreme electric current present in SPS is a challenge.

We can see that there is a great opportunity to investigate the creation of tailored structures and net-shaping in SPS, in particular by examining the development of grain size and density, using different materials, and different sintering conditions (different die shapes, extrusion processing, etc.).

## **Chapter 2. Research Objectives**

Based on the conclusions of the conducted literature survey, the following research objectives and the respective research tasks are formulated:

1. The effects of structure and complex tooling shape on tailoring in Spark Plasma Sintering will be investigated.
2. The tailoring of structures, such as grain size retention and structure directional alignment, through combining extrusion processes with SPS, will be investigated.
3. SPS' ability to retain and enhance material properties (such as strength and structure uniformity), for several material systems, will be investigated.
4. A better understanding of the specifics of the grain size v. density trajectory under SPS will be gained, and in particular, certain sintering conditions will be examined that fit a simpler model for densification behavior than is usual for SPS.



## Chapter 3. Shape factor in SPS processing

### *3.1. Introduction to spark plasma sintering of alumina*

As mentioned in the introduction, spark plasma sintering (SPS), also known as electric current sintering or field assisted sintering techniques, is becoming a widely used process for sintering research that relies on heating powder specimens with electric current, instead of an external heating source. Pressure is usually applied during the SPS process to ensure proper electrical contact between the electrodes and the conductive dies which hold the powder, which is similar to Hot Pressing. The advantages of the SPS method, which have been widely publicized in research, are faster heating rates, shorter holding times, smaller grain sizes, and denser final materials.<sup>133,134,135,136,137</sup>

Most of the current research in spark plasma sintering uses a cylindrical die, composed of graphite, with the specimen powder placed in the hollow center of the die, surrounded by punches on the top and bottom, with graphite foil used both to lubricate the specimen for removal, and also to increase material (and therefore electrical) contact between the die and the two punches. Few papers use prismatic or rectangular dies, and none have the die shape as a focus of the research.<sup>138</sup> There has been no investigation into the effects of die shape anisotropy on SPS. Most of the industrial applications of sintering, require dies with complex shapes to produce parts, and rarely is a final product in the shape of a perfect cylinder.

Alumina is a perfect material for this application, due to its non-conductive nature, and well understood and established properties. Alumina ( $\text{Al}_2\text{O}_3$ ) has been widely

studied, both in conventional sintering and spark plasma sintering (and in virtually every other field).<sup>139,140</sup> Because of this extensive background, and a thorough understanding of the material properties, alumina is a good candidate for further research in spark plasma sintering. One of the important material properties of alumina for our research is the high electrical resistivity (making alumina an electrical insulator), with values ranging from  $10 \times 10^{14} \Omega\text{m}$  at 25 °C to  $2 \times 10^6 \Omega\text{m}$  at 1000 °C<sup>141</sup>. This high resistivity emphasizes the heating effects of the die from Joule heating (the main heating mechanism in SPS), which is dependent on electric current, since little or no electric current flows through the specimen powder itself due to the extremely low resistivity of graphite ( $1.4 \times 10^{-5} \Omega\text{m}$ ) compared to that of alumina, making alumina a good representative material for other non-conductive ceramics.<sup>142,143,144</sup>

To understand the fundamental aspects of SPS, particularly in regard to complex, non-cylindrical shapes, we conducted a study using several different die shapes. The goal of the research is to investigate what effects the die shape has on the densification and grain growth behavior of non-conductive powder specimens in SPS. Very little research (if any) has been carried out in this area, with SPS entirely conducted in cylindrical shapes due to a desire for symmetry with respect to current flow and current density. This current flow symmetry translates to heat flow symmetry in non-conductive specimens. However, real sintered parts rarely are simple, or have such symmetry, and it is unknown what differences will exist in a complex shape specimen sintered by SPS.

To analyze the effects created by the shape change for study, we used a square prismatic die with a 30 mm outer side length, and a central hole with a 15.4 mm side length for the square specimen. This allowed for a standard 15.4 mm circle to be

inscribed inside the square, corresponding to a cylindrical die with a 15.4 mm inner diameter for the specimen. This layout would allow us to see what variations in sintering, based on final density and density distribution, occurred in the central area of the square (where the inscribed circle lies), and the corner areas (outside the inscribed circle). These results could be compared directly to a specimen produced in a cylindrical die of 15.4 diameter, the same as the inscribed circle, due to both specimens having the same aspect ratio. The cylindrical die we used was designed with a 30 mm outer diameter, and a 15.4 mm inner diameter. The .4 mm is to accommodate graphite paper with a .2 mm thickness. The die is 30 mm in height, and the punches are 15 mm in diameter.

Since the desired specimen is electrically insulating, all heat for sintering is generated in the die. The amount of heat produced is dependent on shape anisotropy, where thicker die walls will produce more heat than thinner ones (assuming a uniform current density), and sintering in vacuum insures that heat will flow into the die and through the system. The dies, both square prismatic and cylindrical, were designed with the same wall thickness (7.5 mm).

Using the simplest case of circular and square specimens, we can evaluate these effects based on the common standard of aspect ratio, which is the relationship between the width and length of an object. Since the thickness of all the specimens if the same, we will only concern ourselves with the cross-sectional areas of the specimens, and their aspect ratio. For a circle, and a square, this value is 1, as the width and the side length are both equal, and equal to the radius.

### ***3.2. Fundamental experiments on the specimen's shape impact on the SPS densification and grain growth kinetics***

#### **3.2.1. Experimental work on the shape impact in spark plasma sintering of alumina using two die designs**

We started with 2.5 grams of -325 mesh alumina powder (no particles larger than 44  $\mu\text{m}$ , average particle size 0.5  $\mu\text{m}$ ) (Alfa Aesar, USA), and 1.5 grams of 50 nm average particle size alumina powder (LECO Co., USA) were sintered separately in the Doctor Sinter Lab 515S Spark plasma sintering machine (SPSS Syntex, Co. Japan). The difference in weight for the two powders for the specimens is due to the lack of pre-pressing and the higher powder volume of the nanometer sized powder, allowing only 1.5 grams of 50 nm alumina powder to fit in the 30 mm die where 2.5 grams of the -325 mesh powder would fit.

For the square specimens, a square prismatic graphite die with side length of 15.4 mm was used, with the same preparation (graphite foil, etc.) as for the cylindrical die. To match the contours of the die, the punches also have rounded corners. The flat portion of each side of the square is 12 mm, with the radius of curvature at the corners being 1.5 mm. The resultant specimens were squares with 15 mm side length, with rounded corners.

The sintering temperatures were 1200, 1300, and 1400  $^{\circ}\text{C}$ , based on the conventional sintering and hot pressing temperature<sup>145</sup> of alumina being 1450  $^{\circ}\text{C}$ , and a report that alumina could be sintered at 1175  $^{\circ}\text{C}$  using SPS<sup>146</sup>. The holding times were 8 minutes, 15 minutes, and 40 minutes, based on similar experiments conducted by Shen et al. for SPS of alumina in a traditional die.

The pyrometer we used functions in the range of 570-3000 °C, so the starting temperature was set at 565 °C. The temperature profile used was 3 minutes to 600 °C, hold at 600 °C for 1 minute, 1 minute to 800 °C (200 °C /minute heating rate), hold at 800 °C for 1 minute, 6 minutes to either 1160, 1260, or 1360 °C (depending on the sintering temperature, and with rates of 60, 77, or 93 °C /minute respectively), 1 minute to 1200, 1300, or 1400 °C (40 °C /minute), holding at 1200, 1300, or 1400 for the specified time. The initial slow start-up and holding at 600 and 800 °C was to allow for proper alignment of the pyrometer without accidental overheating, due to the high minimum measured temperature. The final 40 °C /minute heating rate before reaching the sintering temperature was to prevent overshoot of the sintering temperature by the SPS machine. The total time for the different sintering temperatures was kept constant, so there is variability in the heating rates for the different experiments. We chose this profile because it allowed for safe and accurate measurement of the temperature by our pyrometer, while also providing heating rates (between 60 and 200 °C per minute) that exceed those available in Hot Pressing.

The pressure applied during sintering was either 36.8 MPa or 48 MPa. The powder was loose and only slightly compacted by the addition of the punches to the die, before insertion. No pre-pressing of the powder was performed -- rather the powder was inserted into the die, and die was placed in the SPS machine for the sintering process. Pressure was applied starting at the beginning of the sintering process, continuing throughout the process until the die was removed from the machine.

After sintering, the specimens were cut and/or fractured (Buehler Isomet 1000), and standard Archimedes Method measurements were performed to calculate overall

density. Also, the z-axis displacement of the press in the SPS machine was used to calculate the density, taking into account the thermal expansion of the graphite die and spacers, during sintering (an explanation of this procedure can be found in the Appendix, under the description of the SPS equipment). The data required for this analysis were the diameter, height, and weight for the specimen, which were measured with digital calipers and a digital scale, respectively. The density measurements between Archimedes method and the computer output were compared for accuracy and found to vary by less than one percent. Image analysis/manipulation software (Adobe Photoshop CS5.5) was used to measure localized density and calculate average grain size. The software was necessary, due to the small weight of the specimens introducing significant error into Archimedes method (due to the similarity between the weight of the wire and the weight of the specimens).

Cut specimens were polished (Tegra Pol T-1000), and then thermally etched at 1300 °C for 1.5 hours before observation in the Scanning Electron Microscope (Phillips XL-40 and Quanta FEI 450).

For the grain size measurements, the error was calculated from the standard deviation of the measurements made from the linear intercept method for each experiment, and the average value from all experiments of 0.05  $\mu\text{m}$  was found, rounded up to 0.1  $\mu\text{m}$ , and inserted in the tables.

### **3.2.2. Initial experimental design with two die designs**

Eighteen initial experiments were conducted (3 experiments at 3 different temperatures with 2 different pressures), and five potential parameters were identified as the most likely parameters affecting the porosity. They were sintering temperature, holding time, particle size, die shape, and applied pressure, and they are the standard parameters analyzed in sintering experiments related to porosity (except for die shape). In order to minimize the number of experiments that would be required to identify which parameters are important, a two level orthogonal Taguchi L12 designed experiment was used to identify which of these five parameters has a significant impact on the resulting porosity. The twelve experiments of the Taguchi L12 designed experiment were taken from the initial 18 conducted experiments (a selection that remove repeated experiments), the resulting porosity values were utilized, and these values were used for the analysis (data for the Taguchi experiments is available in the Appendix). This process used a linear model to compute the coefficients of the factor values that will minimize the sum of the squared errors between the experimental and predicted values of porosity for all experiments. The analysis results identified three of the five parameters as strongly significant, with the fourth parameter (die shape) having a p-value of .49, and with the fifth parameter (particle size) having negligible impact over the range selected. The probabilities of being insignificant (p-values) for the four significant factors were all in the range of 0% to 6%. This clearly showed that particle size did not have a significant impact on porosity in these future set of experiments.

Once the fifth parameter was eliminated, the Taguchi design was modified to 18 experiments to give three levels for a second order model. This gave us reasonable

agreement with the experimental data thus far, with an adjusted coefficient of determination ( $R^2$ ) of 0.626, with four degrees of freedom.

This analysis showed, with good confidence, that the contribution of particle size to final density was much less significant than sintering temperature, holding time, die shape, or applied pressure. Due to these results, we excluded particle size as a parameter in the subsequent experimental work, and only used the -325 mesh powder. That is not to say that particle size is not important to the final density, but rather that in this case, particle size does not have any different influence specifically relating to the die shape, compared to the four other factors.

For the circular specimens, a cylindrical graphite die of 15.4 mm interior diameter (Electrodes, Inc.), with graphite punches of 15 mm diameter, was used for sintering in the SPS, and the die had its interior surface wrapped in either .13 or .2 micron thick graphite foil (for lubrication purposes, and to prevent interaction between the die and sample). The resultant diameter for the specimen was 15 mm.

### **3.2.3. Experimental Results on shape impact on SPS of alumina with two die designs**

The goal of the experimentation with the two sets of dies is to see how density evolves during sintering and compare the final densities for each type of specimen (circular and square). Based on the different temperature profiles in the die, we expect different final densities, but also some variation in density distribution, although it is unknown how large that variation will be.



Since each experiment follows the same heating profile in the beginning, and the SPS machine uses a standard output power level when the temperature doesn't change (based on the desired temperature), we can safely assume that the heating profile in the sample is consistent in each experiment until the pyrometer is engaged. There is some variation in density evolution, applied power by the SPS machine, and heating rate in some of the figures, and this has been taken into account.

Figure 10a shows the density evolution over time for three different cylindrical specimens, each sintered at a different final sintering temperature (1200, 1300, and 1400 °C), but the same holding time (8 minutes) and pressure (37 MPa). There is a significant density difference in the specimens heated to 1200, 1300 and 1400 °C, despite the starting densities were nearly identical, with the higher sintering temperature corresponding to higher final density. Because of the differing heating rates, but constant time, for each experiment, we can see that the 1200 °C experiment densifies more slowly than the other two, due to its lower heating rate from 800 to 1160 °C.

Figure 10b shows the density evolution with the same conditions as Figure 10a, but for square specimens. We can see from these plots that density evolves similarly in each corresponding case, but the final densities of the square specimens is lower than for the circular specimens (as much as 10% lower).

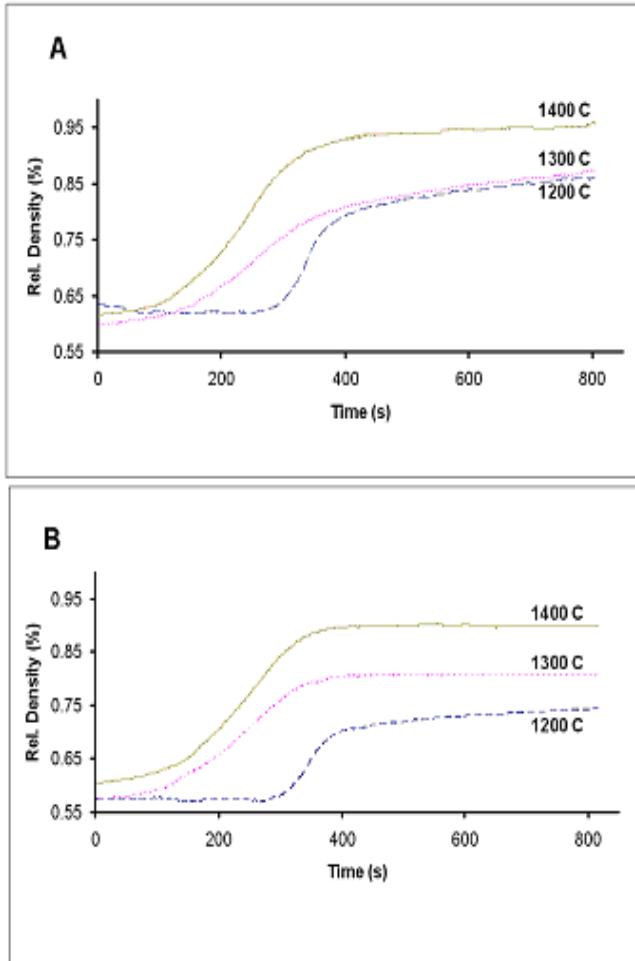


Figure 10. Density evolution curves for -325 mesh alumina powder, sintered for 8 minutes at pressure 37 MPa in a cylindrical (A) and prismatic (B) die, at 1200, 1300 and 1400 C.

To see whether the extensive holding time is important, we sintered several specimens for 40 minutes, with pressures and holding times coinciding with previous experiments. Figure 11 shows the comparison of density evolution for specimens sintered at 1300 °C, with holding times of 8, 15, and 40 minutes, at 50 MPa pressure in both a circular and square die. Figure 11a shows the comparison when sintering for 8 minutes, Figure 11b shows sintering for 15 minutes, and Figure 11c shows sintering for 40 minutes.

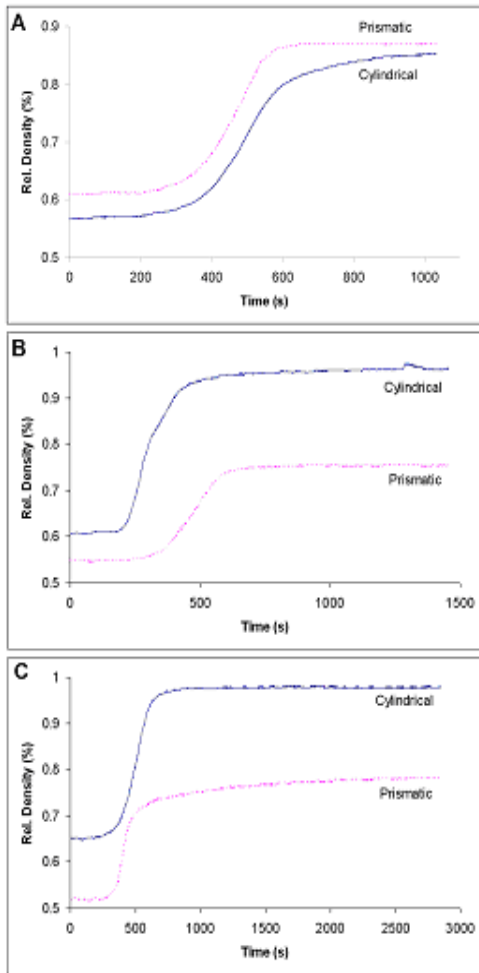


Figure 11. Comparison of density vs. time of alumina powder sintered in two shaped dies, with holding temperature 1300 C and an applied pressure of 50 MPa. (A) 8 minutes at the holding temperature, (B) 15 minutes at the holding temperature, and (C) 40 minutes at the holding temperature.

We can see that the increased holding time may have some effect on final density, but that this densification does not occur during the extended holding time (up to 40 minutes). The effects are the same for both the circular and square die.

Now that we have seen some variations in densities for experiments run with different dies but similar parameters, we need to verify that the results for these

experiments are comparable, and we can do this by introducing a third die with slightly different shape and comparing it to these original two dies. The goal of this next experiment is to determine if the die shapes (circular and square) we have chosen are truly comparable, and if slight variations in die design would actually have an impact on the final specimens. We are specifically looking at die volume and wall thickness as parameters influencing densification. Figure 12 shows a comparison of density at the same temperature range (1300 °C), holding time (15 min), and pressure (50 MPa), for (A) the cylindrical die, (B) a square prismatic die where the outside corners of the die are sharp (unlike the specimen), and (C) a square prismatic die where the outside die corners are rounded (as the specimen corners are rounded). A and C are the two dies investigated previously, while B is a new die used only for this experiment. Die B only differs from C in that the outside corners of the die are not rounded, but every other parameter is the same.

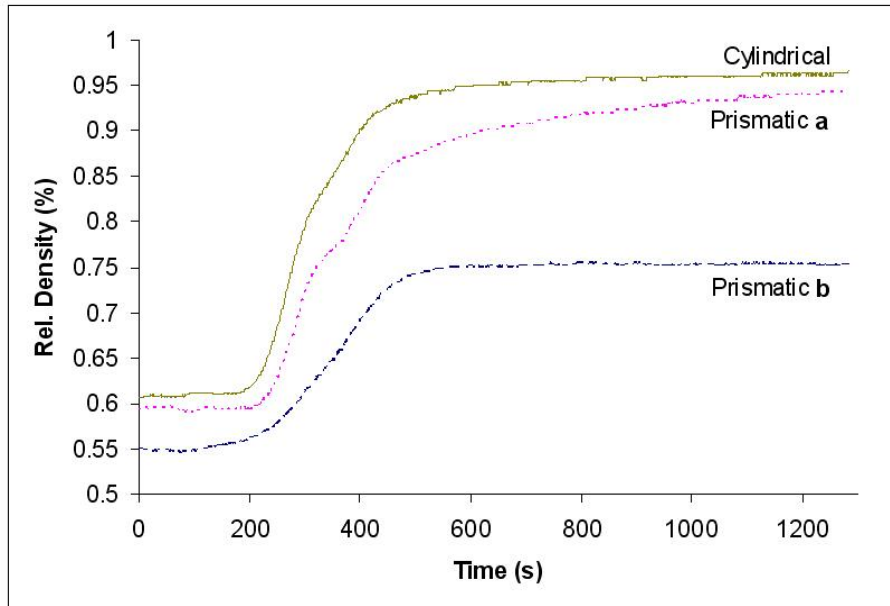


Figure 12. Density evolution for alumina powder in circular, square a (with sharp outside corners), and square b (with rounded outer corners) dies, sintered at 1300 C for 15 minutes, with an applied pressure of 50 MPa.

We can see that the final density is different in each case, and develops in a slightly different manner. The circular specimen has the highest density, as predicted by Figure 11, but interestingly the prismatic b (rounded) die has lower density than the prismatic a (sharp) die. For the difference between the two dies, there is a competition between the current density and heat flow. The prismatic die with sharp outside corners has a higher area in the corner for current to flow, and a higher overall surface area for the die, which indicates a lower current density compared to the prismatic die with rounded corners. However, this higher surface area indicates a larger area to heat, and subsequently a higher heat flow from the die into the material. If we consider that the SPS machine is measuring the temperature of the die, and regulating its power output based on that temperature, then we can see that the case of decreased current density for the larger area prismatic die is not relevant. Because the SPS machine control is based on temperature, it will output higher power into a die with larger surface area to maintain a

temperature, removing the possibility of a lower current density simply due to different area size. The current density in the sharp prismatic and rounded prismatic dies is different, but it is controlled to maintain a particular sintering temperature in the die, and because of this higher area and higher power, the sharp prismatic die will contribute higher heat flow into the specimen versus the rounded prismatic die. We conclude that the two dies used are directly comparable, despite having different shapes, due to the similar die volume and wall thickness.

Returning to the original two dies, cylindrical and square prismatic, we wanted to test the effects of pressure, so we conducted experiments at each of the sintering temperatures, using only 37 MPa of pressure instead of 50 MPa, and a holding time of 15 minutes. The holding time was chosen because it made the effects of the die shape less pronounced, which would allow us to filter them out and see what effect the pressure had. We noted a significant difference in density dependent on die shape, indicating that adequate pressure (above 37 MPa) is required. Conventional sintering and HIP experiments of alumina require much higher pressures than we are using, and it is only due to the limitation of the strength of the graphite dies that we have chosen such low pressures. However, these experiments show that 50 MPa is enough pressure to densify alumina in SPS, even at these lowered sintering temperatures.

This is confirmed by sintering at 1300 °C for 40 minutes, in each of the three types of die. Not only does the density remain constant for the majority of the extended holding time, but the curves for the three different die shapes look remarkably similar, with similar densification rates and nearly the same final density. It seems one way to

even out the effects of the die shape is a higher sintering temperature (1300 vs. 1200 °C) and a longer holding time (40 minutes vs. 8 minutes).

Although both overall density behaviors during sintering and final overall density are important, they do not provide a clear picture as to what is happening in individual sections of the material. Due to our design and the computational predictions, we expect some density variation through the material. Figure 13 shows a comparison of the grain structure and porosity (in an SEM image) between the edge and the center portions of a cylindrical specimen (left) and a square specimen (right), where the cross section was taken along the diameter in both. The parameters for the sintering of this specimen were a sintering temperature of 1400 C, a holding time of 15 minutes, and a pressure of 38 MPa.

The images clearly show a striking similarity between the grain structures in the two different areas for the cylindrical specimen. We can see a clear density variation and grain structure between the two areas in the prismatic specimen, shown in Table 1, and we calculated this density variation to be 2-5% between the corner and the center (for all of the experiments conducted). This variation was not present in the cylindrical specimen. The grain size difference is also pronounced, with a 50% increase in both average and maximum grain size in the center of prismatic specimen, and 20% increase in the corner, compared to the cylindrical. Grain size was calculated through the linear intercept method.

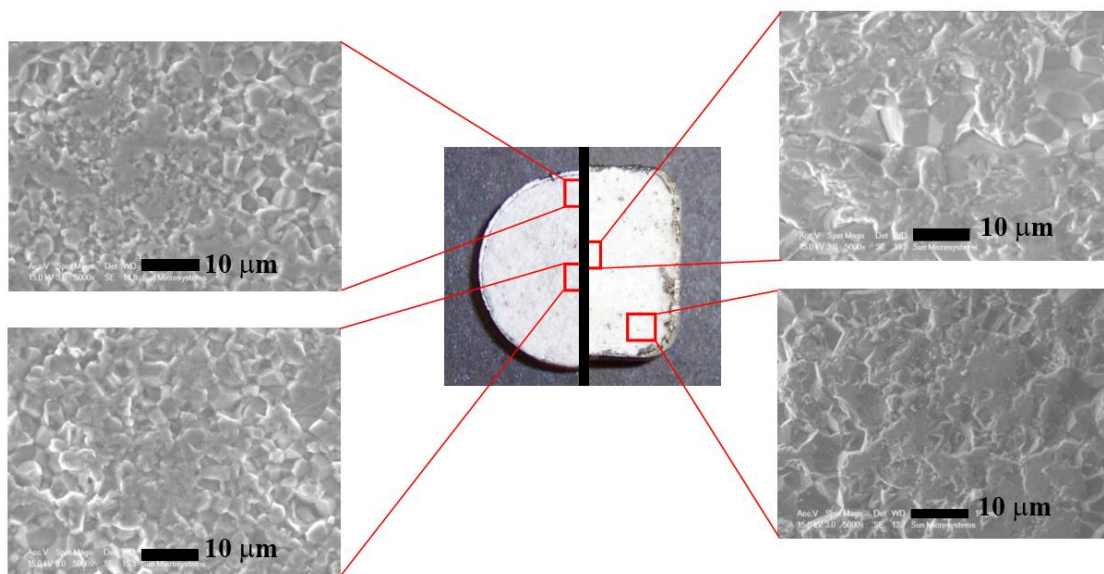


Figure 13. A diagram showing a sintered cylindrical specimen (left) and a prismatic specimen (right), with images (at 5,000x magnification) of the center and edge of a cross-section of the specimen.



Table 1. A comparison between grain size and porosity between the corner and center for a cylindrical and prismatic specimen.

Specimen	Average Grain size (center), ( $\pm 0.1 \mu\text{m}$ )	Grain size range, $\mu\text{m}$ ( $\pm 0.1 \mu\text{m}$ )	Porosity (center), %	Average Grain size (corner), ( $\pm 0.1 \mu\text{m}$ )	Grain size range, ( $\pm 0.1 \mu\text{m}$ )	Porosity (corner), %
Cylindrical	4.23	.53 – 8.72	1.9	4.0	.30 – 8.9	2.3
Prismatic	7.7	.4 – 13.3	2.9	5.0	.25 – 10.48	4.5

Figure 14 shows how the image analysis was conducted to calculate porosity from SEM images for the various areas in the specimens. The contrast and white/black levels of the image were manipulated (the right side of the figure) from an initial SEM image (left side of the figure) until only the pores were visible (black) and all of the other material is removed (white). The image analysis program (Adobe Photoshop) can calculate the amount of black or white in the image, and give the percentage of each that is present. The error in the porosity from this method, is about 1-2%, and comes from the user manipulation of the color levels in the image.

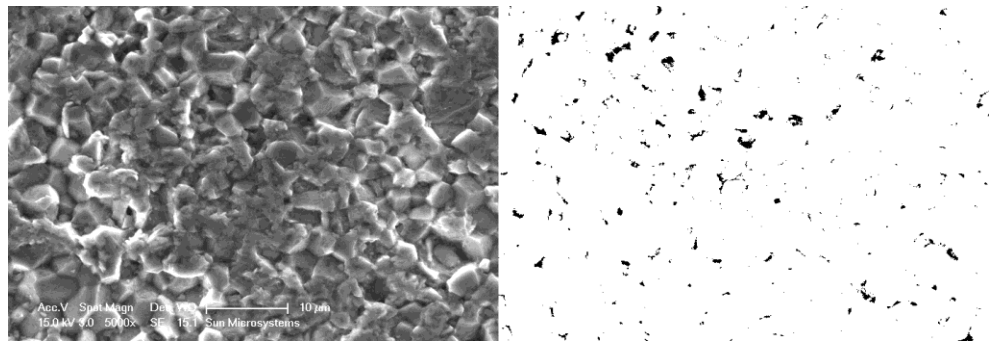


Figure 14. The image on the left is the initial SEM image, and the right is the manipulated image with only the pores showing.

#### **3.2.4. Discussion of shape impact on SPS of alumina with two die designs**

We have conducted an investigation into SPS-induced structure variation of alumina in square prismatic and cylindrical dies. It has been shown that sintering of a circular specimen produces a different grain structure and larger local porosity difference compared to a square specimen sintered under the same conditions, despite a small total porosity difference. Increasing the pressure or sintering time (or a combination of both) can reduce or remove the differences in overall final density, but there is still a variation in porosity in different areas of the prismatic-type specimens (unless 100% density is reached). Extended sintering times beyond a certain threshold do not improve densification in either case, once densification has stopped and reached its maximum for the sintering conditions. The sintering temperature and pressure in SPS can both be lowered far below the requirements in conventional sintering and hot isostatic pressing. Further investigation into more complex die shapes will shed more light on the variations in densification, and possibly on any additional mechanisms of sintering in the SPS process.

#### **3.2.5. Introduction to shape impact on spark plasma sintering of alumina with four die designs**

In this section we address, in more detail, the question of what role die/specimen shape takes in affecting the densification and grain growth of non-electrically conductive specimens during spark plasma sintering. The theory behind this is that heating of a non-electrically conductive in spark plasma sintering occurs as conduction into the specimen

from the graphite die, which is being heated through joule (resistance) heating by electric current passing through it. In this situation, uniform heating of the specimen can only occur when there is symmetry of the die and specimen around the main axis. By creating a series of die, and therefore specimens, that are not symmetrical around the axis, we can examine what effect this change in symmetry has.

To achieve this goal, similar to section 3.2.1, we used alumina (a widely studied material) as the material, and created four different dies – one isotropic around the axis, and three that were progressively anisotropic. We used the aspect ratio to evaluate this anisotropy without regards to the specific die shapes we utilized.

The four dies used were:

1. A cylindrical die, which created circular specimens of 15 mm diameter, with thickness of 3 mm, and an aspect ratio of 1.
2. A square prismatic die, which created square specimens with side length 15 mm diameter, a thickness of 3 mm, and an aspect ratio of 1.
3. A rectangular prismatic die, which created rectangular specimens with dimensions 22.5 mm by 10 mm, a thickness of 3 mm, and an aspect ratio of 2.25.
4. A rectangular prismatic die, which created rectangular specimens with dimensions 32.15 mm by 7 mm, a thickness of 3 mm, and an aspect ratio of 4.59.

The area of the prismatic specimens was designed to be the same, so that the specimen volume for heating would be the same (as they have the same thickness). The circular specimen was designed to be an inscribed circle inside the square specimen. The

theory is that the circular specimen could be directly compared to the center of the square specimens.

We designed a pressure and temperature profile (through a series of experiments and a mathematical analysis) and created, and evaluated, specimens from all four dies, looking at grain size and porosity in different regions of each specimen. We created four specimens from each die shape, except for the AR 4.59 die, and averaged the results for all the tables and reports of the data. For the AR 4.59 die, due to the extreme shape, we were only able to successfully produce one specimen before all the supplied dies were broken.

### **3.2.6. Experimental work conducted on shape impact on SPS of alumina using four die designs**

As mentioned earlier in section 3.2.1, to further investigate the shape-induced effects, we expanded our experiments to include two new shapes of die that enhance the differences previously seen.

2.5 grams of alumina powder (Alfa Aesar, USA) were placed in four differently shaped dies, to investigate the effects of die shape on local and overall densification during sintering. Each of the dies and punches (Electrodes, Inc., USA) is made of the same graphite material (I-85). The holding temperature for all experiments was 1300 °C, the pressure during the entire experiment was 38 MPa, and the holding time was 15 minutes. The heating profile was the following: 2 minutes to 600 °C, hold for 1 minute, 1 minute to 800 °C, hold for 1 minute, 3 minutes to 1260 °C, and 1 minute to 1300 °C, followed by holding. The heating and holding before 800 °C was to allow for careful

alignment of the pyrometer, which has a minimum reading temperature of 570 °C. The average heating rate for the entire experiment is 123 C/minute, from the beginning of heating until holding, with shorter duration heating rates reaching 300 °C /minute. This temperature and pressure profile was determined to be the best at emphasizing the grain growth and densification differences from the original two die experiments.

The shape of the dies was determined using three different principles. The first principle relates the cylindrical die and the square prismatic die, where the square prismatic die was designed to contain the cylindrical die as an inscribed circle, but also with the prismatic square retaining the same wall thickness as the cylindrical die to retain a similar amount of heating in the die during sintering, and both dies creating specimens with the same aspect ratio.

The second principle applied to the dies, relates the square prismatic to the two rectangular prismatic dies, where the surface area of the specimen and the die wall thickness is retained in all three cases. Since the side length of the square in the square prismatic die is 15mm, the area is 225 mm<sup>2</sup>. These parameters are preserved so that the heating rate and heat flow into the material are the same during sintering. This is due to joule heating being the primary mechanism of heating in the die wall, which is an area-dependent phenomenon.

The third principle relates the shapes of the rectangular prismatic dies to the square prismatic die. If we utilize the aspect ratio (as mentioned previously), we can create specimens that meet the first two principles but that also have a non-specific parameter that is relevant to many different die shapes. For a circle and a square, the aspect ratio (AR) is 1. For the wider rectangular prism, the aspect ratio is 2.25 (this die is

referred to as 2.25 AR from here on). And finally, for the widest rectangular prism (most deviated from a square), the aspect ratio is 4.59 (this die is referred to as 4.59 AR from now on).

A schematic of the 2.25 AR and 4.59 AR dies is presented in Figure 15 and Figure 16, respectively, where R is the radius of curvature of the corner area. This radius of curvature is determined by the smallest tooling that could be utilized to round the corners (1/16 inch, or 1.6 mm).

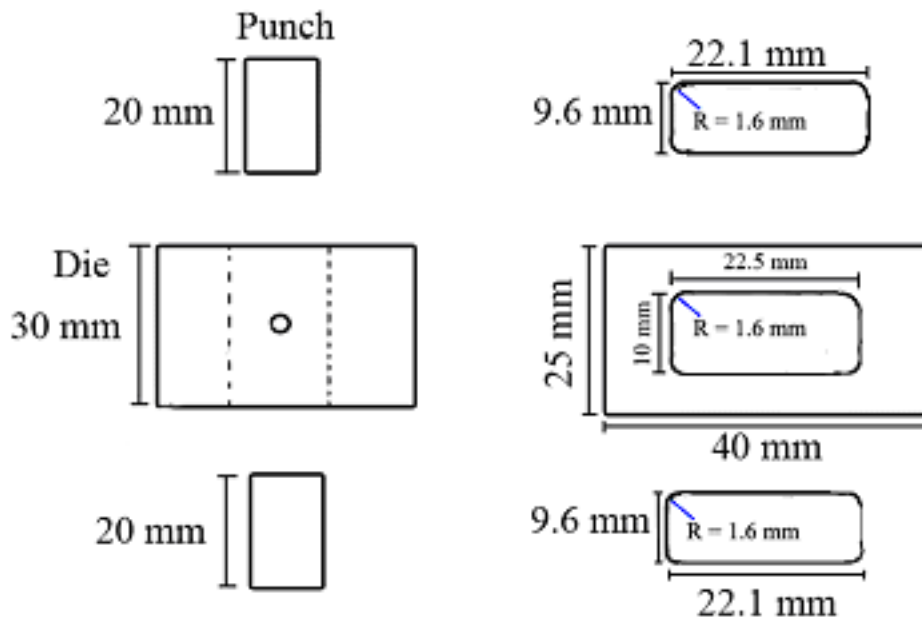


Figure 15. Prismatic die design, with aspect ratio of 2.25.

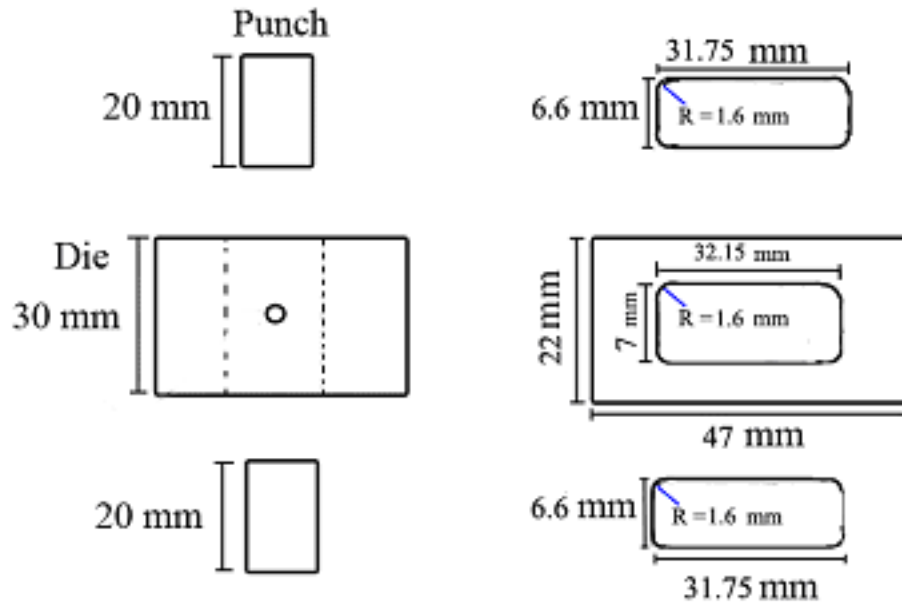


Figure 16. Prismatic die design with an aspect ratio of 4.59.

The alumina specimen is electrically non-conductive at low temperature (10 femto  $\Omega$ -cm), and slightly semiconducting at sintering temperature (10 micro  $\Omega$ -cm), and the primary heating mechanism is therefore heat conduction, which is a length-dependent phenomenon. Because 3 of the 4 dies are non-isotropic in length in different dimensions (except the cylindrical die), this will produce uneven heat flow from the die into different portions of the specimen (until thermal equilibrium is achieved). We believe that this heat flow difference in the dies will produce a local density difference in the final specimen, and different density development during sintering, based on our previous experiments with two dies

To evaluate these differences, several techniques were used. The specimens were cut, polished, and etched with a thermal etching process at 1300 °C in air for 1.5 hours. SEM was used to evaluate the grain structure, and image analysis was used on the SEM

images to evaluate the density in each area. Archimedes method was used to calculate the overall density of the specimens. This procedure is the same as conducted during the previous two die experiments.

### **3.2.7. Results and discussion of shape impact on SPS of alumina using four die designs**

Electron microscopy of key areas shows a slight variation in density and grain structure among these four specimens. The areas examined are a) the center of the specimen, and b) the corner of the specimen. These are depicted in Figure 17. The thickness of the specimen is small (2-3 mm), and no variation was seen in the specimens that was dependent on height.

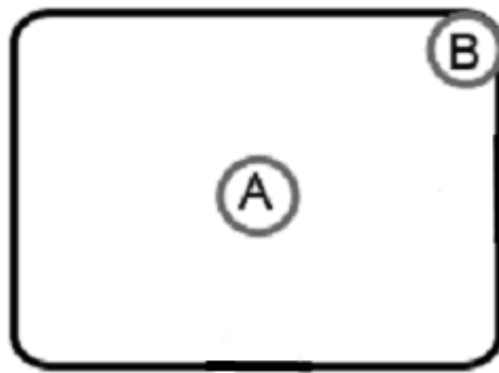


Figure 17. A description of where the two SEM images were taken for each specimen, to examine grain structure.



Table 2. Comparison of grain size and porosity in the center and corner of each of the four specimens, sintered at 1300 °C for 15 minutes.

Specimen <sup>1</sup>	Average Grain Size (Center), ( $\pm 0.1 \mu\text{m}$ )	Grain Size Range, $\mu\text{m}$ ( $\pm 0.1 \mu\text{m}$ )	Porosity (Center), %	Average Grain Size (Corner), ( $\pm 0.1 \mu\text{m}$ )	Grain Size Range, ( $\pm 0.1 \mu\text{m}$ )	Porosity (Corner), % ( $\pm 1$ )
Circular, AR 1	2.5	0.9 - 16.7	1.8	2.6	0.9 – 11.4	0.4
Square, AR 1	3.3	0.9 – 10.0	0.6	2.9	1.0 – 10.6	0.8
Rectangular, AR 2.25	1.86	0.6 – 5.2	1.6	1.6	0.2 – 4.0	3.5
Rectangular, AR 4.59	1.22	0.3 – 3.5	1.9	1.6	0.5 – 4.8	1.9

Table 2 shows a comparison between the grain size and porosity in the center and corner of each of the four specimens (the data for each specimen shape is the average of 4 samples for each shape, see footnote), calculated from SEM images of these areas. Also included is a range of grain sizes, indicating the smallest, and largest, visible particles in the image. Porosity was again calculated by creating a high contrast, black/white image from the SEM image, and counting the pixels the percentage of pixels that fell into the “pore” (black) range. The error in the porosity is 1-2%, as mentioned previously. The grain size was calculated using the linear intercept method, with the De Hoff correction included. Figure 18 shows the grain size comparison in chart form.

<sup>1</sup> The data presented is an average of four specimens for each shape, except for the AR 4.59 die. The data represents only one specimen, as it was the only one produced (as mentioned previously).

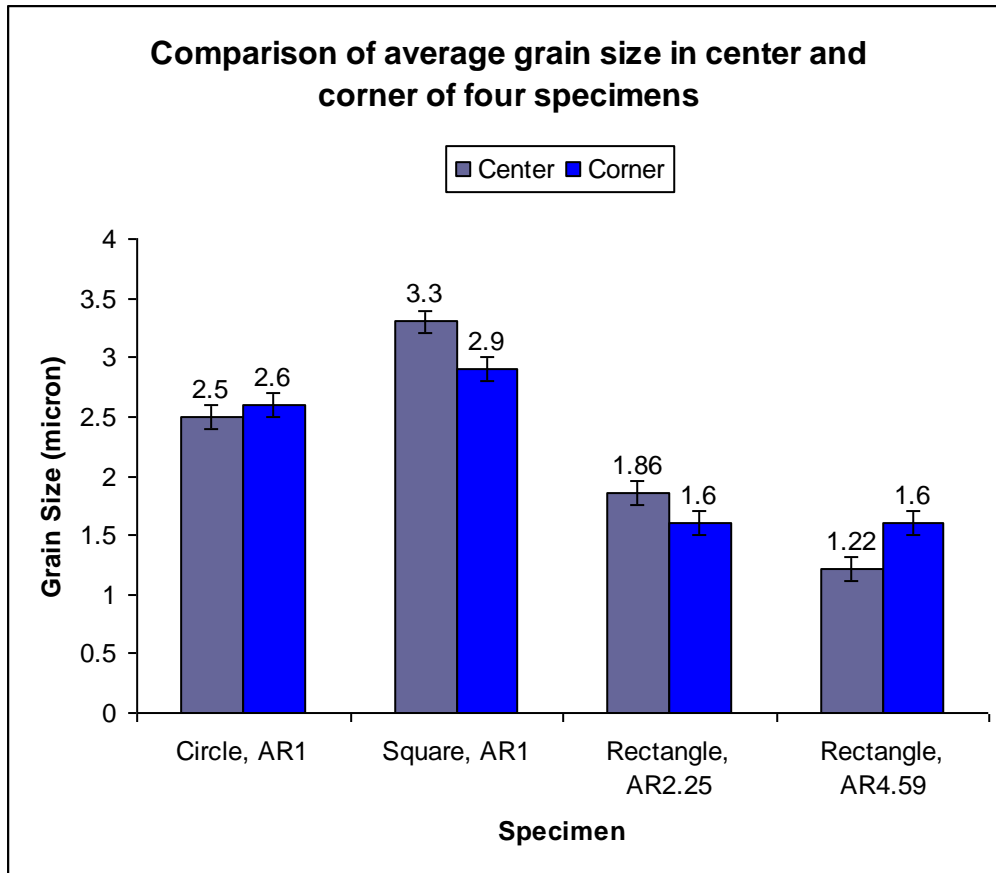


Figure 18. A chart showing the grain size difference in each area, by specimen.

We can see from this table that there is a discrepancy between the total porosity from the previous figure for the rectangular specimen with 2.25 AR, but not for the other specimens. This may be due to error inherent in the image analysis system (these measured values are within the expected error), or it may be due to significant closed porosity in the specimens that was not detected.

It is clear from the data that the higher the aspect ratio, the smaller the grain size, both average and largest, as can be seen in Figure 19. The smallest particles in each section, and each specimen, are in the same range, around 1-2  $\mu\text{m}$ . This contradicts the previous idea about the discrepancy in the porosity in the image analysis being due to

hidden, closed porosity, and we can safely attribute the porosity error to the ability of the software to accurately calculate the porosity. It is also clear from the analysis of grain size, that there is little difference in grain size between the center and corner of the specimens.

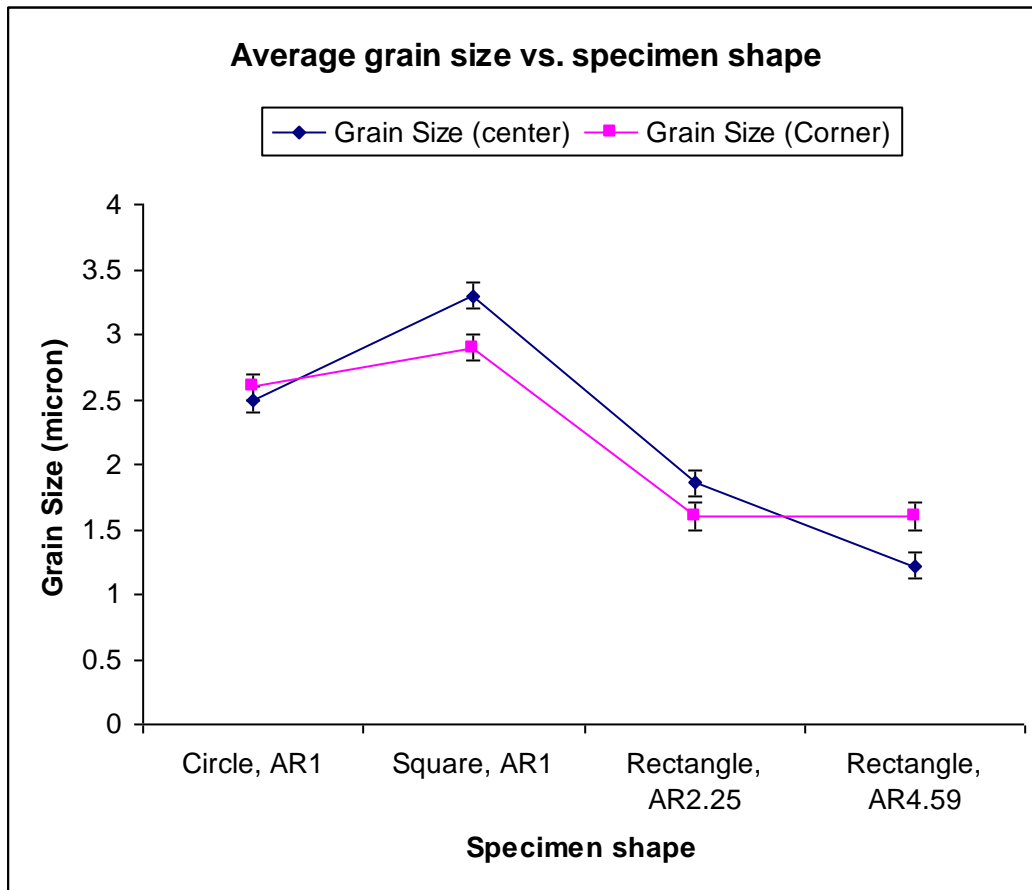


Figure 19. A plot of grain size versus specimen shape shows that average grain size decreases as the aspect ratio of the specimen increases.

Because the grain size in the corner and center are similar for all four of these specimens, the previous square specimen from the two die experiments, and images, which show the different grain structure in the corner of the square specimen, compared to the center, must be an anomaly. Since there is a large distribution of grain sizes in

each specimen, due to a wide distribution of particle size in the initial powder, the variation in the square specimen may be an anomaly where only large grains were present at the fracture surface. Further examination and more microscopy of the previous square specimen indicate an overall grain growth problem in that specimen, and it is unclear why its properties differ from these four specimens.

Figure 20 shows the grain structure of the center (left) and corner (right) for each of the four specimens, at 10,000x magnification. We can see the increased grain size in the circular and square specimens, compared to the other two. We can also see the variation in grain size, from large to small, in each specimen. The white spots in some of the center images are impurities obtained during thermal etching.

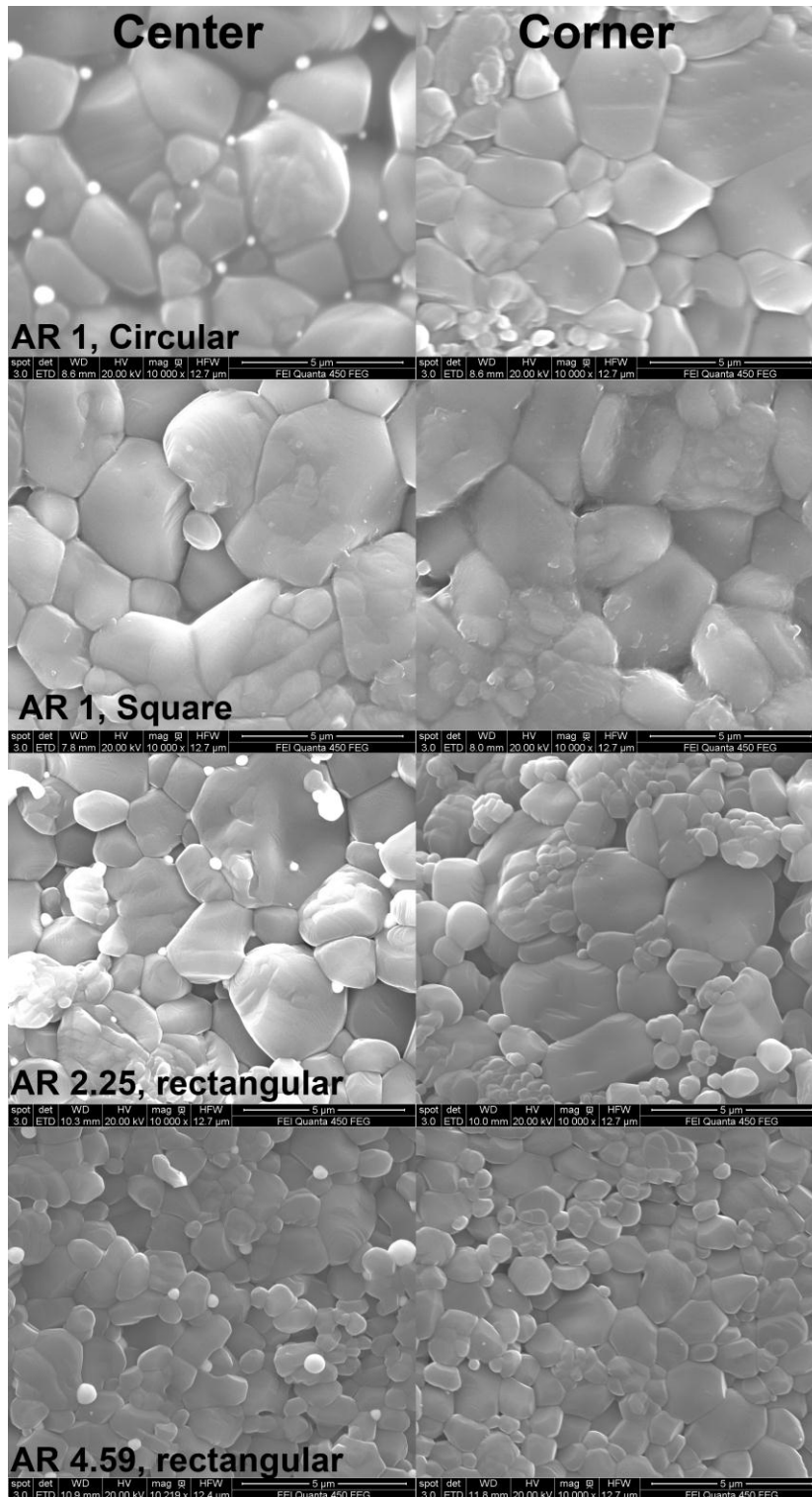


Figure 20. The grain structure in the center and corner of the four specimens can be seen. There is little difference between the areas in each specimen.

### ***3.3. Modeling of the influence of the specimen's shape in SPS***

The goal of the modeling section was first to verify and identify the mechanisms of the variation in densification of the different die shapes. If we could model the results in our simplest two cases, then we should be able to extend the model to predict the response of any die shape, particularly significantly complex ones for real sintered parts (like a gear). A second goal of the modeling was to use the prediction to then modify the original die into a new shape to compensate for the differences that were detected during experiment. In this way, we could predict a new die shape, which is a slight variation on an existing real or theoretical shape, such that the differences were reduced or exacerbated, depending on our desire. For applications requiring uniform density, we could design a new die that provided uniformity, and if a porous, or complex, internal structure was desired, we could design a new die that emphasized that porosity in the desired areas.

Numerical modeling of the assemblies was computed through a finite element simulation using COMSOL Multiphysics software. The modules used in COMSOL Multiphysics are the Conductive Media DC, and the Heat Transfer by Conduction.

For the electrical component a constant voltage of 4 V was applied across the assembly, the surfaces were regarded as electrically isolated, and the contact surfaces between parts were considered ideal with zero resistance. For the temperature component the initial temperature was set to 300 K, the temperature of the two extreme upper and lower surfaces of the punches was held constant to 300 K, and heat loss by

radiation was considered in lateral surfaces. The parameters used for the modeling correspond to typical values for graphite:

$$\sigma = 7.273 \times 10^4 \text{ S/m}, \rho = 2100 \text{ kg/m}^3, C = 709.12 \text{ J/kg K}, k = 155 \text{ W/mK}$$

The assemblies employed for sintering were modeled with finite element software and results for current, and temperature, distribution were obtained. The SPS assembly was reduced to a simplified version composed by a graphite die and two punches in contact with the die, because the specimen is non-electrically conductive and not required for modeling of the heat flow. Two different shapes of die were considered: one prismatic and one cylindrical, per the actual fabricated dies. Figure 21a displays the prismatic configuration with the punches highlighted, while Figure 22a shows the corresponding cylindrical configuration. For the prismatic geometry, the die has an external edge of 30 mm and is 30 mm tall and the punches are 15 mm in a rounded edge (fillet radius equal to 1.5 mm) and 20 mm long. For the cylindrical geometry, the die has an external diameter of 30 mm and is 30 mm tall and the punches are 15 mm in diameter and 20 mm long. In both cases, the punches are set 10 mm apart, to account for a 10 mm thick specimen. To study the influence of the geometry, both sets of dies, and punches, are subjected to similar conditions using the same physical parameters for graphite.

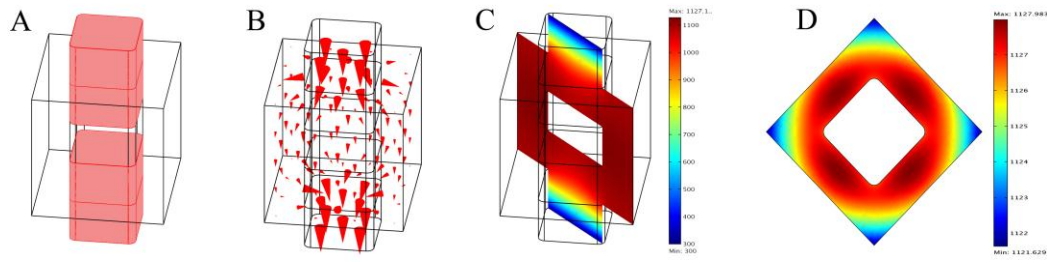


Figure 21. (A) The configuration used for square die modeling in COMSOL, with the die being transparent and the punches highlighted. (B) The die model with arrows indicating current density during sintering. The temperature distribution during sintering in a (C) longitudinal cross-section, and (D) a transverse cross-section.

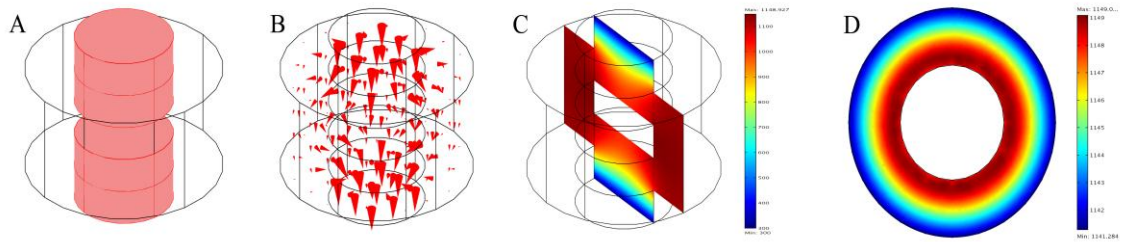


Figure 22. (A) The configuration used for cylindrical die modeling in COMSOL, with the die being transparent and the punches highlighted. (B) A die model with arrows indicating current density during sintering. The temperature distribution during sintering in a (C) longitudinal cross-section, and (D) a transverse cross-section.

Figure 21b shows an arrow distribution of the current density for the prismatic geometry during sintering, where the increase in size of the arrow corresponds with an increase in current density. Figure 21 also displays different views of the temperature distribution for the prismatic geometry: (c) is a longitudinal slice and (d) is a transverse slice, corresponding to the middle of the die. Accordingly, Figure 22b shows an arrow distribution of the current density for the cylindrical geometry, and Figure 22 displays the temperature distribution for the cylindrical geometry in corresponding planes, (c) longitudinal, (d) transverse – middle. It can be noted that the distribution of heat



generation is related to current distribution, and that the current distribution depends on die geometry. The higher current densities are in the exposed portions of the punches. At the same time, the temperature is highest at the interior lateral surface of the dies. Also, in the latter case the temperature in the edges is slightly higher than the temperature in the corners.

From these computational results, we expect there to be differences in the sintering of the alumina specimen that is dependent on die configuration. Because the cylindrical die has uniform temperature distribution around the specimen, the heat flow into the specimen, and therefore the sintering behavior, will not be influenced by die shape. For the cubic die, we can predict the hot spots and the larger size of specimen (compared to the cylindrical) will have an effect on the sintering behavior. The hot spots on the edges indicate that those areas may have higher density and grain size, due to higher temperature and heat flow, which makes it easier for those areas to reach the activation energies for densification and grain growth. The center of the square die will have lower density and smaller grain size, due to the greater distance that heat has to flow (accounting for the corners) to reach the center of the die. The corners of the specimen in the cubic die are complicated, because although the corners of the die themselves are not hot spots, the material is adjacent to two hot spots, and this may lead to higher densification and grain growth, as on the edges. However, the temperature difference is only 25 °C between the corner and center of the square die in the simulation, so the effect on densification may be small.

### ***3.4. Discussion***

From our experiments on net-shaping of alumina using various die designs, there is strong evidence that die shape does not have an influence on densification and grain growth related to the location in the specimen. However, there is also strong evidence that die shape has an impact on overall densification and grain growth.

In the early experiments with only two dies, and only a few specimens, we did notice a variation between the corner and the center areas of the specimens, in terms of final grain size, final density, and grain size distribution. However, although our sintering conditions did not change when we expanded to four dies, with significantly more specimens analyzed, and despite the four dies had progressively more complex shapes, this variation was not present.

A possible explanation for this variation in the first set of experiments can be seen in Table 2 (examining the second set of experiments), where it is seen that there is a large variation in grain size in each area (from 1 to 16  $\mu\text{m}$  in some specimens). Although we examined several different sections of each “corner” of the first two specimens, it is possible, based on cutting, polishing etc., that the surface that was examined in those specimens had an uneven distribution of larger particles compared to other areas. It is unclear if this abnormal distribution is then a result of the sintering conditions, however, given that the results were not repeated in several other experiments, it is likely a statistical anomaly. If we average all of the data from both sets of experiments together, we find that the location-based variation is severely minimized

We did notice that as the aspect ratio increased, the final grain size decreased in both areas of the specimen, and the final density was slightly higher. The grain size distribution in the specimens was also smaller. This shows that die shape does have an effect on overall densification and grain size, just not on the localized properties (as mentioned previously).

Modeling of the first two experiments showed a slight temperature difference in the sides of the square die, with a lower current density in that area. However, the expected 25 °C difference between the two areas, at holding temperature, may have a limited effect on the densification. In the final set of conducted experiments, we did not see a higher densification in the sides of the square die, despite the expected concentration of heat. We also did not see different densification in the center. This is likely due to the slight temperature difference.

## **Chapter 4. SPS combined with extrusion**

In this section we address the possibility of combining spark sintering and extrusion processing (named Spark Plasma Extrusion), to see if the shaping by extrusion is possible during SPS and if there are significant advantages in terms of retaining and refining grain size. In traditional extrusion processes, the feed material used in extrusion is often produced in a way that does not minimize or control grain size, and extrusion is sometimes used to decrease the grain size and improve the strength of the material. Also, the material is rarely consolidated through sintering before extrusion.

The theory behind combining these two processes is based on the preservation of small grain size during densification with SPS, and the possible refinement of grain size in extrusion. By consolidating a material at a low temperature for sintering, and then extruding it, we hope to minimize grain growth and create high density, fine-grained materials.

We chose aluminum for these experiments due to the low sintering temperature (300-600 °C) and low extrusion pressure (30-150 MPa). This would allow us to attempt the experiments with low-cost graphite dies, with which we are very familiar with the heating, cooling, and strength characteristics, before committing to stainless steel or tungsten carbide dies.

The extrusion die used was a streamlined die with a parabolic curve that minimized both stress on the die wall and upsetting pressure. The dies were originally composed of graphite, but due to the lack of sufficient strength of this material, stainless steel dies were then used to successfully complete experiments. Due to the limitations of

the applied pressure of our SPS machine, suitable extruded specimens were only produced using the streamlined die with the parabolic curve shape. The die is shown in Figure 23.

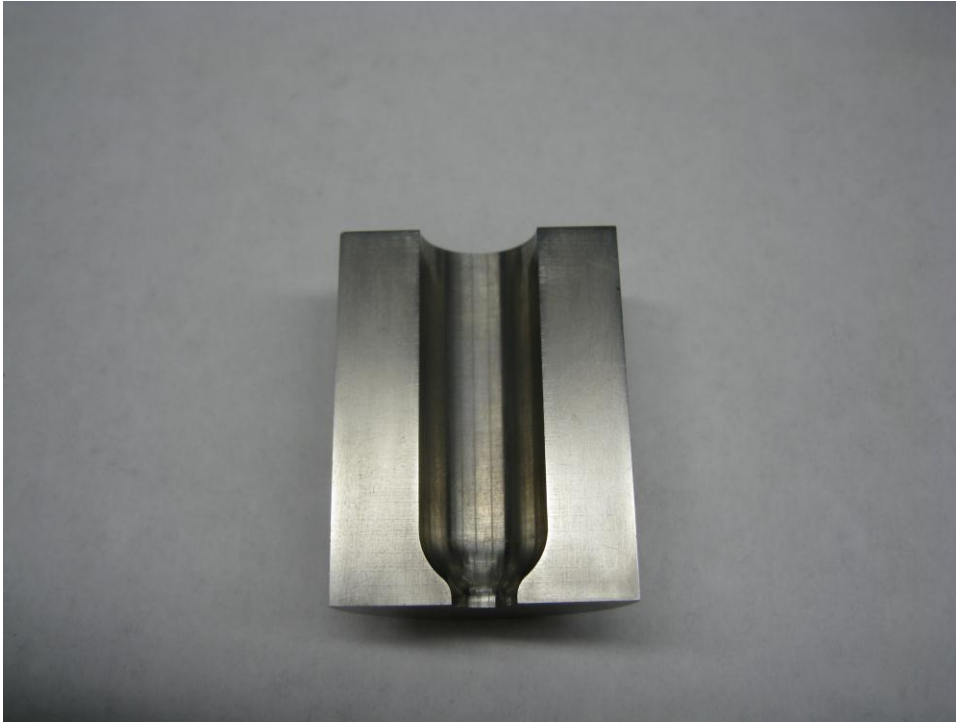


Figure 23. A picture of the extrusion die, with the parabolic curve for extrusion.

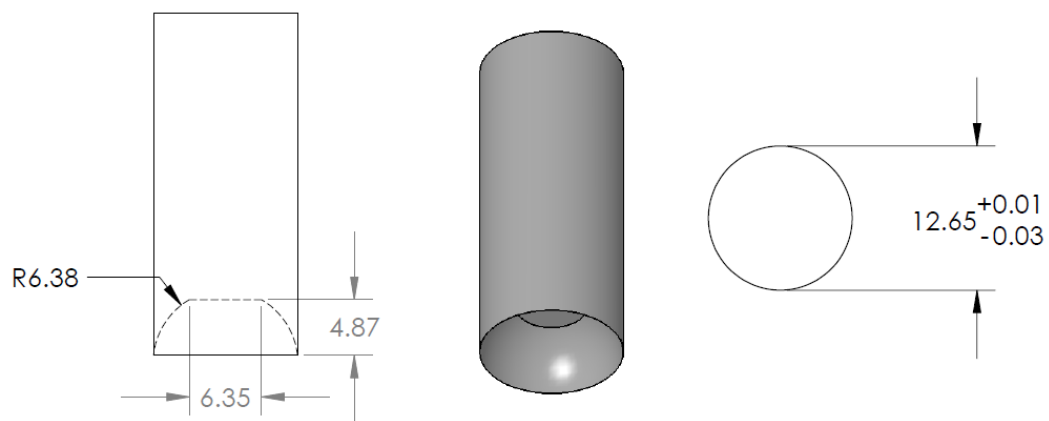


Figure 24. The design of the curved punch, used for creating specimens with the opposite shape of the die.

Due to the necessary minimum applied pressure of our SPS machine (of approximately 20 MPa), the specimens had to be pre-sintered before the sintering and extrusion process could occur, otherwise the green specimens would be destroyed upon initial application of pressure. The specimens were pre-sintered using special convex punches (Figure 24), to allow the partially sintered specimens (72% density) to sit perfectly inside the non-standard die shapes and resist the initial pressure, without being extruded before the sintering temperature was reached.

3 temperatures and 2 pressures were chosen for the experiments (6 experiments total), based on 15 experiments that were conducted to determine suitable temperatures and pressure for full densification and extrusion.

#### ***4.1. Spark plasma extrusion setup and experimental results***

Simple extrusion is a common process in industry for the refinement of particular properties of a material (such as grain size or structure), and is performed in both hot and cold environments. Refining these properties through extrusion is often the simplest, and most cost effective, method of doing so. A variation of standard extrusion is equal channel angular extrusion, where the extruded material is forced through a channel with some angle (often 90 degrees). Research has shown that forcing the material through this turn causes significant grain refinement (especially stretching and anisotropy), and has the capability to transform micron-sized grains down to nano-sized if repeated several times.

Combining SPS with these extrusion processes serves several purposes. The first is to further refine the grain structure beyond that which is retained through SPS, for example sintering a small nanopowder and then extruding the finished specimen to produce even finer nanograins. The second is to enhance anisotropy and create oriented structures (for example pores, or additives in a matrix composite) in a material, to enhance the properties, particularly in one direction. The third option is to create more complex shapes that can not be produced normally in SPS, perhaps in combination with other types of extrusion (angular extrusion that is not equal channel).

Using these techniques will open new avenues into the types of samples that can be produced in SPS.

#### **4.1.1. Experimental description for Spark Plasma Extrusion**

A die has been designed to contain the powder during sintering, and allow for extrusion afterward. The die is split in the middle and composed of two separable parts (that are mirror images of each other), to allow for easy extraction of the specimen after the experiment is complete. The parts are together by a designed stainless steel ring, with a hole for allowing the thermocouple to enter the die during experiments, and another hole for the specimen to exit during equal channel extrusion, a feature we had intended to utilize in these experiments but did not (Figure 25). The ring inner diameter is the same as the exterior diameter of the die, and the tolerances of both parts have been carefully controlled, and measured, to ensure a close fit. The interior of the stainless steel ring is coated with boron nitride to prevent its action as an electrical conductor. The die and

ring sit on top of a 60 mm height graphite block with a hole drilled for the extrusion material. The other spacers used are graphite, and a stainless steel 12.7 mm punch is used to apply pressure on the specimen. The graphite spacer above the punch has a hole 12.7 mm in diameter and 3 mm deep, to accommodate the punch, and to ensure proper contact between the dissimilar materials is maintained.

Initially, several experiments were conducted using a graphite die with the same specifications as the steel die (but with the same steel ring holding them together). However, due to the pressure applied during extrusion, and the high localized pressure areas, the graphite dies were all destroyed during the experiment before experiment completion. It was necessary to convert to a stronger material to continue the experiments, and the material chosen as a high strength vanadium carbide steel. This presented some drawbacks related to heating, mentioned below, but allowed for successful experiments.



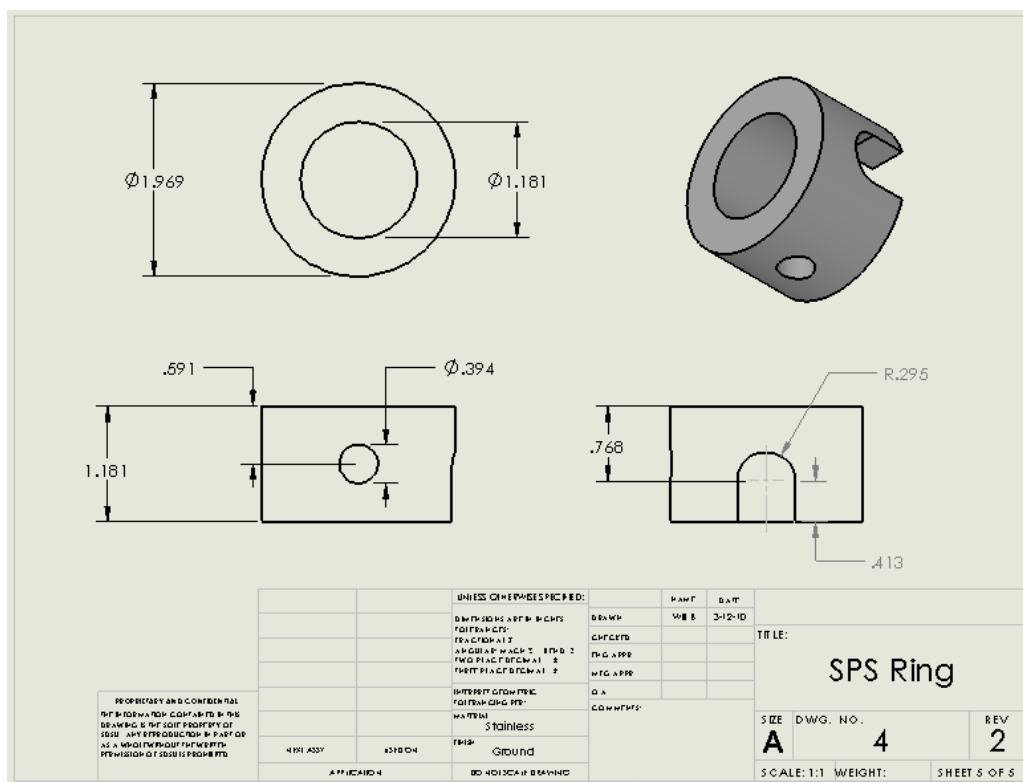


Figure 25. A diagram of the steel ring that will hold the graphite SPS extrusion fixture during the sintering process.

For the standard extrusion, the initial specimen size is 12.7 mm, and the final extrusion outlet is 6.35 mm, for a total diameter reduction of 50% when the specimen is pressed through the die (Figure 26), and an extrusion ratio of 4.



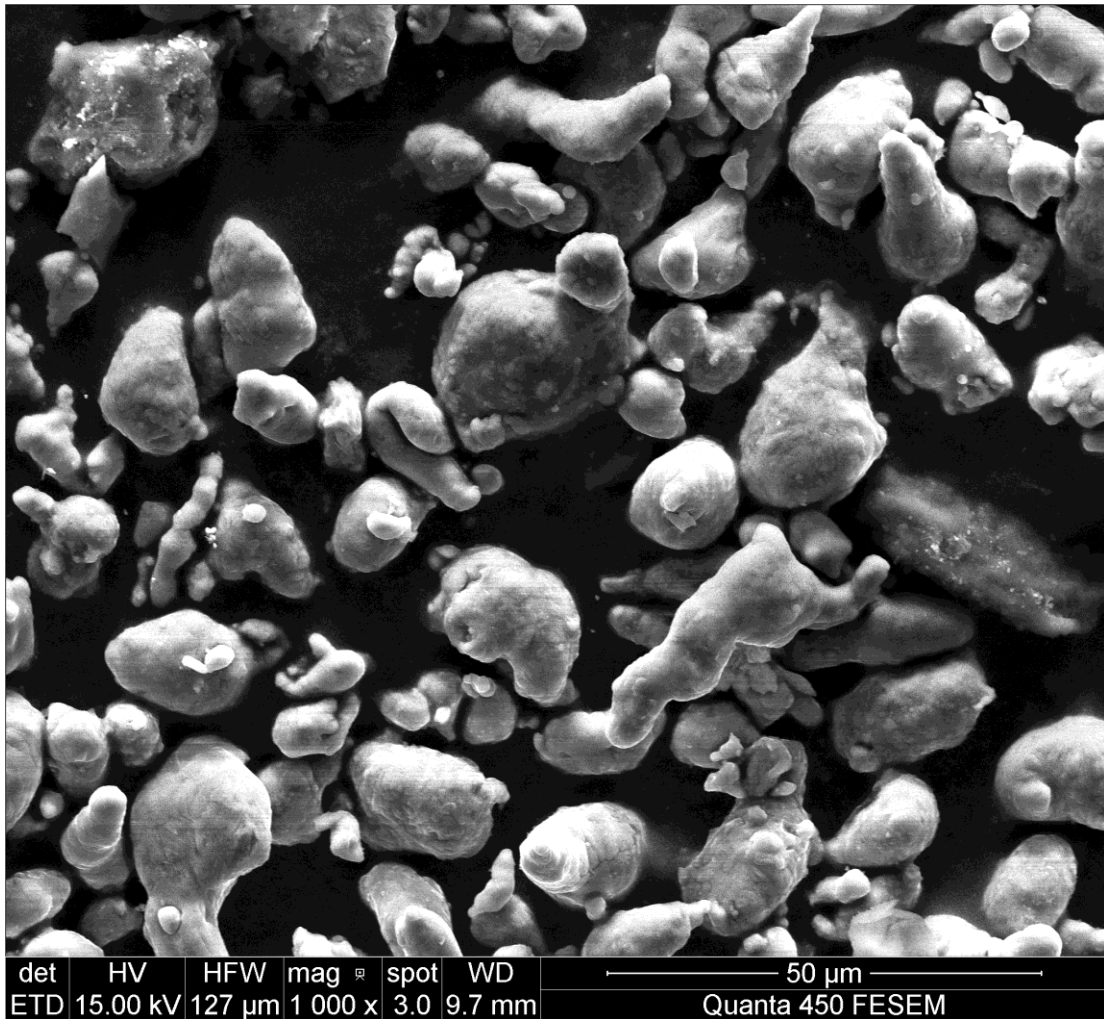


Figure 27. The initial aluminum powder used in all of the SPS and extrusion experiments is non-uniform in size and irregularly shaped.

Several tests were conducted using a standard flat punch and die to pre-press the specimens, however during the sintering process, these specimens experienced high stress and the small contact area with the dies, and subsequently the specimens (or occasionally the die) were fractured before the subsequent experiments were completed successfully.

It was then necessary to create a specially designed punch which would minimize high localized stress in the specimen due to minimal contact area, and this was accomplished by giving the green specimen the same shape as the curvature of the

extrusion die. All successful experiments reported here used this specially shaped punch during pre-pressing, with non-cylindrical specimens used in the subsequent experiments.

These green specimens were then pre-sintered at 500 °C (with a heating rate of 250 °C /minute and holding for 8 minutes) using free pressureless spark plasma sintering (FP-SPS) to achieve a density of 72%. FP-SPS was used, rather than conventional SPS, to minimize densification during the pre-sintering process related to applied pressure. Initially, four experiments were conducted to determine the appropriate temperature profile to reach a suitable density, followed by nine more experiments at the designated temperature to create pre-sintered specimens with the average density of 72.6% ( $\sigma = 0.6\%$ ). This density value was suitable for continuing the experiments, and the low deviation between experiments removed any error in the final density that would be introduced from different initial density between specimens. Figure 28 shows the specimen after pre-sintering has been conducted. We can see grains of varying sizes and shapes present in the specimen, and the average grain size of 12.3  $\mu\text{m}$ .

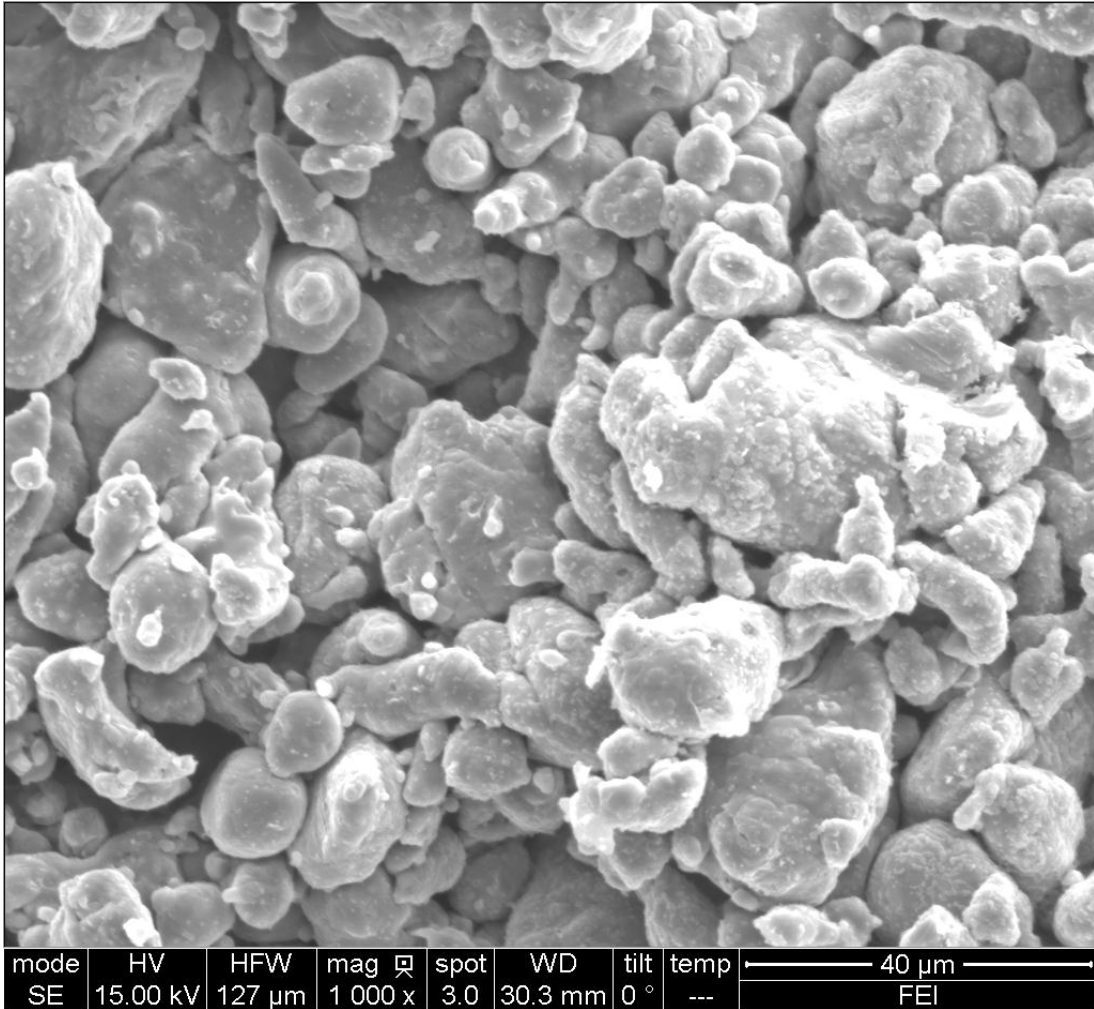


Figure 28. Grains of varying sizes and shapes are present in the pre-sintered specimen.

The goal of this pre-sintering process is to create inter-particle bonding and necks in the green specimen, to allow the specimen to survive the minimum pressures required in the SPS machine during the initial sintering before extrusion. In our SPS extrusion setup, a green specimen would be destroyed through the minimal applied pressure (approximately 20-25 MPa) before sintering had begun. The drawback is that any initial pre-densification has an impact on the final specimen and minimizes the variance in the final density of the specimens.

This pre-sintering could potentially be conducted using conventional sintering, rather than SPS (or FP-SPS). However, due to the slow heating rate, and length of time required for conventional sintering, it would be impossible to obtain a specimen with only the slightest amount of densification. Even with the use of a dilatometer, the environment in the furnace would extend the sintering time until it slowly cooled. The only option would be to use a dilatometer and then rapidly remove the specimen as soon as the desired amount of sintering was reached. Besides potentially damaging the equipment, this rapid quenching (even more rapid than SPS) might have an adverse effect on the specimen.

Six experiments were conducted to analyze the effects of extrusion combined with SPS. The specimens were heated to the designated temperature at minimal pressure (~25 MPa), and held at this temperature and pressure to allow for full densification. After the specimen was fully densified, pressure was increased rapidly and sustained at a designated level while extrusion occurred. The pressure and temperature used for densification and extrusion were determined by conducting a series of experiments, and analyzing these test specimens based on final density, fracturing, and amount of melting.

Due to the use of steel dies and equipment, automatic temperature control could not be used, and power in the experiment was controlled manually, which indirectly controlled the temperature and heating rate. The initial experiments that determined temperature and pressure were also used to determine a power level and heating profile using manual control. The reason for this issue is that the heat capacity of stainless steel is significantly higher than graphite, and thus the thermocouple cannot accurately measure instantaneous temperature during periods of high heating rate ( $>20\text{ }^{\circ}\text{C}/\text{minute}$ ).

This creates a delayed feedback response with the control system, and the control logic is not designed, nor is sufficient, to deal with this lack of information without triggering a warning due to overheating and overuse of the power supply. The only way to overcome this control limitation, while using tooling that had sufficient strength for the experiments, was through manual control.

Three temperatures (130, 230, and 330 °C) and two pressures (69.4 MPa and 104.2 MPa) were used to create the six specimens. The heating rate was approximately 25 °C /minute, and the specimens were held at the sintering temperature for 5 minutes before pressure was increased (from the minimum) to the desired level for extrusion. The extrusion pressure was held, and the experiment continued, until the z-axis displacement showed no change (of 0.01 mm) for 30 seconds, and therefore extrusion was completed. Then, all power and pressure was removed, and the specimen was cooled in the chamber before removal.

This extrusion pressure was chosen due to a simple calculation, using the approximation,

$$\text{Equation 10. } P = K \ln R$$

where P is the extrusion pressure, K is the extrusion constant (based on frictional forces and flow stress), and R is the extrusion ratio. From Sachs and Eischen<sup>147</sup>, we get this equation, and the values of K for aluminum of 34.5-69.0 MPa, dependent on temperature. For our extrusion temperature, K is 34.5 MPa, and our extrusion ratio R is 4, so Equation 10 shows that the expected extrusion pressure is 47.8 MPa for our experiments. We chose a minimum pressure value (69.5 MPa) that is approximately 1.5 times the value

from Equation 10. Even with the maximum value of  $K$  at room temperature (69.0 MPa), the expected extrusion pressure is 95.6 MPa, which is less than the higher pressure we used in the experiments.

Specimens were cut in a diamond saw and then hot mounted in epoxy. They were polished thoroughly, using 320 to 4000 grit SiC paper followed by diamond polish, and then etched with Murakami's reagent for 15-90 seconds. The quality of etching was examined in the optical microscope, and further etching may have been applied, before the specimens were observed (and images taken) in the electron microscope.

For the grain size measurements, the error was calculated from the standard deviation of the measurements made from the linear intercept method for each experiment, and the average value from all experiments of 0.3  $\mu\text{m}$  was found, and inserted in the tables and figures.

It is interesting to note that the steel die became magnetized after the first experiment in the SPS machine. This was obviously due to the large amount of uniaxial current from the SPS aligning the domains in the steel material and revealing (or enhancing) its ferromagnetism. The magnetic force of the die was strong enough to hold the die together without the need for the steel ring, and it prevented any spreading or escape of the specimen material through the split between the two dies. The steel ring was still used throughout the experiments as a reinforcement, and to help hold the thermocouple in place.

#### **4.1.2. Results for densification and grain growth in spark plasma extrusion**



Table 3 below shows a comparison between the average grain size, large and small particle sizes, average final porosity, and particle shape between the 6 specimens that were sintered and then extruded, the starting powder before sintering, the pre-sintered green specimen, and a specimen that was sintered to 100% relative density using similar temperature and pressure conditions but used traditional SPS with no extrusion. We can see that although there is significant densification during sintering, there is not significant grain growth, with the average grain size, and largest and smallest grains, of all sintered specimens comparable to that of the pre-sintered specimen. Compared to the initial powder, we can see that the average grain size did not increase during sintering, although the largest and smallest grains in the specimens were significantly larger.

Table 3. Average values for all 6 experiments, and the pre-sintered specimen

Specimen	Temperature (°C)	Pressure (MPa)	Ave. grain size ( $\pm 0.3 \mu\text{m}$ )	Ave. large st grain ( $\mu\text{m}$ )	Ave. smallest grain ( $\mu\text{m}$ )	Average micro-hardness (HV0.5, $\pm 2$ )	Ave. porosity (%)
1	330	69.5	12.1	52.9	3.5	26	3.1
2	330	104.2	14.7	53.9	1.75	26	3.1
3	230	104.2	16.0	60.4	2.3	36	3.0
4	230	69.5	13.9	48.9	2.1	29	1.8
5	130	104.2	15.9	58.1	2.6	25	3.4
6	130	69.5	15.9	54.6	2.2	29	4.0
Pre-sinter	500	0.0	12.3	59.2	1.5		28.0
Initial Powder			12.0	37.3	1.2		

When we compare the extruded specimens with the initial powder, it is clear that SPS and extrusion is capable of minimizing or decreasing grain size during sintering, as all of the specimens appear to be very similar to the initial powder.

## 4.2. Results and discussion

Table 4-Table 9 show the average grain size, porosity, largest and smallest grains, and shape of the grains in seven different regions of each of the six specimens. We can describe the grains in the different areas (as seen in SEM images) as having four particular shapes, using the terminology of the British Standards Institute<sup>148</sup>: 1) Lamellar, which are grains that have a large aspect ratio and which are polygons, 2) Modular, which are grains that are round (polygons with many sides) but have a slight elliptical shape, 3) Irregular, lacking any symmetry, and 4) Spherical, which are grains that are about the same size in every direction, and which likely represent spherical grains in three dimensions.

Figure 29-Figure 34 show the grain structure in the seven areas of each specimen, in their relative positions in the specimen. The left side of the image is the “center” of the specimen, as it is cut in half for these figures due to the symmetry of the specimen. The right side of the specimen is the “side” which contacts the die wall. The “top” of the specimen is at the top of the image, and the bottom of the image is the “extrusion” area. We can see for an area such as “side @ extrusion” the SEM image is superimposed at the right side of the image, at the bottom. “Side at streamline” describes the side where the streamlined portion of the specimen begins, and “center of streamline” describes the area in the center of the streamline between the beginning of the streamline and the extrusion zone.

Table 4. Values for different regions in Specimen 1, processed @ 330 °C and 69.5 MPa.

Region	Ave. Grain size ( $\mu\text{m}$ , $\pm 0.3$ )	Largest grain ( $\mu\text{m}$ )	Smallest grain ( $\mu\text{m}$ )	Average microhardness (HV0.5, $\pm 2$ )	Porosity (%, $\pm 1$ )	Grain shape / orientation
Top corner	10.7	62.8	4.1	20	2.9	Mostly modular
Top center	15.4	43.0	2.2	26	4.0	Randomly modular, spherical, or lamellar
Center	18.0	41.8	2.0	29	2.6	Mostly modular
Side at streamline	7.3	50.6	5.2	29	2.0	Mostly modular and irregular, slight orientation
Center of streamline	7.1	54.8	4.9	32	2.1	Mostly lamellar and irregular
Side at extrusion	9.4	67.0	4.1	28	4.0	Modular and lamellar
Center at extrusion	16.4	50.6	1.9	19	4.5	Mostly spherical
Average	12.1	52.9	3.5	26	3.1	

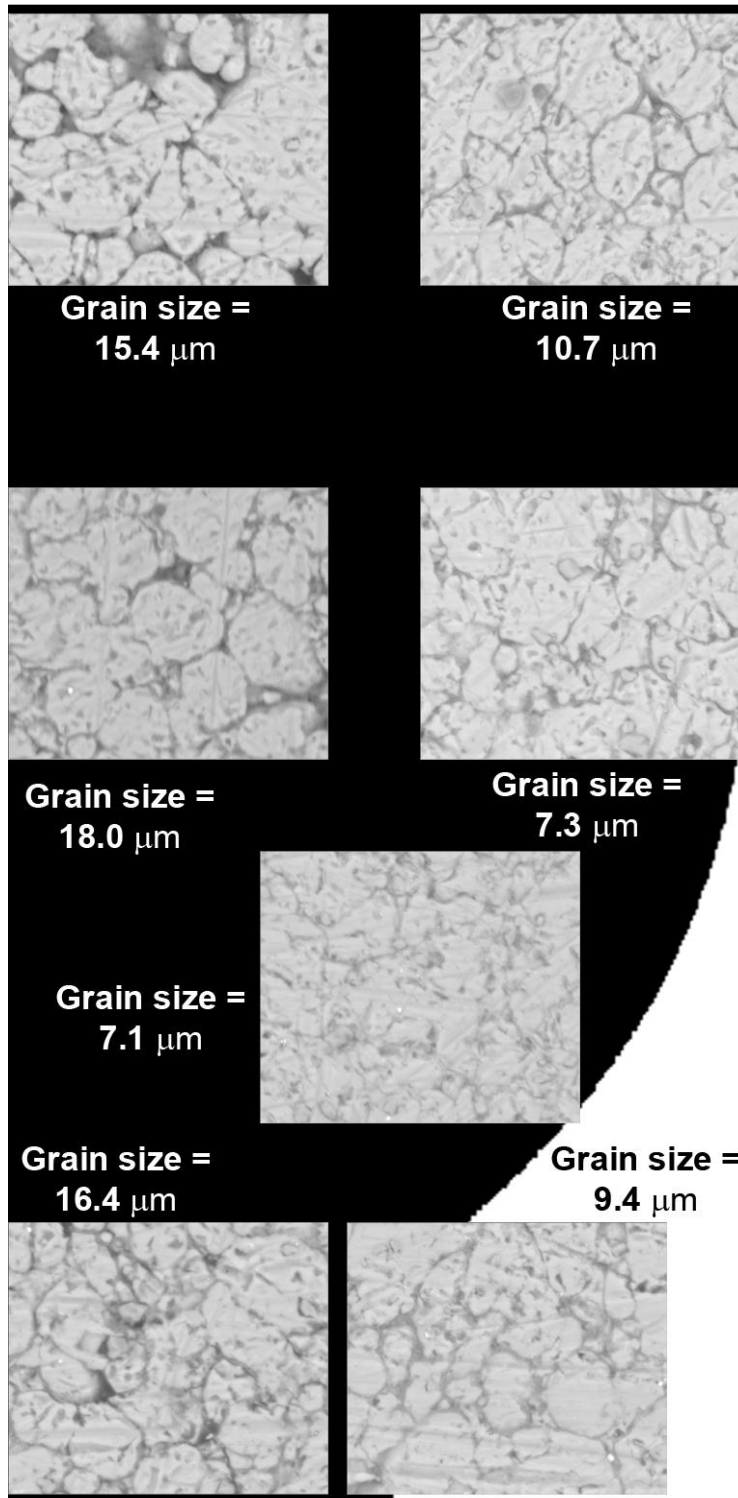


Figure 29. A cross-sectional view of the specimen 1, with SEM images of the approximate regions superimposed. Average grain size is 12.1  $\mu\text{m}$ , and average porosity is 3.1%.

Table 5. Values for different regions in Specimen 2, processed @ 330 °C and 104.2 MPa.

Region	Ave. Grain size ( $\mu\text{m}$ , $\pm 0.3$ )	Largest grain ( $\mu\text{m}$ )	Smallest grain ( $\mu\text{m}$ )	Average microhardness (HV0.5, $\pm 2$ )	Porosity (%, $\pm 1$ )	Grain shape / orientation
Top corner	13.4	47.9	1.1	31	1.9	Mostly modular, some lamellar
Top center	15.8	65.0	1.2	32	2.5	Random
Center	12.7	54.0	1.7	25	3.8	Mostly modular
Side at streamline	14.3	45.0	1.6	29	3.6	Mostly spherical, some lamellar
Center of streamline	19.2	66.2	2.3	30	2.6	Mostly lamellar and irregular
Side at extrusion	14.3	43.2	2.3	15	3.0	Mostly modular, some spherical
Center at extrusion	13.2	55.4	2.2	18	4.4	Some spherical, mostly lamellar and irregular
Average	14.7	53.9	1.75	26	3.1	

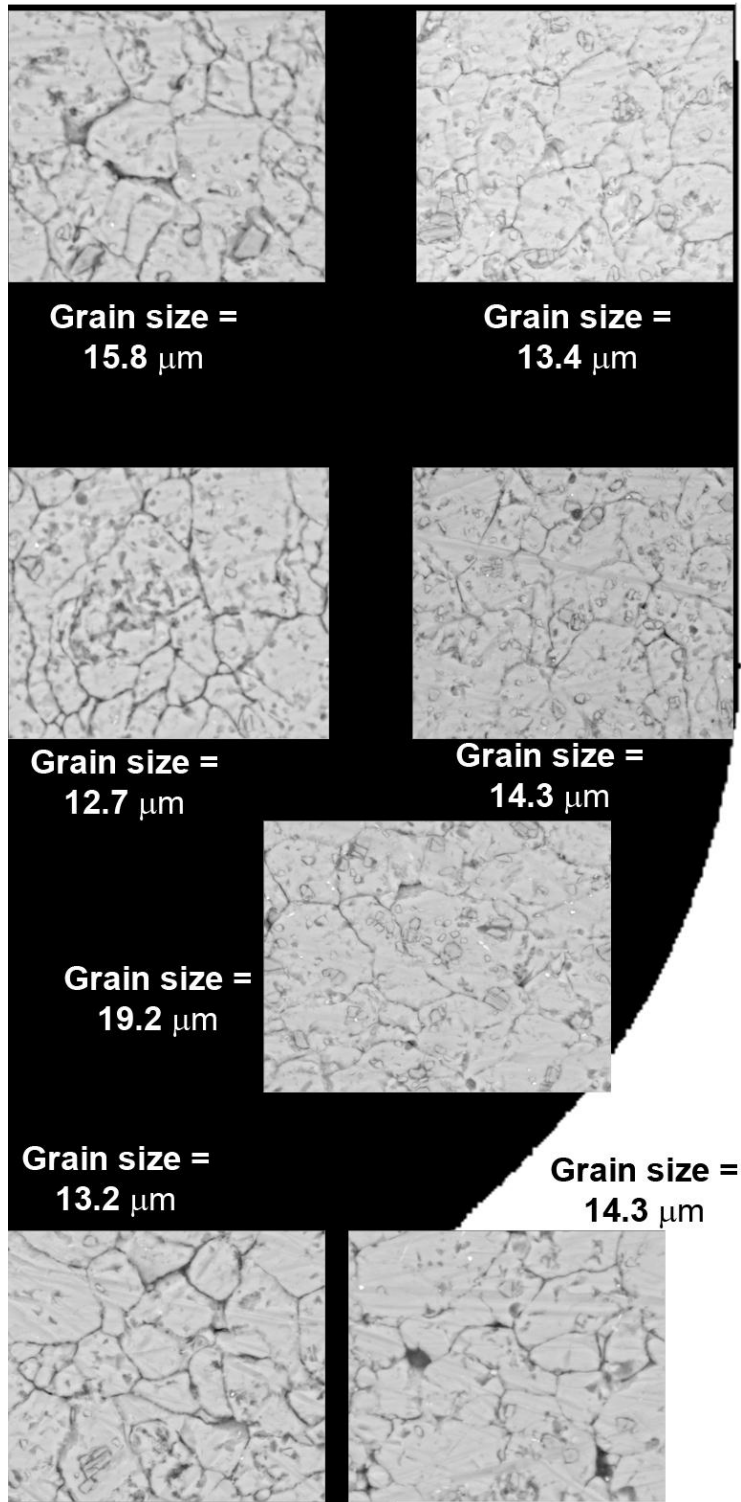


Figure 30. A cross-sectional view of the specimen 2, with SEM images of the approximate regions superimposed. Average grain size is 14.7  $\mu\text{m}$ , and average porosity is 3.1%.

Table 6. Values for different regions in Specimen 3, processed @ 230 °C and 104.2 MPa.

Region	Ave. Grain size ( $\mu\text{m}$ , $\pm 0.3$ )	Largest grain ( $\mu\text{m}$ )	Smallest grain ( $\mu\text{m}$ )	Average microhardness (HV0.5, $\pm 2$ )	Porosity (%, $\pm 1$ )	Grain shape / orientation
Top corner	17.6	52.5	2.7	38	2.0	Modular, and lamellar
Top center	15.8	62.9	2.5	40	3.2	Random
Center	16.7	66.6	1.7	37	5.1	Mostly spherical, some lamellar
Side at streamline	13.2	58.5	2.5	37	2.6	Some spherical, mostly lamellar
Center of streamline	15.6	54.9	2.3	38	2.8	Mostly lamellar, some orientation
Side at extrusion	17.0	58.1	2.1	31	2.9	Modular and spherical, some orientation
Center at extrusion	16.1	75.8	2.4	30	1.9	Mostly spherical
Average	16.0	60.4	2.3	36	3.0	

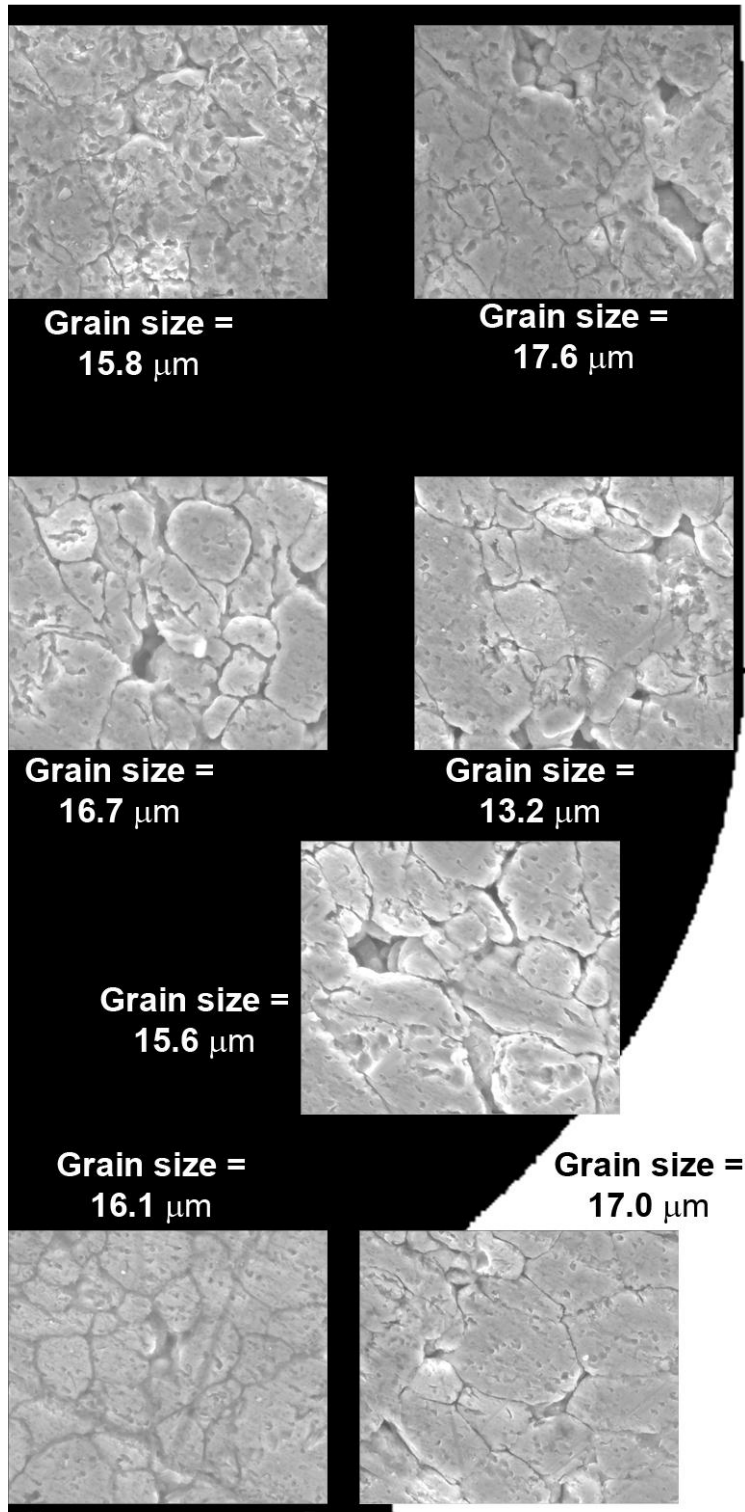


Figure 31. A cross-sectional view of the specimen 3, with SEM images of the approximate regions superimposed. Average grain size is 16.0  $\mu\text{m}$ , and average porosity is 3.0%.



Table 7. Values for different regions in Specimen 4, processed @ 230 °C and 69.5 MPa.

Region	Ave. Grain size ( $\mu\text{m}$ , $\pm 0.3$ )	Largest grain ( $\mu\text{m}$ )	Smallest grain ( $\mu\text{m}$ )	Average microhardness (HV0.5, $\pm 2$ )	Porosity (% $\pm 1$ )	Grain shape / orientation
Top corner	13.8	38.8	1.2	32	1.9	Modular and lamellar, slight orientation
Top center	9.0	35.7	1.8	30	1.3	Random
Center	15.3	44.1	2.0	33	1.6	Spherical and modular
Side at streamline	10.2	31.8	1.4	26	2.0	Mostly lamellar, slight orientation
Center of streamline	13.6	36.2	1.2	31	1.6	Mostly lamellar, some orientation
Side at extrusion	18.8	69.3	2.0	32	3.0	Mostly modular, some orientation
Center at extrusion	16.7	40.7	2.5	22	1.6	Mostly spherical
Average	13.9	48.9	2.1	29	1.8	

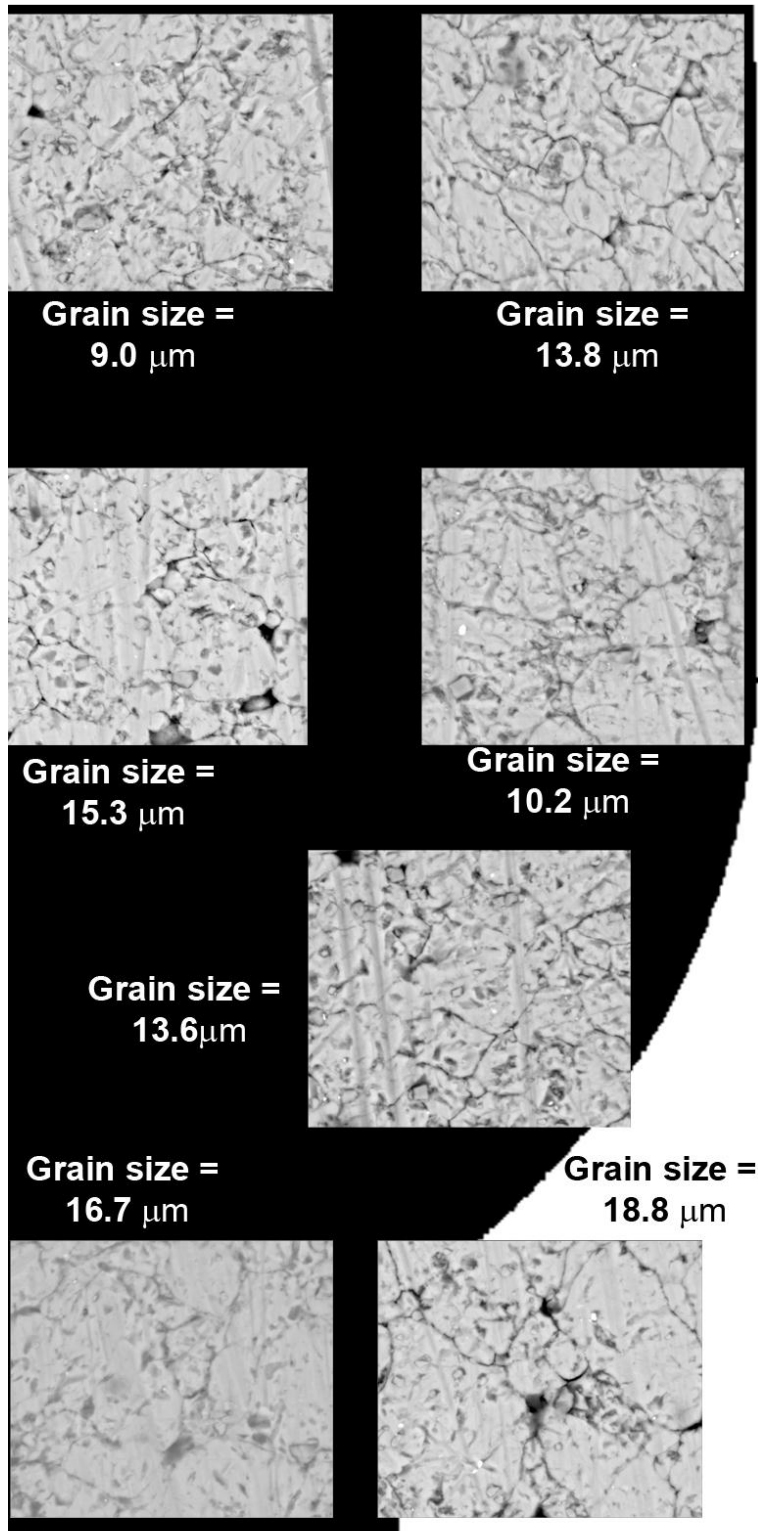


Figure 32. A cross-sectional view of the specimen 4, with SEM images of the approximate regions superimposed. Average grain size is 13.9  $\mu\text{m}$ , and average porosity is 1.8%.

Table 8. Values for different regions in Specimen 5, processed @ 130 °C and 104.2 MPa.

Region	Ave. Grain size ( $\mu\text{m}$ , $\pm 0.3$ )	Largest grain ( $\mu\text{m}$ )	Smallest grain ( $\mu\text{m}$ )	Average microhardness (HV0.5, $\pm 2$ )	Porosity (%, $\pm 1$ )	Grain shape / orientation
Top corner	13.9	69.7	2.0	35	2.8	Mostly ovoid
Top center	15.0	43.1	2.1	31	4.6	Modular and spherical, some orientation
Center	16.1	70.4	2.5	29	3.5	Mostly modular, some spherical
Side at streamline	16.1	67.0	2.6	23	3.0	Mostly modular, some lamellar
Center of streamline	16.1	55.4	3.4	28	3.5	Mostly modular
Side at extrusion	17.0	47.3	2.0	16	2.8	Mostly lamellar, some spherical, slight orientation
Center at extrusion	17.1	54.2	2.0	16	3.3	Mostly spherical, some modular
Average	15.9	58.1	2.6	25	3.4	

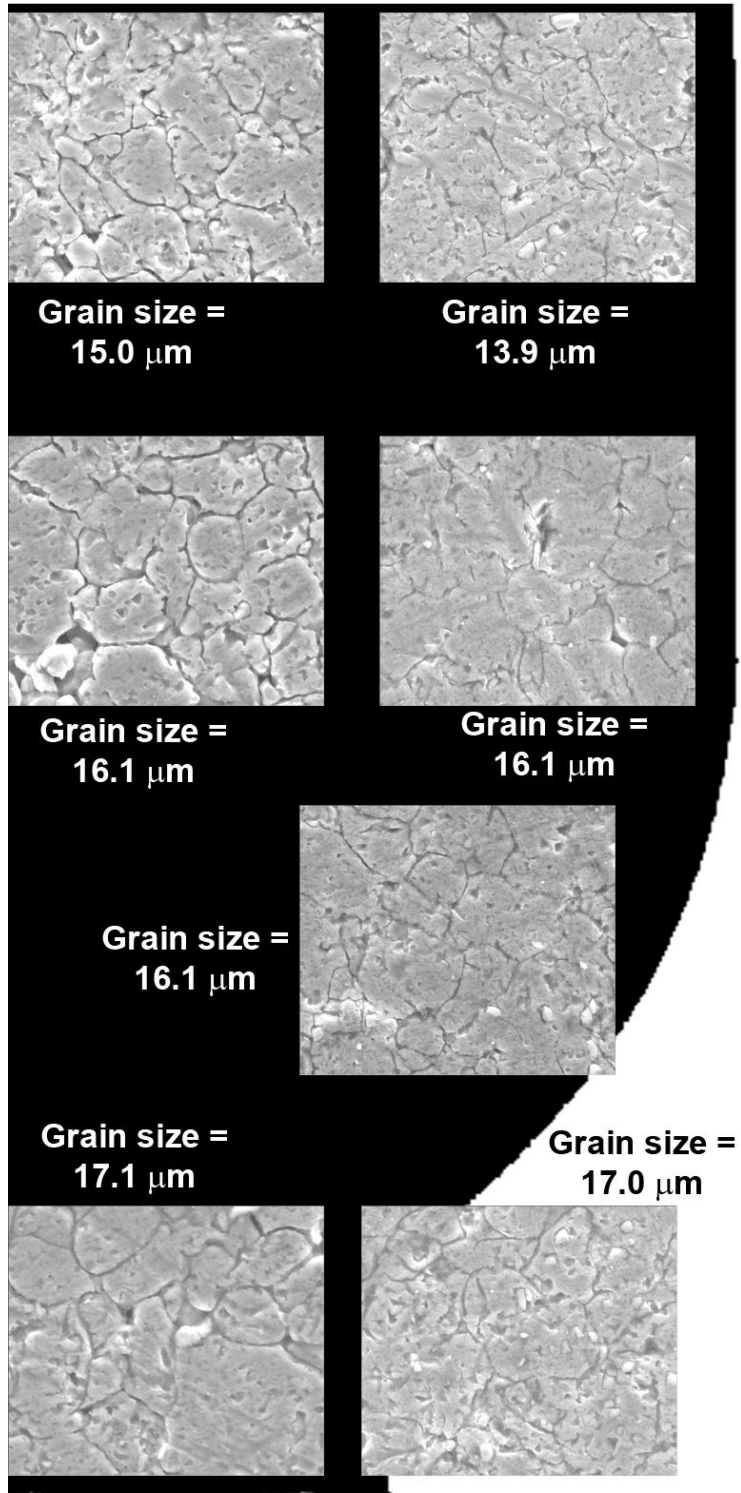


Figure 33. A cross-sectional view of the specimen 5, with SEM images of the approximate regions superimposed. Average grain size is 15.9  $\mu\text{m}$ , and average porosity is 3.4%.

Table 9. Values for different regions in Specimen 6, processed @ 130 °C and 69.5 MPa

Region	Ave. Grain size ( $\mu\text{m}$ , $\pm 0.3$ )	Largest grain ( $\mu\text{m}$ )	Smallest grain ( $\mu\text{m}$ )	Average microhardness (HV0.5, $\pm 2$ )	Porosity (% $\pm 1$ )	Grain shape / orientation
Top corner	15.8	42.7	1.2	39	3.4	Mostly lamellar, some orientation
Top center	13.9	51.5	1.7	31	3.8	Random
Center	13.4	61.2	2.3	29	3.9	Modular, some orientation
Side at streamline	14.8	45.8	1.9	28	4.5	Mostly modular, some orientation
Center of streamline	19.2	56.6	3.0	28	4.5	Mostly lamellar, some modular, some orientation
Side at extrusion	16.7	62.9	2.9	19	4.8	Mostly lamellar, some ovoid
Center at extrusion	17.3	54.5	2.3	29	2.9	Mostly spherical, some modular
Average	15.9	54.6	2.2	29	4.0	

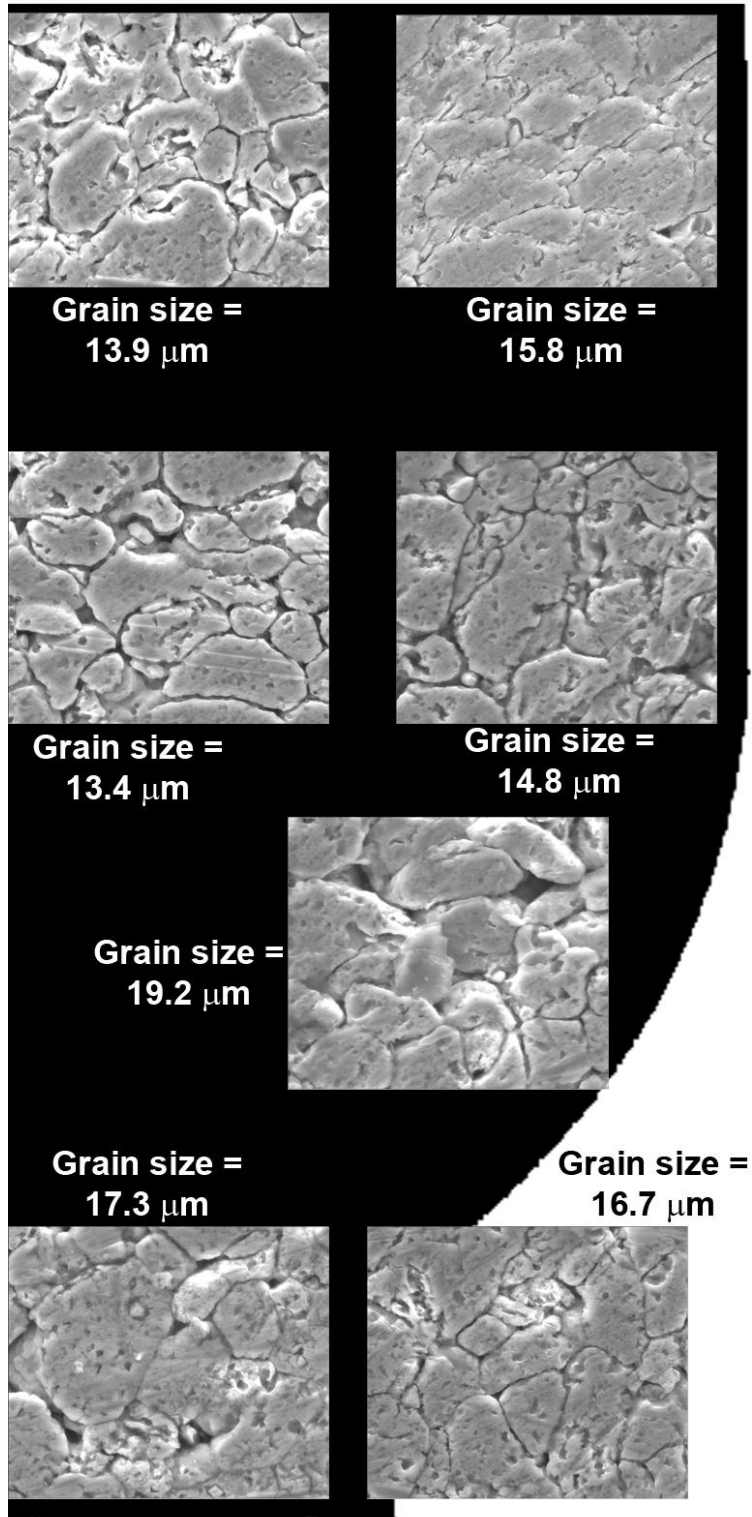


Figure 34. A cross-sectional view of the specimen 6, with SEM images of the approximate regions superimposed. Average grain size is 15.9 mm, and average porosity is 4.0%.

We can see that each of the six specimens looks approximately the same as each other in each of the seven different locations. On the side of the specimen, where there is contact with the die wall, we can see deformation and elongation of the grains increase as we travel down from the top corner to the center of the streamline. We can also see as we travel down the specimen that there is a granular orientation in the areas with significant deformation and grain elongation (along the streamline), caused by the stress field in this area due to the die shape, forcing the grains to align along this stress field (and is expected). As the specimen is extruded and leaves the die, we can see a change in grain shape on the side of the specimen from elongated and polygonal to an ovoid shape, where the stress along the die wall is removed.

In the center of the specimen, the top surface, in contact with the punch, shows a random orientation and collection of grain types. As we travel down through the specimen to the area that is extruded, we see the grains become uniformly ovoid and of similar size in the center of the specimen, and round and mostly equiaxed in the extrusion area. The difference in grain structure in the center of the extruded area, and the side near the wall, shows that the center channel of material flows directly down the center of the specimen and experiences little deformation due to the die shape or extrusion. This may mean that the extrusion ratio of 4 is too small to have an effect on the whole specimen.

Looking at Table 10 and Table 11, we can see some interesting results in localized grain growth. In the specimens with an applied extrusion pressure of 69.5 MPa, we see that the center area of the specimen has larger grain growth than the center of the specimen. However for the specimens at 104.2 MPa, it is not clear. In specimens 2 and 5

there is higher grain growth in the side area, but specimen 3 has higher densification in the center. Specimens 2 and 3 have grain size reduction in the area that has no grain growth, so they may not be comparable to specimen 5, which has only grain growth. We can also see that specimen 4, which has the lowest porosity of all the specimens, also has the most significant grain growth in both areas. In some specimens, the grains are refined as they head down the side, or the center, of the specimen during extrusion. However, in others the grains experience periods of grain growth and grain refinement, without any pattern. Based solely on temperature or pressure, it seems impossible to predict whether grain growth or grain refinement will occur in the specimens, and to what extent.

Table 10. Average grain size development in the side area of 6 specimens.

Specimen	Temp. (°C)	Pressure (MPa)	GS top corner (μm)	GS side at streamline (μm, ±0.3)	GS center of streamline (μm)	GS side of extrusion (μm)	% change, top to bottom	Average porosity
1	330	69.5	10.7	7.3	7.1	9.4	-12.1	2.8
2	330	104.2	13.4	14.3	19.2	14.3	6.7	2.8
3	230	104.2	17.6	13.2	15.6	16.1	-8.1	2.6
4	230	69.5	13.8	10.2	13.6	18.8	36.2	2.1
5	130	104.2	13.9	16.1	16.1	17.0	22.3	3.0
6	130	69.5	15.8	14.8	19.2	16.7	5.7	4.3

Table 11. Average grain size development in the center area of 6 specimens.

Specimen	Temp. (°C)	Pressure (MPa)	GS Top Center (μm, ±0.2)	GS center (μm)	GS center at extrusion (μm)	% change	Average porosity
1	330	69.5	15.4	18.0	16.4	6.5	3.7
2	330	104.2	15.8	12.7	13.2	-16.5	3.6
3	230	104.2	15.8	16.7	16.1	1.9	3.4
4	230	69.5	9.0	15.3	16.7	85.6	1.5
5	130	104.2	15.0	16.1	17.1	14.0	3.8
6	130	69.5	13.9	13.4	17.3	24.5	3.5

We can plot the average grain size gradients (the grain size difference in two areas divided by the distance between them) versus temperature and pressure, and see if there



is a dependence. Figure 35 and Figure 36 show the gradients versus temperature and pressure, respectively. We can see that as the extrusion temperature increases, the grain size differences between the center and sides of the specimen increases significantly (gradients range from 0.7 to 3). For pressure, we can see that the grain size does not vary between the two areas (gradients increase from 1.7 to 1.9).

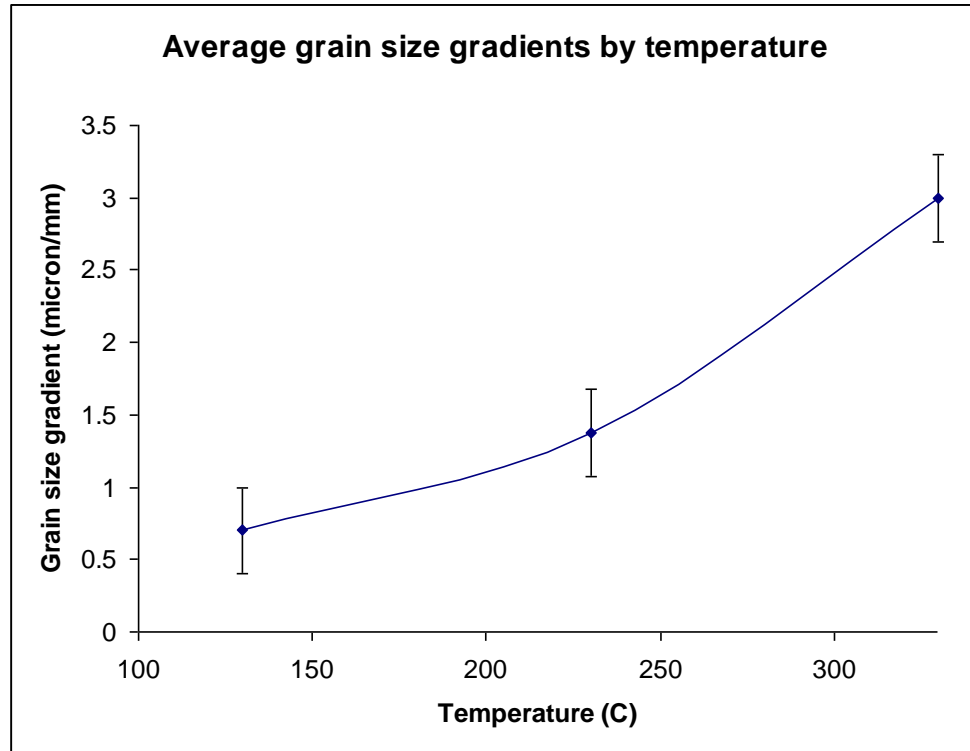


Figure 35. Average grain size gradients versus temperature, showing an increasing grain size difference between the center and side of the specimens as temperature is increased.

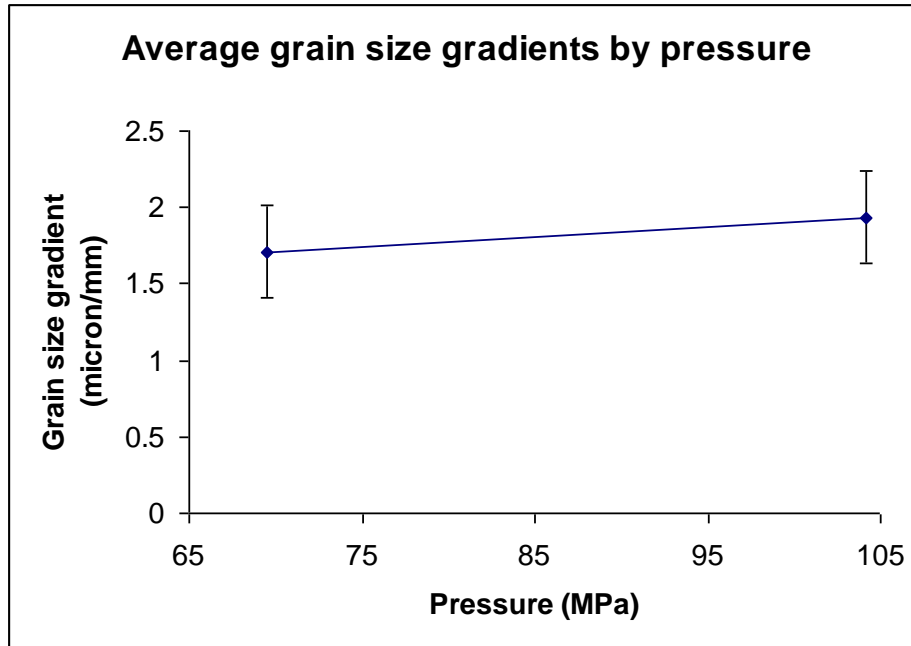


Figure 36. Average grain size gradients versus temperature, showing a slight increase in grain size difference between the center and side of the specimens as temperature increased.

Overall, spark plasma extrusion was conducted successfully on aluminum, at a significantly lower temperature than conventional extrusion processes. The extrusion process produced a decrease in grain size and change in the grain shape compared to SPS of aluminum. By observing the grain size and porosity in the specimen left in the die, and comparing it to the extrudate, we can see the traditional deformation of extrusion occurring in the SPE process. Due to the chosen extrusion ratio, the center of the specimens did not experience similar conditions to those in contact with the die wall (likely due to different shear stresses in each area), and the final specimen had variations in the edge and center in terms of grain size, grain shape, and porosity.

## **Chapter 5. Processing by SPS of tailored powder composites**

### ***5.1. SPS of tantalum carbide and tantalum carbide-carbon nanotube composites***

In this section, we investigate the ability of spark sintering to densify materials that are difficult or impossible to densify fully using traditional methods, and find the relationship between densification and grain growth for this type of material. A material that is hard to densify or deform should provide more insight into the grain growth and densification relationship.

Specifically, we investigated the densification of Tantalum Carbide, which has the highest melting point of any stoichiometric compound (3880 °C). Research has shown the ability to densify this material with a large range of pressures (from 0-1.5 GPa), and temperatures (from 1300-3200 °C), but full density is rarely achieved. Due to the extreme nature (and range of temperatures and pressures) of the reviewed consolidation methods, we attempted a series of sintering experiments starting at approximately 50% of the melting point (1900 °C), using a small applied pressure, and increased the holding temperature until nearly full density was reached. Once we had reached a sufficient density with pure tantalum carbide, we created a tantalum carbide and carbon nanotube composite, a material with promising hardness and toughness properties, but which is difficult to create and densify without spark sintering

We tested the hardness and rupture strength of all of the specimens, to determine the quality of the specimens, and to see if the composite had improved properties over the base material. We also compared our results to specimens (from literature) that were

produced using hot pressing. The quality of the specimens was necessary to assess due to the large range of strength values (anywhere from 200-1500 GPa) reported in the literature for this material system.

Due to the difficulty in fracturing these hard ceramic specimens, we created a new method for fracture testing that is comparable to the ASTM standard, but more flexible than the standard. This was necessary because the standard diameter of the specimen would have required extremely low thickness (less than .5 mm) for the ASTM standard test, which is too thin to produce in SPS. We successfully created the testing apparatus and used it to evaluate the specimens.

#### **5.1.1. Experimental Procedure for SPS of TaC**

6.5 grams of TaC powder, with particle size -325 mesh (less than 44  $\mu\text{m}$ ), and greater than 99.5% purity (Diversified Advanced Technologies, Reno, NV) was sintered in the Dr. Sinter Lab 515S spark sintering machine (SPS Syntex, Co., Japan), using a set temperature profile under a constant 30 or 75 MPa load, in a nitrogen atmosphere. The load of 30 MPa is lowered, compared to hot pressing experiments, for two reasons: due to the possibility of damaging the die during high temperature sintering with a higher load, and also this load level provides a direct comparison to the results of Zhang et al. who used 30 MPa in hot pressing of TaC. The temperature profile was designed to heat the specimen rapidly, and to prevent overheating of the specimen and the die at high temperature. The heating rates varied from 233  $^{\circ}\text{C}/\text{min}$  at the beginning of the experiment, to 33  $^{\circ}\text{C}/\text{min}$  before reaching the holding temperature. The temperature

profile for each specimen is shown in Figure 21, along with the relative density evolution during sintering. The holding temperature was also chosen for comparison with Zhang et al. and for sintering was 1900 °C or 2300 °C, and the holding time was 5 minutes or 20 minutes. There was no pre-pressing of the powder before insertion into the SPS machine, and the pressure was applied continuously from the start of heating.

The die used in SPS was composed of graphite, with a cylindrical shape and a 15.4 mm inner diameter. Graphite foil (.2 mm thickness) was placed inside the cylinder, around the powder, to allow for lubrication and extraction of the finished specimen after processing, which produced a final specimen with a diameter of 15 mm and a height of 3 mm.

For Tensile Rupture Strength (TRS) testing, the sample was fractured by applying pressure through a tungsten carbide ball-shaped indenter, onto the disc-shaped specimen, as shown in Figure 37.

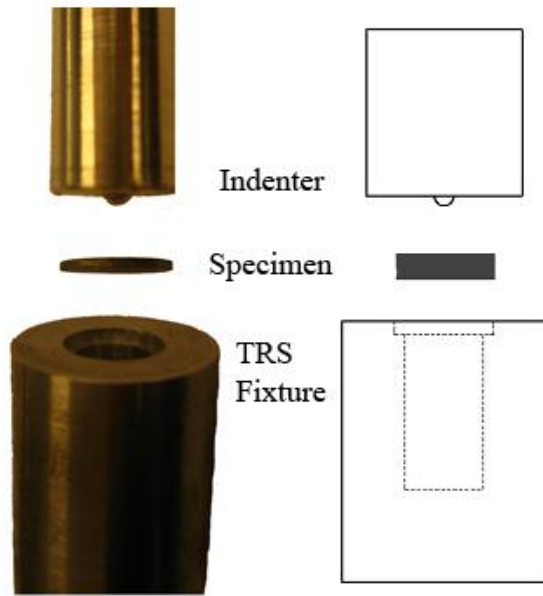


Figure 37. A picture and schematic drawing of our Tensile Rupture Strength setup.

Due to the difference of our setup with the ASTM C1499–09<sup>149</sup> standard for transverse rupture strength testing, the equation for our particular setup of TRS is as follows, which allows us to compute the strength based on the non-standard (non-prismatic) cylindrical geometry of our specimen:<sup>150</sup>

$$\text{Equation 11. } \sigma_{\max} = \frac{P}{h^2} \left[ (1 + \nu) \left( 0.485 \log \frac{a}{h} + 0.52 \right) + 0.48 \right]$$

where  $P$  is the force,  $h$  is the thickness of the specimen,  $a$  is the radius of the disk sample, and  $\nu$  is Poisson's ratio. Poisson's ratio for the above equation (0.24) was obtained from Lopez-de-la-Torre et al.<sup>151</sup> This is a novel TRS procedure that makes the approach more versatile for varying specimen sizes, particularly when using hard to machine materials like TaC, and processes like SPS where the die size determines the

specimen size. The novel TRS setup manifests the necessity to employ new characterization techniques for new tailored material systems.

The equation for TRS under ASTM C1499-09 is:

$$\text{Equation 12. } \sigma_{\max} = \frac{3F}{2\pi h^2} \left[ (1+\nu) \ln \frac{D_s}{D_L} + (1-\nu) \frac{D_s^2 - D_L^2}{2D^2} \right]$$

where  $F$  is the measured load,  $h$  is the thickness of the specimen,  $D$  is the specimen diameter,  $D_s$  is the diameter of the support ring,  $D_L$  is the diameter of the loading ring, and  $\nu$  is Poisson's ratio. This equation is very similar in form to our equation, with the only difference being geometry related terms.

To show that the two equations are directly relatable, we can use values from our experiments on TaC, with  $D = D_s = 15$  mm,  $h = 3$  mm,  $\nu = .21$  (from Lopez-de-la-Torre et al.<sup>151</sup>), and  $F$  as the results from our TRS test using our setup, and input them into the ASTM equation to calculate  $\sigma$ .

The only unknown is  $D_L$ , as our impinging device is a sphere and not a ring, per the standard. The actual amount of contact area for a rigid sphere contacting a deformable plate is a complex problem only solvable numerically through the Hertz Elastic Theory of Contact, and is beyond the scope of this work.

We can resolve this issue by solving the problem by choosing values for  $D_L$  between the maximum (3 mm, the diameter of the sphere) and the minimum (0, for a point contact). We find that the ASTM standard and our TRS setup result values are equal when the sphere is considered to be a ring with diameter  $D_L = .75$  mm. This is a reasonable result, as it does not approximate the sphere as a point contact, nor does it

approximate the sphere as a loading ring with the same diameter, and the approximate is closer to a point than a ring.

This result for  $D_L$  was derived from one set of TaC experimental data, and then applied to the other sets of our TaC experimental data.  $\sigma$  was found to be the same (within 3%) using both our TRS setup calculation and the ASTM standard calculation in all cases.

This shows that the results obtained from our setup for TRS are applicable, and directly relatable, to the ASTM standard results, although our setup provides more flexibility for specimen size and specimen material than the ASTM standard.

Vickers Hardness macrohardness testing was performed, using both a 5 N and a 15 N load, with a standard diamond indenter tip. The specimen was indented at the center, at the edge, and halfway between these two points. The reported values, in Table 2, are the average of these three data points.

For Scanning Electron Microscopy (SEM), the ceramic specimens were fractured, sputtered with Platinum, and then examined in a Phillips XL-40 microscope.

Density was calculated using the standard Archimedes method, and also by using the z-axis (vertical) position data from the SPS machine during processing, taking into account thermal expansion of the graphite dies, punches, and spacers.

### **5.1.2. Results on the spark sintering of TaC**

A plot of the relative density versus time, including the temperature profile, is shown for each of the five specimens in the following Figures: Figure 38 sintered at 1900



°C, with a pressure of 30 MPa and holding time 5 minutes, Figure 39 sintered at 2300 °C, with a pressure of 30 MPa and holding time 5 minutes, Figure 40 sintered at 2300 °C with a pressure of 30 MPa and holding time 20 minutes, Figure 41 sintered at 2400 °C with holding time 10 minutes and a pressure of 75 MPa, and Figure 42 the composite specimen sintered at 2300 °C with a pressure of 30 MPa and holding time 20 minutes. The first three specimens were designed to match Zhang et al.<sup>114</sup> however since nearly full density was achieved in these specimens, the fourth specimen at higher temperature and pressure was designed to both reach full density and show how grain growth develops under the new conditions. The fifth specimen was designed to match the addition of carbon to create a non-stoichiometric compound, while also creating a composite based on the type of carbon chosen (carbon nanotubes instead of graphite). We can see, in all cases, that densification does not begin until the temperature exceeds 1500 °C, and after reaching the holding temperature, densification continues for the entire holding duration (even when holding for 20 minutes). The plot for the specimen sintered at 1900 °C shows little or no densification, with the final relative density of this specimen of 68%, increasing from a green relative density of 65%.

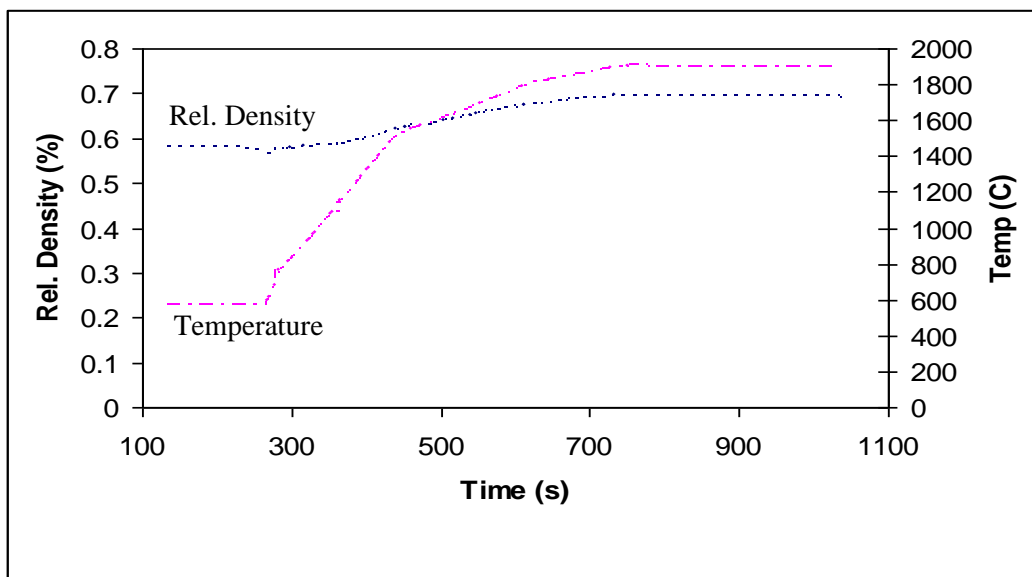


Figure 38. Temperature and density evolution during sintering of TaC powder heated to 1900 C, with 30 MPA pressure and 5 minutes holding time.

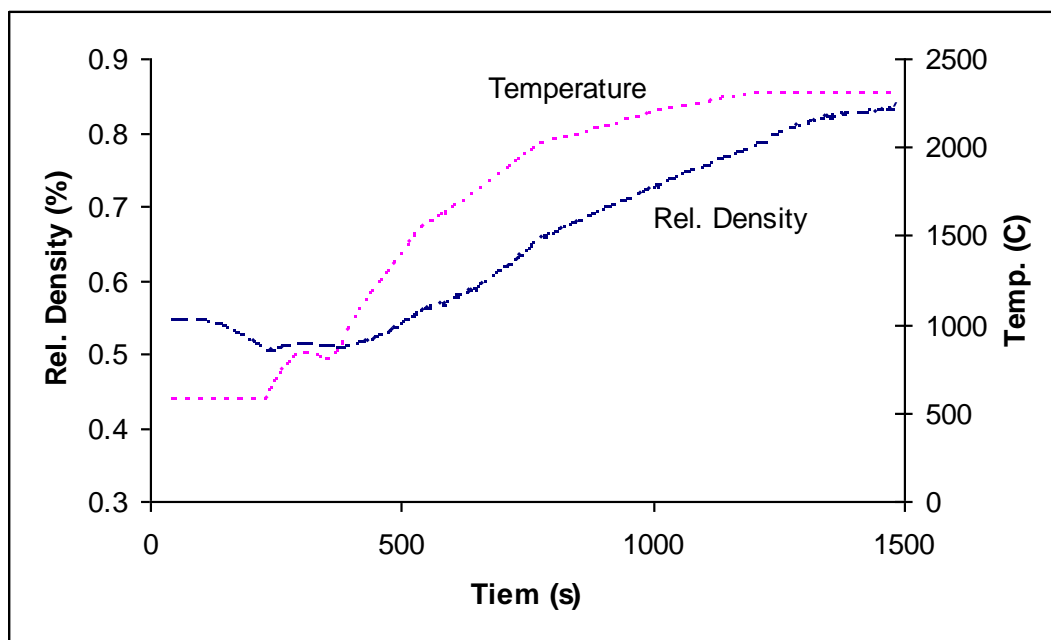


Figure 39. Temperature and density evolution during sintering of TaC powder heated to 2300 C, with 30 MPA pressure and 5 minutes holding time.

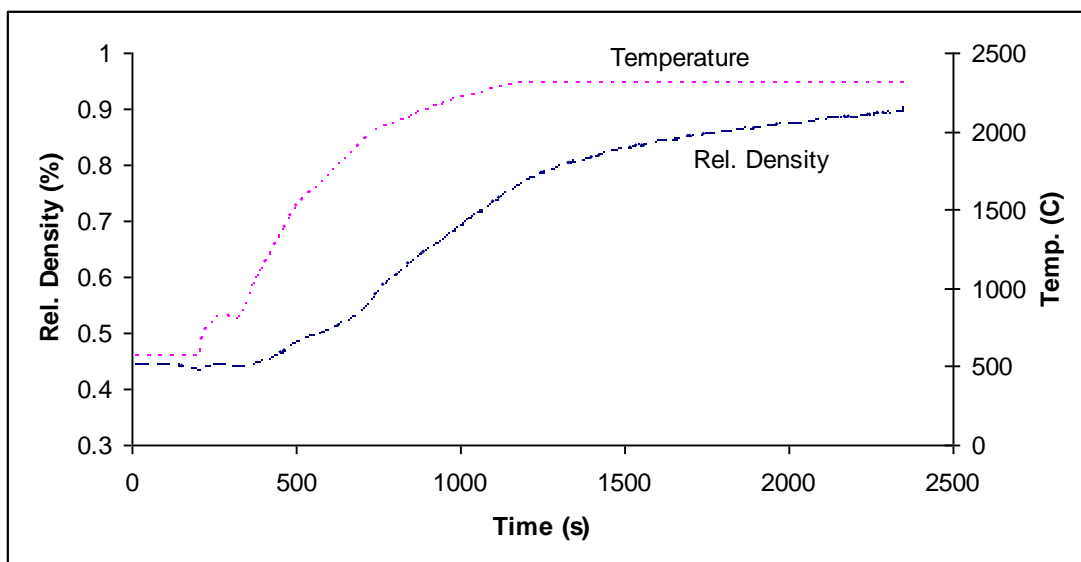


Figure 40. Temperature and density evolution during sintering of TaC powder heated to 2300 C, with 30 MPA pressure and 20 minutes holding time.

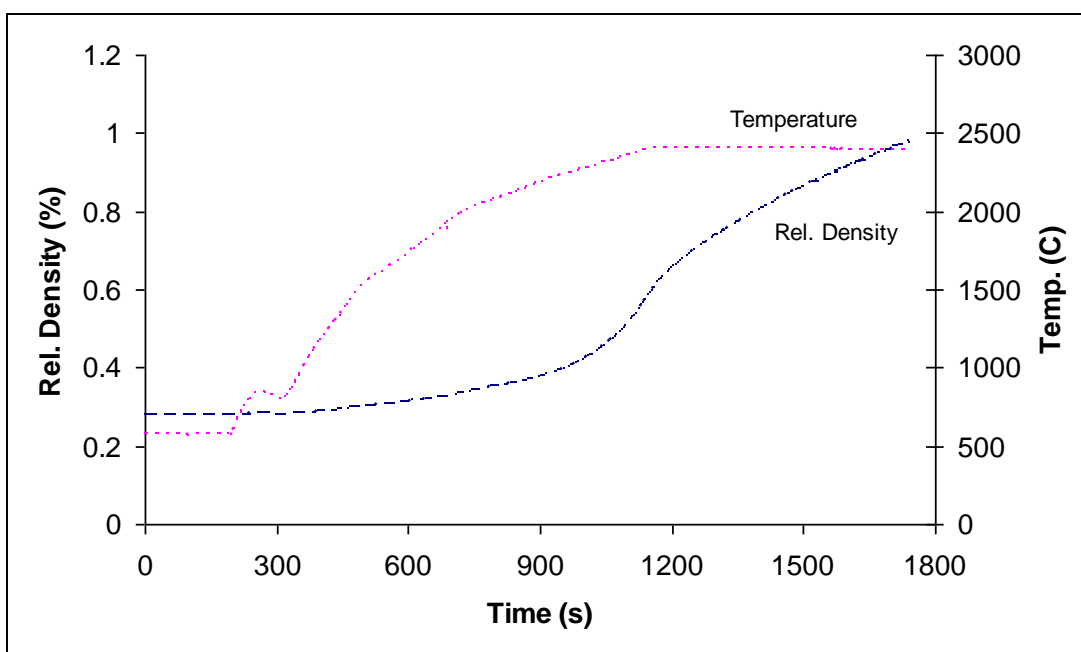


Figure 41. Temperature and density evolution during sintering of TaC powder heated to 2400 C, with 75 MPA pressure and 10 minutes holding time.

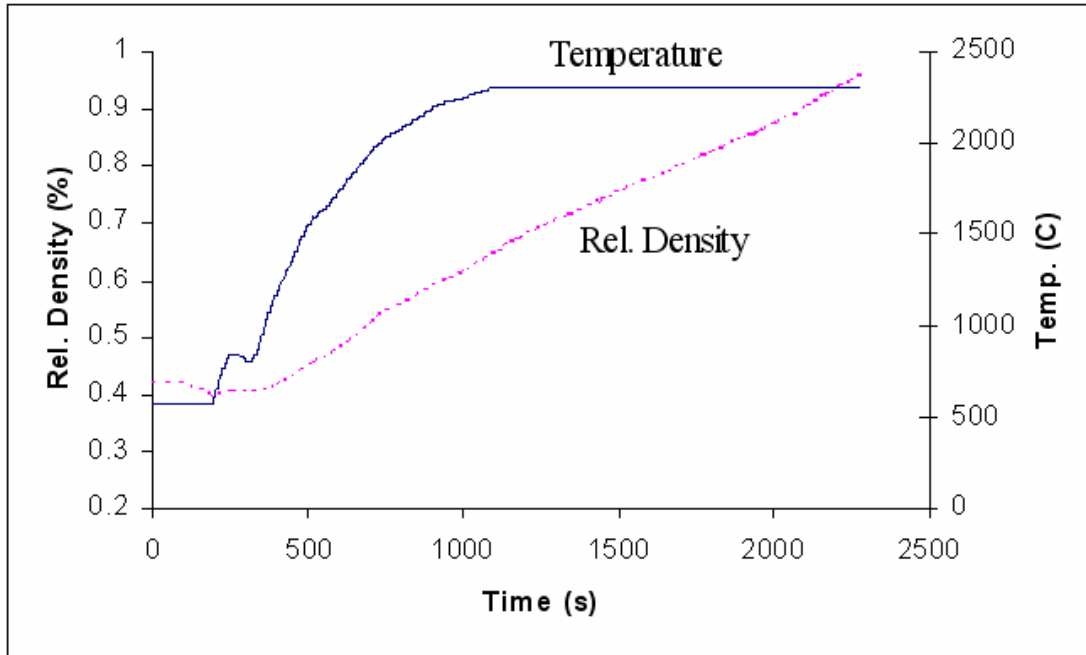


Figure 42. Temperature and density evolution during sintering of TaC-CNT composite powder heated to 2300 °C with 30 MPa pressure and 20 minutes holding time.

An SEM analysis of the fractured surfaces of the TaC specimens allows for the examination of grain size and porosity. The following figures show the SEM images of the specimens sintered at (Figure 43) 1900 °C for 5 minutes, (Figure 44) 2300 °C for 5 minutes, (Figure 45) 2300 °C for 20 minutes, (Figure 46) 2400 °C for 10 minutes, and (Figure 47) the composite at 2300 °C for 20 minutes. We can see from Figure 43 that very little contact growth and densification occurred at 1900 °C, with many of the particles undeformed similar to an unsintered green specimen. This is the expected outcome from the densification data based on the SPS experiment, shown in Figure 38. This indicates that the density increase is most likely due to pressing at 30 MPa for an extended time period. Figure 39 shows densification occurred, but there is still very high porosity. Since the holding time was short, we can expect densification will increase with a longer holding time. The final relative density of this specimen is 83%. Figure 40

shows a higher density than Figure 39, due to the extension of the holding time from 5 to 20 minutes. The final relative density observed for this specimen is 92%. Due to the dependence of final density on pressure and sintering temperature, we increased the temperature to 2400 C and the pressure to 75 MPa (see Figure 41). Relative density of 97% was achieved and with significant grain growth. Figure 42 shows rapid densification and a high density (96%) achieved with the same conditions as Figure 40. This change is due to the addition of the carbon nanotubes, which had a significant impact on the densification and final density.

We can see from Figure 43, that the starting particle size is as low as 200 nm, with most particles smaller than 5  $\mu\text{m}$ , and only a few larger than 10  $\mu\text{m}$ . Figure 44 shows that grain growth occurred during densification, with no grains present on the 500 nm scale and most above 5  $\mu\text{m}$ . Figure 45 shows further densification, due to the extended holding time, with few particles smaller than 10  $\mu\text{m}$ . This grain growth hindered the specimens from achieving full density, as evidenced by the amount of closed porosity present in the images. The specimen sintered at 2400 °C, as shown in Figure 46, shows significant grain growth but also decreased porosity. The porosity, in this case, is shared evenly between closed pores and pores in the grain boundaries (approximately 50% in each area). This is different than the similarly made hot-pressed specimen by Zhang et al.<sup>104</sup> which has a mix of a few grain boundary pores (18% of pores) and significant closed porosity inside the grains (82% of pores). Figure 47 shows a slight decrease (10%) in grain size from Figure 45, likely due to the addition of the carbon nanotubes. The pore structure is similar, with approximately 50% in the boundary and 50% as closed porosity, to the specimen without the added nanotubes.

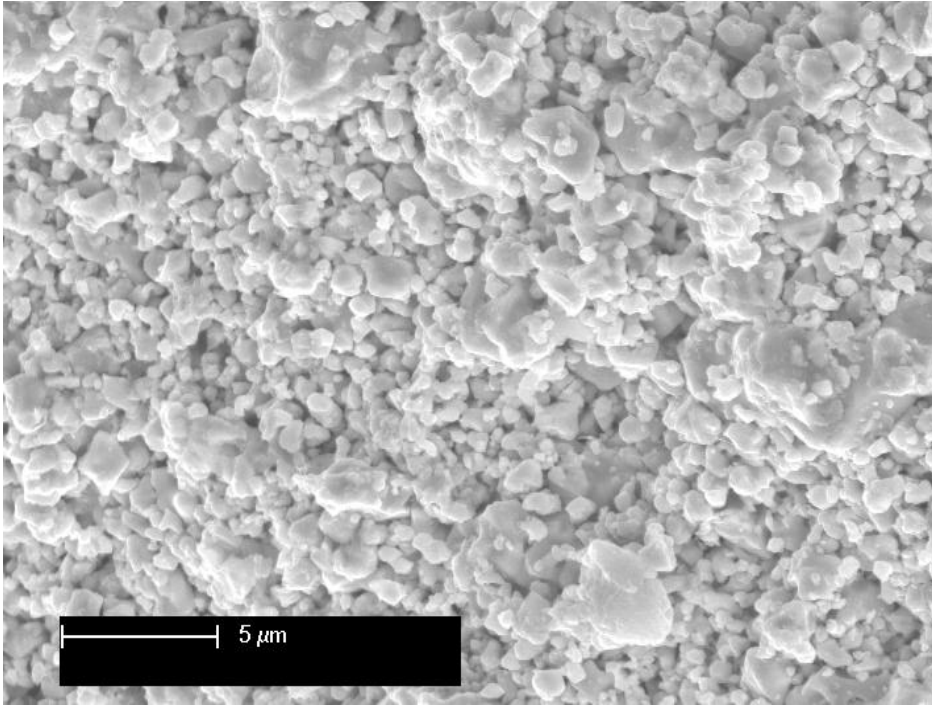


Figure 43. TaC specimen heated to 1900 C, with 30 MPa pressure, 5 minutes holding time, and 68% relative density.

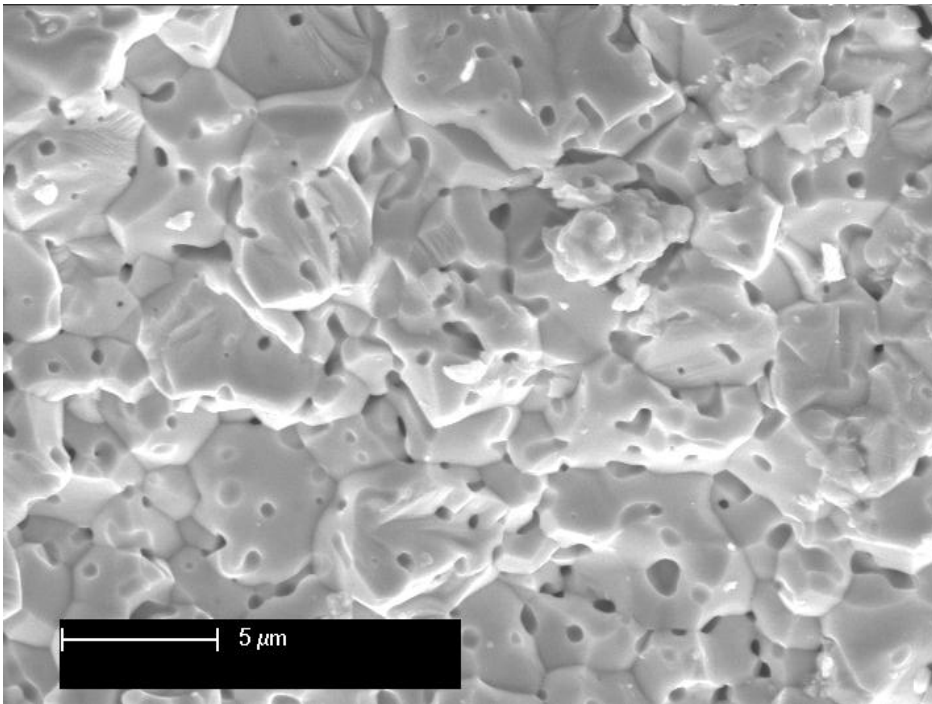


Figure 44. TaC specimen heated to 2300 C, with 30 MPa pressure, 5 minutes holding time, and 83% relative density.

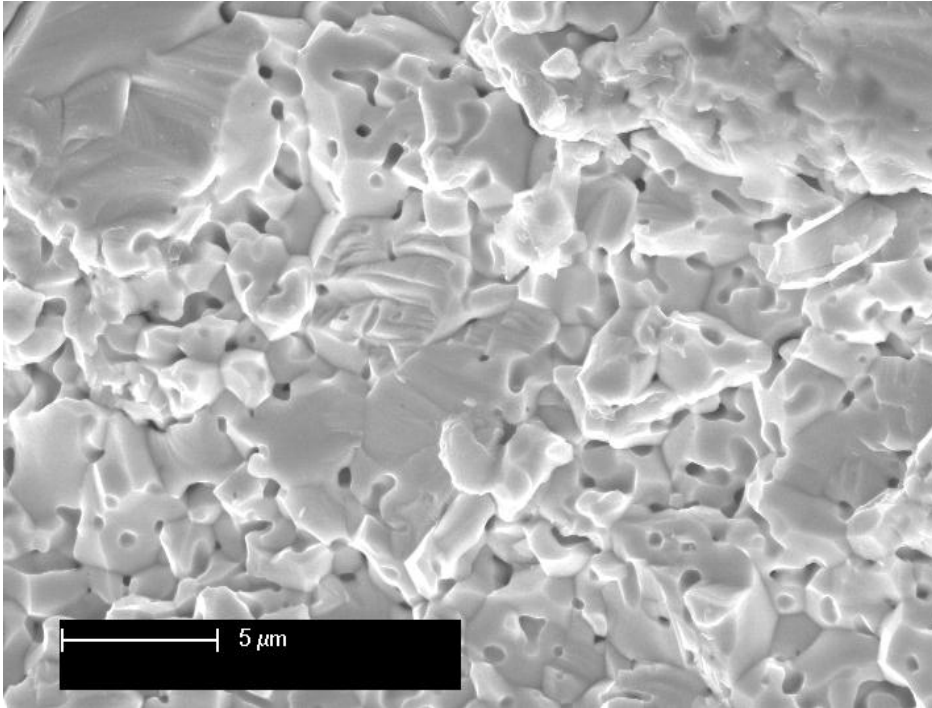


Figure 45. TaC specimen heated to 2300 C, with 30 MPa pressure, 20 minutes holding time, and 92% relative density. Significant grain growth is present compared to Figure 20.

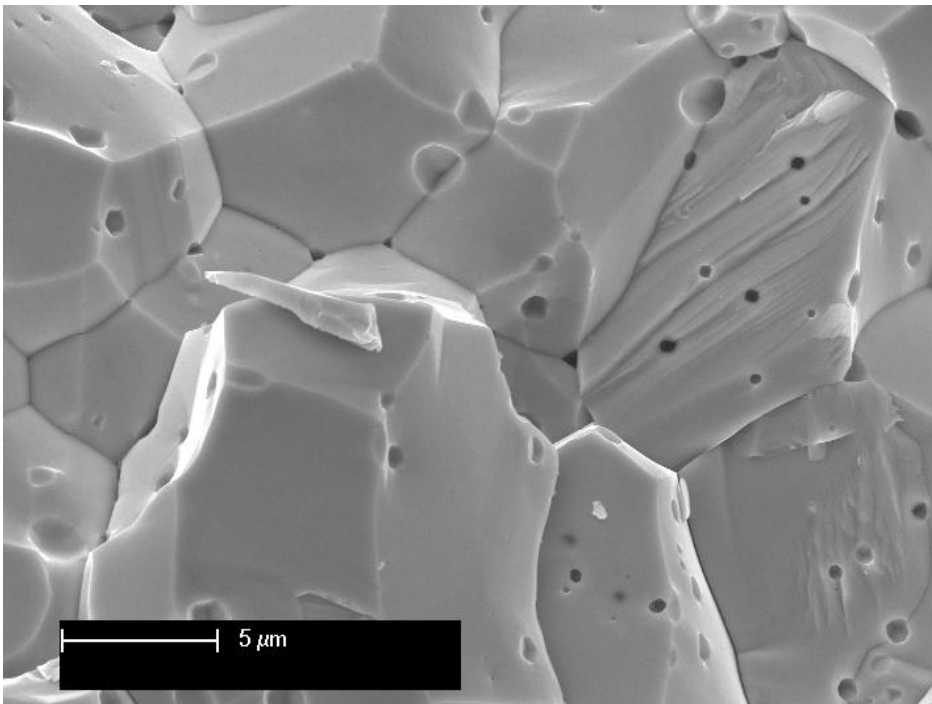


Figure 46. TaC specimen heated to 2400 C, with 75 MPa pressure, 10 minutes holding time, and 97% relative density. The significant grain growth and grain boundary porosity are evident.

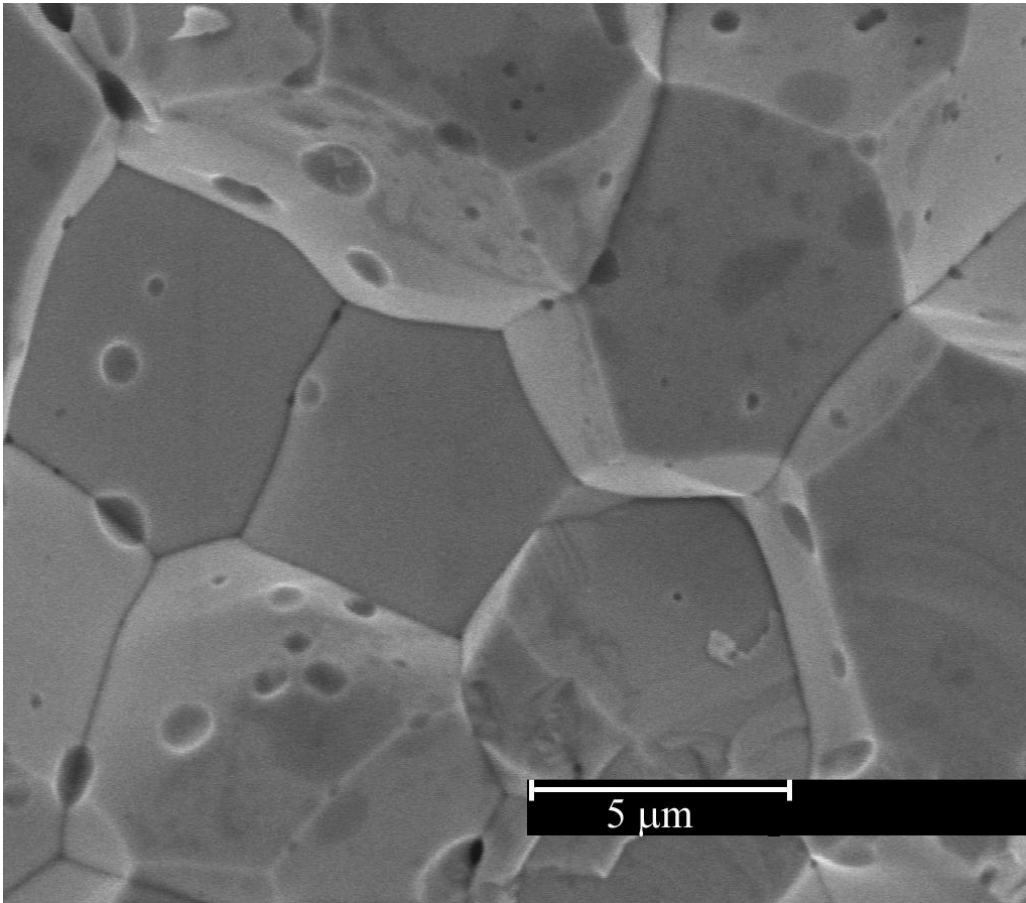


Figure 47. TaC-CNT composite specimen, heated to 2300 C, with 30 MPa pressure, 20 minutes holding time, and 96% relative density.

Table 12 shows a summary of the density, hardness, and tensile rupture strength, and other parameters, of the four TaC specimens and one TaC-CNT composite specimen (listed at the bottom).



Table 12. Density, hardness, grain size, and rupture strength data for five TaC specimens.

Temperature (°C)	Holding Time (min)	Relative Density (%)	Hardness (GPa)	Rupture Strength (MPa)	Average Grain Size
1900	5	68	NA <sup>2</sup>	NA <sup>2</sup>	330 nm
2300	5	83	11	315	3.45 $\mu\text{m}$
2300	20	92	11	336	4.25 $\mu\text{m}$
2400	10	97	11	372	9.0 $\mu\text{m}$
2300 <sup>3</sup>	20	96	11	550 <sup>3</sup>	3.81 $\mu\text{m}$

We can see from the table that the increased densification from the extended holding time at 2300 °C had an impact on the rupture strength. The measured values for rupture strength for TaC vary from 240 to 750 MPa, and our specimens fall in this range. The hardness was not affected by density, as is expected for Vickers' hardness testing. The grain size increased during sintering, with higher grain growth corresponding to longer holding time. This grain growth is similar to the results of Sommer et al.<sup>112</sup> and Zhang. et al.<sup>104</sup> for conventional sintering and hot pressing, respectively, using low pressure. At 2400 °C, with 75 MPa pressure, there is a perceptible competition between the impact on the grain growth of high pressure and of the higher sintering temperature (compared to Zhang et al.<sup>104</sup>). We can see from Figure 46, and the increased grain size, that the sintering temperature had apparently bigger impact on the grain growth. However, the small size of our TaC particles, with the average size calculated at 330 nm, is an additional reason for the rapid growth in grain size during sintering. These values

<sup>2</sup> Since the specimen sintered at 1900 C had very low structural integrity, hardness and strength measurements could not be conducted.

<sup>3</sup> This specimen is a composite made of .77% wt carbon nanotubes in a TaC matrix.

for the mechanical properties fit within the known values for densified TaC, and are the same as for TaC specimens produced through other consolidation methods.

For the composite CNT and TaC specimen, we note a significant increase in rupture strength (65%), but little change in grain growth. The grain growth diminished 10% compared to the same experiment without the addition of CNTs, but still showed a significant change from the initial particle size. This increase in strength is simply due to the reinforcement of the TaC matrix by the CNTs. We also note an increase in final density from 92% to 96% compared to the identical experiment without any nanotube addition.

### **5.1.3. Conclusions on the densification and grain growth in spark sintering of TaC**

The results obtained by spark sintering of a TaC powder are comparable to the outcomes of hot pressing under the same conditions, in terms of final density and mechanical properties. We have shown the applicability of the spark sintering process to the consolidation of difficult to deform materials, such as tantalum carbide. The advantage of SPS for the consolidation of TaC is the high heating rate, where specimens can be sintered in short periods of time and produce superior results as much longer processes (like HIP). A small increase in final density (4%) and a significant increase in strength can be achieved by adding a very small amount (.77% wt) of carbon nanotubes, with a shift of the densification curve downward and a decrease in final relative density. However, this form of carbon does not have the same grain growth reducing effect as

other additives, such as creating a simple non-stoichiometric TaC compound using graphite.

Chapter 5, in part, is a reprint of the material as it appears in *Scripta Materialia*:

E Khaleghi, YS Lin, MA Meyers, EA Olevsky, "Spark Plasma Sintering of Tantalum Carbide," *Scripta Materialia* 63, 577-80 (2010).

The dissertation author was the primary investigator and author of this paper.

## ***5.2. SPS of Fe-VC high strength steel***

In this section, we address the capability of using spark sintering to consolidate rapidly solidified powders, and investigate the relationship between grain growth and densification for these powders. We also investigate whether SPS improves the properties of the final specimen due to the retention of properties present in the specially produced powder.

The theory behind this section is that rapidly solidified powders are produced using a complex process to give unique properties to the powder, and during traditional processing and consolidation methods these properties are mostly lost. The main disadvantage of traditional techniques is the long holding times at high temperature to densify the materials. Because of the high heating rates and short holding times, SPS is a perfect candidate for the densification of these materials. The aim is to evaluate structural decomposition during sintering, the possibility to maintain high degrees of metastable conditions after full densification, and the effect on densification.

The material system chosen was iron-vanadium-carbide (Fe-V-C). The powders used were mixtures of iron, vanadium, and carbon, produced through gas atomization to

increase the solubility of vanadium carbide in iron, which would combine during consolidation to produce steel with vanadium carbide inclusions. This high strength steel would have improved corrosion resistance and mechanical properties.

We conducted a series of experiments to determine how to reach full density with the powders, and then investigated different heating patterns and mixtures of powders to determine the most advantageous for V-C formation and property enhancement. Thorough characterization was conducted (using SEM and TEM) to determine the presence of vanadium carbide, and hardness measurements were taken.

In the present work, the ability of SPS in preserving the large solid solubility extensions of carbon and vanadium in iron in RS powders after consolidation has been evaluated. Gas atomization of carbon steel powders was carried out by Osprey Metals LTD (Great Britain). The solubility of vanadium carbides in ferrite is very low, but large extensions of solid solubility can be obtained through gas atomization processing. Such an extension is lost during sintering at 900-1000 °C, because of the precipitation of incoherent, and coarse, vanadium carbides. In this work, low carbon (0.2 %C) and vanadium (0.5 %V) steels as well as high carbon (1.0 %C) and high vanadium (15 %V) steel powders have been combined and compacted via SPS processing, with the aim to evaluate structural decomposition during sintering and the possibility to maintain high degrees of metastable conditions after full densification. Such an occurrence is believed to be very useful, since a strong C/V-supersaturation of the ferrite matrix could be used to obtain a strong increase in mechanical properties by precipitation hardening of coherent vanadium carbides during tempering treatments.

### **5.2.1. Preliminary experimental work on Fe-V-C from Fe-0.5V powder**

The original powder ordered from OSPREY LTD (United Kingdom) was to be RS atomized powders with the following nominal composition: Balance Fe, 0.4-0.6% V, 0.1-0.3% C, 0.6% max Mn, 0.5% max Si.

Unfortunately, the real chemical composition was closer to: Bal Fe, 0.5% V, 0.6% max Mn, 0.5% max Si, 0.045% C, where the carbon content was much lower than required. Such an occurrence would strongly reduce the desired carbon supersaturation of the as-quenched steel powders and, therefore, of vanadium carbides during subsequent sintering thermal exposure. Under these circumstances, results obtained from these powders would not have the required characteristics. As-received powders were instead sintered by SPS in order to check possible processing difficulties, and prepare for future powders. Figure 48 shows the composition and particle structure of the as-received powder.

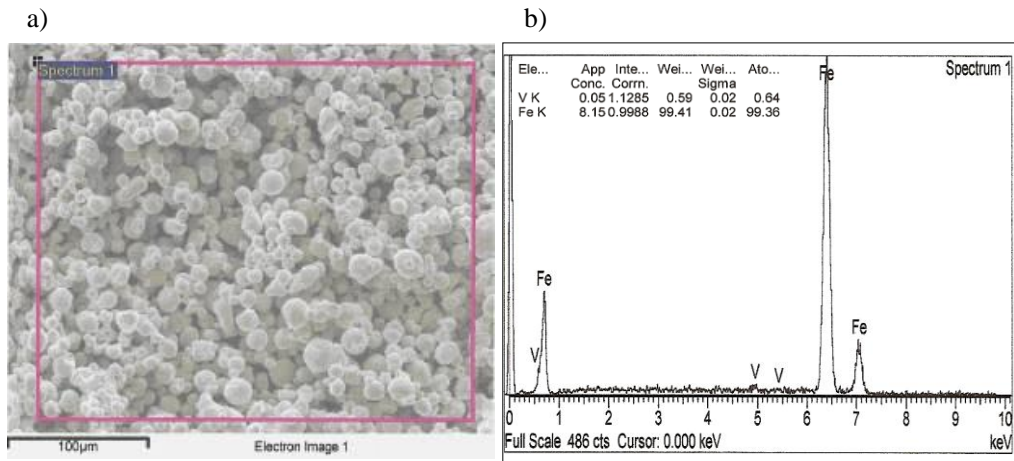


Figure 48. . Fe-0.5 V RS powders: a) SEM micrograph and b) EDS microanalysis from metallic powders.

We used 8 grams of Fe-V powder were sintered using the spark sintering process, in a standard 15 or 15.4 mm cylindrical die with two punches. Two sizes of Fe-V powders were used, one with average particle size less than 10 μm with  $d_{10} = 2.9 \mu\text{m}$ ,  $d_{50} = 5.4 \mu\text{m}$ , and  $d_{90} = 9.4 \mu\text{m}$ , and another with average particle size less than 22 μm, with  $n d_{10} = 4.8 \mu\text{m}$ ,  $d_{50} = 11.8 \mu\text{m}$ , and  $d_{90} = 21.5 \mu\text{m}$ . The graphite die was used both with carbon paper applied (.2 mm thick) in the 15.4 mm die, and without carbon paper in the 15 mm die, using a boron nitride spray coating, during the experiments. The boron nitride coating was applied during several experiments due to the noted diffusion of carbon from the die into the specimen during the sintering process during analysis.

There were two differently sized powders (D90 -10  $\mu\text{m}$  and D90 -22  $\mu\text{m}$ ), and they were sintered with a heating rate 100  $^{\circ}\text{C}$  /min to 700  $^{\circ}\text{C}$ , held for 15 min, with a pressure of 75 MPa applied..

The temperature profile was selected based on several experiments where we attempted to reach 100% density with the powder, however full density was not achieved. The temperature profile that reached the highest density for the original Fe-V powder proved unable to reach full density with any of the mixed powders, so variations in holding temperature, heating rate, and applied pressure were used to reach full density with these powders.

#### **5.2.2. Preliminary results on Fe-V-C from Fe-0.5V powder**

Table 13 reports the specimens produced. Some of the specimens were isolated from the graphite die by boron nitride spray, to prevent carbon infiltration. One specimen was not wrapped in graphite paper, also to see the effects on carbon infiltration.

Table 13. Experimental Parameters for Individual Fe-VC Samples

Sample ID	D90 Particle Size ( $\mu\text{m}$ )	BN Isolation	Graphite Paper	Heat Treatment	Ball Milling with Graphite	Final Density ( $\text{g}/\text{cm}^3$ )
I	10	No	Yes	No	No	7.4 (94%)
II	10	No	Yes	Yes	No	7.4 (94%)
III	22	No	Yes	No	No	7.7 (98%)
IV	22	No	Yes	Yes	No	7.7 (98%)
V	10	Yes	No	No	Yes	6.7 (84%)

We obtained the following results:

- 1 – there was no difficulty in sintering, and densifying, small, conductive steel powders;
- 2 – it was possible to obtain full densification at temperature below 800 °C using relatively short holding times;
- 3 – The best densification was obtained using D90 -22 $\mu\text{m}$  sized powders with the addition of graphite paper to line the die (98% theoretical density);
- 4 – the central regions of the cylindrical specimens are denser than regions close to the edge, see Figure 49 and Figure 50;
- 5 – there was diffusion of carbon into the specimens from the graphite paper lining the die, likely due to the high temperature, see Figure 51.



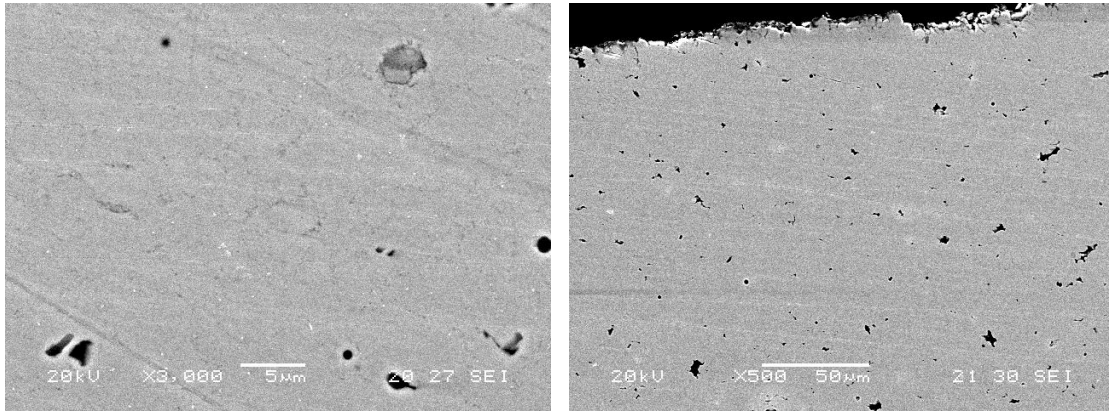


Figure 49. Sample N. 4 –  $D < 22$  mm, SPS at 700 °C, 15min, 75MPa: (left) center and (right) edge regions.

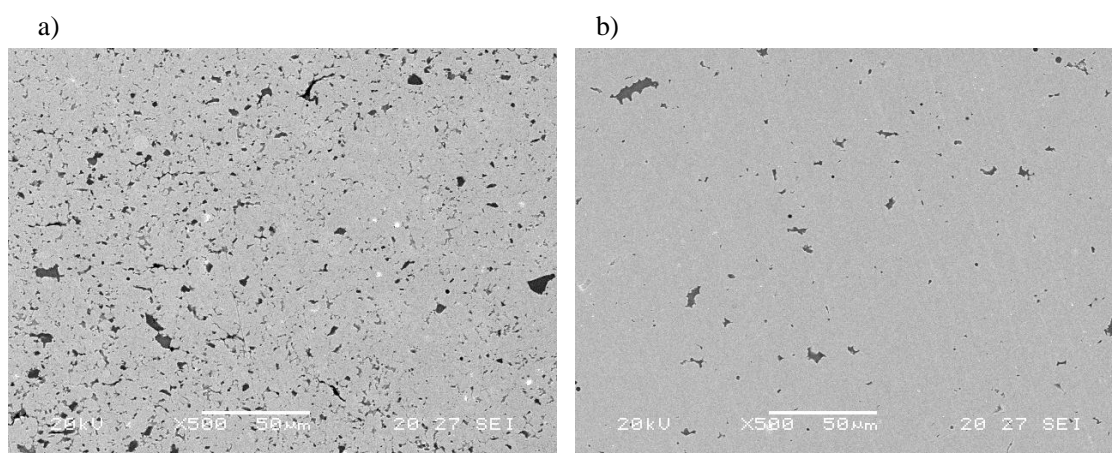


Figure 50. Sample N. 2,  $D < 10$  mm, 700 °C, 75MPa: a) external and b) central regions.

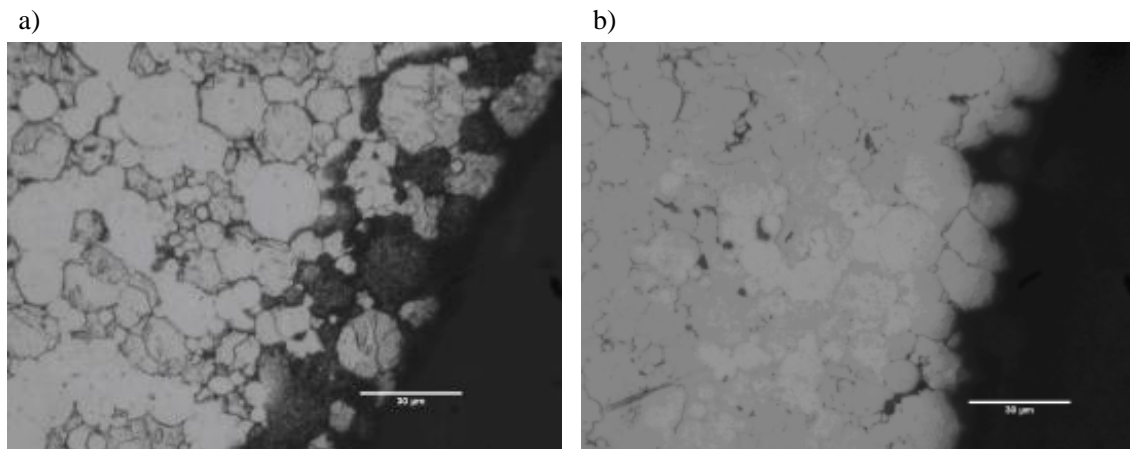


Figure 51. SPS specimens prepared using a die lined with: a) carbon paper, b) BN.

6 – there was no apparent decomposition of the supersaturated solid solution during sintering, see Figure 52. EDX microanalysis on densified specimens were the same as the nominal composition of the alloy – see Figure 53. Chemical etching did not indicate the presence of small precipitates within the ferrite matrix, see Figure 54;

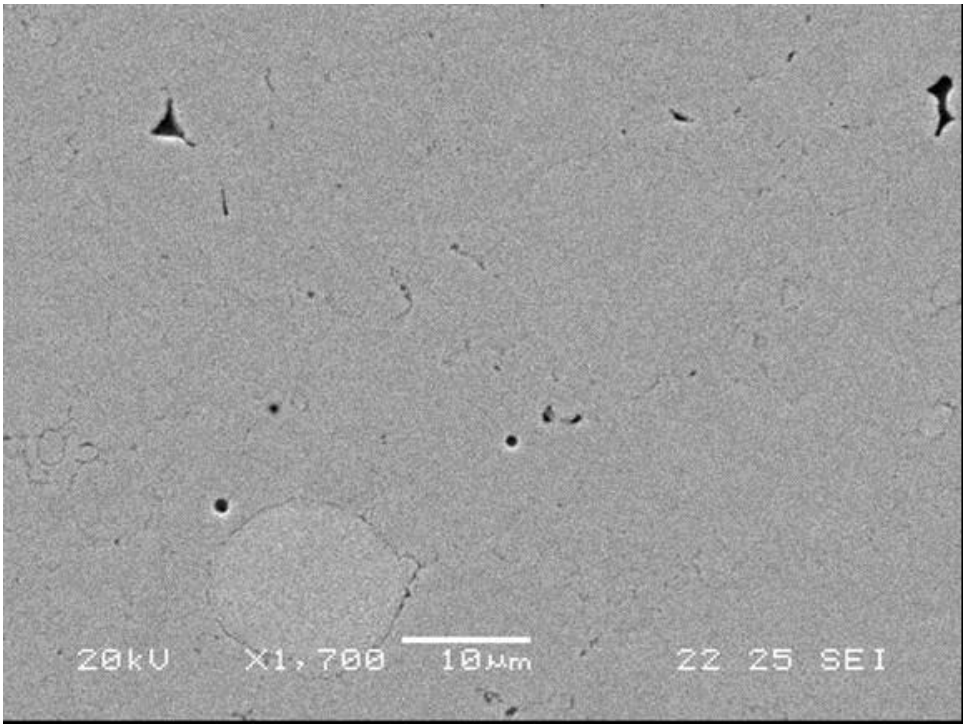


Figure 52. Sample N.4: 22μm (not etched). A particle that did not incorporate during sintering is evident in the lower center of the image.

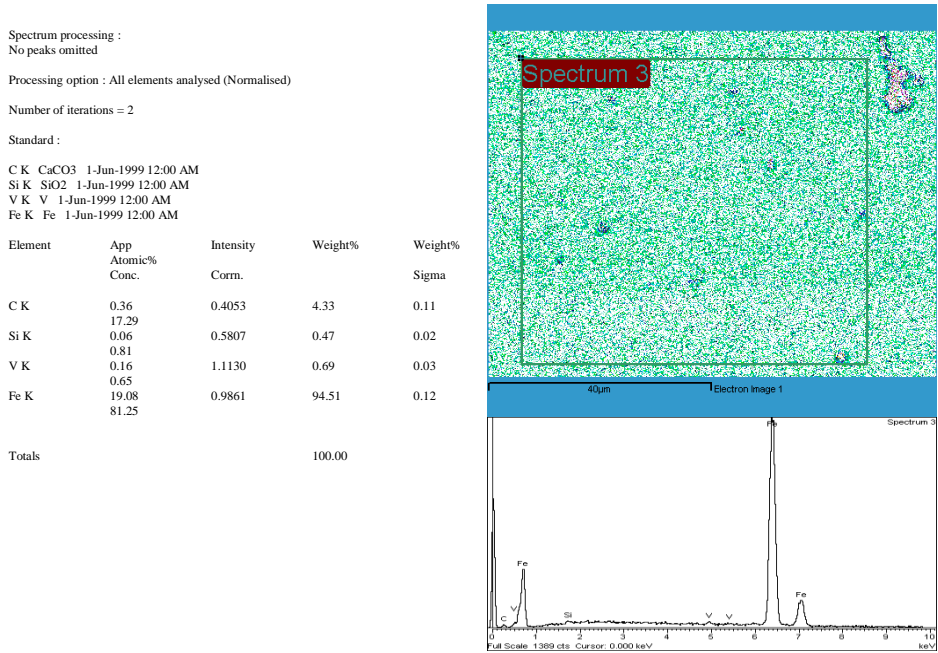


Figure 53. EDX-microanalysis from SPS sintered samples.

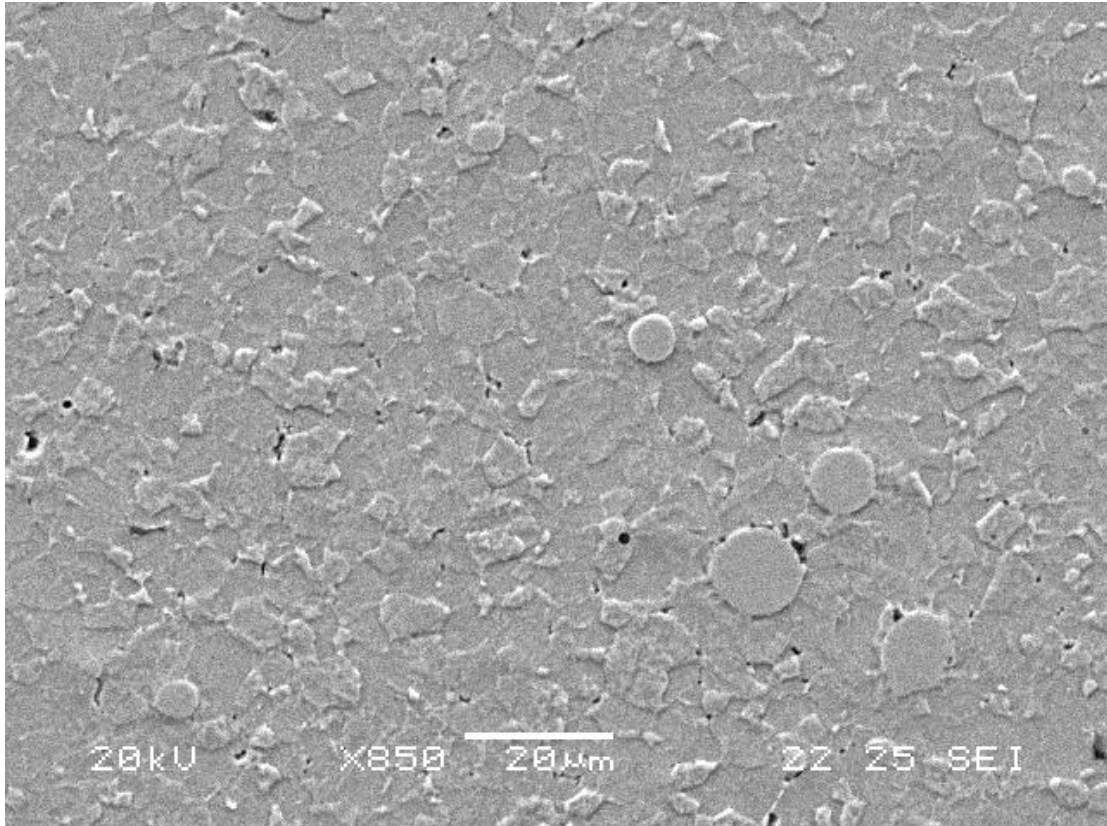


Figure 54. Sample N.4: 22μm (etched).

7 – The only second phase particles present were Al or Si rich inclusions, and they were few in number, see Figure 55. Some spherical grains exhibiting no response to the etching solution (NITAL 2%) were observed, see Figure 56. EDX microanalysis showed evidence for the presence of austenitic spherulites embedded within the ferrite matrix, see Figure 57.

Element	App Atomic% Conc.	Intensity Corrn.	Weight%	Weight%
				Sigma
O K	3.93	1.1558	15.74	0.27
	36.65			
Al K	0.51	0.5056	4.71	0.04
	6.50			
Si K	0.70	0.6050	5.33	0.04
	7.07			
V K	0.27	1.0288	1.20	0.03
	0.88			
Cr K	0.63	1.1122	2.63	0.04
	1.89			
Mn K	0.75	0.9261	3.77	0.06
	2.55			
Fe K	13.55	0.9422	66.62	0.23
	44.45			
Totals			100.00	

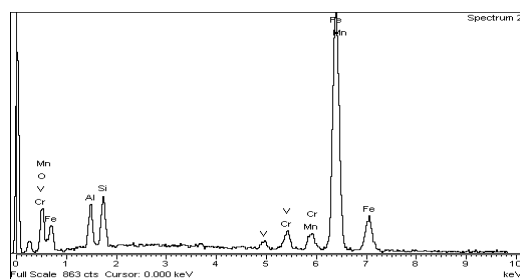
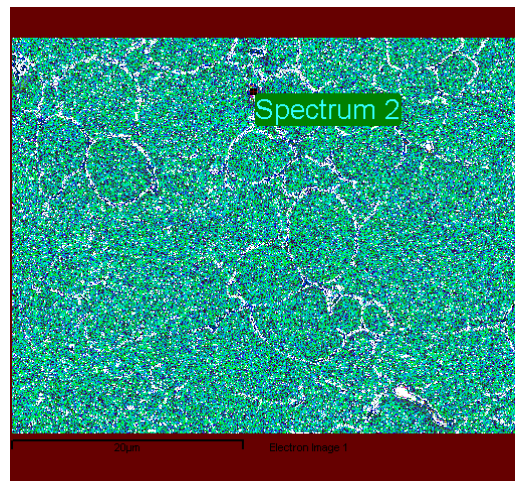


Figure 55. EDX-microanalysis from SPS sintered samples.

Element	App Atomic% Conc.	Intensity	Weight%	Weight%
		Corm.		Sigma
C K	0.34	0.3951	4.29	0.11
Si K	16.89	0.5903	1.00	0.02
S K	0.12	0.8146	0.81	0.02
Cr K	1.68	3.75	17.11	0.06
Mn K	0.13	15.56	1.82	0.05
Fe K	1.19	0.9696	65.79	0.12
Ni K	3.75	12.47	9.19	0.08
	15.56	55.71		
	0.35	1.59		
	1.56	7.40		
Totals			100.00	

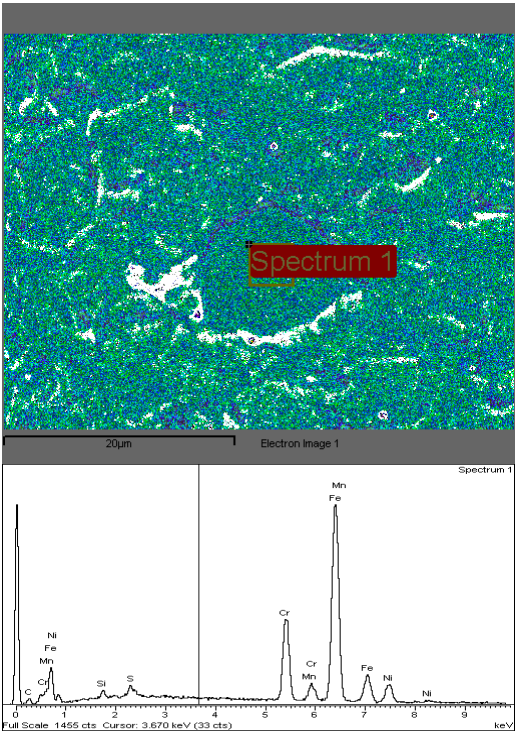


Figure 56. EDX-microanalysis from SPS sintered samples. Stainless steel inclusion indicated.



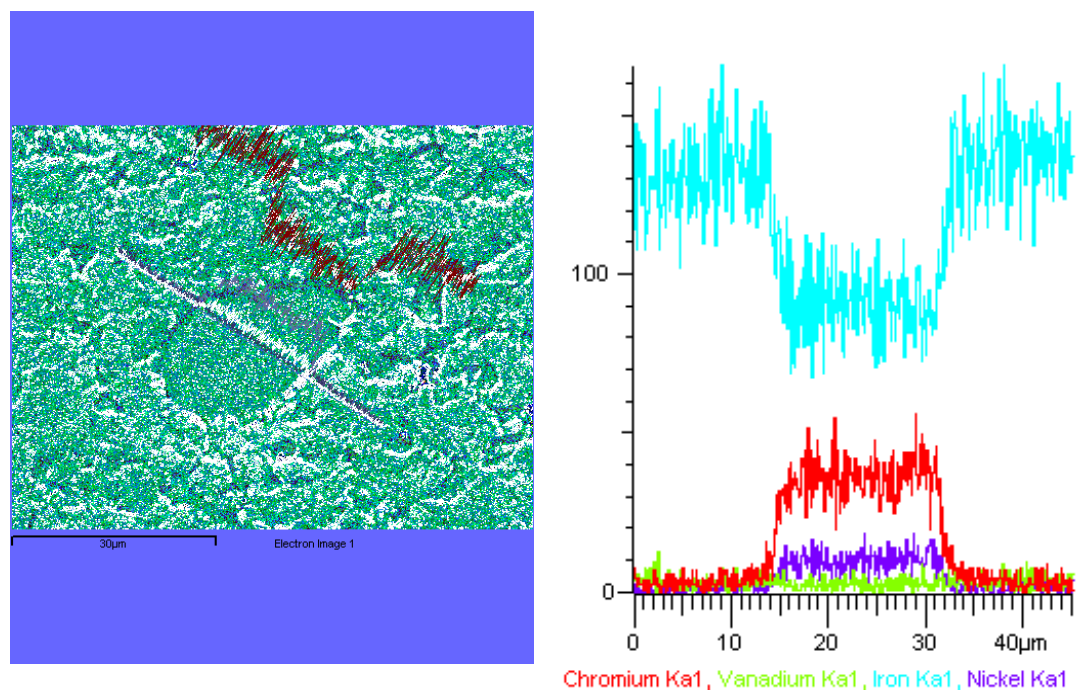


Figure 57. EDX-microanalysis from SPS sintered samples. Stainless steel inclusion characterized.

Vicker's hardness tests were performed to characterize some mechanical properties of the sintered samples. Also, thermal treatments at 550 °C for 1 h were conducted on some samples to highlight the hardening effects induced by the retention of solute (C/V) supersaturation. Figure 58 illustrates where the hardness tests were conducted on the transverse section of the cylindrical samples.



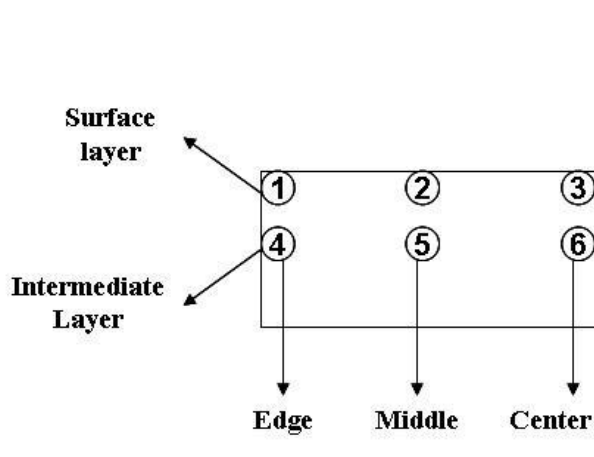


Figure 58. Hardness test points (quarter of cross sectional area)

As shown in Table 14, Table 15, and in Figure 59, Figure 60, Figure 61, the as-sintered steel exhibits a relatively low hardness ranging from 150 to 180 HV, and this value is not strongly affected by thermal treatments at 550 ° C. However, the reason for such low hardness values, and for a rather low effect of thermal treatments, could have been the wrong composition of the alloy (very low carbon content). Microhardness measurements (HV 0.05) carried out on samples with a graphite-lined sintering die (causing diffusion of carbon into the powder at the interface) showed that carbon enrichment of the ferritic matrix gave rise to strong hardening effects – Figure 62 and Figure 63 - possibly because of the further precipitation of V-carbides within the matrix.

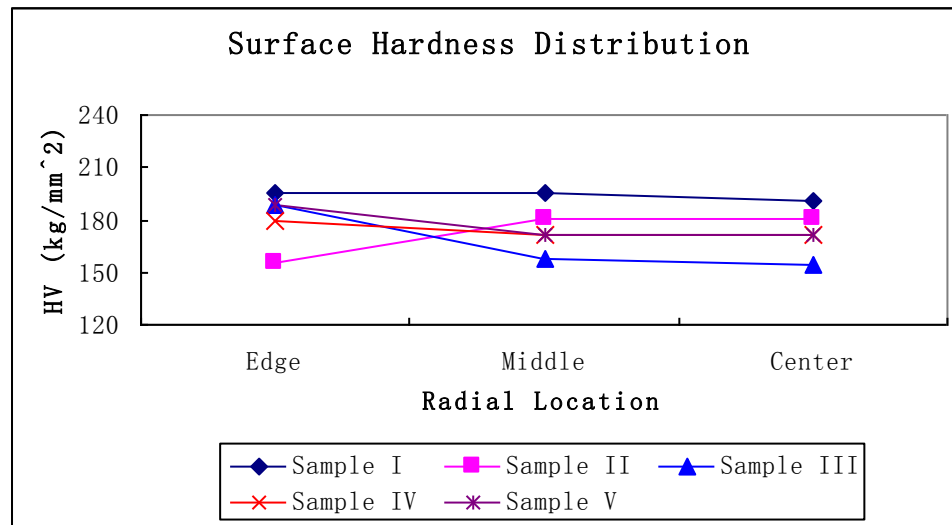
Table 14. Hardness test spot ID and position description for Fe-VC specimens

Surface Layer		Intermediate Layer	
Test Spot ID	Radial Position	Test Spot ID	Radial Position
1	Edge	4	Edge
2	Middle	5	Middle
3	Center	6	Center

Table 15. Hardness value for five Fe-VC specimens

Sample ID	Surface Layer			Intermediate Layer			Average HV (kg/mm <sup>2</sup> )
	Edge	Middle	Center	Edge	Middle	Center	
	SP1	SP2	SP3	SP4	SP5	SP6	
I	195	196	191	184	145	172	181
II	156	181	181	118	169	122	155
III	189	158	154	191	158	158	168
IV	179	172	172	176	150	152	167
V	189	172	172	143	174	172	170

(a)



(b)

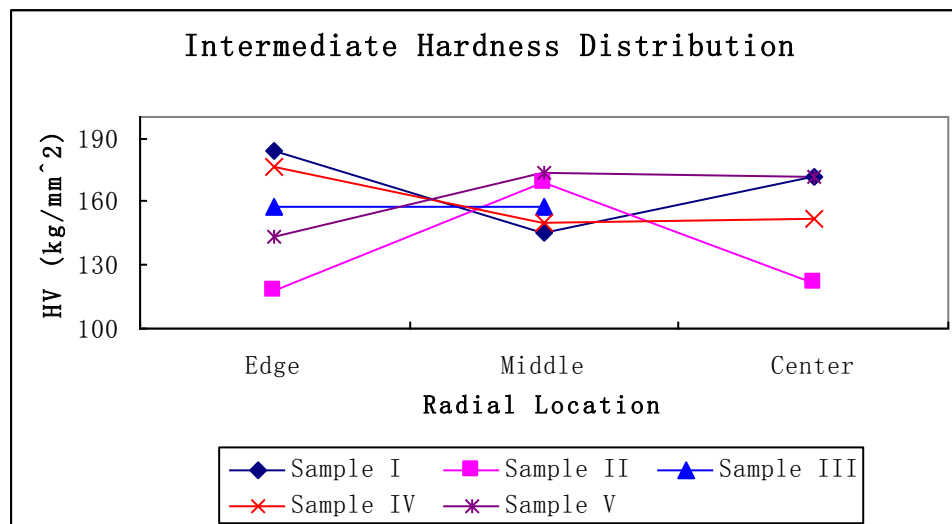
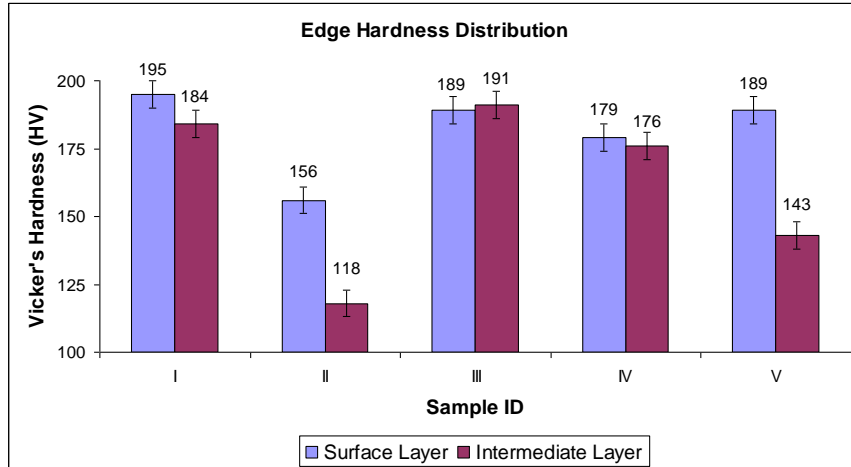
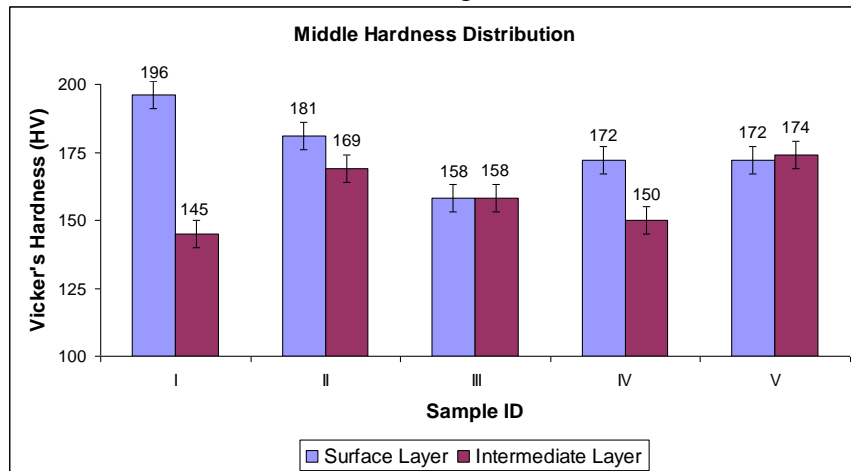


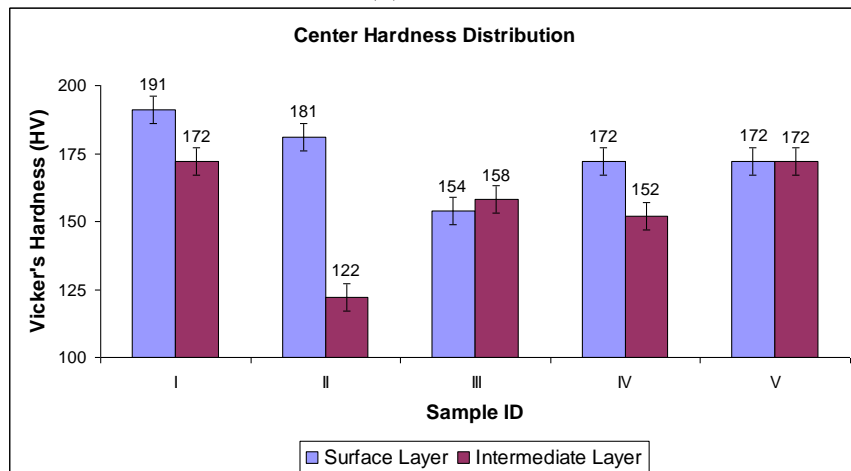
Figure 59. . Hardness distribution along different radial locations - (a) Surface layer, (b) Intermediate layer.



(a) Edge



(b) Middle



(c) Center

Figure 60. Hardness distribution along different axial layers - (a) Edge, (b) Middle, (c) Center.

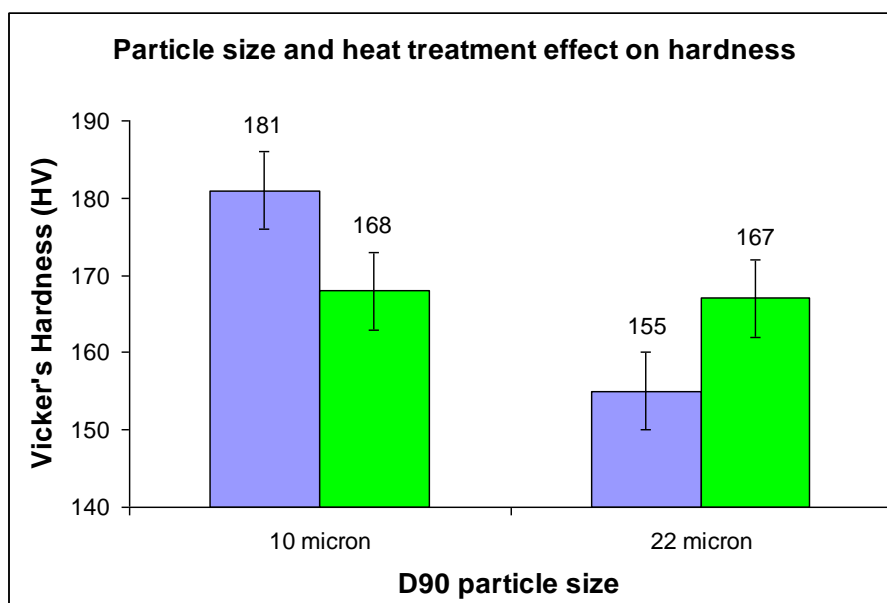


Figure 61. Particle size and heat treatment effects on hardness.

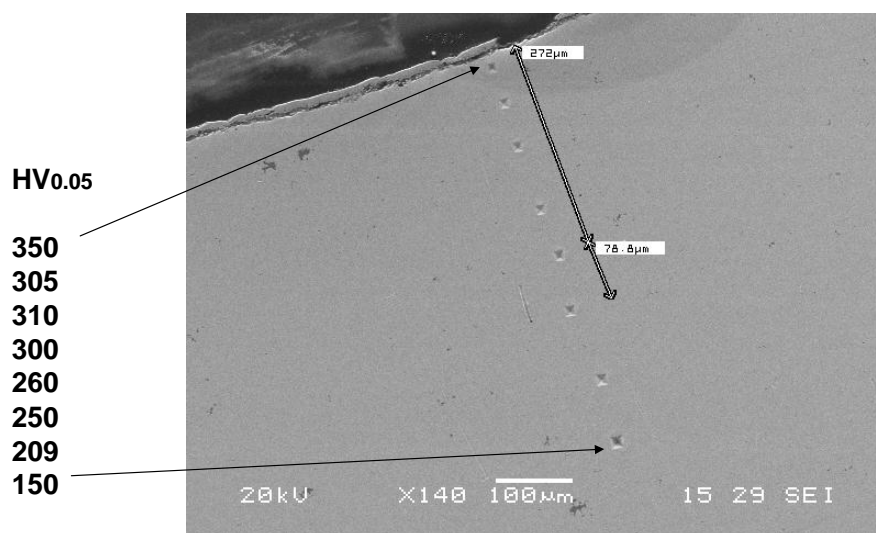


Figure 62. Specimen from 22μm powder. Carbon paper coated die. Effect of carbon diffusion is evident in the increase in hardness value from edge to center.

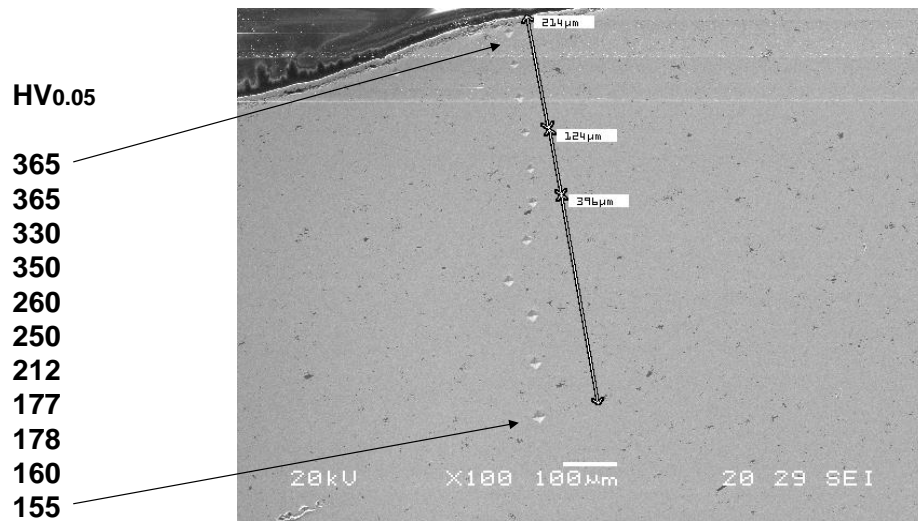
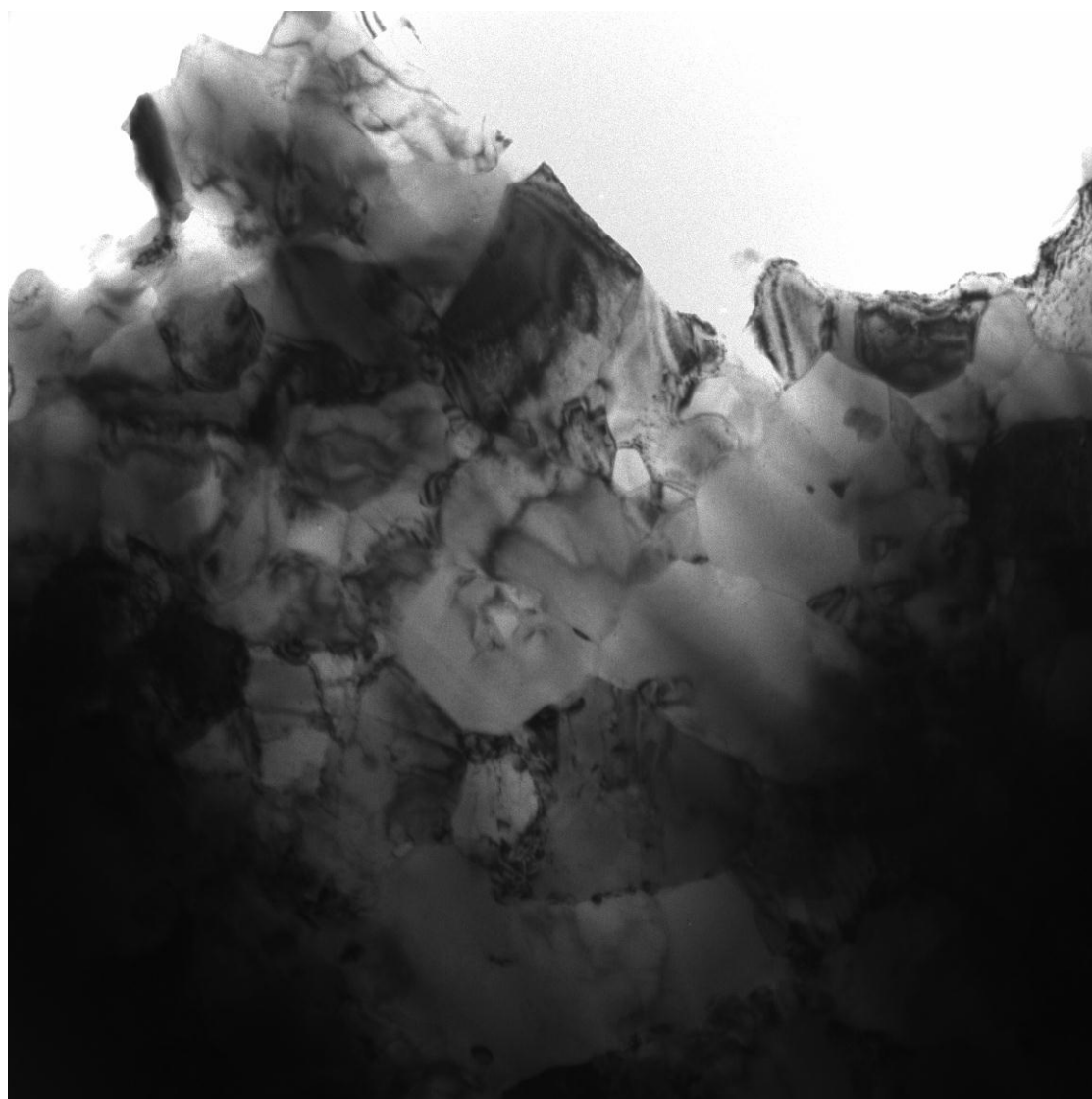


Figure 63. Specimen from 10 μm powder. Carbon paper coated die. Effect of carbon diffusion is again evident from the increase in hardness from edge to center.

In order to better understand the microstructural features of this first batch of RS powders, TEM analysis was conducted. Thin foils, transparent to electrons, have been prepared by mechanical thinning, and final perforation was conducted using ion milling. Sample number 4 was considered in as-sintered conditions as well as after thermal treatment of 1 hour at 600 °C in a vacuum furnace.

Figure 64 shows some microstructural features of as-sintered Fe-0.5V powders. The grain size was strongly refined, and was below 1 μm in some regions. Within the ferrite grains, no decomposition effect was apparent, see Figure 65 and Figure 66. In a few regions, the presence of second phase particles was observed along grain boundary regions, see Figure 67.



rs59.tif  
Cal: 0.00137 um/pix  
TEM Mode: Imaging

500 nm  
Direct Mag: 10000x

Figure 64. TEM micrograph showing microstructural features of as-sintered SPS Fe-0.5V RS powders.

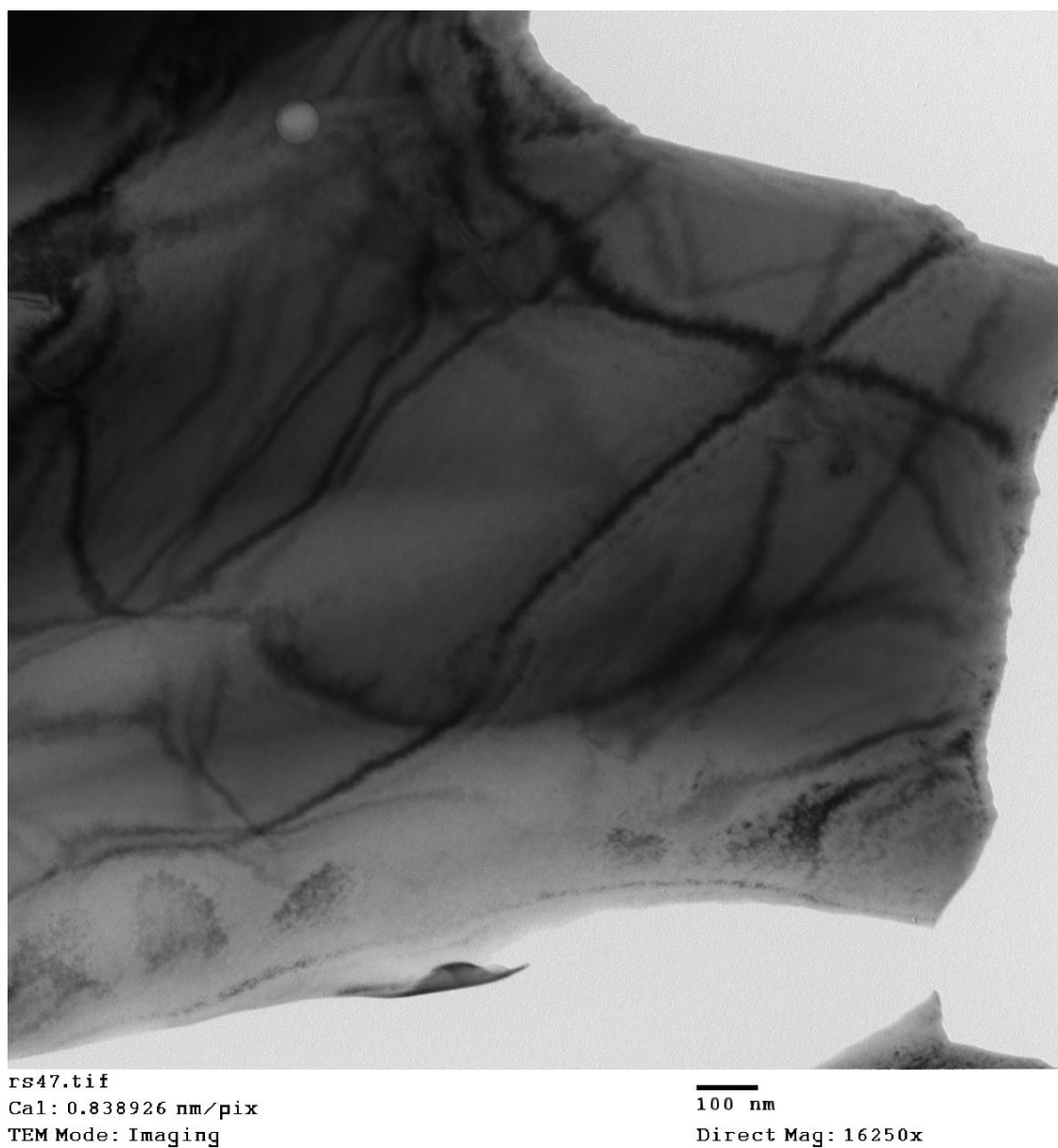


Figure 65. TEM micrograph showing microstructural features of as-sintered SPS Fe-0.5V RS powders.

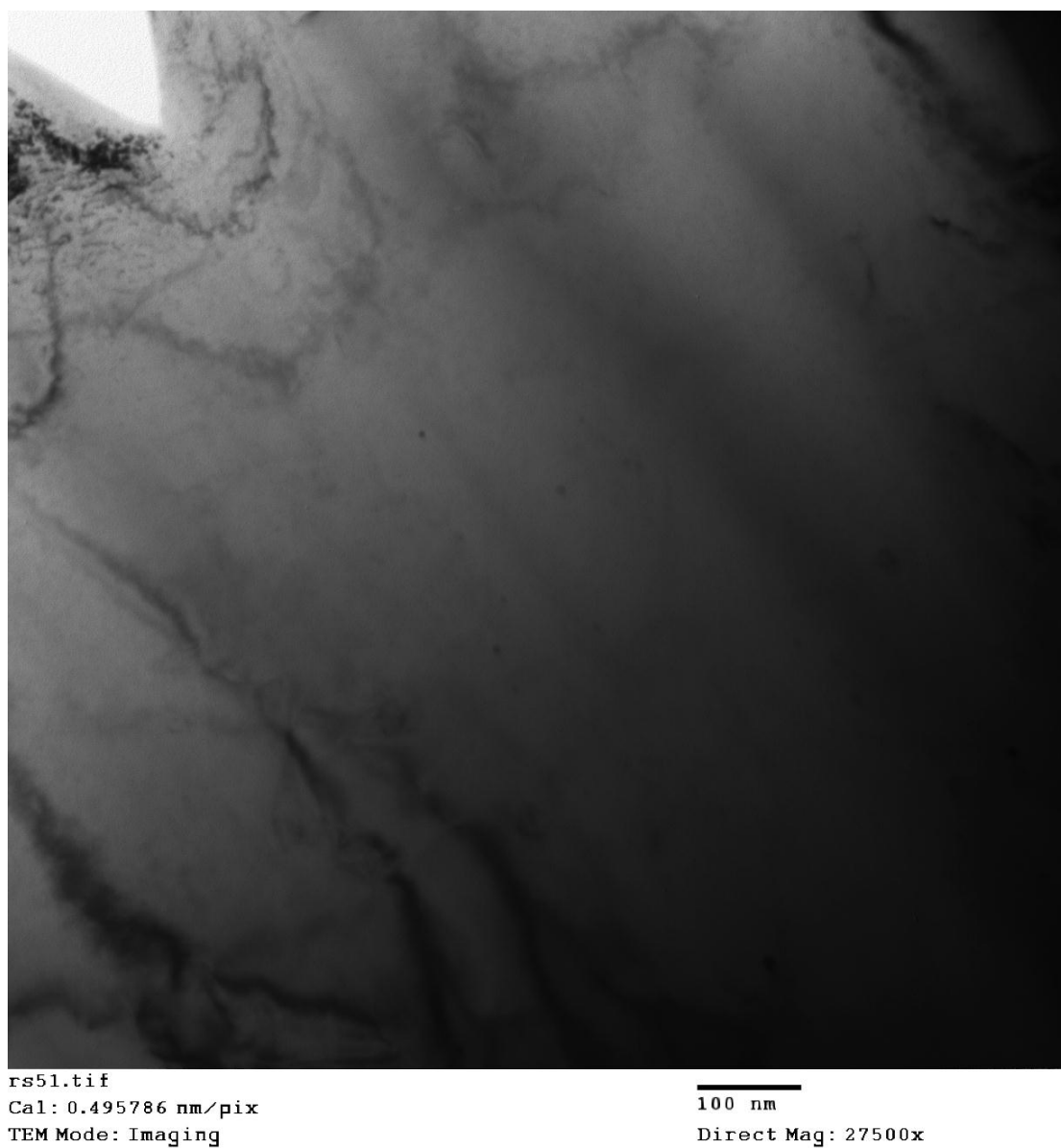


Figure 66. TEM micrograph showing microstructural features of as-sintered SPS Fe-0.5V RS powders.



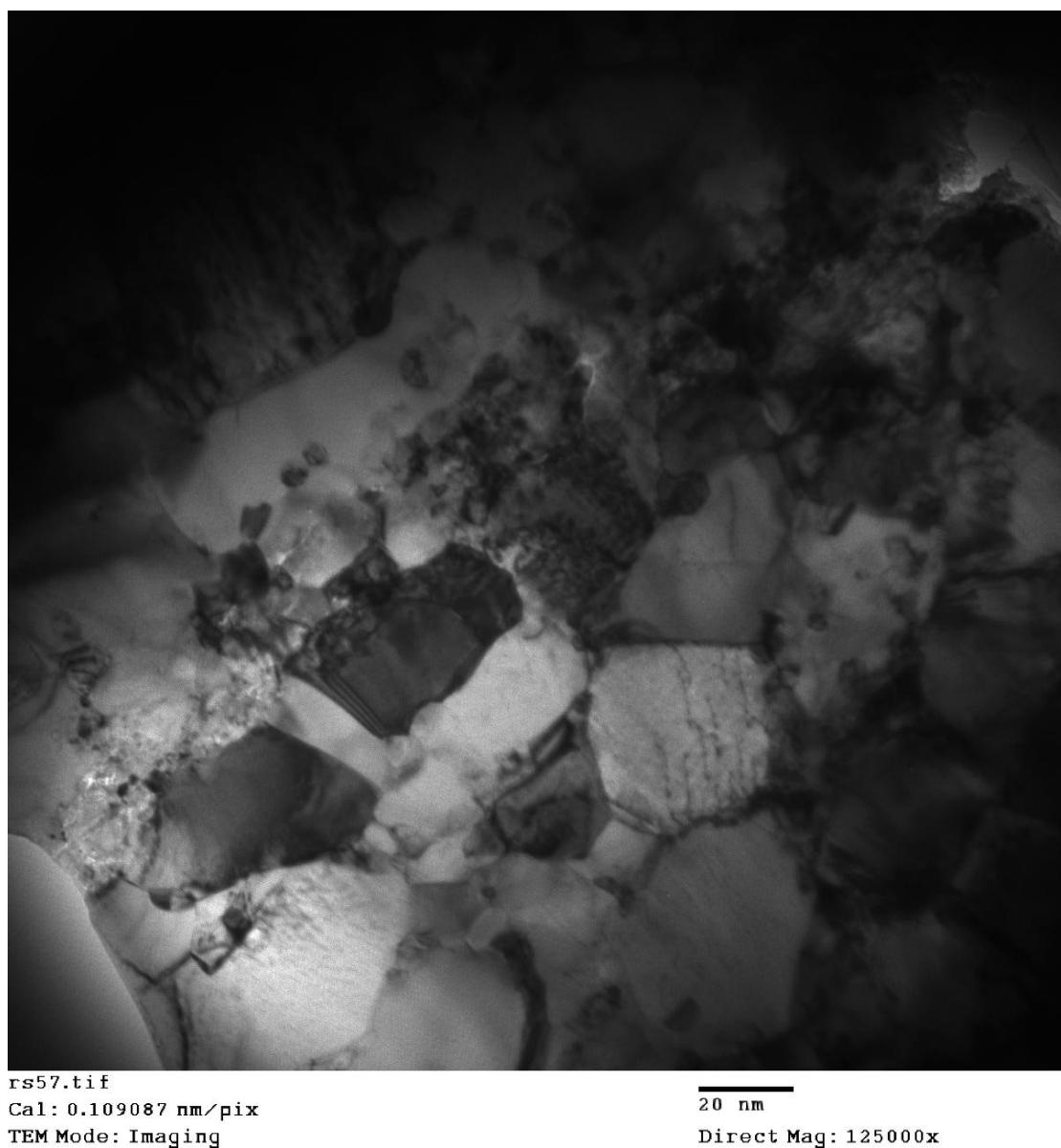


Figure 67. TEM micrograph showing microstructural features of as-sintered SPS Fe-0.5V RS powders.

From these preliminary results, it appears evident that the thermal exposure of the RS materials was weak enough to avoid structural decomposition and, presumably, the ferrite matrix remained to large extent supersaturated in vanadium and carbon.

After thermal exposure at 600 °C, a significant precipitation of extremely small sized vanadium-rich carbides took place. As shown in Figure 68 and Figure 69, the size

of hardening carbides was limited to a very few nanometers ( $< 5$  nm) and they are barely visible in the figures. Figure 70 is the indexed diffraction pattern from the  $[110]$  zone axis of cubic  $\alpha$ -ferrite, with evidence for extra spots arising from the presence of small vanadium carbides. The precipitation of hardening particles was non-homogeneous within the material, possibly due to different initial carbon content among the powders. The low amount of carbon in the steel may have limited the hardening effect in the first alloy.

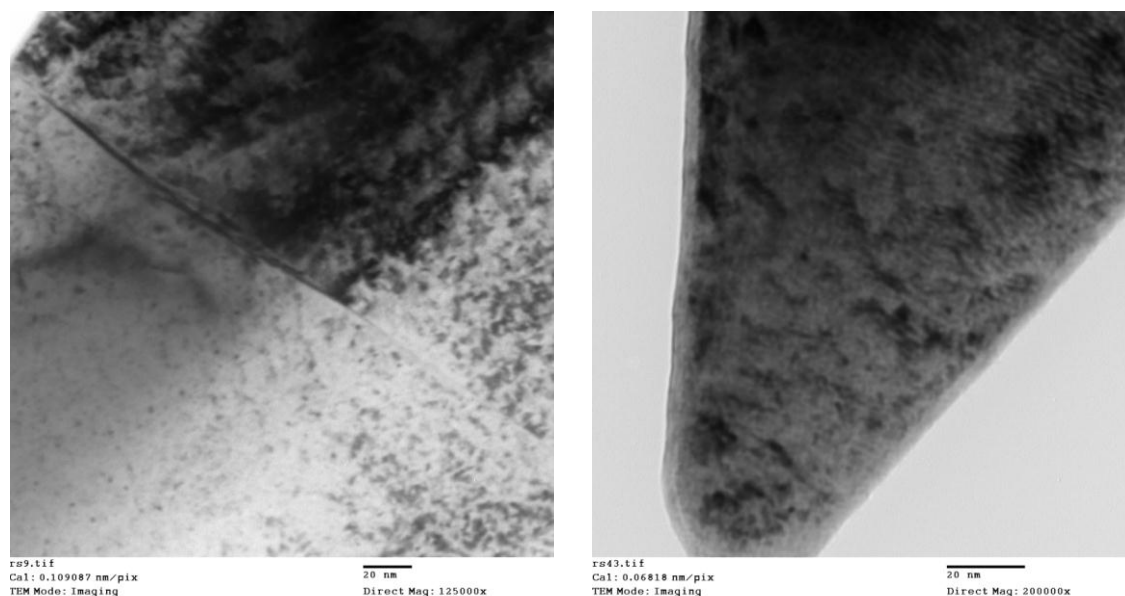


Figure 68. TEM micrograph showing microstructural features of sintered Fe-0.5V powders, after heat treatment at 600 °C for 1 hour.

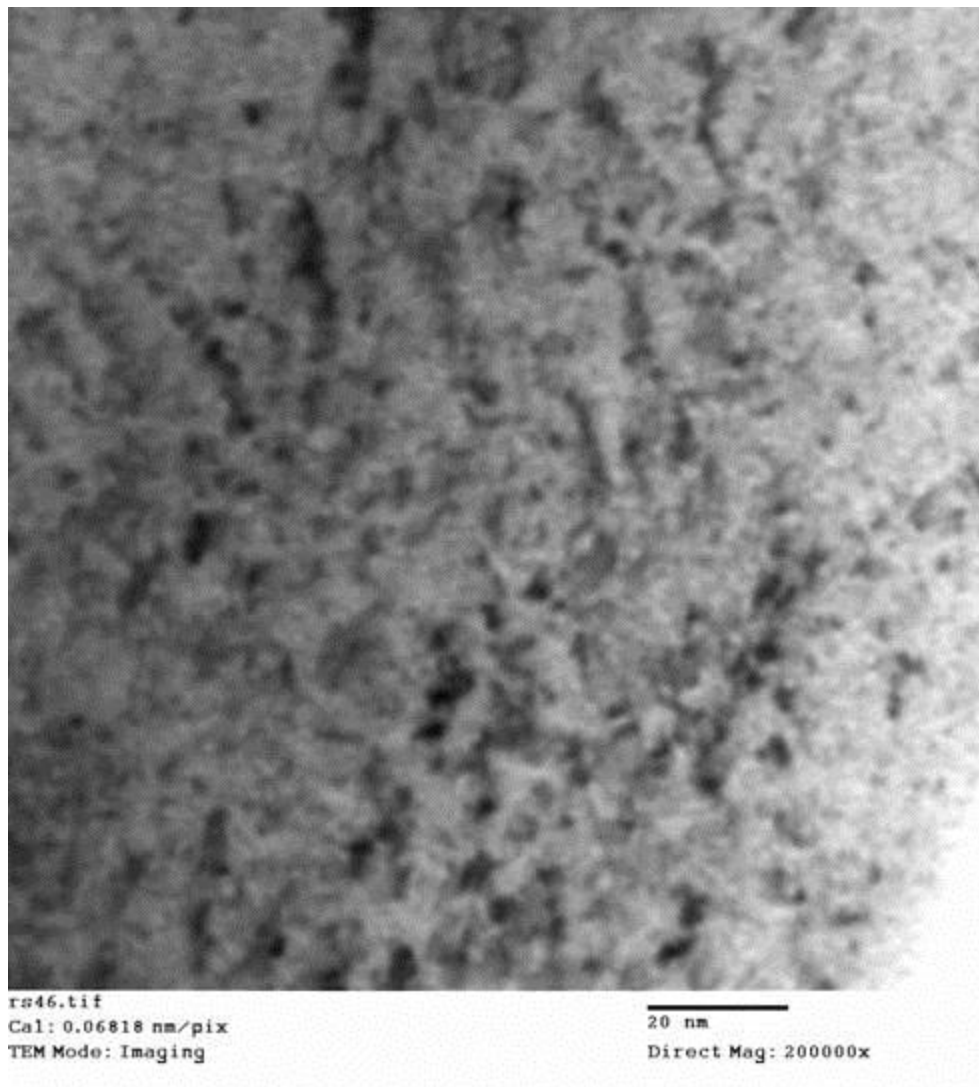


Figure 69. TEM micrograph showing precipitation of nanosized ( $< 5$  nm), coherent VC particles in the ferritic matrix, after SPS and heat treatment at 600 °C for 1 hour.

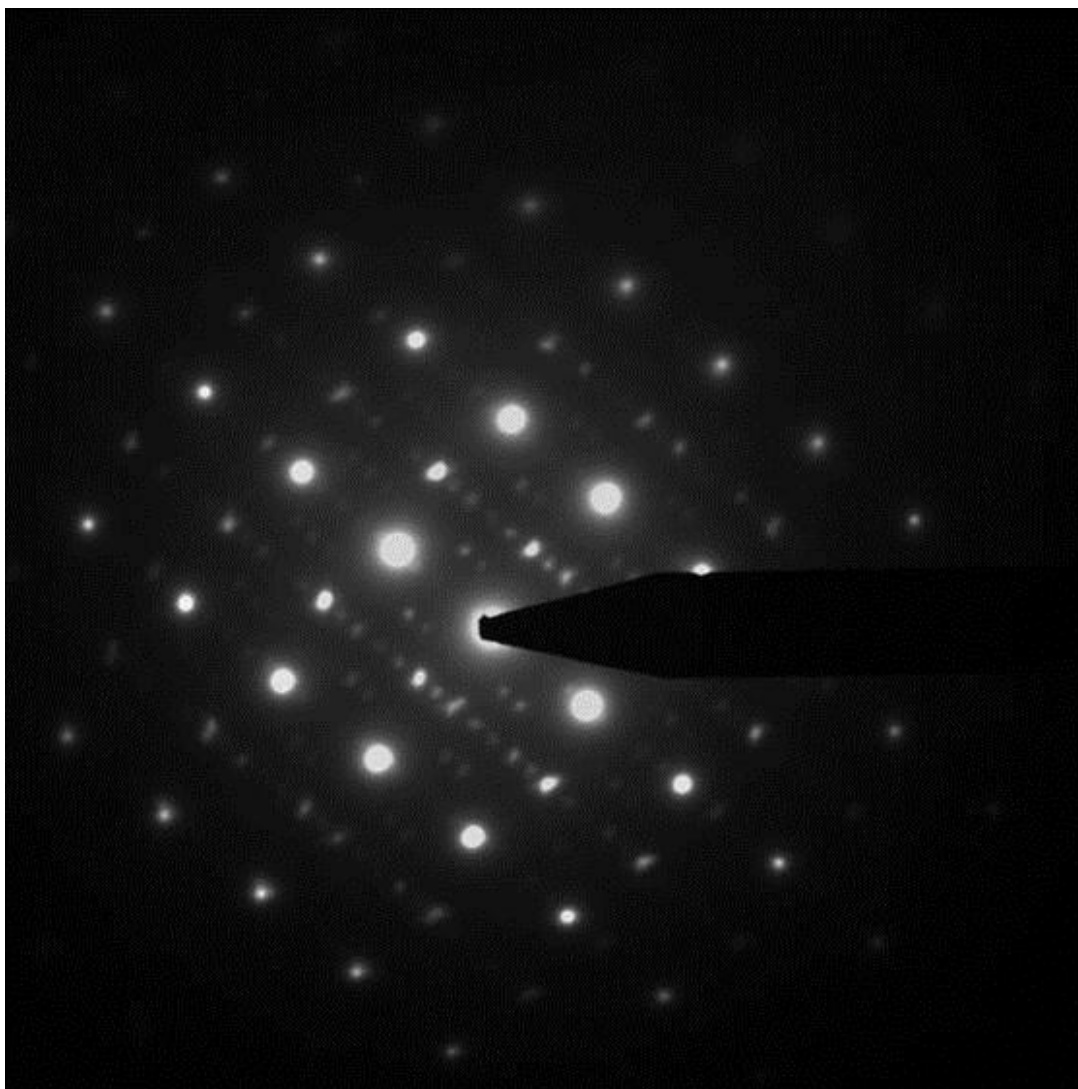


Figure 70. Selected Area Diffraction Pattern (SADP) with B close to  $[110]$   $\alpha$ -Fe with evidence of extra-spots from  $V_4C_3$  and surface  $Fe_3O_4$ .

### 5.2.3. Experimental work on Fe-15V and Fe-0.5V/Fe-15V mixed powders

After this first batch of RS powders, a second batch of RS Fe-V-C powders was provisioned by OPSREY LTD. The first powder, named Fe-0.5V, has composition 0.4-0.6% V, 0.1-0.3% C, 0.6% max Mn, 0.5% max Si, and the balance Fe. The size distribution of the Fe-0.5V particles was 0-10% between 22 and 500  $\mu m$ , 90-100%

between 10 and 22  $\mu\text{m}$ , and 0-10% between 0 and 10  $\mu\text{m}$ . The second powder, named Fe-15V, has composition 14-16% V, 0.95-1.05% C, 0.6% max Mn, 0.5% max Si, and the balance Fe. The size distribution of the Fe-15V particles was the same as for the Fe-0.5V powder. The main difference between the Fe-0.5V and the Fe-15V powders is the significantly higher vanadium content in the Fe-15V powder (15% vs. 0.5%) and the higher carbon content in the Fe-15V powder (1.0% vs. 0.2%). Grain size analysis was conducted (in the SEM) to calculate the average particle size, given the distribution.

XRD spectra was obtained from Fe-0.5V and Fe-15V RS mixed powders, in order to check if rapidly solidification was effective in avoiding solute segregation and formation of significant amounts of secondary phases. Figure 71 shows the morphology and chemical composition of Fe-15V powders.

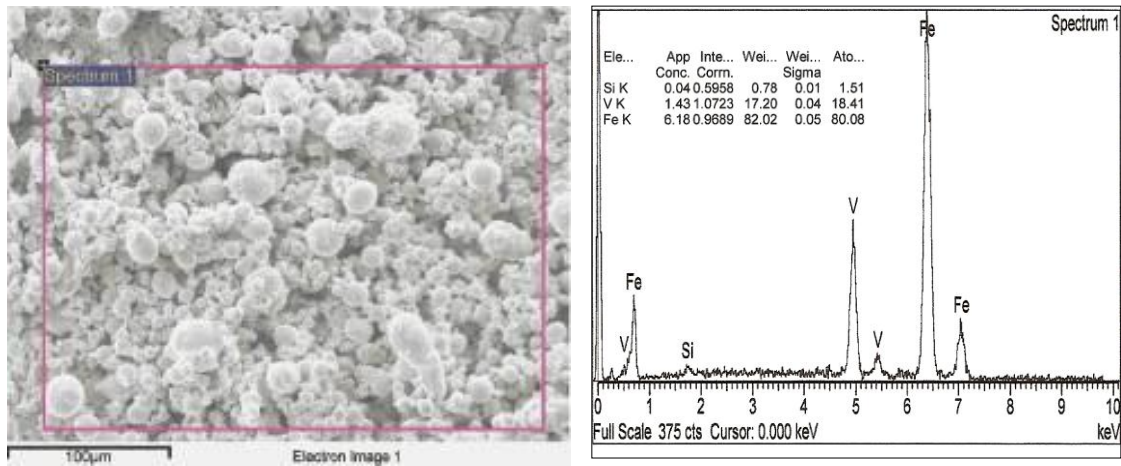


Figure 71. Fe-15V RS powders: left) SEM micrograph and right) EDS microanalysis from metallic powders

Figure 72 and Figure 73 show the XRD spectra from these powders. Both powders only show the presence of x-ray peaks from the cubic  $\alpha$ -Fe phase. With high carbon (about 1% C) and vanadium (about 15% V) content, rapid solidification should be able to minimize secondary phase precipitation during solidification and strongly extend solute supersaturation at room temperature (similar to the previous powders).

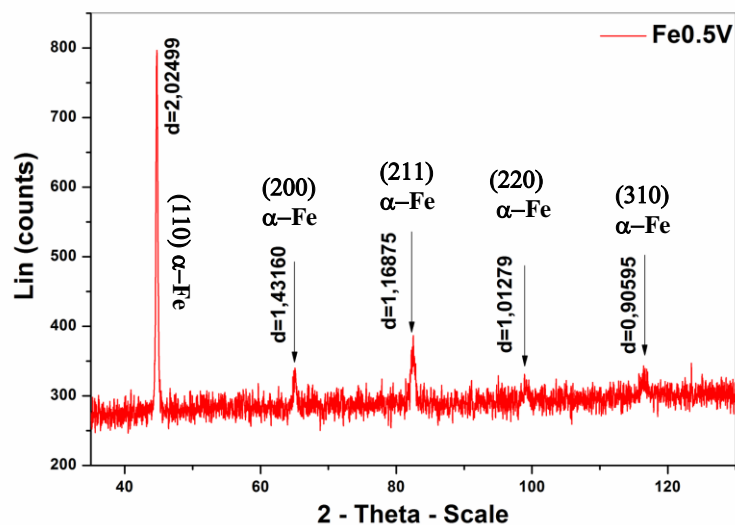


Figure 72. XRD spectrum from Fe-0.5V powders.

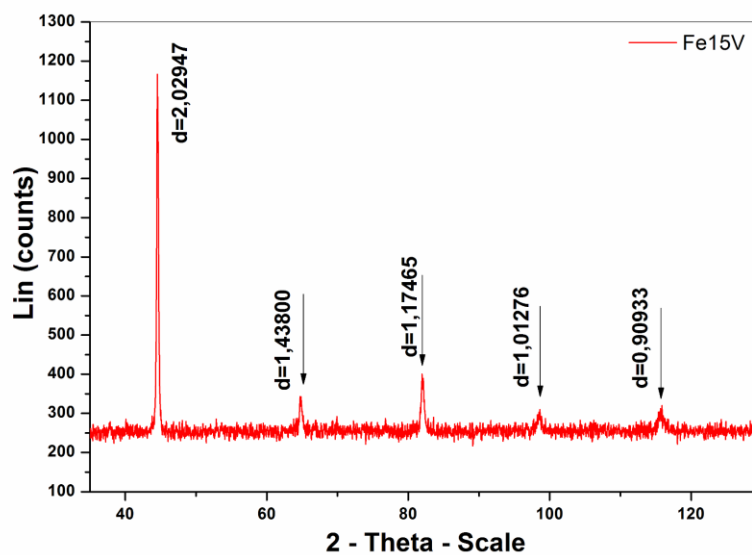


Figure 73. XRD spectrum from Fe-15V powders.

An initial test specimen of 7.0 grams was produced with a 50/50 mixture (by weight) of Fe-0.5V and Fe-15V powders (named specimen X) to note any problems with

sintering before the complete set of experiments with the combined powders. It's temperature profile was 7 minutes to 700 °C, hold for 3 minutes, 4 minutes to 400 °C (75 °C/min), hold 3 minutes, 3 minutes to 700 °C (100 °C/min), hold 3 minutes. This two-stage heating process was to provide insight into densification behavior. The pressure profile was constant application of 75 MPa pressure.

For the main set of experiments, 6 samples of 2 different types (12 specimens total) were produced from 7.0 grams of Fe-V powder, of two differing compositions. The goal was to provide enough carbon to the steel to have all (theoretically) of the vanadium form vanadium carbide, and to have enough carbon remaining to form a steel. One set of specimens was produced with 99.2 wt% Fe-0.5V powder and 0.8 wt% C (graphite), to produce a total average carbon content of 1.0 % C, and a vanadium content of 0.5%. A second set of specimens was produced with 49.8 wt% Fe-0.5V powder, 49.8 wt% Fe-15V powder, and 0.4% C (graphite), for a total average carbon content of 1.0 % C, and an average vanadium content of 7.75%.

The sintering profile for the complete set of experiments (excluding specimen X) was heating approximately 100 °C per minute to the holding temperature (600-850 °C), and holding for 15 minutes. The lengthy holding time was to allow for diffusion and reactions to occur during sintering. 75 MPa pressure was applied to all specimens for the duration of sintering.

All the powders were mechanically alloyed by ball milling in a planetary ball mill with an alumina jar and alumina spheres for 16 hours at 150 rpm (in cycles of 20 minutes on, 10 minutes rest) in an isopropyl alcohol solution. The powders were heated to 150 °C in a vacuum furnace to remove the IPA before placement in the graphite die.



For all the experiments, a 12.7 mm diameter graphite die was used, with graphite punches, and with the interior surface spray coated with boron nitride. The boron nitride was to directly counter the carbon diffusion from the die that was experienced in the previous experiments.

For the heat treatment, the twelve specimens were heated to 600 °C in a CM tube furnace in a vacuum atmosphere at a heating rate of 10 °C per minute, then they were held for one hour. After the holding time, the specimens were removed rapidly from the furnace and quenched in liquid nitrogen (cryo-forging) until they reached room temperature. The temperature of the specimens before immersion in liquid nitrogen was approximately 550 °C, only a slight decrease from the treatment temperature.

The specimens were prepared for SEM and hardness testing by cutting and polishing with SiC paper (320-4000 grit), followed by polishing with silica particles. They were etched with one or more of the following, depending on what phases were present: Murakami's Reagent, 5% Nital, and 50% hydrochloric acid.

For the grain size measurements, the error was calculated from the standard deviation of the measurements made from the linear intercept method for each experiment, and the average value from all experiments of 0.4  $\mu\text{m}$  was found and inserted in the tables.

#### **5.2.4. Preliminary results on the Fe-0.5V/Fe-15V mixed steel**

For SPS consolidated specimen X, XRD analysis was repeated, and Figure 74 shows the results. There is a total absence of x-ray peaks except from the ferrite matrix.

This suggests that thermal exposure during SPS processing was low enough to avoid solid state decomposition, without massive precipitation of secondary phases. It is surprising that the Fe-15V powders were also able to preserve their original metastable conditions after SPS.

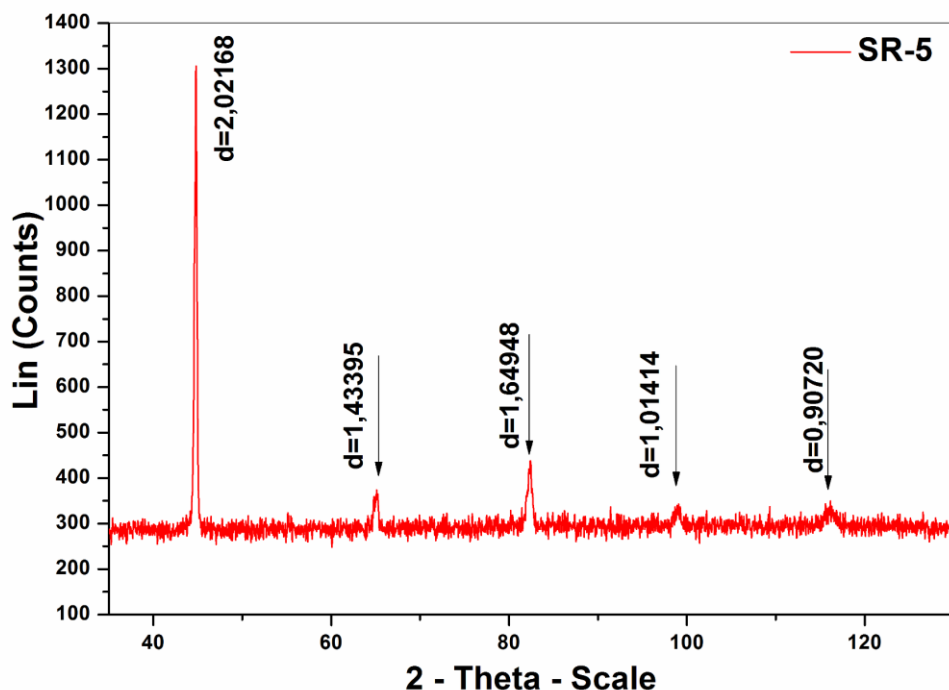


Figure 74. XRD spectrum from as-consolidated (SPS) specimen X.

The samples consolidated from the new powders showed similar results to those previously reported for the original Fe-0.5V powders. Also in this case, the external regions of the specimen were less dense than the central regions, as seen in Figure 75. The different types of powders were easily discernible on transverse sections of samples due to a small difference in color (greyscale), as well due to a stronger response from chemical etching, as seen in Figure 76.

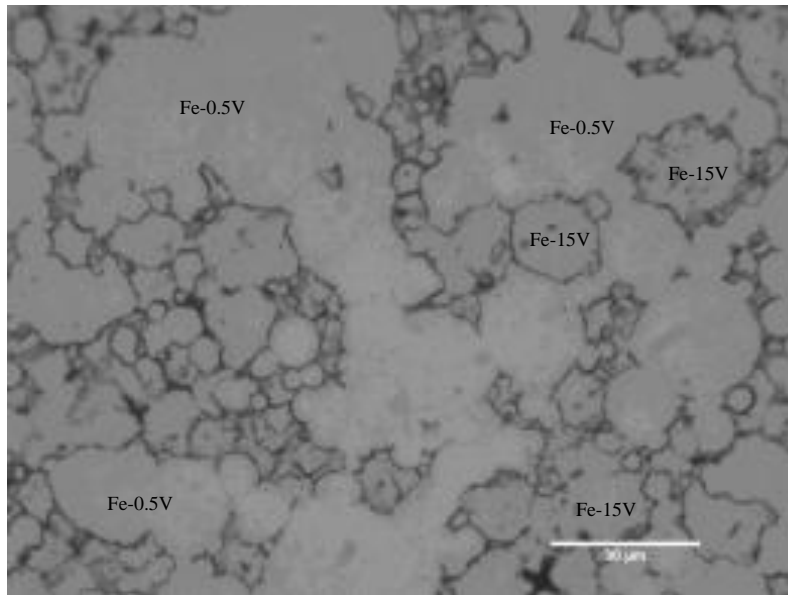


Figure 75. . Different etching response from Fe.0.5V and Fe-15V SPS consolidated powders (in the same specimen).

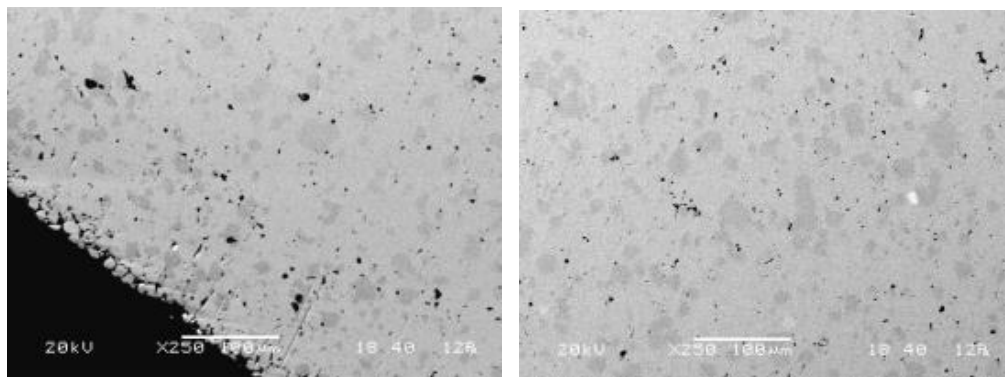


Figure 76. Different density between left) external and right) central regions of mixed Fe-0.5V/Fe-15V SPS sample V.

It was possible to distinguish the grains from different powders in the consolidated specimens, so we carried out selective micro-hardness indentation on transverse sections of consolidated specimens. The mean values for the different regions were 220 micro-hardness (HV0.05) in Fe-0.5V regions, and 360 micro-hardness (HV0.05) in Fe-15V regions.

Specimen X was further heat treated 1 hour at 600 °C, with the aim to induce loss of solute supersaturation and precipitation of small, secondary particles. Figure 77 shows the XRD spectrum from the heat-treated specimen X. The existence of several x-ray peaks from secondary phases (V-rich carbides) can be seen.

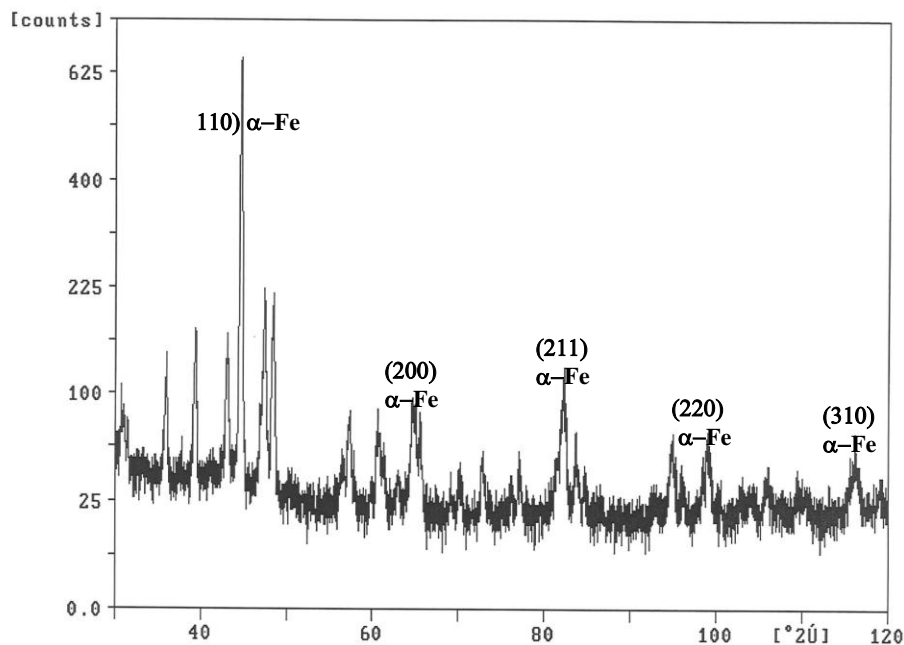


Figure 77. XRD spectrum from SPS consolidated Sample V + heat treating 1 hour at 600 °C.

In this heat treated sample, mean hardness values increased significantly from the previous, non-heat treated specimen, with micro- hardness 280 (HV0.05) in Fe-0.5V regions (a 27% increase), and 440 (HV0.05) in Fe-15V regions (a 22% increase).

Figure 78 shows a TEM image of specimen X, with the sections from each of the primary powders visible (and indicated by arrows). Figure 79 shows a TEM image with  $V_4C_3$  particles clearly visible in the matrix. Finally, Figure 80 shows a diffraction pattern of the specimen that clearly shows the  $V_4C_3$  presence.

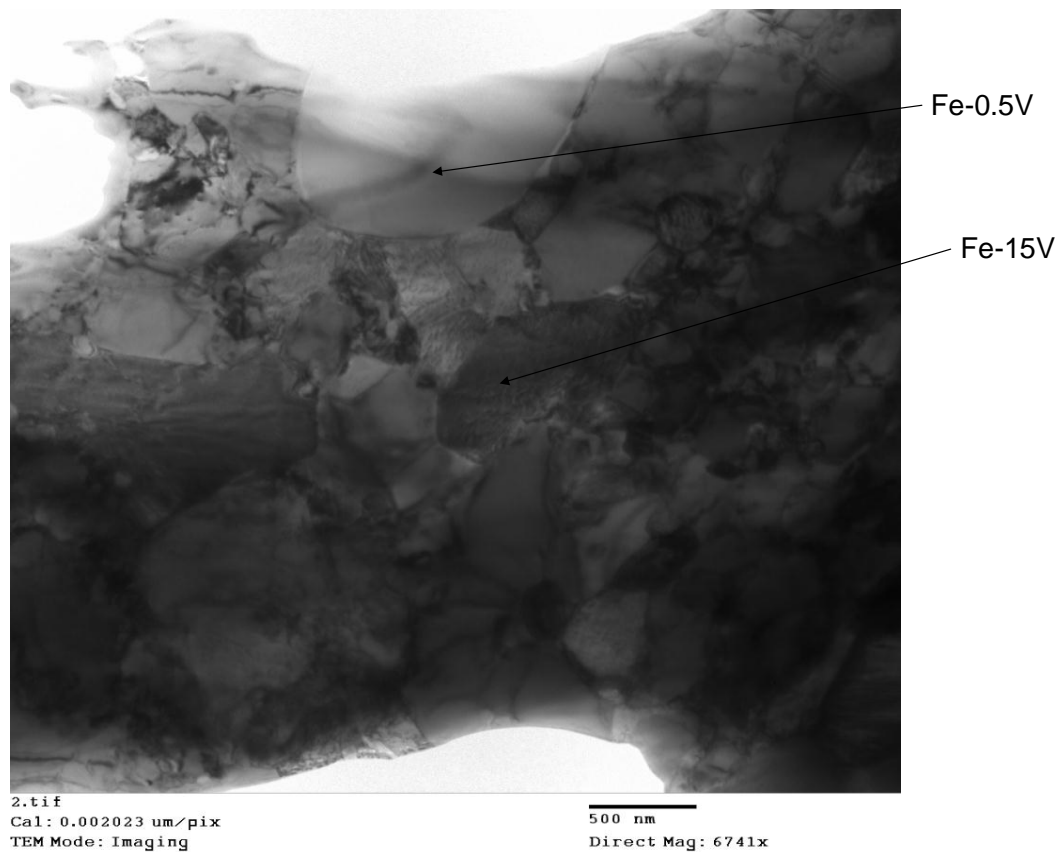


Figure 78. TEM image of specimen X, as-consolidated.

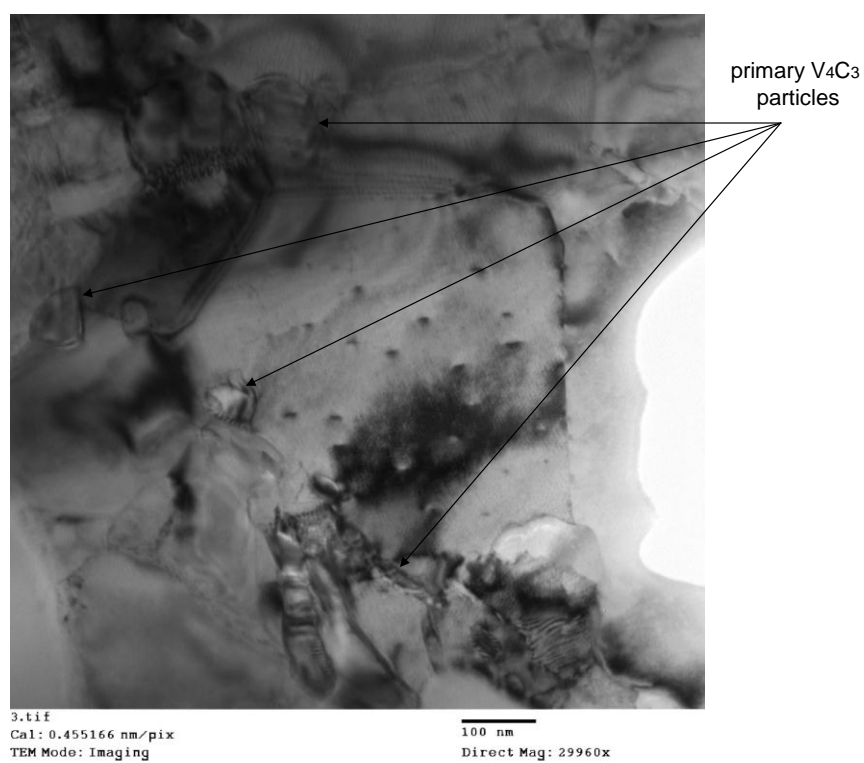
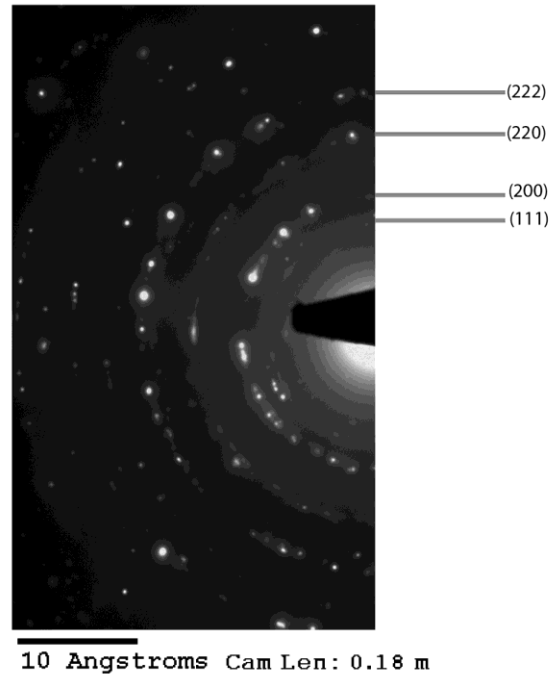


Figure 79. Another TEM image of specimen X, as-consolidated.



d ( <i>hkl</i> )	Theoretical (Å)	Experimental (Å)
(111)	2.4047	2.40
(200)	2.0825	2.05
(220)	1.4726	1.47
(222)	1.2023	1.20

f.c.c. Vanadium Carbide (V<sub>4</sub>C<sub>3</sub>) phase

Figure 80. XRD analysis of specimen X, as-consolidated.

#### 5.2.5. Results of densification and grain growth of Fe-0.5V/Fe-15V mixed steels

Table 16 and Table 17 show the data collected from the 12 experiments on Fe-0.5V with 1% total carbon, and Fe-0.5 with Fe-15V and 1% total carbon (6 of each). We can see that hardness and microhardness increase with relative density. We also see that Vicker's macro and micro hardness are very different, most likely due to the

microhardness indenter impinging on pores (in the not fully dense specimens), or less likely in areas of different phases (and therefore hardness).

Table 16. Data from Fe-0.5V, with carbon additives, specimens.

Specimen #	Temperature (°C)	Relative Density (%)	Average Grain size ( $\mu\text{m}, \pm 0.4$ )	Rockwell Hardness A (HRA)	Vicker's Micro-hardness (HV)	Vicker's Hardness (HV)
1	600	71.6	12.9	62.8	94	266
2	650	87.7	16.1	72.9	192	442
3	700	88.7	17.3	70.6	172	394
4	750	92.5	18.8	72.2	187	427
5	800	97.8	22.0	75.9	243	482
6	850	100.0	20.1	83.6	329	716

Table 17. Data from mixed Fe-0.5V with Fe-15V, with carbon additives, specimens

Specimen #	Temperature (°C)	Relative Density (%)	Average Grain size ( $\mu\text{m}, \pm 0.4$ )	Rockwell Hardness A (HRA)	Vicker's Micro-hardness (HV)	Vicker's Hardness (HV)
7	600	73.1	11.3	33.7	76	
8	650	80.9	11.5	57.5	95	205
9	700	87.3	12.5	67.2	137	333
10	750	93.7	14.0	69.5	192	372
11	800	99.0	21.4	75.1	232	450
12	850	100.0	21.4	76.4	245	445

Based on the previous results from heat treatment of specimen X, we heat treated the 12 specimens in a cryoforging process (as described previously). We can see the hardness results in Table 18 and Table 19. There was no noticeable grain size change for either set of specimens. For the specimens without Fe-15V, the hardness values decrease slightly through the heat treatment. This is likely due to phase change and loss of some of the properties of the rapidly saturated powder during the extended holding time without enough vanadium to react and form carbides. For the specimens with both Fe-



0.5V and Fe-15V, we see a slight increase in hardness after heat treatment. Due to the high amount of vanadium in this mixed powder, the holding time likely gave time for vanadium carbides to form in the steel, although at the expense of carbon diffusing out of the matrix due to the high inequality between vanadium and carbon content.

Table 18. Hardness data comparison between pre-heat treatment and post-heat treatment Fe-0.5V, with carbon additives.

Specimen #	HRA pre-heat treatment	HRA post-heat treatment	HV pre-heat treatment	HV post-heat treatment
1	62.8	52.0	266	162
2	72.9	69.3	442	369
3	70.6	59.7	394	229
4	72.2	68.2	427	350
5	75.9	68.5	482	410
6	83.6	82.3	716	672

Table 19. Hardness data comparison between pre-heat treatment and post-heat treatment mixed Fe-0.5V with Fe-15V, with carbon additives.

Specimen #	HRA pre-heat treatment	HRA post-heat treatment	HV pre-heat treatment	HV post-heat treatment
7	33.7	39.4		108
8	57.5	55.6	205	191
9	67.2	67.4	333	335
10	69.5	70.3	372	388
11	75.1	74.3	450	473
12	76.4	75.1	445	493

Overall, SPS processing of RS powders has been shown to preserve structural and metastable properties created during the powder production. It has also been shown to enhance these properties by creating new phases during the sinter process, and retaining them in the final specimen. However, the proportion of components (such as vanadium and carbon) must be in the proper ratios for this process to be successful. Also, carbon, and other impurity, infiltration is a hazard in the SPS process, but one that can be

mitigated by boron nitride isolation, or even used to enhance material properties (in the case of our Fe-0.5V powder that had too little carbon). The powders were densified to nearly full density in a very short time, with reduced temperature and pressure compared to the traditional processing techniques

## Chapter 6. Densification and grain growth kinetics in SPS

In the free sintering of conventional, crystalline powders, grain boundary diffusion is the primary mechanism for both densification and grain growth. The activation energy for both is on the same order, both are dependent on temperature and time, and they compete during the sintering process. When full density is reached, grain growth is the only available option, and it is established that significant grain growth occurs during long holding times at full density. Since the change in grain size follows with the change in porosity, some conditions of temperature, holding time, etc. may exist where a density and grain size trajectory can be formulated (again, for free sintering) that is proposed by German in Equation 9.

If we would like to show the various equations for densification and grain growth in free sintering from the literature, we need to find a general relationship between the two, of the form:

$$\text{Equation 13. } \frac{dG}{dt} = f(\rho, T) \frac{1}{G^{n_1}} \text{ for grain growth}$$

$$\text{Equation 14. } \frac{d\rho}{dt} = g(\rho, T) \frac{1}{G^{n_2}} \text{ for densification}$$

We would like to find out if a grain size-relative density trajectory exists of the form  $G = G(\rho)$ , and we can do this by examining whether the derivative  $dG/d\rho$  depends on  $\rho$ , as:

$$\frac{dG}{d\rho} = \frac{nG_0 k}{(1-\rho)^{n+1}}$$

Since  $G = kG_0(1 - \rho)^{-n}$  from Equation 9.

So we can find that, for our general equations:

$$\frac{dG}{d\rho} = \frac{dG/dt}{d\rho/dt} = \frac{f(\rho, T)}{g(\rho, T)} G^{n_2 - n_1}$$

$$\text{Equation 15. } \frac{f(\rho, T)}{g(\rho, T)} G^{n_2 - n_1} = \frac{nG_0k}{(1 - \rho)^{n+1}}$$

To satisfy this last equation, two conditions must be met:

$$(1) \ n_2 - n_1 = 0 \Rightarrow n_2 = n_1$$

$$(2) \ \frac{f(\rho, T)}{g(\rho, T)} = \frac{nG_0k}{(1 - \rho)^{n+1}}$$

(1) indicates the exponents for the grain size should be the same for both kinetic equations. (2) means that the ratios of f and g should be temperature independent and proportional to  $\frac{nG_0k}{(1 - \rho)^{n+1}}$ . From all the possible cases of free sintering, it is necessary to

identify kinetic equations that meet these two conditions.

We can find equations that meet the two conditions, such as  $\frac{dG}{dt} = \frac{C_1 D_s}{G^3 (1 - \rho)^{4/3}}$

and  $\frac{d\rho}{dt} = \frac{C_2 \gamma_s D}{G^3}$  from Zhao and Harmer<sup>64</sup>. In these equations  $C_1$  and  $C_2$  both contain

an RT term, which is derived from the activation energy, and show an activation energy equality as of condition (2) (where R is the gas constant and T is temperature). This

shows that there are kinetic equations for free sintering, with certain experimental conditions, where a relationship of the form of Equation 9 is valid.

To further our investigation of free sintering, here we derive Equation 9, from the densification rate and grain growth rate, as Bernard-Granger<sup>65</sup>, et al. did. From Bernard-Granger, the grain growth rate for conventional sintering can be expressed by:

$$\text{Equation 16. } \frac{dG}{dt} = \frac{2\Omega\gamma_b D_b^\perp}{RT\delta_b G}$$

$$\text{Which can be simply re-arranged to: } \frac{dG}{dt} = \frac{2\Omega\gamma_b D_b^\perp}{RT\delta_b} \frac{1}{G}$$

Where G is the grain size,  $\Omega$  is the molar volume of the solid, R is the gas constant, T is temperature,  $\gamma_b$  is the grain boundary surface tensions,  $\delta_b$  is the grain boundary thickness, and  $D_b^\perp$  is the diffusion coefficient through the grain boundary.

Similar to Kang, et al.<sup>152</sup>, we can find a relationship for densification rate as:

$$\text{Equation 17. } \frac{d\rho}{dt} \approx 400 \frac{\Omega\gamma_{sv}\delta_b D_b}{RTG^4}$$

$$\text{Which can be simply rearranged to: } \frac{d\rho}{dt} = 400 \frac{\Omega\gamma_{sv}\delta_b D_b}{RT} \frac{1}{G^4}$$

Where  $\rho$  is the relative density,  $\gamma_{sv}$  is the solid-vapor surface tension,  $D_b$  is the diffusion coefficient along the grain boundary, and the other constants are described previously.

To determine if a grain size-density trajectory can be established, such as Equation 9, we must determine an equation of the form  $G=G(\rho)$ . We can start by finding if  $dG/d\rho$  depends on  $\rho$ . We can combine Equation 16 and Equation 17, to find:

$$\frac{\frac{dG}{dt}}{\frac{d\rho}{dt}} = \frac{\frac{2\Omega\gamma_b D_b^\perp}{RT\delta_b} \frac{1}{G}}{400 \frac{\Omega\gamma_{sv}\delta_b D_b}{RT} \frac{1}{G^4}} = \frac{\gamma_b D_b^\perp G^3}{200\delta_b^2 \gamma_{sv} D_b} = \frac{\gamma_b D_b^\perp}{200\delta_b^2 \gamma_{sv} D_b} G^3$$

which is clearly expressed as:

$$\text{Equation 18. } \frac{dG}{d\rho} = \frac{\gamma_b D_b^\perp}{200\delta_b^2 \gamma_{sv} D_b} G^3 = k_0 G^3$$

$$\text{Where } k_0 = \frac{\gamma_b D_b^\perp}{200\delta_b^2 \gamma_{sv} D_b}$$

Re-arranging Equation 18, we find  $\frac{dG}{G^3} = k_0 d\rho$ . We can integrate this

equation easily, as  $k_0$  is not dependent on  $G$  or  $\rho$ .

$$\int \frac{dG}{G^3} = k_0 \int d\rho$$

$$\frac{1}{2G^2} - \frac{1}{2G_0^2} = -k_0\rho + k_0\rho_0$$

where  $G_0$  and  $\rho_0$  are the initial grain size and initial relative density, respectively.

If we determine that  $\frac{\gamma_b D_b^\perp}{\gamma_{sv} D_b} = \text{constant}$  at any temperature, which Bernard-Granger concluded after confirming with experimental data, we find:

$$\text{Equation 19. } \frac{1}{G^2} = -k_1\rho + k_2$$

which can be rewritten as:

$$\text{Equation 20. } G = \frac{1}{(k_2 - k_1\rho)^{1/2}}$$

$$\text{Where } k_1 = \frac{\gamma_b D_b^\perp}{100\delta_b^2 \gamma_{sv} D_b} \text{ and } k_2 = \frac{\gamma_b D_b^\perp}{100\delta_b^2 \gamma_{sv} D_b} \rho_0 + \frac{1}{G_0^2}.$$

This is similar to Equation 9, however, further modification is necessary.

By separating the  $G_0$  terms from  $k_2$  and isolating  $\rho$ , we can find:

$$G = \frac{1}{\frac{k_1^2}{G_0^2} \left(\frac{k_2}{k_1} - \rho\right)^{1/2}} = \frac{\frac{G_0^2}{k_1^2}}{\left(\frac{k_2}{k_1} - \rho\right)^{1/2}} = \frac{k_3 G_0}{\left(\frac{k_2}{k_1} - \rho\right)^{1/2}}$$

$$\text{where } k_3 = \frac{1}{k_1^2 G_0}.$$

$$\text{Equation 21. } G = \frac{k_3 G_0}{\left(\frac{k_2}{k_1} - \rho\right)^{1/2}}$$

Equation 21 is very similar to Equation 9 in form, as shown:

$$G = \frac{k_3 G_0}{\left(\frac{k_2}{k_1} - \rho\right)^{1/2}} \approx \frac{k G_0}{(1 - \rho)^{1/2}}$$

In this way, we have shown that a mathematical basis for a temperature-independent grain size-porosity relationship exists for conventional sintering, similar to Equation 9. Bernard-Granger, et al.<sup>65</sup> defined this method in limited scope compared to

Equation 9, asserting Equation 21's validity only for a particular sintering experiment that would follow a particular trajectory given its sintering conditions.

In hot-pressing, the main mechanism for densification is power-law creep, while the main mechanism for grain growth is grain boundary diffusion. Depending on the material system, each mechanism may be favored differently due to their dependence on different material parameters (such as diffusion constant, strain rate, etc.), but for most materials, densification is favored over grain growth and studies have shown improved densification with decreased grain growth when comparing hot-pressing to free sintering. As a counter-example, there are a minority of certain material systems, like carbides (particularly Tantalum Carbide) where grain growth is the dominant mechanism, and during hot-pressing rampant grain growth occurs and full density is very difficult to achieve.<sup>153</sup>

In spark plasma sintering, the picture is not clear. Due to the application of pressure during SPS (although not necessary for certain pressureless modifications to standard SPS), it is most comparable to hot-pressing, with the only difference being the method of heating the powder. However, the literature on SPS shows improved densification with reduced grain growth compared to hot-pressing for many different material systems. A simple explanation for the difference is that since the main difference between SPS and hot-pressing is time (affecting total sintering time and heating rate), and both mechanisms are time-dependent, the higher order equation will dominate (power-law creep). This does not include the influence of other possible factors, such as heating rate or any electric field related effects which may exist in SPS.



However, there are other minor differences between SPS and hot-pressing that confound the issue. We know in specific situations of power-law creep that creep can be significantly reduced, usually in the cases of decreased pressure and temperature during hot-pressing. One of the main advantages claimed in the literature for SPS is the ability to sinter at lower temperatures than expected, and this may have an effect on the creep behavior. Typically, the threshold for temperature above which creep proceeds normally is  $0.4 T_M$ , and the reduced sintering temperatures in SPS approach this value but rarely pass it for any material systems. As an example, alumina can be sintered in SPS as low as 1100 °C, while hot-pressing usually occurs at 1600 °C, however, the reduced SPS temperature is still 53% of the melting temperature (which is above the creep threshold). Still, a case might be made that approaching this low temperature in SPS may have an effect on the creep behavior, and therefore densification.

We also know that power-law creep is significantly affected by the applied pressure, with low pressure, below a certain material threshold, significantly reducing the creep rate. The threshold can be anywhere from 0.2 MPa to 42 MPa, depending on the material and the particle size of the powder (with no particular relationship between grain size and threshold). Due to the nature of SPS, most of the dies and punches used are made of graphite, which has a low strength compared to steel or carbides (which are more common in hot-pressing, although graphite is also used). Because of the low strength of graphite, there is a maximum pressure limitation which may fall into the range of affecting creep behavior dependent on what material is used (the pressure limitation for our machine and graphite tooling is 50-75 MPa, although certain die shapes failed several times at pressures as low as 20 MPa).

What this means for SPS is unclear, but what it may mean is that certain experimental conditions in SPS could follow a grain size and densification trajectory similar to Equation 9. The SPS conditions required would be a low pressure, below the creep threshold for the particular material and particle size in the experiment, and a low temperature near  $0.4T_M$  for sintering, without any additional effects related to phase changes or recrystallization that may occur in the material.

Here we derive specific conditions for density-grain size trajectory for SPS. We can use general equations to express the dependence of grain growth and densification rate on other parameters, as Equation 13 and Equation 14:

$$\frac{dG}{dt} = f(\rho, T, P) \frac{1}{G^{n_1}}$$

$$\frac{d\rho}{dt} = g(\rho, T, P) \frac{1}{G^{n_2}}$$

Where P is pressure. Here we neglect any dependence on the electromagnetic field, as the literature is unclear about the exact contribution of the field on kinetics.

For processing under externally applied pressure, we know that:

$$\dot{G} = \frac{dG}{dt} = \dot{G}_{static} + \dot{G}_{dynamic}$$

And from Du and Cocks<sup>154</sup>, we know for hot pressing:

$$\text{Equation 22. } \dot{G}_{static} = \dot{G}_0 \left( \frac{G_0}{G} \right)^3 (1 - \rho)^{-3/2}$$

Where  $G$  is the grain size,  $G_0$  is the initial grain size,  $\rho$  is the relative density, and  $\dot{G}_0$  is the grain growth after reaching full density (a temperature dependent, and often constant, material parameter).

We know from Kim, et al.<sup>155</sup>, that:

$$\text{Equation 23. } \dot{G}_{dynamic} = k_1 \frac{G}{\phi} \left[ (\dot{\gamma}_{ij} \dot{\gamma}_{ij}) + \frac{1}{3} (\dot{\epsilon}_{kk}^*)^2 \right]^{1/2}$$

Where  $k_1$ ,  $\phi$ ,  $\dot{\gamma}_{ij}$  and  $\dot{\epsilon}_{kk}^*$  are a constant, the stress concentration factor, deviatoric strain rate, and volumetric strain rate by external load, respectively. The dependence on dynamic grain growth of  $G$  is proportional to  $G$ .

We can again try and find a dependence of  $G$  on  $\rho$  as  $G=G(\rho)$ , as we did for free sintering. However, we must be aware that pressure is now a factor in the densification rate. We exclude any effects of the electric field on SPS, as they are not definitive in the literature.

From Olevsky's constitutive theory of sintering<sup>18</sup>:

$$\sigma_{ij} = \frac{\sigma(W)}{W} \left[ \phi \dot{\epsilon}_{ij} + \left( \psi - \frac{1}{3} \phi \right) \dot{\epsilon} \delta_{ij} \right] + P_L \delta_{ij}$$

Where  $W$  is the equivalent strain rate and  $\sigma(W)$  is the equivalent stress,  $\phi$  and  $\psi$  are the normalized shear and bulk viscosities (dependent on porosity),  $\delta_{ij}$  is the Kronecker delta, and  $\dot{\epsilon}$  is the first invariant of the strain rate tensor (the volumetric shrinkage rate). For hot-pressing (or SPS),  $P_L$  is negligible.

For hot-pressing, the dominant mechanism of mass transport is power-law creep, and the stress has the form:

$$\sigma(W) = BW^m$$

We can then modify the constitutive equation for hot-pressing in a rigid die (as SPS):

$$\text{Equation 24. } \sigma_{ij} = \frac{BW^m}{W} \left[ \phi \dot{\epsilon}_z + \left( \psi - \frac{1}{3} \phi \right) \dot{\epsilon} \right]$$

where  $\dot{\epsilon} = \dot{\epsilon}_z + 2\dot{\epsilon}_r$ . For a rigid, constrained die,  $\dot{\epsilon}_r = 0$ , so  $\dot{\epsilon} = \dot{\epsilon}_z$ .

The constitutive equation then becomes:

$$\text{Equation 25. } \sigma_z = BW^{m-1} \left[ \left( \psi + \frac{2}{3} \phi \right) \dot{\epsilon}_z \right]$$

where we define the following terms:

$$W = \frac{1}{\sqrt{1-\theta}} \sqrt{\phi \dot{\gamma}^2 + \psi \dot{\epsilon}^2} = \frac{1}{\sqrt{1-\theta}} \sqrt{\frac{2}{3} \phi + \psi} |\dot{\epsilon}_z|,$$

$$\dot{\gamma} = \sqrt{\frac{2}{3}} |\dot{\epsilon}_z - \dot{\epsilon}_r| = \sqrt{\frac{2}{3}} |\dot{\epsilon}_z|$$

Substituting these into the constitutive equation, we find:

$$\text{Equation 26. } \sigma_z = B \left[ \frac{1}{\sqrt{1-\theta}} \sqrt{\frac{2}{3} \phi + \psi} |\dot{\epsilon}_z| \right]^{m-1} \left[ \left( \psi + \frac{2}{3} \phi \right) \dot{\epsilon}_z \right]$$

we define the following terms, where  $\theta$  is porosity:

$$\phi = (1-\theta)^2$$

$$\psi = \frac{2}{3} \frac{(1-\theta)^3}{\theta}$$

And we can rewrite the constitutive equation again:

Equation 27.  $\sigma_z = B[1 - \theta]^{\frac{m-1}{2}} \left( \psi + \frac{2}{3} \varphi \right)^{\frac{1+m}{2}} |\dot{\epsilon}_z|^m$

Since  $\dot{\epsilon}_z < 0$ ,  $|\dot{\epsilon}_z| = -\dot{\epsilon}_z$ , therefore  $\sigma_z < 0$ , so we can rearrange the

constitutive equation to:

Equation 28.  $|\dot{\epsilon}_z| = -\left(\frac{\sigma_z}{B}\right)^{\frac{1}{m}} [1 - \theta]^{\frac{m-1}{2m}} \left( \psi + \frac{2}{3} \varphi \right)^{\frac{1+m}{2m}}$

Using the following relationships, where  $\rho$  is density:

$$\dot{\epsilon} = \dot{\epsilon}_z = -\frac{\dot{\rho}}{\rho}$$

$$\theta = 1 - \rho$$

We can find:

$$\begin{aligned} \varphi &= (1 - \theta)^2 = \rho^2 \\ \psi &= \frac{2}{3} \frac{(1 - \theta)^3}{\theta} = \frac{2}{3} \frac{\rho^3}{1 - \rho} \end{aligned}$$

and substituting these into the constitutive equation, we can find a relationship for densification rate:

$$\frac{\dot{\rho}}{\rho} = \left(\frac{\sigma_z}{B}\right)^{\frac{1}{m}} \rho^{\frac{m-1}{2m}} \left( \frac{2}{3} \frac{\rho^3}{1 - \rho} + \frac{2}{3} \rho^2 \right)^{\frac{1+m}{2m}}$$

which simplifies to:

$$\text{Equation 29. } \frac{\dot{\rho}}{\rho} = \left( \frac{\sigma_z}{B} \right)^{\frac{1}{m}} \rho^{\frac{m-1}{2m}} \left( \frac{2}{3} \frac{\rho^2}{1-\rho} \right)^{\frac{1+m}{2m}}$$

Finally, we can use the expression for B from power-law creep, where p is 3 or 4 depending on the diffusion mechanism:

$$B = G^p B_0 \exp\left(\frac{-Q_{cr}}{RT}\right)$$

To show that:

$$\text{Equation 30. } \dot{\rho} = \left( \frac{\sigma_z}{G^p B_0 \exp\left(\frac{-Q_{cr}}{RT}\right)} \right)^{\frac{1}{m}} \rho^{\frac{3m-1}{2m}} \left( \frac{2}{3} \frac{\rho^2}{1-\rho} \right)^{\frac{1+m}{2m}}$$

$$\text{so } \dot{\rho} \propto G^{-p/m} h(\rho)$$

And from above:

$$\dot{G} = \dot{G}_{static} + \dot{G}_{dynamic}$$

$$\dot{G} = \dot{G}_0 \left( \frac{G_0}{G} \right)^3 (1-\rho)^{-3/2} + k_1 \frac{G}{\phi} \left[ \left( \dot{\gamma}_{ij} \dot{\gamma}_{ij} \right) + \frac{1}{3} \left( \dot{\epsilon}_{kk}^* \right)^2 \right]^{\frac{1}{2}}$$

$$\circ \dot{G} \propto G^{-3} s(\rho) + G$$

Following the analysis from free sintering, we can say:

$$\frac{f(\rho, T, P)}{g(\rho, T, P)} G^{n_2 - n_1} = \frac{nG_0 k}{(1-\rho)^{n+1}}$$

With the same two conditions that must be met:

$$(1) \ n_2 - n_1 = 0 \Rightarrow n_2 = n_1$$

$$(2) \ \frac{f(\rho, T, P)}{g(\rho, T, P)} = \frac{nG_0 k}{(1-\rho)^{n+1}}$$

If we ignore the dynamic grain growth term in the grain growth rate equation, then it should be possible to find a valid  $p$  and  $m$  to satisfy the two conditions.  $P$  is usually 3 or 4, depending on the mechanism, and  $m$  is between 0 and 1 (with specific values depending on creep mechanism). However, finding values for  $p/m = 3$  (to satisfy condition (1)) doesn't make much sense in terms of densification mechanisms and physical phenomenon. It may be that such a situation exists in hot-pressing and SPS, but it is not the common scenario. It does not mean that experiments with those specific conditions do not exist, as there could be particular powders where applied pressure does not enhance their densification due to extreme hardness or lack of atomic mobility and diffusion. However, the most common scenario is  $p = 3$  and  $m = 0.5$ , for an exponent  $p/m = 6$ , which violates the necessary condition (1).

If we ignore the dynamic grain growth term, we are putting severe, and unrealistic, limits on the validity of the model. The main feature of hot-pressing and SPS is the addition of the dynamic grain growth and densification change due to creep. If we include the dynamic grain growth term, we can see that the grain growth rate will be dominated by the dynamic grain growth, and the effects of the static grain growth will be negligible in comparison. Then we must find values for  $p/m = 1$ , which is only possible

for  $p$  and  $m$  both equal to 1. This is an impossible scenario, and goes against the commonly known (and literature investigated) densification and grain growth methods in hot-pressing and SPS.

It is possible, however, to analyze our previous experiments and test Equation 9 for SPS, with the caveat that we expect the results will not fit, or represent some extreme conditions that are completely atypical and against the physics-based analysis.

In Figure 81, we plot the data from alumina experiments conducted at 1300 °C, with either 37 or 49 MPa of applied pressure, and show density and grain size data along with the model data fitting Equation 9. We can see that the data fits perfectly with  $n = 0.5$  and  $k = 0.56$  (correlation 0.987). Although Suzuki et al. and Bernard-Granger et al. both found this relationship to be true in conventional sintering of alumina, Zhao and Harmer only found it true for alumina with MgO additives, and no work had been done on spark sintering of alumina. This data may fit the equation well due to the two pressures used (37 and 49 MPa) being less than the creep threshold for the powder (average particle size 0.5  $\mu\text{m}$  99.5% pure alumina), although the temperature of 1300 °C being 0.627  $T_M$  likely met any temperature threshold. In Figure 82, we can see the same results as Figure 81, but with a zeroing of the axis for a clearer view of the model over all densities, not just the final densification.



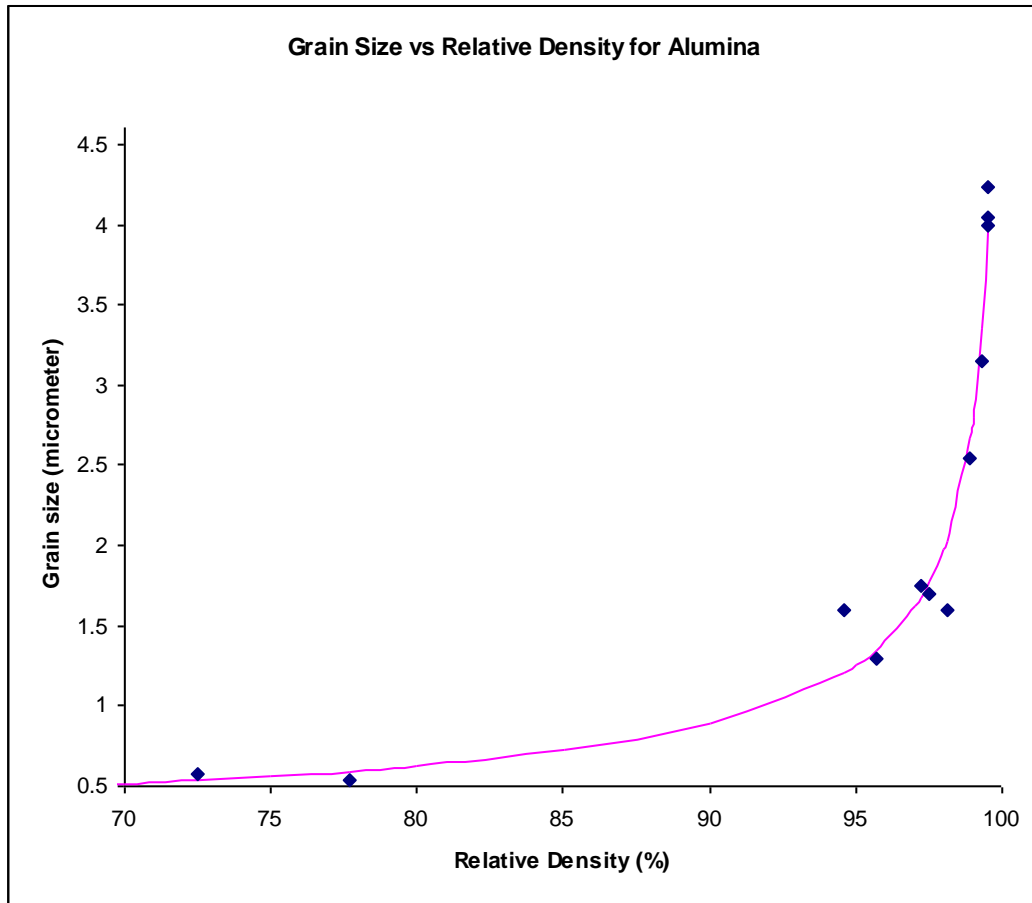


Figure 81. Densification and grain growth behavior for spark sintering of alumina, with a focus on the high density area. We can see that the data clearly fits an  $\epsilon^{-1/2}$  relationship, with  $k = 0.56$ , a perfect fit for the model (correlation 0.987).

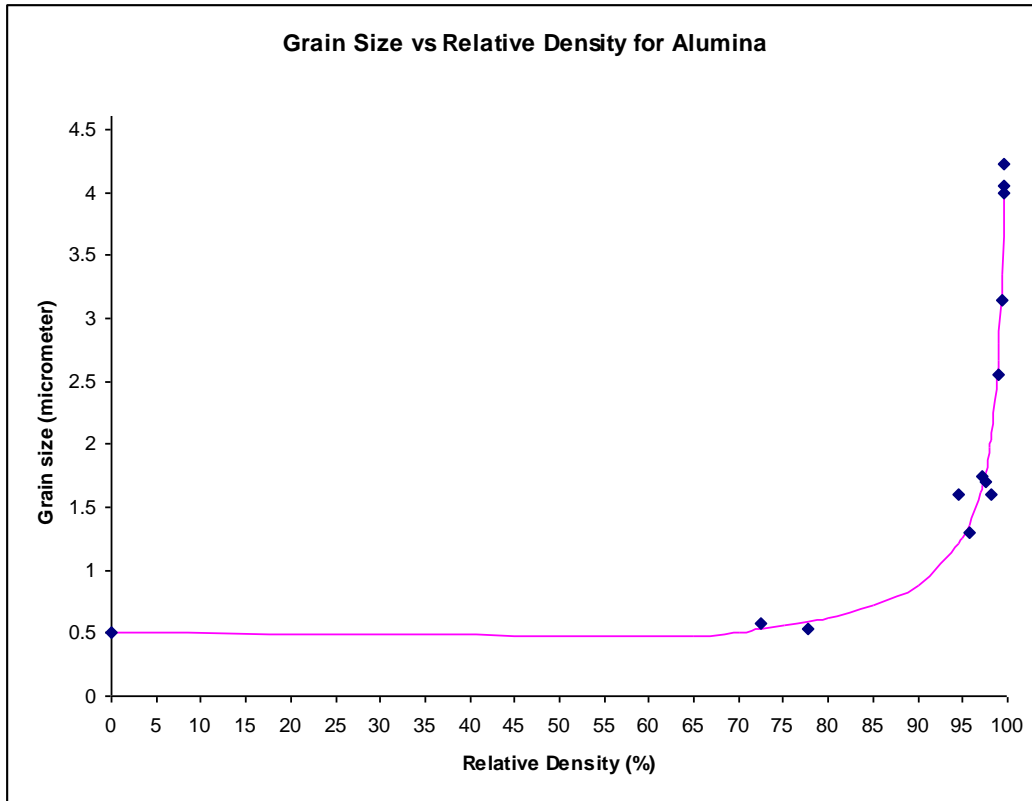


Figure 82. Similar to Figure 81, but without the focus on high density.

Our other conducted experiments were not suitable for this type of analysis, as the TaC specimens were sintered at 3 different temperatures, the Fe-VC specimens had phase transformations during sintering, and the aluminum extrusion experiments underwent significant plastic deformation immediately after sintering. We expect in each of these cases the simple model would not suffice.

In German's paper<sup>62</sup>, he uses an example of spark plasma sintering of titanium carbide to emphasize how the grain size and density trajectory equation is valid in these circumstances, however, the data he provides is limited. It is interesting to note that the sintering conditions for this powder were 60 MPa applied pressure, and a variety of sintering temperatures from 700-1150 °C. Previously, we have expected this simple

model to be relevant for specimens produced at the same sintering temperature, however German's analysis indicates this is not always the case. We have taken the data from two plots in the original paper by Zadra<sup>156</sup> (grain size vs. temperature and density vs. temperature) and fit it to the Equation 9, with the results shown in Figure 83 and Figure 85 below, to see the temperature dependence. We can see that spark plasma sintering for both grades of titanium fits the model. Figure 84 and Figure 86 show the same results as Figure 83 and Figure 85, respectively, but with a zeroing of the x-axis to give a clearer picture of overall densification, rather than just the final densification.

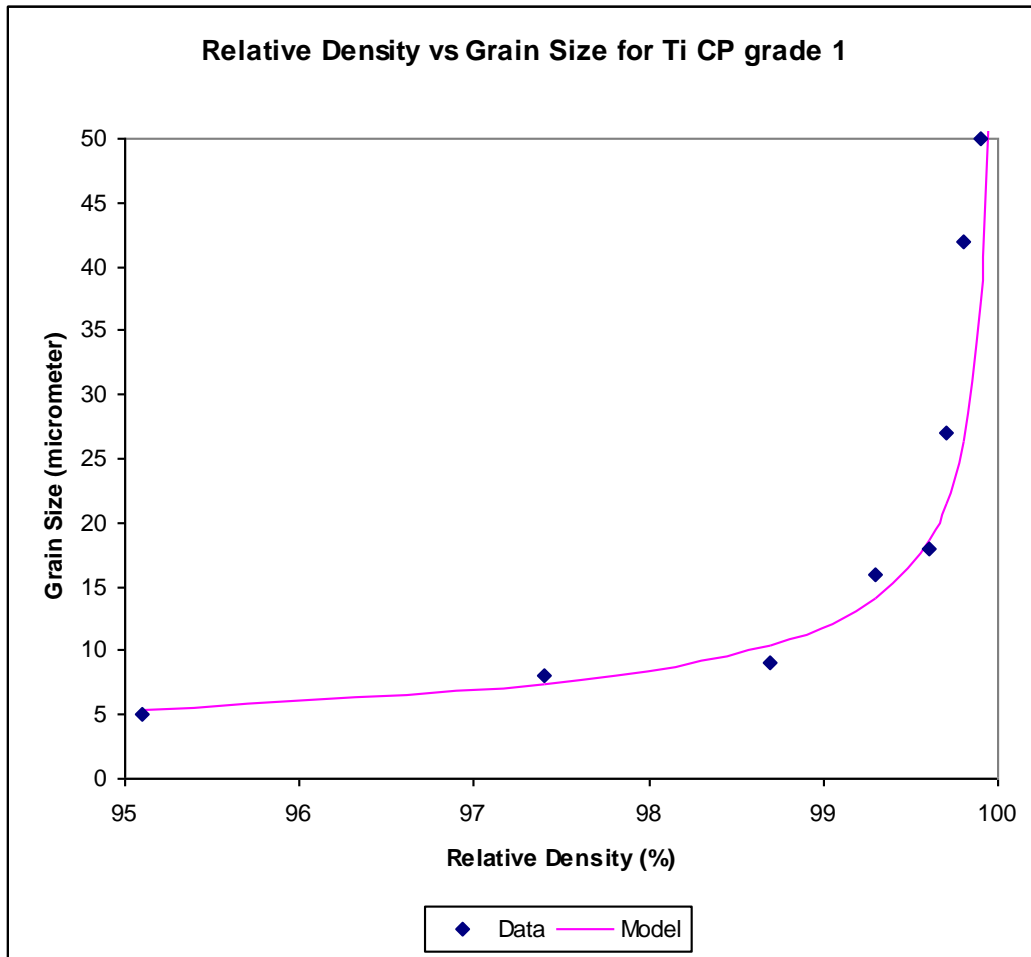


Figure 83. Spark sintering of one grade of titanium, focused on the high density area, shows a  $\epsilon^{-1/2}$  relationship between grain size and porosity, with  $n = 0.5$  and  $k = .59$ , like the ideal model (correlation 0.96).

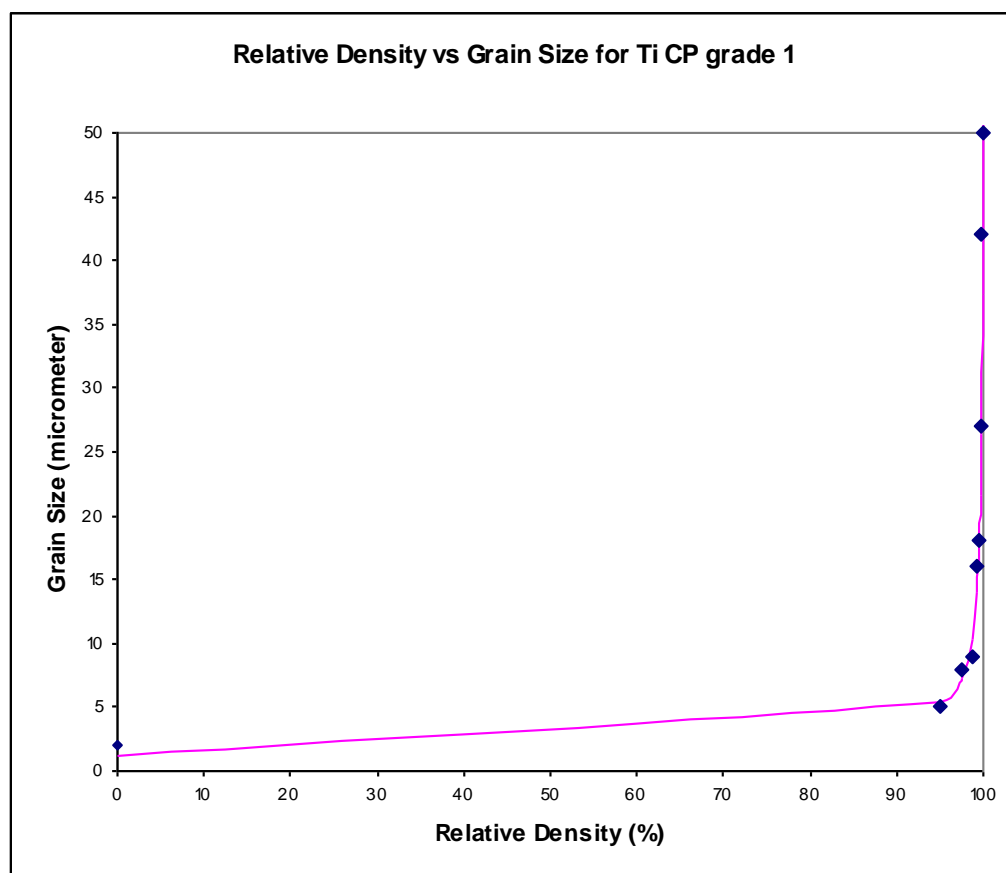


Figure 84. Similar to Figure 83, but without the focus on high density.

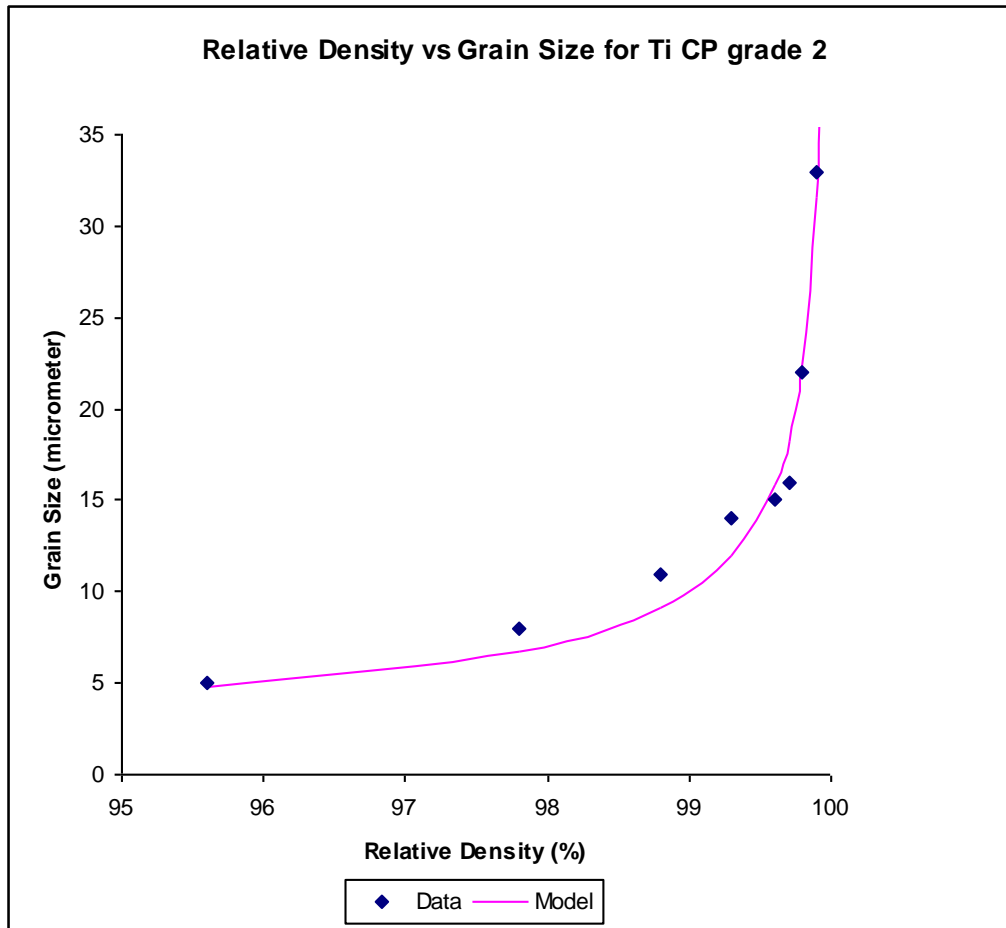


Figure 85. Spark sintering of another grade of titanium, focused on the high density area, shows a  $\varepsilon^{-1/2}$  relationship between grain size and porosity, with  $n = 0.5$  and  $k = .5$ , exactly like the ideal model (correlation 0.99).

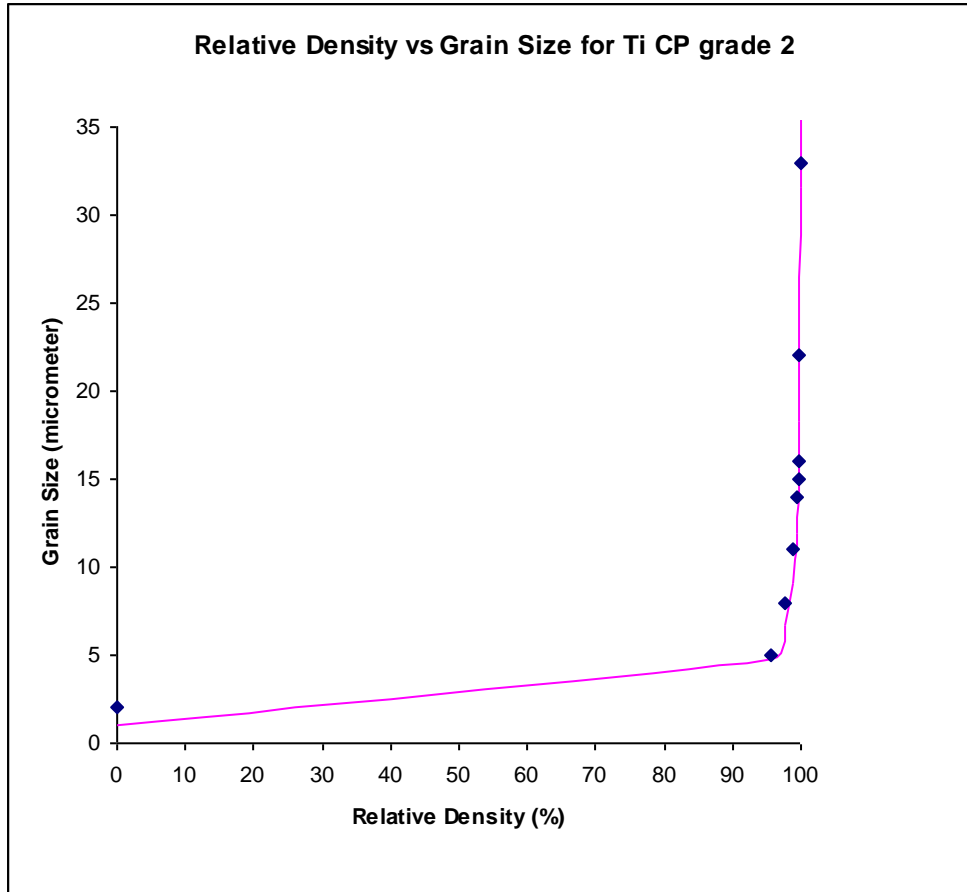


Figure 86. Similar to Figure 85, but without the focus on high density.

There appears to be a trajectory that is independent of temperature for grain size and densification in SPS, with a high correlation of data to the simple model, but it is not clear why this is the case, as an in-depth analysis of the physics behind densification and grain growth in SPS show this is only possible under extreme, abnormal conditions. It is possible to fit data to many models, and a correlation does not indicate the reasoning or physical evidence behind the phenomenon. Even if we consider a series of experiments that stumbled on the perfect sintering conditions (by accident) that would create this unlikely scenario and simple relationship, the results are not expected and not typical of densification and grain growth behavior in SPS.

## Chapter 7. Conclusions

We investigated (a) the net-shaping potential of SPS, the impact of the specimen's shape on the consolidation kinetics and structure development during SPS; (b) grain growth and densification during SPS; and (c) possibilities of structure tailoring through SPS combined with extrusion.

In the investigation on die/specimen shape with alumina, we found that the specimen's shape had a significant impact on the overall densification of a specimen, but did not have the impact we expected on the localized properties. We expected different areas of the specimen to densify differently, or to have higher grain growth dependent on proximity to the outer wall and distance to the center of the specimen. Preliminary results indicated this was occurring, but further investigation was more thorough and provided contradictory results. An overall change in densification and grain growth behavior was noted, with a reduction in grain size and decrease in porosity correlated with increasing aspect ratio, but with no localized variation.

In each of the conducted experiments we noted SPS's ability to decrease grain size (relative to other methods) and improve densification. In the TaC specimens, we noticed improved densification but also significant grain growth, and even adding fiber materials into a TaC matrix did not retard grain growth (as often happens with composites).

In Fe-V-C we noticed grains of a particular phase (VC) being produced during the powder densification, which we desired. We also noted that the type of lubricant material (or electrical insulation) was important, due to the rapid diffusion of carbon into the steel

specimen when boron nitride was not observed. SPS was also able to retain all of the unique properties imparted into the rapidly solidified powder, which are usually destroyed by the higher temperature and long holding times of conventional sintering of this powder.

Finally, we examined the ability of Spark Plasma Extrusion to affect the microstructure of specimens. The ability of SPS and extrusion to perform this task independently is well known, but the possibility of improved refinement by combining the two processes had only barely been investigated. We found, through an analysis of the grain structure, that SPE did have a grain deformation potential (although our extrusion ratio was perhaps too low to fully investigate this), but no grain refinement occurred. Dynamic recrystallization also did not occur, but this may have been due to the reduced temperatures were able to extrude at, due to the superior ability to densify materials with SPS.

By examining the grain growth and density kinetics in our experiments, we theorized there are a particular set of experimental conditions that allow for a simplification of the densification and grain growth kinetics for free sintering, but they are not applicable to SPS. Through a complete analysis of the physical phenomena behind densification and grain growth in SPS, it seems there may be extreme conditions where the densification and grain growth relationships break down to a simpler form, but finding these conditions would be impossible, and would indicate completely abnormal behavior for SPS.



We have achieved the goals we set out, and shown SPS to be a versatile and useful tool with the potential for producing net-shaped specimens and composites that retain tailored properties introduced during green processing.

## **Chapter 8. Scientific and engineering novelty of research results**

1. First-of-a-kind direct study of the net-shaping potential of SPS has been conducted; the impact of the SPS tooling shape on the uniformity of the SPS-processed specimens' structure has been analyzed.
2. First-of-a-kind study of the SPS-based extrusion process has been carried out in terms of the densification and grain growth kinetics as well as the spatial distribution of porosity and grain size.
3. The possibilities of the SPS-based fabrication of tailored composites have been studied for the three powder systems (isolative: alumina, semi-conductive: TaC, and conductive: Fe-VC).

## Chapter 9. Appendix

### 9.1. Equipment Overview



DR. SINTER® LAB 515S; Spark plasma sintering Device produced by SPSS Syntex, Co. in Japan. Pulsed direct current is driven through a die encased powder sample held under uniaxial load, generating Joule heat. Capable of producing approximately 50kN force, and temperatures up to approximately 3000 C, with heating rates up to 500 °C /minute. Pressure accuracy is  $\pm 0.2$  kN with the built in measurement system, while K-type thermocouple temperature accuracy is  $\pm 2$  °C, and one-color pyrometer (570-3000 K) accuracy is  $\pm 3\%$  °C.

Calibration for the pressure was conducted by inserting a load cell into the standard SPS setup with dies and spacers, and comparing the pressure reading on the SPS machine to the reading on the load cell, from forces of 3 to 50 kN. 3 kN is approximately the minimum applied force for the SPS machine. The variance of the SPS readout at 3 kN was -0.3 kN, at 5 kN was +0.2 kN, at 8.8 kN was +0.2 kN, and above 8.8 kN was  $\pm 0.1$  kN. Since most experiments were conducted at 8.8 kN or below, we used the  $\pm 0.2$  kN as the average.

Temperature calibration was conducted by heating a die and spacer setup from 100 – 1500 °C, without powder, and comparing the recorded temperature data from the installed K-type thermocouple, the installed one-color pyrometer, an external two-color pyrometer, and an external K-type thermocouple. The error in the measurement for each device was greater than the published error for the devices given by the manufacturer.

The coefficient of thermal expansion (CTE) of the graphite was calculated by measuring the z-axis displacement versus temperature during a simulated experiment with spacers, die, and no powder. The total height of the graphite equipment was measured. A curve was fit for the data, and the coefficient of thermal expansion was calculated to be  $0.0000004 T + 0.0004$ , where T is the temperature. This equation does not include variances for different die/spacer configurations (which would change the height), and all experiments were conducted with the same die/spacer configuration. Fig. below shows a z-axis displacement versus temperature plot that was used to calculate the CTE equation.

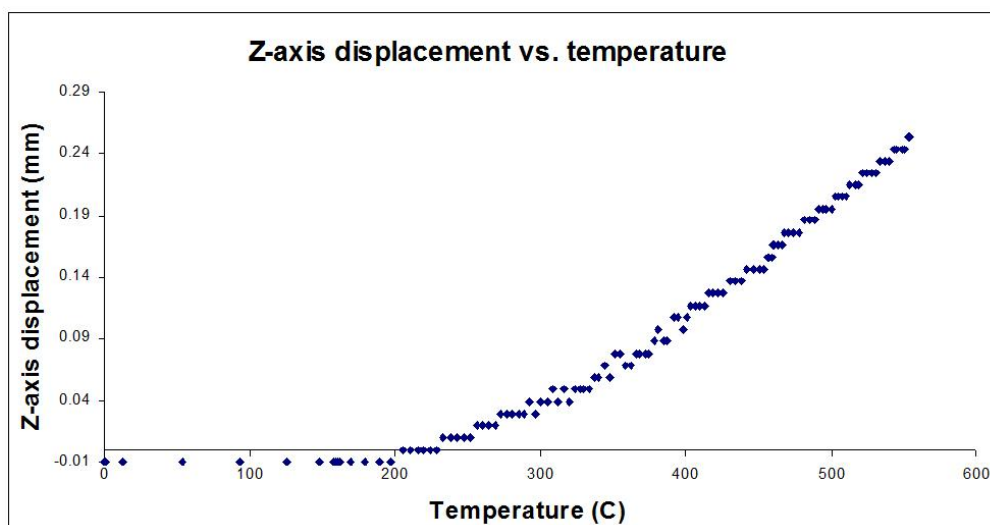


Figure 87. Z-axis displacement versus temperature curve used to find the CTE equation for the graphite tooling.

The data from the SPS machine is recorded as voltage, current, temperature, pressure, and z-axis displacement. We set the data to record every second.

To create a plot of density versus temperature, we need to manipulate the output data as-received. We experimentally measure the specimen's final weight, height, and surface area. Since the specimen has shrunk in height during sintering, we use the measured final height and add back the z-axis change during sintering to get the initial height. We also confirm the initial height with measurements before the experiment is conducted, after pressure has been applied. The z-axis data and the measured parameters (including initial height) are used to calculate density at each time step. We then use the equation for the thermal expansion coefficient for graphite (above), and use the incremental temperature change at each time step to calculate the height difference due to temperature, and subtract that from the z-axis change (at each time step). This gives us the density at each time step during the SPS process, corrected for thermal expansion of the graphite. We use the published value for the density of the material to calculate the relative density at each time step, and we plot this versus temperature to get the densification curves.



Keyence VHX-600 digital HD CCD microscope with 3-D capability. Equipped with 20 to 200x and 200 to 1000x hand-held or mounted magnification lenses and a tilting stage. Primarily utilized for initial characterization of samples including color, impurity, average grain size and morphology.



Precision Vacuum Oven and Pump; necessary for rapid evacuation/ desiccation of powder mixtures, green samples and slurries.



Denton Vacuum Desk IV Cold Sputter Coating device. Bombardment of a sputter target will generate particulate vapor which will condense into very thin, amorphous layers onto available surfaces within the device vacuum chamber. This instrument is primarily utilized for SEM sample preparation.



Struers Tegra Sample Polishing System, used for polishing all specimens.



Buehler ISOMET 1000 precision saw with diamond wafering blades, used for cutting specimens.



"Tinius-Olsen" Universal Testing Machine; This device is utilized for tensile rupture strength (TRS) testing. Compressive and tensile loading data is obtained via rate or force controlled DAQ software and can be exported in Excel executable files.



Large Ney Furnace for pre-sintering, binder burnout and conventional powder sintering with a two-stage heating regime control up to 1100°C.



Ohaus analytical balance with 200g capacity, with readability of 0.1 mg and precision of 0.2 mg.

Calibration was conducted using standards of known mass (25, 50, and 100 grams), which were independently weighed by another balance, and the measured value was compared to the standard.



Leitz Wetzlar Vickers Microhardness tester, with 40x magnification lens (from Germany). Uses a 500 gram load. The crosshairs in the microscope have an accuracy of  $\pm 0.5$  mm. The final HV0.5 has an accuracy of  $\pm 2$ . Calibration was conducted by taking multiple measurements across one pure aluminum and one pure copper specimen, and comparing the values to each other, and the published standard for those materials

## 9.2. Statistical Analysis of Data for Curve-fitting

In this section, I present the results of statistical analysis (f-test, t-test, and correlation) done on the data from experiments and papers. Each analysis compares the experimental data with the predicted data from the model(s) used.

### **My alumina data, $n = 0.5$ , $k = 0.56$**

F-test: 0.994      T-test: 0.95      Correlation: 0.987

### **My TaC data, $n = 0.5$ , $k = 3.8$**

F-test: 0.97      T-test: 0.475      Correlation: 0.982

Since the t-test analyzes whether the data follows a normal distribution, the value is low due to the small number of data points used (three).

### **My Fe-VC data:**

Fitting both data sets,  $n = 0.148$ ,  $k = 0.98$

F-test: 0.997      T-test: 0.559      Correlation: 0.856

The t-test is low here due to the use of two data sets with similar values for each point.

Fitting Fe-0.5V only,  $n = 0.1558$ ,  $k = 1.065$

F-test: 0.995      T-test: 0.85      Correlation: 0.955

Fitting Fe-15V only,  $n = 0.178$ ,  $k = 0.8$

F-test: 0.976      T-test: 0.984      Correlation: 0.983

### **My aluminum data:**

Using a non-linear model,  $n = 0.037$ ,  $k = 1.06$

F-test: 0.012      T-test: 0.955      Correlation: 0.451

The f-test is very low because of the incredibly poor fit of the data to the model.

Using a linear model,  $G_T = 16.1$ ,  $C_x = -15.24$

F-test: 0.874      T-test: 0.36      Correlation: 0.862

The t-test is low due to the similarity in the data of the six specimens.

**Zhao and Harmer's alumina data:**Alumina undoped,  $n = 0.5$ ,  $k = 2.08$ 

F-test: 0.763      T-test: 0.67      Correlation: 0.89

Alumina undoped,  $n = 1.11$ ,  $k = 0.2$ 

F-test: 0.986      T-test: 0.196      Correlation: 0.973

Alumina doped with MgO,  $n = 0.5$ ,  $k = 0.8$ 

F-test: 0.94      T-test: 0.89      Correlation: 0.996

Alumina doped with FeO,  $n = 0.5$ ,  $k = 2.87$ 

F-test: 0.781      T-test: 0.45      Correlation: 0.896

Alumina doped with FeO,  $n = 1.23$ ,  $k = 0.184$ 

F-test: 0.972      T-test: 0.953      Correlation: 0.998

**Zadra et al.'s CP titanium data:**Grade 1,  $n = 0.5$ ,  $k = 0.59$ 

F-test: 0.275      T-test: 0.552      Correlation: 0.958

Grade 2,  $n = 0.5$ ,  $k = 0.5$ 

F-test: 0.962      T-test: 0.926      Correlation: 0.99

**Guillard et al.'s SiC data,  $n = 1.31$ ,  $k = 0.137$** 

F-test: 0.981      T-test: 0.956      Correlation: 0.945

**Olevsky et al.'s aluminum data,  $k = 0.77$ ,  $n = 0.5$** 

F-test: 0.73      T-test: 0.991      Correlation: 0.91

**Cabibbo et al.'s Fe-Mo data,  $n = 0.5$ ,  $k = 0.135$** 

F-test: 0.912      T-test: 0.978      Correlation: 0.993

**Zhang's TaC data,  $n = 0.84$ ,  $k = 0.176$** 

F-test: 0.89      T-test: 0.75      Correlation: 0.942



### 9.3. Taguchi DOE data for Alumina

Initial 12 experiments:

Sample	Time (min)	Temperature (°C)	Pressure (kN)	Die Shape <sup>4</sup>	Particle Size <sup>5</sup>	Final Density
1	15	1400	6.67	1	1	93.0
2	15	1400	6.67	2	1	100.0
3	8	1400	6.67	1	1	100.0
4	8	1400	6.67	2	1	85.0
5	8	1200	6.67	1	2	84.0
6	8	1200	6.67	2	2	89.0
7	8	1300	8.8	1	1	100
8	8	1300	8.8	2	1	94.6
9	15	1300	8.8	1	1	97.7
10	15	1300	8.8	2	1	98.9
11	40	1300	8.8	1	1	86.6
12	40	1300	8.8	2	1	83.9

Minitab results:

A is Time, B is Temperature, C is Pressure, and D is die shape. We can see from the p-values that die shape only has a .491 while the others are less than .06. The overall p-value is .021, while the adjusted  $R^2$  value is .639.

#### Regression Analysis: C6 versus A, B, C, D, E

- \* Particle Size is highly correlated with other X variables
- \* Particle Size has been removed from the equation.

The regression equation is

$$C6 = -0.166 - 0.00373 A + 0.000685 B + 0.0290 C + 0.0168 D$$

Predictor	Coef	SE Coef	T	P
Constant	-0.1662	0.2717	-0.61	0.560
A	-0.003730	0.001166	-3.20	0.015
B	0.0006853	0.0001748	3.92	0.006
C	0.02901	0.01278	2.27	0.058
D	0.01683	0.02314	0.73	0.491

<sup>4</sup> For die shape, a '1' indicates a circular die, and a '2' indicates a square die.

<sup>5</sup> For particle size, a '1' indicates -325 mesh powder, and a '2' indicates a 330 nm powder.

S = 0.0400867    R-Sq = 77.1%    R-Sq(adj) = 63.9%

#### Analysis of Variance

Source	DF	SS	MS	F	P
Regression	4	0.037784	0.009446	5.88	0.021
Residual Error	7	0.011249	0.001607		
Total	11	0.049032			

#### Next 18 Experiments:

Sample	Time (min)	Temperature (°C)	Pressure (kN)	Die Shape <sup>6</sup>	Final Density
1	15	1400	6.67	1	0.930
2	8	1400	6.67	2	1.000
3	8	1400	6.67	1	1.000
4	40	1300	6.67	1	0.950
5	40	1300	6.67	2	0.950
6	8	1300	8.80	1	0.890
7	8	1300	8.80	2	1.000
8	15	1400	6.67	2	0.946
9	15	1300	8.80	1	0.977
10	15	1300	8.80	2	0.989
11	40	1300	8.80	1	1.000
12	40	1300	8.80	2	1.000
13	8	1200	6.67	1	0.857
14	8	1200	6.67	2	0.755
15	15	1200	6.67	1	0.835
16	15	1200	6.67	2	0.772
17	8	1300	6.67	2	0.980
18	15	1300	6.67	1	0.950

#### Minitab Results:

A is Time, B is Temperature, C is Pressure, and D is die shape. We can see from the p-values that die shape only has a .954 while the others are less than .03 (except for temperature, which is .198). The overall p-value is .002, while the adjusted  $R^2$  value is .626.

---

<sup>6</sup> For die shape, a '1' indicates a circular die, and a '2' indicates a square die.

### Regression Analysis: C5 versus A, B, C, D

The regression equation is

$$C5 = -0.366 + 0.00128 A + 0.000821 B + 0.0279 C + 0.0013 D$$

Predictor	Coef	SE Coef	T	P
Constant	-0.3663	0.2393	-1.53	0.150
A	0.0012799	0.0009437	1.36	0.198
B	0.0008213	0.0001703	4.82	0.000
C	0.02794	0.01150	2.43	0.030
D	0.00133	0.02272	0.06	0.954

S = 0.0481710    R-Sq = 71.4%    R-Sq(adj) = 62.6%

### Analysis of Variance

Source	DF	SS	MS	F	P
Regression	4	0.075430	0.018857	8.13	0.002
Residual Error	13	0.030166	0.002320		
Total	17	0.105596			

## Chapter 10. References

- 
- <sup>1</sup> ZA Munir, U Anselmi-Tamburini, M Ohyanagi. “The effect of electric field and pressure on the synthesis and consolidation of materials: A review of the spark plasma sintering method,” *J. Mat. Sci.* 41, 763-77 (2006).
  - <sup>2</sup> M Nygren, ZJ Shen. “On the preparation of bio-, nano- and structural ceramics and composites by spark plasma sintering,” *Solid State Sciences* 5, 125-31 (2003).
  - <sup>3</sup> N Tamari, T Tanaka, K Tanaka, I Kondoh, M Kawahara, M Tokita. “Effect of Spark Plasma Sintering on Densification and Mechanical Properties of Silicon Carbide.” *Journal of the Ceramic Society of Japan* 103, 740-2 (1995).
  - <sup>4</sup> T Nishimura, M Mitomo, H Hirotsumi, M Kawahara. “Fabrication of Silicon Nitride Nanoceramics by Spark Plasma Sintering.” *Journal of Materials Science Letters* 14, 1046-7 (1995).
  - <sup>5</sup> M Omori. “Sintering, consolidation, reaction and crystal growth by the spark plasma system (SPS).” *Mat. Sci. and Eng. A – Structural Materials Properties Micro. And Proc.* 287, 183-8 (2000).
  - <sup>6</sup> ZA Munir, U Anselmi-Tamburini, M Ohyanagi. “The effect of electric field and pressure on the synthesis and consolidation of materials: A review of the spark plasma sintering method.” *J. Mat. Sci.* 41, 763-77 (2006).
  - <sup>7</sup> M Nygren, ZJ Shen. “On the preparation of bio-, nano- and structural ceramics and composites by spark plasma sintering.” *Solid State Sciences* 5, 125-31 (2003).
  - <sup>8</sup> EA Olevsky, S Kandukuri, L Froyen, “Consolidation enhancement in spark-plasma sintering: Impact of high heating rates.” *Journal App. Physics* 102, 114913 (2007).
  - <sup>9</sup> E Olevsky and L Froyen, “Influence of thermal diffusion on spark-plasma sintering”, *J. Amer. Ceram. Soc.*, 92, 122-132 (2009).
  - <sup>10</sup> R Orrù, R Licheri, A Locci, A Cincotti, and G Cao, “Consolidation/synthesis of materials by electric current activated/assisted sintering,” *Materials Science and Engineering R*, 63, 127–287, (2009).
  - <sup>11</sup> DM Hulbert, A Anders, DV Dudina, J Andersson, D Jiang, “The absence of plasma in spark plasma sintering” *J. Appl. Phys.* 104:033305 (2008).

- 
- <sup>12</sup> YH Han, M Nagata, N Uekawa, and K Kakegawa, "Eutectic  $\text{Al}_2\text{O}_3$ - $\text{GdAlO}_3$  composite consolidated by combined rapid quenching and spark plasma sintering technique," *British Ceram. Trans.* 103, 219-222 (2004).
- <sup>13</sup> YS Kwon, DV Dudina, MA Korchagin and OI Lomovsky, "Microstructure changes in  $\text{TiB}_2$ -Cu nanocomposite under sintering," *J. Mater. Sci.* 39, 5325 (2004).
- <sup>14</sup> U Anselmi-Tamburini, JE Garay, ZA Munir, A Tacca, F Maglia, and G Spinolo, "Spark plasma sintering and characterization of bulk nanostructured fully stabilized zirconia: Part I. Densification studies," *J. Mater. Res.* 19, 3255 (2004).
- <sup>15</sup> M Yue, JX Zhang, WQ Liu and GP Wang, "Chemical stability and microstructure of Nd-Fe-B magnet prepared by spark plasma sintering," *J. Magnetism Magnet. Mater.* 271, 364 (2004).
- <sup>16</sup> M Nygren and Z Shen, "Novel assemblies via spark plasma sintering," *Silicates Industr.* 69, 211 (2004).
- <sup>17</sup> B Basu, JH Lee, and DY Kim, "Development of Nanocrystalline Wear-Resistant Y-TZP Ceramics," *J. Amer. Ceram. Soc.* 87, 1771 (2004).
- <sup>18</sup> E Olevsky, "Theory of sintering: from discrete to continuum," *Mat. Sci. and Eng.* R23, 41-100 (1998).
- <sup>19</sup> W Li, EA Olevsky, J McKittrick, AL Maximenko, RM German, "Densification mechanisms of spark plasma sintering: multi-step pressure dilatometry," *J. Mater. Sci.* 47, 7036-46 (2012).
- <sup>20</sup> E Olevsky and L Froyen, Constitutive modeling of spark-plasma sintering of conductive materials, *Scripta Mater.* 55, 1175-1178 (2006).
- <sup>21</sup> R. Chaim, R. Marder-Jaeckel, and J.Z. Shen: Transparent YAG ceramics by surface softening of nanoparticles in spark plasma sintering. *Mater. Sci. Eng.*, A 429, 74 (2006).
- <sup>22</sup> R. Chaim and M. Margulis: Densification maps for spark plasma sintering of nanocrystalline MgO ceramics. *Mater. Sci. Eng.*, A 407, 180 (2005).
- <sup>23</sup> V. Mamedov: Spark plasma sintering as advanced PM sintering method. *Powder Metall.* 45, 322 (2002).
- <sup>24</sup> P Asoka-Kumar, M Alatalo, VJ Ghosh, AC Kruseman, B Nielsen, and KG Lynn, "Increased Elemental Specificity of Positron Annihilation Spectra," *Phys. Rev. Lett.* 77, 2097 (1996).

- 
- <sup>25</sup> JE Garay, SC Glade, U Anselmi-Tamburini, P Asoka-Kumar, and ZA Munir, "Electric Current Enhanced Defect Mobility in  $\text{Ni}_3\text{Ti}$  Intermetallics" *Appl. Phys. Lett.* **85**, 573 (2004).
- <sup>26</sup> R Raj, M Cologna, and JSC Francis, "Influence of externally imposed and internally generated electrical fields on grain growth, diffusional creep, sintering and related phenomena in ceramics," *J. Am. Ceram. Soc.* **94**, 1941-1965 (2011).
- <sup>27</sup> A. Zavaliangos, J. Zhang, M. Krammer, and J. R. Groza, "Temperature Evolution During Field Activated Sintering," *Mater. Sci. Eng. A*, **379**, 218–28 (2004).
- <sup>28</sup> A. Cincotti, A. M. Locci, R. Orru, and G. Cao, "Modeling of SPS Apparatus: Temperature, Current and Strain Distribution with No Powders," *AICHE J.*, **53**, 703–19 (2007).
- <sup>29</sup> X. Wang, S. R. Casolco, G. Xu, and J. E. Garay, "Finite Element Modeling of Electric Current-Activated Sintering: The Effect of Coupled Electrical Potential, Temperature and Stress," *Acta Mater.*, **55**, 3611–22 (2007).
- <sup>30</sup> G. Antou, G. Mathieu, G. Trolliard, and A. Maitre, "Spark Plasma Sintering of Zirconium Carbide and Oxycarbide: Finite Element Modeling of Current Density, Temperature, and Stress Distributions," *J. Mater. Res.*, **24**, 404–12 (2009).
- <sup>31</sup> D. Tiwari, B. Basu, and K. Biswas, "Simulation of Thermal and Electric Field Evolution During Spark Plasma Sintering," *Ceram. Int.*, **35**, 699–708 (2009).
- <sup>32</sup> Vanmeensel, A. Laptev, O. Van der Biest, and J. Vleugels, "Field Assisted Sintering of Electro-Conductive  $\text{ZrO}_2$ -Based Composites," *J. Eur. Ceram. Soc.*, **27**, 979–85 (2007).
- <sup>33</sup> C. Wang, L. F. Cheng, and Z. Zhao, "FEM Analysis of the Temperature and Stress Distribution in Spark Plasma Sintering: Modelling and Experimental Validation," *Comp. Mater. Sci.*, **49**, 351–62 (2010).
- <sup>34</sup> G. Maizza, S. Grasso, and Y. Sakka, "Moving Finite-Element Mesh Model for Aiding Spark Plasma Sintering in Current Control Mode of Pure Ultrafine WC Powder," *J. Mater. Sci.*, **44**, 1219–36 (2009).
- <sup>35</sup> U Anselmi-Tamburini, S Gennari, JE Garay, ZA Munir, "Fundamental investigations on the spark plasma sintering/synthesis process II. Modeling of current and temperature distributions," *Mat. Sci. and Eng. A* **394**, 139-48 (2005).
- <sup>36</sup> JR Groza, A Zavaliangos, "Nanostructured Bulk Solid by Field Activated Sintering," *Rev. Adv. Mater. Sci.* **5**, 24-33 (2003).
- <sup>37</sup> JR Groza, A Zavaliangos, "Sintering Activation by External Electric Field," *Materials Science and Engineering A* **287**, 171-177 (2000).

- 
- <sup>38</sup> JR Groza, JD Curtis, M Kraemer, "Field Assisted Sintering of Nanocrystalline TiN," *J. Am. Cer. Soc.* 83, 1281-83 (2000).
- <sup>39</sup> JR Groza, SH Risbud, K Yamazaki, "PAS of Additive-free AlN Powders to Near-theoretical Density in 5 Minutes," *J. Mater. Res.* 7, 2643-5 (1992).
- <sup>40</sup> O El-Atwani, , DV Quach, M Efe, PR Cantwell, B Heim, B Schultz, EA Stach, JR Groza, JP Allain, "Multimodal grain size distribution and high hardness in fine grained tungsten fabricated by spark plasma sintering", *Materials Science And Engineering A-Structural Materials Properties Microstructure and Processing* 528, 5670-5677, (2011).
- <sup>41</sup> Y Aman, V Garnier, E Djurado, "A Screening Design Approach for the Understanding of Spark Plasma Sintering Parameters: A Case of Translucent Polycrystalline Undoped Alumina", *International Journal of Applied Ceramic Technology* 7, 574-586, (2010).
- <sup>42</sup> RM German, *Sintering Theory and Practice*, (Wiley, New York, 1996).
- <sup>43</sup> DE Clark, and WH Sutton, "Microwave processing of materials," *Ann. Rev. Mater. Sci.* 26, 299 (1996).
- <sup>44</sup> LA Stanciu, VY Kodash, and JR Groza, "Effects of Heating Rate in Field Asisted Sintering," *Metall. Mater. Trans. A* 32A 2633 (2001).
- <sup>45</sup> YW Gua, NH Loha, KA Khor, SB Tor, and P Cheang, "Spark plasma sintering of hydroxyapatite powders", *Biomaterials* 23, 37-43, (2002).
- <sup>46</sup> Y Zhou, K Hirao, Y Yamauchi, and S Kanzaki, "Effects of heating rate and particle size on pulse electric current sintering of alumina," *Scripta Mater.* 48, 1631-6 (2003).
- <sup>47</sup> H Conrad (Ed.), *Mater Sci. Engin.* (special issue), A287(2) (2000), 125-315.
- <sup>48</sup> ZA Munir and H Schmalzried, "The Effect of External Fields on Mass-Transport and Defect-Related Phenomena," *J. Mater Synth. Process.* 1, 3 (1993)..
- <sup>49</sup> R Chaim, "Densification mechanisms in spark plasma sintering of nanocrystalline ceramics," *Materials Science and Engineering A* 443, 25-32 (2007).
- <sup>50</sup> D Tiwari, B Basu, and K Biswas, "Simulation of thermal and electric field evolution during spark plasma sintering," *Ceramics Int.* 35, 699-708 (2009).
- <sup>51</sup> G Xie,, O Ohashi, K Chiba, N Yamaguchi, M Song, K Furuya, and T Noda, "Frequency effect on pulse electric current sintering process of pure aluminum powder," *Mater. Sci. Eng.* A359, 384-90 (2003).

- 
- <sup>52</sup> D Ehre, EY Gutmanas and R Chaim, "Densification of nanocrystalline MgO Ceramics by hot-pressing", *J. Eur. Ceram. Soc.* 25, 3579-3585 (2005).
- <sup>53</sup> A Weibel, R Bouchet, P Bouvier and P Knauth, "Hot compaction of nanocrystalline TiO<sub>2</sub> (anatase) ceramics. Mechanisms of densification: Grain size and doping effects," *Acta Mater.* 54, 3575–3583 (2006).
- <sup>54</sup> SC Liao, YJ Chen, W E Mayo and BH Kear, "Transformation-assisted consolidation of bulk nanocrystalline TiO<sub>2</sub>," *NanoStruct. Mater.* 11, 553– 557 (1999).
- <sup>55</sup> G Skandan, H Hahn, BH Kear, M Roddy and WR Cannon, "The effect of applied stress on densification of nanostructured zirconia during sinter forging," *Mater. Lett.* 20, 305-9 (1994).
- <sup>56</sup> J Xu, SR Casolco, JE Garay, "Effect of varying displacement rates on the densification of nanostructured zirconia by current activation," *J. Am. Ceram. Soc.* 92, 1506–13 (2009).
- <sup>57</sup> R Chaim, L Levin, A Shlayer, and C Estournes, "Sintering and Densification of Nanocrystalline Ceramic Oxide Powders: A Review", *Advances in Applied Ceramics*, 107, 159-169 (2008).
- <sup>58</sup> R Chaim. "Superfast densification of nanocrystalline oxide powders by spark plasma sintering," *J. Mater Sci* 41, 7862–7871 (2006).
- <sup>59</sup> N Millot, S Le Gallet, D Aymes, F Bernard, and Y Grin. "Spark plasma sintering of cobalt ferrite nanopowders prepared by coprecipitation and hydrothermal synthesis," *J. Eur. Cer. Soc.* 27, 921–926 (2007).
- <sup>60</sup> KH Kim, SH Shim, KB Shim, K Niihara, and J Hojo. "Microstructural and Thermoelectric Characteristics of Zinc Oxide-Based Thermoelectric Materials Fabricated Using a Spark Plasma Sintering Process," *J. Am. Ceram. Soc.* 88, 628–632 (2005).
- <sup>61</sup> CA Bruch. "Sintering kinetics for the high density alumina process," *Ceramic Bulletin* 41, 799-806 (1962).
- <sup>62</sup> RM German. "Coarsening in Sintering: Grain Shape Distribution, Grain Size Distribution, and Grain Growth Kinetics in Solid-Pore Systems," *Critical Reviews in Solid State and Materials Sciences* 35, 263–305 (2010).
- <sup>63</sup> HY Suzuki, K Shinozaki, H Kuroki, and S Tashima. "Sintered microstructure and mechanical properties of high purity alumina ceramics made by high-speed centrifugal compaction process," *Key Engineering Materials* Vols. 159-160, 187-192 (1999).



- 
- <sup>64</sup> J Zhao and MP Harmer. "Sintering of ultra-high purity alumina doped simultaneously with MgO and FeO," *J. Am. Ceram. Soc.*, 70, 860 (1987).
- <sup>65</sup> G Bernard-Granger, N Monchalain, and C Guizard. "Sintering of ceramic powders: Determination of the densification and grain growth mechanisms from the 'grain size/relative density' trajectory," *Scripta Materialia* 57, 137–140 (2007).
- <sup>66</sup> G Bernard-Granger and C Guizard. "New relationships between relative density and grain size during solid-state sintering of ceramic powders," *Acta Materialia* 56, 6273–6282 (2008).
- <sup>67</sup> Z He, J Ma, "Grain-growth rate constant of hot-pressed alumina ceramics", *Materials Letters* 44, 14–18 (2000).
- <sup>68</sup> F Guillard, A Allemand, JD Lulewicz, and J Galy. "Densification of SiC by SPS-effects of time, temperature and pressure," *J. Eur. Cer. Soc.* 27, 2725–2728 ((2007).
- <sup>69</sup> EA Olevsky, S Kandukuri, L Froyen. "Consolidation enhancement in spark-plasma sintering: Impact of high heating rates," *J. App. Phys.* 102, 114913 (2007).
- <sup>70</sup> M Cabibbo, C Paternoster, R Cecchini, A Fabrizi, A Molinari, S Libardi, and M Zadra. "A microstructure study of nanostructured Fe–Mo+ 1.5 wt.%SiO<sub>2</sub> and +1.5 wt.%TiO<sub>2</sub> powders compacted by spark plasma sintering," *Materials Science and Engineering A* 496, 121–132 (2008).
- <sup>71</sup> G Bernard-Granger, N Monchalain, C Guizard, "Comparisons of grain size-density trajectory during spark plasma sintering and hot-pressing of zirconia", *Materials Letters* 62, 4555–4558 (2008).
- <sup>72</sup> J Langer, M Hoffman, and O Guillon, "Direct comparison between hot pressing and electric field-assisted sintering of submicron alumina" *Acta Materialia* 57, 5454–5465 (2009).
- <sup>73</sup> J Langer, M Hoffman, and O Guillon, "Electric Field-Assisted Sintering and Hot Pressing of Semiconductive Zinc Oxide: A Comparative Study," *J. Am. Ceram. Soc.*, 94, 2344–2353 (2011).
- <sup>74</sup> J Langer, M Hoffman, and O Guillon, "Electric Field-Assisted Sintering in Comparison with the Hot Pressing of Ytria-Stabilized Zirconia," *J. Am. Ceram. Soc.* 94, 131–138 (2011).

- 
- <sup>75</sup> DS Perera, M Tokita, and S Moricca, "Comparative Study of Fabrication of  $\text{Si}_3\text{N}_4/\text{SiC}$  Composites by Spark Plasma Sintering and Hot Isostatic Pressing," *Journal of the European Ceramic Society* 18, 401-404 (1998).
- <sup>76</sup> F Monteverde, "Ultra-high temperature  $\text{HfB}_2\text{-SiC}$  ceramics consolidated by hot-pressing and spark plasma sintering," *Journal of Alloys and Compounds* 428, 197-205 (2007).
- <sup>77</sup> SW Wang, LD Chen, T Hirai. "Densification of  $\text{Al}_2\text{O}_3$  powder using spark plasma sintering." *Jour. Mat. Res.* 15, 982-7 (2000).
- <sup>78</sup> L Gao, JS Hong, SDDL Torre. "Bending strength and microstructure of  $\text{Al}_2\text{O}_3$  ceramics densified by spark plasma sintering." *Jour. Eur. Cer. Soc.* 20, 2149-52 (2000).
- <sup>79</sup> Lide, David R. *CRC Handbook of Chemistry and Physics 75th ed.* Boca Raton, CRC Press, 1994: 959.
- <sup>80</sup> A Sawaguchi, K Toda, K Niihara. "Mechanical And Electrical Properties of  $\text{Al}_2\text{O}_3/\text{SiC}$  Nanocomposites." *Journal of the Ceramic Society of Japan* 99, 523-6 (1991).
- <sup>81</sup> J Kolodzey, EA Chowdhury, TN Adam, GH Qui, I Rau, JO Olowolafe, JS Suehle, Y Chen. "Electrical conduction and dielectric breakdown in aluminum oxide insulators on silicon." *IEEE Transactions on Electron Devices* 47, 121-8 (2000).
- <sup>82</sup> SW Huang, JG Hwu. "Electrical characterization and process control of cost-effective high-k aluminum oxide gate dielectrics prepared by anodization followed by furnace annealing." *IEEE Transactions on Electron Devices* 50, 1658-64 (2003).
- <sup>83</sup> L Gao, JS Hong, H Miyamoto, SD De La Torre, "Bending strength and microstructure of  $\text{Al}_2\text{O}_3$  ceramics densified by spark plasma sintering," *J. Eur. Ceram. Soc.* 20, 2149-52 (2000).
- <sup>84</sup> SW Wang, LD Chen, T Hirai, "Densification of  $\text{Al}_2\text{O}_3$  powder using spark plasma sintering," *J. Mater. Res.* 15, 982 (2000).
- <sup>85</sup> S Kishimoto, N Shinya. "Compressive behavior of micro-metallic closed cellular materials fabricated by spark-plasma sintering." *Materials Science and Engineering A* 483-484, 679-682 (2008).
- <sup>86</sup> DM Herlach, "Nonequilibrium solidification of undercooled metallic melts," *Mat Sci. and Eng. R - Reports* 12, 177-272 (1994).

- 
- <sup>87</sup> K Matsugi, Y Wang, T Hatayama, O Yanagisawa, M Kiritani, "Rapid consolidation by spark sintering of rapidly solidified 7075 aluminum alloy powder," *Radiat. Eff. Defects* 157, 233 (2002).
- <sup>88</sup> R Nicula, VD Cojocaru, M Stir, J Hennicke, E Burkel, "High-energy ball-milling synthesis and desifcation of Fe-Co alloy nanopowders by field-activated sintering (FAST)," *J. Alloy Compd.* 434, 362-6 (2007).
- <sup>89</sup> RA Oriani, PH Josephic, "Equilibrium aspects of hydrogen-induced cracking of steels," *Acta Metallurgica* 22, 165-74 (1974).
- <sup>90</sup> WJ Hui, H Dong, YQ Weng, "Delayed fracture behavior of CrMo type high strength steel containing vanadium," *J. Iron and Steel Res. Int.* 10, 63-7 (2003).
- <sup>91</sup> R Warren, "Microstructural development during liquid phase sintering of VC-Co alloys," *J. Mat. Sci.* 7, 1434-42 (1972).
- <sup>92</sup> B Chicco, WE Borbidge, E Summerville, "Experimental study of vanadium carbide and carbonitride coatings," *Materials Science and Engineering A* 266, 62-72 (1999).
- <sup>93</sup> T Tanaka, S Nasu, KN Ishihara, PH Shingu, "Mechanical alloying of the high carbon Fe-C system," *Journal of the Less-Common Metals* I71, 237-247 (1991).
- <sup>94</sup> K Feng, M Hong, Y Yang, and W Wang. "Combustion synthesis of VC/Fe composites under the action of an electric field," *Int. J. Refr. Metals & Hard Cer.* 27, 852-7 (2009).
- <sup>95</sup> L He, Y Liu, B Li, H Cao, J Li, "Reaction synthesis of in situ vanadium carbide particulatesreinforced iron matrix composites by spark plasma sintering," *J Mater Sci* 45, 2538-42 (2010).
- <sup>96</sup> R Lagneborg, T Siwecki, S Zajac, and B Hutchinson, "The role of vanadium in microalloyed steels," *Scan. J. Metal.* 28, 186-241 (1999).
- <sup>97</sup> M Eissa, K El-Fawakhry, M Mekkawy, AH Hussein, and A Tafwik, "Low carbon manganese steels microalloyed with vanadium and nitrogen" *Steel Res.* 69, 334-342 (1998).
- <sup>98</sup> AG Rakhshadt, TT Yausheva, KA Lanskaya, and BV Bychkov, "Properties of die steels hardened with vanadium carbonitride," *Metal Sci. and Heat Treat.* 23, 774-80 (1981).
- <sup>99</sup> F Li, A Ardehali Barani, D Ponge, and D Raabe, "Austenite grain coarsening behaviour in a medium carbon Si-Cr spring steel with and without vanadium," *Steel Res. Int.* 77, 590-4 (2006).

- 
- <sup>100</sup> Y Yazawa, T Furuhashi, and T Maki, "Effect of matrix recrystallization on morphology, crystallography and coarsening behavior of vanadium carbide in austenite," *Acta Mat.* 52, 3727-36 (2004).
- <sup>101</sup> E Fras, M Kawalec, and HF Lopez, "Solidification microstructures and mechanical properties of high-vanadium Fe-C-V and Fe-C-V-Si alloys," *Mat. Sci and Eng. A* 594, 193-203 (2009).
- <sup>102</sup> AL Giorgi, EG Szklarz, EK Storms, AL Bowman, BT Matthias. "Effect of composition on the superconducting transition temperature of tantalum carbide and niobium carbide." *Physical Review* 125, 837-8 (1962).
- <sup>103</sup> A.M. Fillippi. "The influence of composition and thermomechanical condition on mechanical properties of TaC and TaB strengthened chromium." *Metallurgical Transactions* 5, 1423-7 (1974).
- <sup>104</sup> X. Zhang, G.E. Hilmas, W.G. Fahrenholtz, D.M. Deason, "Hot Pressing of Tantalum Carbide With and Without Sintering Additives." *J. Am. Ceram. Soc.*, 90 393-401 (2007).
- <sup>105</sup> J.S. Jackson, "Hot Pressing High-Temperature Compounds," *Powder Metall.*, 8, 73-100 (1961).
- <sup>106</sup> L Ramqvist, "Hot Pressing of Metallic Carbides," *Powder Metall.*, 9 26-46 (1966).
- <sup>107</sup> E Roeder and M Klerk, "Studies With the Electron-Beam Microanalyzer on Hot-Pressed Tantalum Carbide Having Small Additions of Manganese and Nickel," *Z. Metalkunde*, 54, 462-70 (1963).
- <sup>108</sup> JJ Fischer, "Hot-Pressing Mixed Carbides of Ta, Hf, and Zr," *Ceram. Bull.*, 43 183-85 (1964).
- <sup>109</sup> G.V. Samonov and R.Y. Petrikina, "Sintering of Metals, Carbides, and Oxides by Hot Pressing," *Phys. Sintering* 2, 1-20 (1970).
- <sup>110</sup> W.C. Yohe and A.L. Ruoff, "Ultrafine-Grain Tantalum Carbide by High Pressure Hot Pressing," *Ceram. Bull.*, 57 [12] 647-51 (1978).
- <sup>111</sup> Z. Shen, M. Johnsson, Z. Zhao, M. Nygren, "Spark plasma sintering of alumina," *J. Am. Ceram. Soc.* 85, 1921-1927 (2002).
- <sup>112</sup> M Sommer, WD Schubert, E Zobetz, P Warbichler, "On the formation of very large WC crystals during sintering of ultrafine WC-Co alloys," *Int. J. Refract. Met. Hard Mater.* 20, 41-50 (2002).

- 
- <sup>113</sup> BR Kim, KD Woo, JM. Doh, JK Yoon, IJ Shon, “Mechanical properties and rapid consolidation of binderless nanostructured tantalum carbide,” *Ceramics International* (*in press*) (2009).
- <sup>114</sup> X Zhang, GE Hilmas, WG Fahrenholtz, DM Deason, “Hot Pressing of Tantalum Carbide With and Without Sintering Additives.” *J. Am. Ceram. Soc.*, 90 393–401 (2007).
- <sup>115</sup> M Tokita, “Development of Square-shaped Large-size WC/Co/Ni system FGM Fabricated by Spark Plasma Sintering (SPS) Method and Its Industrial Applications,” *Materials Science Forum* 492-493, 711-718 (2005).
- <sup>116</sup> S Grasso, Y Sakka, G Maizza, “Electric current activated/assisted sintering (ECAS): a review of patents 1906–2008,” *Sci. Technol. Adv. Mater.* 10, 053001 (2009).
- <sup>117</sup> Kaneuchi A and Morita H 2004 *JP Patent* No. JP 2004-168632 A
- <sup>118</sup> Yamashita F and Wada M 1993 *JP Patent* No. JP 05-198452 A
- <sup>119</sup> Okano M and Izui H 2007 *World Intellectual Property Patent Publ.* No. WO2007069623.
- <sup>120</sup> Ikeda H 2005 *JP Patent* No. JP 2005-272254 A.
- <sup>121</sup> Nakano T, Ide H and Nakamura H 1989 *JP Patent* No. JP 01-228730 A.
- <sup>122</sup> Ward M 1984 *US Patent* No. 4,456,578.
- <sup>123</sup> ASM International. M. Bauser, G. Sauer, K. Siegert, editors. *Extrusion: Second Edition*, p 195-321 (2006).
- <sup>124</sup> ASM International. *Fundamentals of Extrusion*. (2000).
- <sup>125</sup> M Mabuchi, K Kubota, K Higashi, “Effect of hot extrusion on mechanical properties of a Mg-Si-Al alloy,” *Materials Letters* 19, 247-250 (1994).
- <sup>126</sup> M Shahzad and L Wagner, “Microstructure development during extrusion in a wrought Mg–Zn–Zr alloy,” *Scripta Materialia* 60, 536–538 (2009).
- <sup>127</sup> M Chandrasekaran, and YMS John, “Effect of materials and temperature on the forward extrusion of magnesium alloys,” *Materials Science and Engineering A* 381, 308–319 (2004).

- 
- <sup>128</sup> K Morsi, N Nanayakkar, HB McShane, M McLean, "Preliminary evaluation of hot extrusion miniaturization," *J. Mat. Sci.* 34, 2801–2806 (1999).
- <sup>129</sup> H Kwon, M Estili, K Takagi, T Miyazaki, and A Kawasaki, "Combination of hot extrusion and spark plasma sintering for producing carbon nanotube reinforced aluminummatrix composites," *Carbon* 47, 570-7 (2009).
- <sup>130</sup> K Morsi, A El-Desouky, B Johnson, A Mar and S Lanka, "Spark plasma extrusion (SPE): Prospects and potential," *Scripta Materialia* 61, 395–398 (2009).
- <sup>131</sup> Klaus Lichtinghagen, US Patent No. 4420294, 1983.
- <sup>132</sup> K Morsi, AMK Esawi, P Borah, S Lanka, A Sayed, and M Taher, "Properties of single and dual matrix aluminum–carbon nanotube composites processed via spark plasma extrusion (SPE)," *Materials Science and Engineering A* 527, 5686–5690 (2010).
- <sup>133</sup> N Tamari, T Tanaka, K Tanaka, I Kondoh, M Kawahara, M Tokita. "Effect of Spark Plasma Sintering on Densification and Mechanical Properties of Silicon Carbide." *Journal of the Ceramic Society of Japan* 103, 740-2 (1995).
- <sup>134</sup> T Nishimura, M Mitomo, H Hirotsumi, M Kawahara. "Fabrication of Silicon Nitride Nanoceramics by Spark Plasma Sintering." *Journal of Materials Science Letters* 14, 1046-7 (1995).
- <sup>135</sup> M Omori. "Sintering, consolidation, reaction and crystal growth by the spark plasma system (SPS)." *Mat. Sci. and Eng. A – Structural Materials Properties Micro. And Proc.* 287, 183-8 (2000).
- <sup>136</sup> ZA Munir, U Anselmi-Tamburini, M Ohyanagi. "The effect of electric field and pressure on the synthesis and consolidation of materials: A review of the spark plasma sintering method." *J. Mat. Sci.* 41, 763-77 (2006).
- <sup>137</sup> M Nygren, ZJ Shen. "On the preparation of bio-, nano- and structural ceramics and composites by spark plasma sintering." *Solid State Sciences* 5, 125-31 (2003).
- <sup>138</sup> S Kishimoto, N Shinya. "Compressive behavior of micro-metallic closed cellular materials fabricated by spark-plasma sintering." *Materials Science and Engineering A* 483–484, 679–682 (2008).
- <sup>139</sup> SW Wang, LD Chen, T Hirai. "Densification of  $Al_2O_3$  powder using spark plasma sintering." *Jour. Mat. Res.* 15, 982-7 (2000).
- <sup>140</sup> L Gao, JS Hong, SDDL Torre. "Bending strength and microstructure of  $Al_2O_3$  ceramics densified by spark plasma sintering." *J. Eur. Cer. Soc.* 20, 2149-52 (2000).

- 
- <sup>141</sup> CRC Handbook of Chemistry and Physics. 85th ed. CRC Press: Boca Raton, FL, 2005; p 959.
- <sup>142</sup> A Sawaguchi, K Toda, K Niihara. "Mechanical And Electrical Properties of Al<sub>2</sub>O<sub>3</sub>-SiC Nanocomposites." *J. of the Ceramic Society of Japan* 99, 523-6 (1991).
- <sup>143</sup> J Kolodzey, EA Chowdhury, TN Adam, GH Qui, I Rau, JO Olowolafe, JS Suehle, Y Chen. "Electrical conduction and dielectric breakdown in aluminum oxide insulators on silicon." *IEEE Transactions on Electron Devices* 47, 121-8 (2000).
- <sup>144</sup> SW Huang, JG Hwu. "Electrical characterization and process control of cost-effective high-k aluminum oxide gate dielectrics prepared by anodization followed by furnace annealing." *IEEE Transactions on Electron Devices* 50, 1658-64 (2003).
- <sup>145</sup> S Chang, RH Doremus, S Schadler, RW Siegel. "Hot-pressing of nano-size alumina powder and the resulting mechanical properties." *International J. Of App. Cer. Tech.* 1, 172-9 (2004).
- <sup>146</sup> Z Shen, M Johnsson, Z Zhao, and M Nygren. "Spark Plasma Sintering of Alumina", *J. Am. Ceram. Soc.*, 85 [8] 1921–27 (2002).
- <sup>147</sup> Sachs, G., W. "Eisben. mitt. Deut. Mater." *Pruf. Anst* 16, 67-96 (2000).
- <sup>148</sup> BS 812:105.1, 1989. BS (British Standards Institution) BS 812:105.1, 1989. Methods for determination of particle shape: flakiness index.
- <sup>149</sup> ASTM Standard C1499, 2009, "Standard Test Method for Monotonic Equibiaxial Flexural Strength of Advanced Ceramics at Ambient Temperature," ASTM International, West Conshohocken, PA, 2009, DOI: 10.1520/C1499-09, [www.astm.org](http://www.astm.org)
- <sup>150</sup> S Timoshenko. Theory of Plates and Shells. New York: McGraw-Hill, 1940.
- <sup>151</sup> L Lopez-de-la-Torre, B Winkler, J Schreuer, K Knorr, and M Avalos-Borja, "Elastic properties of tantalum carbide (TaC)." *Solid State Communications* 134, 245–250 (2005).
- <sup>152</sup> Kang, S.-J.L., and Jung, Y.-I., "Sintering Kinetics at Final Stage Sintering: Model Calculation and Map Construction," *Acta Mater.* 52, 4573–4578 (2004).
- <sup>153</sup> M.F. Ashby, H.J. Frost, Deformation mechanism maps – The Plasticity and Creep of Metals and Ceramics, Pergamon Press, Oxford, UK, 1982.

- 
- <sup>154</sup> ZZ Du and ACF Cocks, “Constitutive models for the sintering of ceramic components – II. Sintering of inhomogeneous bodies,” *Acta Metall. Mater.* 40, 1981-1994 (1992).
- <sup>155</sup> KT Kim, HG Kim, and HM Jang, “Densification behavior and grain growth of zirconia powder compact under high temperature,” *Int. J. Eng. Sci.* 36, 1295-1312 (1998).
- <sup>156</sup> M. Zadra, F. Casari, L. Girardini, and A. Molinari. “Microstructure and mechanical properties of CP titanium produced by spark plasma sintering”, *Powder Metall.*, 51, 59 (2008).